ZOOLOGICAL RESEARCH

CONTENTS

Cover image: *Tylototriton kachinorum* **sp. nov.**. Photo by Nikolay A. Poyarkov, Jr.
Cover design: Li-Bin Wu

Specific function and modulation of teleost monocytes/macrophages: polarization and phagocytosis

Xin-Jiang Lu[1,2], Jiong Chen[1,2,*]

[1] *Laboratory of Biochemistry and Molecular Biology*, *School of Marine Sciences*, *Ningbo University*, *Ningbo Zhejiang* 315211, *China*
[2] *Key Laboratory of Applied Marine Biotechnology of Ministry of Education*, *Ningbo University*, *Ningbo Zhejiang* 315211, *China*

ABSTRACT

Macrophages exist in most tissues and play a variety of functions in vertebrates. Teleost fish species are found in most aquatic environments throughout the world and are quite diverse for a group of vertebrate animals. Due to whole genome duplication and environmental adaptation, teleost monocytes/macrophages possess a variety of different functions and modulations compared with those of mammals. A deeper understanding of teleost monocytes/macrophages in the immune system will not only help develop teleost-specific methods of disease prevention but will also help improve our understanding of the various immune mechanisms in mammals. In this review, we summarize the differences in polarization and phagocytosis of teleost and mammalian macrophages to improve our understanding of the various immune mechanisms in vertebrates.

Keywords: Teleost; Monocytes /Macrophages; Phagocytosis; Cytokine production; Comparative immunology

INTRODUCTION

Macrophages exist in most animal tissues, in which they play a variety of functions. They are known by different names in various groups, such as amebocytes, hemocytes, coelomocytes, granulocytes, monocytes, and macrophages, but have similar morphology and comparable functions (Bilej et al., 2000; Wiegertjes et al., 2016). Macrophages are best known for their role in immunity, as elucidated by Eli Metchnikoff in the late nineteenth century (Tauber, 2003). Several studies have highlighted the wide range of functions of macrophages in vertebrate biology, including systemic metabolism, cold adaptation, tissue homeostasis, and development (Okabe & Medzhitov, 2016; Wynn et al., 2013). The basic functions of macrophages in vertebrates are cytokine production and phagocytosis (Hodgkinson et al., 2015). In both mammals and fish, monocytes give rise to macrophages during inflammatory conditions (Hodgkinson et al., 2015). Moreover, macrophage colony stimulating factor (CSF1) plays a crucial role in macrophage growth and differentiation in both mammals and fish (Hodgkinson et al., 2015). Teleosts are among the evolutionarily oldest vertebrates, possessing both innate and classical adaptive immune systems (Dickerson & Findly, 2017). Environmental factors have been shown to affect the immune system of teleosts (Makrinos & Bowden, 2016), which are widespread in most aquatic environments. Various immune genes in non-model teleosts have been identified, with transcriptome and genome development (Mackintosh & Ferrier, 2017; Qian et al., 2014; Shao et al., 2016), providing an opportunity to conduct studies on the adaptive evolution of the immune system. In this review, we focus on the differences in polarization and phagocytosis of teleost and mammalian macrophages, which should help in the development of a new perspective on macrophages and their role in adaptive evolution.

DEFINITION OF MONOCYTES/MACROPHAGES IN TELEOSTS

Monocytes/macrophages in mammals are an important component of the mononuclear phagocytic system, and play diverse roles during infection, inflammation, and tissue injury and repair (Okabe & Medzhitov, 2016). In mammals, protein markers are used to identify monocytes, macrophages, and dendritic cells by flow cytometry. Monocytes, which mainly

exist in bone marrow, blood, and spleen, can further differentiate into inflammatory macrophages and dendritic cells during inflammation (Ray & Rai, 2017; Shi & Pamer, 2011). Their migration to tissues and differentiation into inflammatory macrophages and dendritic cells are determined by the inflammatory milieu and pattern recognition receptors on the cells (Murray, 2018). Macrophages reside in a variety of tissues, including lymphoid and non-lymphoid tissues. They are equipped with a broad range of pattern recognition receptors to facilitate cytokine production and phagocytosis during inflammatory responses (Franz & Kagan, 2017). Classical dendritic cells are specialized antigen processing and presenting cells that exhibit high phagocytic activity as immature cells and high cytokine-producing capacity as mature cells (Qian & Cao, 2018).

In teleosts, monocytes/macrophages have been identified in a variety of species, including rainbow trout (*Oncorhynchus mykiss*) (Leal et al., 2017), zebrafish (*Danio rerio*) (Yu et al., 2017), goldfish (*Carassius auratus* L.) (Hodgkinson et al., 2017), and ayu (*Plecoglossus altivelis*) (Lu et al., 2017). The human CD14 antigen is highly expressed in monocytes and to a lesser extent in macrophages (Shi & Pamer, 2011; Zhang et al., 2017). However, CD14 has not been identified in the teleost genome (Novoa et al., 2009). Hence, it is difficult to discriminate between teleost monocytes and macrophages based on protein markers using flow cytometry. Stafford et al. (2001) developed a method using cell-conditioned medium to obtain monocyte-like cells in rainbow trout. However, it is unclear whether monocytes can be identified from the culture of teleost monocytes / macrophages based on acute isolation using simple procedures, such as flow cytometry. Although dendritic-like cells have been identified in rainbow trout (Soleto et al., 2018), it is unclear whether such cells exist in other dominant teleost species. As monocytes and macrophages share similar characteristics, most teleost investigations have defined the adhered mononuclear cells of the kidney or head kidney as monocytes/macrophages or macrophages.

Phagocytosis is the defining characteristic of macrophages (large eaters), as classified by Metchnikoff (Tauber, 2003). However, most phagocytes among the peripheral blood mononuclear cells of teleosts are IgM⁺ B lymphocytes, not monocytes / macrophages (Li et al., 2006). Thus, morphological analysis, apart from phagocytosis index analysis, is necessary to identify the monocytes/macrophages in teleosts.

MACROPHAGE POLARIZATION AND CYTOKINE PRODUCTION

In vertebrates, the inflammatory response of macrophages plays an important role against pathogens (Geissmann et al., 2010; Ricci et al., 2018). Macrophage polarization against different inflammatory stimuli depends on environmental cues or pathophysiological conditions (Lawrence & Natoli, 2011). Classically activated macrophages (M1 type) are induced by lipopolysaccharides (LPSs), a major component of the outer membrane of gram-negative bacteria, and IFN-γ, and express

pro-inflammatory mediators. Conversely, alternatively activated macrophages (M2 type) are induced by IL-4 and IL-13, and express high levels of anti-inflammatory mediators (Shapouri-Moghaddam et al., 2018). Macrophage polarization is also regulated by soluble proteins, intracellular signals, and transcription factors. Galectin-dependent regulatory signaling stimulates M2-type macrophage polarization (Blidner et al., 2015). Toll-like receptor (TLR) signaling activates the signal transducer and activator of transcription (STAT) 1 protein to skew macrophage function towards the M1 type, whereas activation of STAT3 by IL-4 and IL-13 skews macrophage function towards the M2 type (Sica & Mantovani, 2012). Similarly, the ablation of protein kinase B α (PKBα/Akt1) or protein kinase B β (PKBβ/Akt2) differentially affect macrophage polarization (Arranz et al., 2012). Tissue milieus with M1 type are biased towards cell-mediated cytotoxicity, whereas the term "M2 type" is used for a variety of conditions that inhibit M1 type (Yamaguchi et al., 2015). The immune milieus are skewed to M2 type in some tissues, like the gills in teleosts and uterus in pregnant mammals (Yamaguchi et al., 2015).

Monocyte / macrophage polarization has also been detected in teleosts (Wiegertjes et al., 2016). Cytokines participate in teleost monocyte / macrophage polarization, particularly IFN-γ and IL-4 / IL-13 (Wiegertjes et al., 2016). Moreover, inducible nitric oxide synthase (iNOS) is a marker for M1 type and arginase 2 is a marker for M2 type in teleost monocytes / macrophages (Wiegertjes et al., 2016). In carp, the expression of pro-inflammatory cytokines IL-1β, TNF-α, and CXCa, peak in peritoneal leukocytes 24 h after zymosan induction, whereas the expression of anti-inflammatory mediators IL-10 and arginase 2 peak 96 h and 168 h after zymosan induction, respectively (Chadzinska et al., 2008). This suggests that monocytes/macrophages display both classic- and alternative pathway-induced polarization upon immune stimulation *in vivo*. Monocyte / macrophage polarization in teleosts has also been investigated *in vitro*. LPSs from gram-negative bacteria are probably the best studied microbial stimuli for macrophage activation. However, the mammalian LPS receptor, TLR4, may not be functional in teleosts (Sepulcre et al., 2009). The presence of LPSs may be sensed by other mechanisms in teleosts, as LPSs are still thought to be important immune stimulators (Meng et al., 2012). Nitrite production in *in vitro* monocyte/macrophage culture is up-regulated after LPS stimulation in teleosts (Joerink et al., 2006). Other pro-inflammatory mediators, such as IL-1β, IL-12, and iNOS are also up-regulated in LPS-stimulated teleost monocytes / macrophages (Joerink et al., 2006), suggesting that LPS induces an M1-type polarization in teleost monocytes / macrophages. In mammals, M2-type polarization is mainly induced by IL-4, IL-13, parasite infection, CSF1, TGF-β, and IL-10 (Sica & Mantovani, 2012). Apart from anti-inflammatory mediators, cAMP plays an important role in M2-type monocyte/ macrophage polarization signaling (Bystrom et al., 2008). In teleosts, at least two IL-4/IL-13 genes exist (IL-4/13A and IL-4/ 13B), both with low homology to IL-4 and IL-13 (Ohtani et al., 2008). In goldfish, recombinant IL-4/13 has been found to induce arginase activity and down-regulate the nitric oxide

(NO) response in primary monocytes/macrophages (Hodgkinson et al., 2017), suggesting IL-4/13 functions to induce M2-type polarization in teleost monocytes / macrophages. In teleost carp (Joerink et al., 2006) and ayu (Chen et al., 2018), cAMP has also been employed to successfully induce M2-type monocyte/macrophage polarization.

Several new mechanisms for macrophage polarization have been identified recently. Mammals possess single IFN-γ molecules that are important in the activation of M1-type macrophages (Grayfer et al., 2018). Many teleosts have multiple IFN-γ molecules, some of which are elicitors of reactive oxygen species (ROS) but not NO, whereas others elicit NO but limited ROS (Grayfer et al., 2018). Although functional analogs of the mammalian M1/M2 macrophage subsets are present in teleosts, defining the regulatory mechanisms governing the polarization of these effector populations is a far more challenging goal (Grayfer et al., 2018). Many immune genes exist in two copies in the teleost genome due to genome duplication (Aghaallaei et al., 2010). These redundant genes may result in sub-functionalization, as in the case of European sea bass (*Dicentrarchus labrax*), in which different hepcidins exhibit different roles (Neves et al., 2015). We observed that ayu has two CXCR3 genes, which contribute to monocyte / macrophage polarization (Lu et al., 2017). In mammals, the chemokine receptor CXCR3 exists as a single gene, and is preferentially expressed on immune cells to aid in cell migration to the sites of inflammation (Bromley et al., 2008). Furthermore, CXCR3.1 (CXCR3b) and CXCR3.2 (CXCR3a) are found in zebrafish (*Danio rerio*), Japanese ricefish (*Oryzias latipes*), spotted green pufferfish (*Tetraodon nigroviridis*), ayu (*Plecoglossus altivelis*), and grass carp (*Ctenopharyngodon idella*) (Aghaallaei et al., 2010; Lu et al., 2017). However, more research is necessary to illustrate the teleost-specific mechanisms of monocyte/ macrophage polarization.

PHAGOCYTOSIS BY MONOCYTES/MACROPHAGES

Phagocytosis is an important cellular process for the induction of antimicrobial responses and regulation of adaptive immunity (Rieger et al., 2012). After phagocytosis, both teleost and mammalian macrophages show pro-inflammatory and homeostatic responses (Rieger et al., 2012). Mammalian neutrophils have the capacity to internalize apoptotic bodies, whereas teleost neutrophils do not possess the same activity (Rieger et al., 2012). Most studies have shown that in fish, monocytes, macrophages, and neutrophils are the main phagocytic cells, as found in mammals (Esteban et al., 2015). Furthermore, phagocytosis in teleosts has been observed in several other kinds of cells, including B-1 cells (Li et al., 2006), γδ-T cells (Wan et al., 2016), and thrombocytes (Nagasawa et al., 2014). Although mammalian phagocytosis has also been observed in B-1 cells (Parra et al., 2012) and γδ-T cells (Wu et al., 2009), its presence in thrombocytes seems unique to teleosts. It is well established that teleost

monocytes/macrophages generate reactive oxygen intermediates as part of antimicrobial defense, similar to that observed in mammalian macrophages (Hodgkinson et al., 2015). However, significant differences between goldfish and mice have been observed in response to pro-inflammatory and homeostatic internalization signals during phagocytosis of immune cells (Rieger et al., 2012). When European sea bass (*Dicentrarchus labrax*) monocytes/macrophages have been incubated with different pathogenic agents, different pathogens have been observed to have different effects on monocyte/ macrophage activity (Bennani et al., 1995). However, further investigation is necessary to illustrate the specific mechanisms of pathogen recognition and phagocytosis in teleosts.

Phagocytosis in mammals is triggered by pathogen recognition, which is a complex process involving a variety of pattern-recognition receptors. The main pattern-recognition receptors include lectin-like recognition molecules, C-type lectins, scavenger receptors, mannose receptors, CD14, and Toll-like receptors (Uribe-Querol & Rosales, 2017). In teleosts, the pathogen recognition mechanism is different from that of mammals. LPSs are sensed by a variety of pattern-recognition receptors (Ranf, 2016) present on the cell surface (Triantafilou & Triantafilou, 2002). Phagocytosis in macrophages is regulated by LPS recognition receptors, such as TLR4 (Lv et al., 2017) and CD14 (Lingnau et al., 2007). TLR4 was the first receptor identified to be involved in the recognition of LPSs. TLR4 must be associated with myeloid differentiation protein 2 (MD2) for interaction with LPSs, and activation of TLR4 is preceded by the transfer of LPSs to CD14 by an LPS-binding protein (Neyen & Lemaitre, 2016). However, CD14 and MD2 do not exist in teleost genomes (Iliev et al., 2005). Thus, it remains unclear how teleost monocytes/macrophages compensate for the CD14 function during phagocytosis of pathogens.

FUTURE DEVELOPMENTS

Teleost fish species are found throughout the world and are quite diverse for a group of vertebrate animals. Monocytes/ macrophages are the basic immune cells not only in mammals but also in teleosts. Monocytes/macrophages are easy to isolate, purify, and segregate, providing us with a useful tool for understanding the differences between the immune systems of mammals and teleosts. Although the basic function of monocytes/macrophages is similar in vertebrates, there are a variety of different points between mammals and teleosts (Figure 1). These differences have likely arisen from genetic factors, such as whole genome duplication, and environmental adaptations. Whole genome duplication in teleosts produces a variety of redundant genes, which may be sub-functional during adaptive evolution. Gene function in teleosts is modulated by environmental factors, such as salinity, hypoxic conditions, and temperature. Therefore, future investigations regarding the mechanisms of teleost monocyte / macrophage polarization and phagocytosis under the influence of various environmental factors are necessary. A deeper understanding of the teleost immune system will not only help develop

teleost-specific methods of disease prevention but will also help improve our understanding of the various immune mechanisms within mammals.
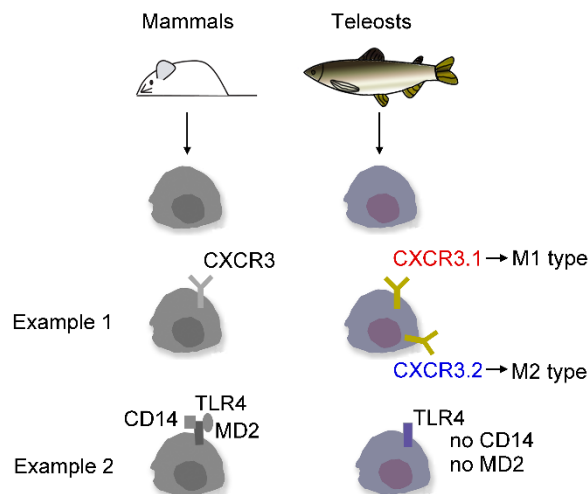

Figure 1 Differences in monocytes/macrophages between mammals and teleosts

COMPETING INTERESTS

The authors declare that they have no competing interests.

AUTHORS' CONTRIBUTIONS

X.J.L. and J.C. designed the study. J.C. and X.J.L. revised the manuscript. All authors read and approved the final version of the manuscript.

REFERENCES

Aghaallaei N, Bajoghli B, Schwarz H, Schorpp M, Boehm T. 2010. Characterization of mononuclear phagocytic cells in medaka fish transgenic for a cxcr3a: gfp reporter. *Proceedings of the National Academy of Sciences of the United States of America*, **107**(42): 18079–18084.

Arranz A, Doxaki C, Vergadi E, Martinez De La Torre Y, Vaporidi K, Lagoudaki ED, Ieronymaki E, Androulidaki A, Venihaki M, Margioris AN, Stathopoulos EN, Tsichlis PN, Tsatsanis C. 2012. Akt1 and Akt2 protein kinases differentially contribute to macrophage polarization. *Proceedings of the National Academy of Sciences of the United States of America*, **109**(24): 9517–9522.

Bennani N, Schmid-Alliana A, Lafaurie M. 1995. Evaluation of phagocytic activity in a teleost fish, *Dicentrarchus labrax*. *Fish & Shellfish Immunology*, **5**(3): 237–246.

Bilej M, De Baetselier P, Beschin A. 2000. Antimicrobial defense of the earthworm. *Folia Microbiologica*, **45**(4): 283.

Blidner AG, Méndez-Huergo SP, Cagnoni AJ, Rabinovich GA. 2015. Re-wiring regulatory cell networks in immunity by galectin-glycan interactions. *Febs Letters*, **589**(22): 3407–3418.

Bromley SK, Mempel TR, Luster AD. 2008. Orchestrating the orchestrators: chemokines in control of T cell traffic. *Nature Immunology*, **9**(9): 970–980.

Bystrom J, Evans I, Newson J, Stables M, Toor I, Van Rooijen N, Crawford M, Colville-Nash P, Farrow S, Gilroy DW. 2008. Resolution-phase macrophages possess a unique inflammatory phenotype that is controlled by cAMP. *Blood*, **112**(10): 4117–4127.

Chadzinska M, Leon-Kloosterziel KM, Plytycz B, Lidy Verburg-Van Kemenade BM. 2008. *In vivo* kinetics of cytokine expression during peritonitis in carp: evidence for innate and alternative macrophage polarization. *Developmental & Comparative Immunology*, **32**(5): 509–518.

Chen F, Lu XJ, Nie L, Ning YJ, Chen J. 2018. Molecular characterization of a CC motif chemokine 19-like gene in ayu (*Plecoglossus altivelis*) and its role in leukocyte trafficking. *Fish & Shellfish Immunology*, **72**: 301–308.

Dickerson HW, Findly RC. 2017. Vertebrate adaptive immunity—comparative insights from a teleost model. *Frontiers in Immunology*, **8**: 1379.

Esteban MÁ, Cuesta A, Chaves-Pozo E, Meseguer J. 2015. Phagocytosis in teleosts. *implications of the new cells involved. Biology*, **4**(4): 907–922.

Franz KM, Kagan JC. 2017. Innate immune receptors as competitive determinants of cell fate. *Molecular Cell*, **66**(6): 750–760.

Geissmann F, Manz MG, Jung S, Sieweke MH, Merad M, Ley K. 2010. Development of monocytes, macrophages, and dendritic cells. *Science*, **327**(5966): 656–661.

Grayfer L, Kerimoglu B, Yaparla A, Hodgkinson JW, Xie J, Belosevic M. 2018. Mechanisms of fish macrophage antimicrobial immunity. *Frontiers in Immunology*, **9**: 1105.

Hodgkinson JW, Fibke C, Belosevic M. 2017. Recombinant IL-4/13A and IL-4/13B induce arginase activity and down-regulate nitric oxide response of primary goldfish (*Carassius auratus* L.) *macrophages. Developmental & Comparative Immunology*, **67**: 377–384.

Hodgkinson JW, Grayfer L, Belosevic M. 2015. Biology of bony fish macrophages. *Biology*, **4**(4): 881–906.

Iliev DB, Roach JC, Mackenzie S, Planas JV, Goetz FW. 2005. Endotoxin recognition: in fish or not in fish?. *Febs Letters*, **579**(29): 6519–6528.

Joerink M, Ribeiro CMS, Stet RJM, Hermsen T, Savelkoul HFJ, Wiegertjes GF. 2006. Head kidney-derived macrophages of common carp (*Cyprinus carpio* L.) *show plasticity and functional polarization upon differential stimulation. The Journal of Immunology*, **177**(1): 61–69.

Lawrence T, Natoli G. 2011. Transcriptional regulation of macrophage polarization: enabling diversity with identity. *Nature Reviews Immunology*, **11**(11): 750–761.

Leal E, Zarza C, Tafalla C. 2017. Effect of vitamin C on innate immune responses of rainbow trout (*Oncorhynchus mykiss*) leukocytes. *Fish & Shellfish Immunology*, **67**: 179–188.

Li J, Barreda DR, Zhang YA, Boshra H, Gelman AE, Lapatra S, Tort L, Sunyer JO. 2006. B lymphocytes from early vertebrates have potent phagocytic and microbicidal abilities. *Nature Immunology*, **7**(10): 1116–1124.

Lingnau M, Höflich C, Volk HD, Sabat R, Döcke WD. 2007. Interleukin-10 enhances the CD14-dependent phagocytosis of bacteria and apoptotic cells by human monocytes. *Human Immunology*, **68**(9): 730–738.

Lu XJ, Chen Q, Rong YJ, Chen F, Chen J. 2017. CXCR3.*1 and CXCR3.2 differentially contribute to macrophage polarization in teleost fish. The Journal of Immunology*, **198**(12): 4692–4706.

Lv JZ, He XY, Wang HT, Wang ZH, Kelly GT, Wang XJ, Chen Y, Wang T, Qian ZQ. 2017. TLR4-NOX2 axis regulates the phagocytosis and killing of mycobacterium tuberculosis by macrophages. *BMC Pulmonary Medicine*, **17**(1): 194.

Mackintosh C, Ferrier DEK . 2017. Recent advances in understanding the roles of whole genome duplications in evolution. F1000*Research*, **6**: 1623.

Makrinos DL, Bowden TJ. 2016. Natural environmental impacts on teleost immune function. *Fish & Shellfish Immunology*, **53**: 50–57.

Meng Z, Zhang XY, Guo J, Xiang LX, Shao JZ. 2012. Scavenger receptor in fish is a lipopolysaccharide recognition molecule involved in negative regulation of NF‑κB activation by competing with TNF receptor-associated factor 2 recruitment into the TNF‑α signaling pathway. *The Journal of Immunology*, **189**(8): 4024–4039.

Murray PJ. 2018. Immune regulation by monocytes. *Seminars in Immunology*, **35**: 12–18.

Nagasawa T, Nakayasu C, Rieger AM, Barreda DR, Somamoto T, Nakao M. 2014. Phagocytosis by thrombocytes is a conserved innate immune mechanism in lower vertebrates. *Frontiers in Immunology*, **5**: 445.

Neves JV, Caldas C, Vieira I, Ramos MF, Rodrigues PNS . 2015. Multiple hepcidins in a teleost fish, *Dicentrarchus labrax*: different hepcidins for different roles. *The Journal of Immunology*, **195**(6): 2696–2709.

Neyen C, Lemaitre B. 2016. Sensing gram-negative bacteria: a phylogenetic perspective. *Current Opinion in Immunology*, **38**: 8–17.

Novoa B, Bowman TV, Zon L, Figueras A. 2009. LPS response and tolerance in the zebrafish (*Danio rerio*). *Fish & Shellfish Immunology*, **26**(2): 326–331.

Ohtani M, Hayashi N, Hashimoto K, Nakanishi T, Dijkstra JM. 2008. Comprehensive clarification of two paralogous interleukin 4/13 loci in teleost fish. *Immunogenetics*, **60**(7): 383–397.

Okabe Y, Medzhitov R. 2016. Tissue biology perspective on macrophages. *Nature Immunology*, **17**(1): 9–17.

Parra D, Rieger AM, Li J, Zhang YA, Randall LM, Hunter CA, Barreda DR, Sunyer JO. 2012. Pivotal advance: peritoneal cavity B-1 B cells have phagocytic and microbicidal capacities and present phagocytosed antigen to CD4+ T cells. *Journal of Leukocyte Biology*, **91**(4): 525–536.

Qian C, Cao XT. 2018. Dendritic cells in the regulation of immunity and inflammation. *Seminars in Immunology*, **35**: 3–11.

Qian X, Ba Y, Zhuang QF, Zhong GF. 2014. RNA-Seq technology and its application in fish transcriptomics. *Omics A Journal of Integrative Biology*, **18**(2): 98–110.

Ranf S. 2016. Immune sensing of lipopolysaccharide in plants and animals: same but different. *PLoS Pathogens*, **12**(6): e1005596.

Ray R, Rai V. 2017. Lysophosphatidic acid converts monocytes into macrophages in both mice and humans. *Blood*, **129**(9): 1177–1183.

Ricci C, Ruscica M, Camera M, Rossetti L, Macchi C, Colciago A, Zanotti I, Lupo MG, Adorni MP, Cicero AFG, Fogacci F, Corsini A, Ferri N. 2018. PCSK9 induces a pro-inflammatory response in macrophages. *Scientific Reports*, **8**(1): 2267.

Rieger AM, Konowalchuk JD, Grayfer L, Katzenback BA, Havixbeck JJ, Kiemele MD, Belosevic M, Barreda DR. 2012. Fish and mammalian phagocytes differentially regulate pro-inflammatory and homeostatic responses in vivo. *PLoS One*, **7**(10): e47070.

Sepulcre MP, Alcaraz-Pérez F, López-Muñoz A, Roca FJ, Meseguer J, Cayuela ML, Mulero V. 2009. Evolution of lipopolysaccharide (LPS) recognition and signaling: fish TLR4 does not recognize LPS and negatively regulates NF-κB activation. *The Journal of Immunology*, **182**(4): 1836–1845.

Shao CW, Bao BL, Xie ZY, Chen XY, Li B, Jia XD, Yao QL, Ortí G, Li WH, Li XH, Hamre K, Xu J, Wang L, Chen FY, Tian YS, Schreiber AM, Wang N, Wei F, Zhang JL, Dong ZD, Gao L, Gai JW, Sakamoto T, Mo SD, Chen WJ, Shi Q, Li H, Xiu YJ, Li YZ, Xu WT, Shi ZY, Zhang GJ, Power DM, Wang QY, Schartl M, Chen SL. 2016. The genome and transcriptome of Japanese flounder provide insights into flatfish asymmetry. *Nature Genetics*, **49**(1): 119–124.

Shapouri-Moghaddam A, Mohammadian S, Vazini H, Taghadosi M, Esmaeili S-A, Mardani F, Seifi B, Mohammadi A, Afshari JT, Sahebkar A. 2018. Macrophage plasticity, polarization, and function in health and disease. *Journal of Cellular Physiology Banner*, **233**(9): 6425–6440.

Shi C, Pamer EG. 2011. Monocyte recruitment during infection and inflammation. *Nature Reviews Immunology*, **11**(11): 762–774.

Sica A, Mantovani A. 2012. Macrophage plasticity and polarization: *in vivo* veritas. *Journal of Clinical Investigation*, **122**(3): 787–795.

Soleto I, Fischer U, Tafalla C, Granja AG. 2018. Identification of a potential common ancestor for mammalian cross-presenting dendritic cells in teleost respiratory surfaces. *Frontiers in Immunology*, **9**:59.

Stafford JL, Mclauchlan PE, Secombes CJ, Ellis AE, Belosevic M. 2001. Generation of primary monocyte-like cultures from rainbow trout head kidney leukocytes. *Developmental & Comparative Immunology*, **25**(5 − 6): 447–459.

Tauber AI. 2003. Metchnikoff and the phagocytosis theory. *Nature Reviews Molecular Cell Biology*, **4**(11): 897–901.

Triantafilou M, Triantafilou K. 2002. Lipopolysaccharide recognition: CD14, TLRs and the LPS-activation cluster. *Trends in Immunology*, **23**(6): 301–304.

Uribe-Querol E, Rosales C. 2017. Control of phagocytosis by microbial pathogens. *Frontiers in Immunology*, **8**:1368.

Wan F, Hu CB, Ma JX, Gao K, Xiang LX, Shao JZ. 2016. Characterization of γδ T cells from zebrafish provides insights into their important role in adaptive humoral immunity. *Frontiers in Immunology*, **7**(3): 675.

Wiegertjes GF, Wentzel AS, Spaink HP, Elks PM, Fink IR. 2016. Polarization of immune responses in fish: the 'macrophages first' point of view. *Molecular Immunology*, **69**(3): 146–156.

Wu Y, Wu WT, Wong WM, Ward E, Thrasher AJ, Goldblatt D, Osman M, Digard P, Canaday DH, Gustafsson K. 2009. Human γδ T cells: a lymphoid lineage cell capable of professional phagocytosis. *The Journal of Immunology*, **183**(9): 5622–5629.

Wynn TA, Chawla A, Pollard JW. 2013. Macrophage biology in development, homeostasis and disease. *Nature*, **496**(7446): 445–455.

Yamaguchi T, Takizawa F, Fischer U, & Dijkstra JM. 2015. Along the axis between type 1 and type 2 immunity; principles conserved in evolution from fish to mammals. *Biology*, **4**(4): 814–859.

Yu T, Guo WL, Tian Y, Xu J, Chen JH, Li L, Wen ZL. 2017. Distinct regulatory networks control the development of macrophages of different origins in zebrafish. *Blood*, **129**(4): 509–519.

Zhang M, Zhu HP, Ding Y, Liu ZY, Cai ZJ, Zou M-H. 2017. AMP-activated protein kinase α1 promotes atherogenesis by increasing monocyte-to-macrophage differentiation. *Journal of Biological Chemistry*, **292**(19): 7888–7903.

A new species of Crocodile Newt, genus *Tylototriton* (Amphibia, Caudata, Salamandridae) from the mountains of Kachin State, northern Myanmar

Than Zaw[1], Paw Lay[2], Parinya Pawangkhanant[3], Vladislav A. Gorin[4], Nikolay A. Poyarkov, Jr.[4,5,*]

[1]*Zoology Department, Mohnyin Degree College, Mohnyin, Kachin State, Myanmar*

[2]*Flora and Fauna International, Lon Ton Village, Indawgyi, Kachin State, Myanmar*

[3]*Bansomdejchaopraya Rajabhat University, Hiran Ruchi, Thon Buri, Bangkok* 10600*, Thailand*

[4]*Department of Vertebrate Zoology, Biological Faculty, Lomonosov Moscow State University, Moscow* 119234*, Russia*

[5]*Joint Russian-Vietnamese Tropical Research and Technological Center, Nghia Do, Cau Giay, Hanoi, Vietnam*

ABSTRACT

We describe a new species of the genus *Tylototriton* from Ingyin Taung Mt., Mohnyin Township, Kachin State, Myanmar, based on morphological and molecular evidence. The new species is assigned to the subgenus *Tylototriton* s. str. and is clearly distinct from all known congeners by the following characters: medium body size; thin, long tail, lacking lateral grooves; rough skin; truncate snout; wide, protruding supratemporal bony ridges on head, beginning at anterior corner of orbit; weak, almost indistinct sagittal ridge; long, thin limbs, broadly overlapping when adpressed along body; distinct, wide, non-segmented vertebral ridge; 13 or 14 rib nodules; brown to dark-brown background coloration with dull orange-brown to yellowish-brown markings on labial regions, parotoids, rib nodules, whole limbs, vent, and ventral tail ridge. We also briefly discuss biogeography and species diversity of the genus *Tylototriton* in Myanmar.

Keywords: *Tylototriton kachinorum* **sp. nov.**; mtDNA genealogy; ND2; 16S rRNA; Shan; Biogeography; Endemism; Taxonomy

INTRODUCTION

The salamandrid genus *Tylototriton* Anderson, 1871, or Crocodile Newts, currently includes 24 recognized species, inhabiting montane forest areas throughout the Asian monsoon climate zone from eastern Himalaya, southern and central China including Hainan Island, to northern Indochina including Vietnam, Laos, Thailand, and Myanmar (Hernandez, 2016; Wang et al., 2018). Recent progress in phylogenetic studies of the genus *Tylototriton* has indicated that the genus is monophyletic (Nishikawa et al., 2013a, 2013b; Phimmachak et al., 2015; Wang et al., 2018) and includes two major groups, corresponding to the subgenera *Tylototriton* s. str. and *Yaotriton* (Wang et al., 2018). Molecular taxonomy methods have proven to be useful for deciphering taxonomic diversity of the genus *Tylototriton*, with 13 species (over 50%) described in the past five years (Grismer et al., 2018a; Hou et al., 2012; Khatiwada et al., 2015; Nishikawa et al., 2013a, 2013b, 2014; Phimmachak et al., 2015; Shen et al., 2012; Yang et al., 2014; Zhao et al., 2012). However, recent molecular surveys indicate that our knowledge on taxonomic diversity of the genus *Tylototriton* is still far from complete, revealing several cryptic lineages likely corresponding to as yet undescribed species (Grismer et al., 2018a; Wang et al., 2018).

Myanmar, previously known as Burma, is the largest country of mainland Southeast Asia. Despite this, its herpetofauna remains one of the least explored in the region (Grismer et al., 2018a). Members of the genus *Tylototriton* have long been recorded from northern and eastern parts of Myanmar and have been traditionally classified as *T. verrucosus* Anderson, 1871 (Gyi, 1969). Nishikawa et al. (2014), based on the examination of specimens assigned to *T. verrucosus* collected from the Shan Plateau in eastern Myanmar and pet-trade animals assumed to originate from Myanmar, recently described a new species, *T. shanorum* Nishikawa, Matsui & Rao, 2014. Soon after, Phimmachak et al. (2015) published sequence

data for specimens collected from the Sagaing Region and Kachin State in northern Myanmar, which were reported as *T. verrucosus*. More recently, Grismer et al. (2018a) demonstrated the presence of two morphologically and genetically distinct lineages of *Tylototriton* in the Shan Plateau and described a new species from its north-western edge, *T. ngarsuensis* Grismer, Wood, Quah, Thura, Espinoza, Grismer, Murdoch & Lin, 2018. The same work of Grismer et al. (2018a) reanalyzed sequences of specimens from the Sagaing and Kachin regions of Myanmar and demonstrated that they belong to a distinct lineage – *Tylototriton* sp. 1, distinct from *T. verrucosus* s. str. Recent work also indicated the presence of *T. himalayanus* Khatiwada, Wang, Ghimire, Vasudevan, Paudel & Jiang, 2015 (a species described from Nepalese Himalaya) in northern Myanmar, but without providing voucher specimen information or any other justification for this identification (Hernandez, 2016; Hernandez et al., 2018). The recent monographic review of the genus *Tylototriton* by Hernandez (2016) also indicated the possibility of the occurrence of *T. uyenoi* Nishikawa, Khonsue, Pomchote & Matsui, 2013 and *T. shanjing* Nussbaum, Brodie & Yang, 1995 in parts of Myanmar adjacent to northern Thailand and the southwestern Yunnan Province of China; however, these records are not supported by voucher specimens. Thus, our knowledge on the taxonomic composition and diversity of the genus *Tylototriton* in Myanmar is still far from complete.

In the present paper, we report on a new population of the genus *Tylototriton* from the Kachin Hills in the southern part of Kachin State, northern Myanmar. We applied morphological and molecular methods to evaluate its taxonomic status and describe it as a new species. We also discuss biogeography and taxonomy of the genus *Tylototriton* in Myanmar.

MATERIALS AND METHODS

Sample collection

Fieldwork was carried out in northern Myanmar, Kachin State, from 14 to 21 July 2018. Specimens of *Tylototriton* sp. were collected by hand in swamps in forest clearings surrounded by montane evergreen tropical forests of Ingyin Taung Mountain, Indawgyi Lake area, Kachin State (Figure 1; samples 22−23). Geographic coordinates and altitude were obtained using a Garmin GPSMAP 60CSx GPS receiver (Garmin Ltd., USA) and recorded in datum WGS 84. Specimens were euthanized by 20% benzocaine and tissue samples for genetic analysis were taken and stored in 96% ethanol (femoral muscles) prior to preservation. Specimens were subsequently preserved in 70% ethanol and deposited in the herpetological collection of the Zoological Museum of Moscow State University (ZMMU) in Moscow, Russia; Zoological Institute of Russian Academy of Sciences (ZISP) in St. Petersburg, Russia; and Zoology Department of University of Mandalay (ZDUM), Mandalay, Myanmar.
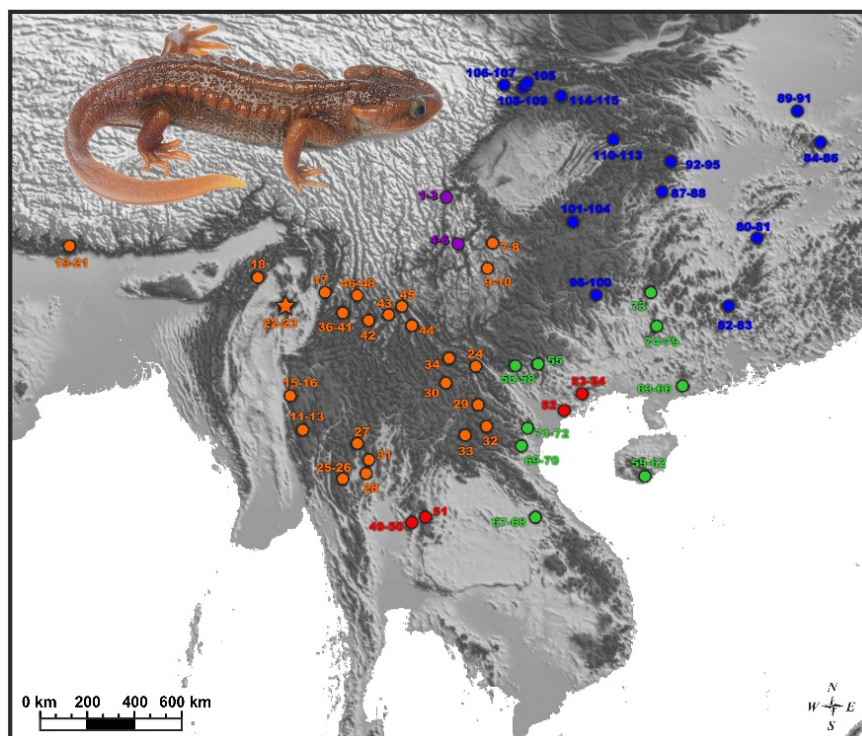

Figure 1 Distribution of *Tylototriton* and sampling localities examined in this study
Colors of dots correspond to clades 1–5 denoted in Figure 2. Sample numbers 1–115 refer to Table 1. Type locality of new species *Tylototriton kachinorum* **sp. nov.** is marked with a star. Photo by Nikolay A. Poyarkov.

Morphological description

Specimens of *Tylototriton* sp. were photographed in life and after preservation. The sex and maturity of the specimens and number of eggs were checked and counted by minor dissections. Measurements were taken using a digital caliper to the nearest 0.01 mm, subsequently rounded to 0.1 mm. We used a stereoscopic light binocular microscope when necessary. Statistical analyses were performed with Statistica 8.0 (Version 8.0; StatSoft, Tulsa, OK, USA).

Adult morphology

Morphometrics followed Nishikawa et al. (2014), Khatiwada et al. (2015), and Okamiya et al. (2018) and included the following 24 measurements: (1) SVL (snout-vent length) from tip of snout to anterior tip of vent; (2) HL (head length); (3) HW (head width); (4) MXHW (maximum head width); (5) IND (internarial distance); (6) AGD (axilla-groin distance); (7) TRL (trunk length); (8) TAL (tail length) from anterior tip of vent to tail tip; (9) VL (vent length); (10) FLL (forelimb length); (11) HLL (hindlimb length); (12) VTW (vomerine tooth series width): greatest width of vomerine tooth series; (13) VTL (vomerine tooth series length): greatest length of vomerine tooth series; (14) LJL (lower jaw length from tip of lower jaw to articulation of upper and lower jaws); (15) SL (snout length from tip of snout to anterior tip of upper eyelid); (16) IOD (minimum interorbital distance); (17) UEW (maximum upper eyelid width); (18) UEL (upper eyelid length, distance between anterior and posterior angles); (19) OL (orbit length); (20) BTAW (basal tail width at level of anterior tip of cloaca); (21) MTAW (tail width at mid-level of tail); (22) MXTAH (maximum tail height); (23) MTAH (tail height at mid-level of tail); (24) ON (orbitonarial distance). For holotype description, we examined the following 12 morphometric and three meristic characters following Poyarkov et al. (2012) and Okamiya et al. (2018): additional morphometric characters: (25) ICD (intercanthal distance); (26) CW (chest width); (27) NSD (nostril-snout distance); (28) 1FL (first finger length from base to tip); (29) 2FL (second finger length from base to tip); (30) 3FL (third finger length from base to tip); (31) 4FL (fourth finger length from base to tip); (32) 1TL (first toe length from base to tip); (33) 2TL (second toe length from base to tip); (34) 3TL (third toe length from base to tip); (35) 4TL (fourth toe length from base to tip); (36) 5TL (fifth toe length from base to tip); meristic characters: (37) UJTN (number of teeth on upper jaw); (38) LJTN (number of teeth on lower jaw); (39) VTN, number of teeth on vomer. We also recorded the following characters as per Nishikawa et al. (2014) and Grismer et al. (2018a): shape of vomerine teeth and their positional relationship relative to choanae; skin texture; number and shape of rib nodules counted from posterior margin of vent to axilla; width and prominence of vertebral ridge and head ridges; and coloration of dorsum, venter, head, labial region, parotoid glands, rib nodules, limbs, soles, palms, tail surfaces, and vent region.

The characters of adult morphology chosen for comparison and data on other *Tylototriton* species were taken from the following sources: Anderson (1871); Böhme et al. (2005); Chen et al. (2010); Fang & Chang (1932); Fei et al. (1984); Grismer et al. (2018a); Hernandez (2016); Hou et al. (2012); Khatiwada et al. (2015); Le et al. (2015); Liu (1950); Nishikawa et al. (2013a; 2013b; 2014); Nussbaum et al. (1995); Phimmachak et al. (2015); Qian et al. (2017); Shen et al. (2012); Stuart et al. (2010); Unterstein (1930); Yang et al. (2014).

Larval morphology

Description of larval morphology followed Okamiya et al. (2018). For larval specimens, we recorded nine morphometric characters including (1) SVL, (2) HL, (3) HW, (4) OL, (5) AGD, (6) TAL, (7) FLL, (8) HLL, and (9) MXTAH (definition same as for adult morphology). Developmental stages were determined following Grosse (2013).

DNA isolation, PCR, and sequencing

Total genomic DNA was extracted from 95% ethanol-preserved muscle tissues using standard phenol-chloroform extraction protocols (Hillis et al., 1996). Total DNA concentration was estimated in 1 µL using a NanoDrop 2000 spectrophotometer (Thermo Scientific, USA), and consequently adjusted to 100 ng DNA/µL.

We amplified two mtDNA fragments consisting of partial sequences of the *ND2* and 16S rRNA mtDNA genes. These markers were chosen as they are useful in studies of *Tylototriton* phylogeny and taxonomy (Nishikawa et al., 2013a, 2013b, 2014; Wang et al., 2018; Zhao et al., 2012 and references therein). We used the 16L-1 (forward) (5'-CTGACCGTGCAAA GGTAGCGTAATCACT-3') and 16H-1 (reverse) (5'- CTCCGG TCTGAACTCAGATCACGTAGG-3') primers to amplify the 16S rRNA fragments (Hedges, 1994). For amplification and sequencing of the *ND2* gene, we used the SL-1 (forward) (5'-ATAGAGGTTCAAACCCTCTC-3') and SL-2 (reverse) (5'-TTAAAGTGTCTGGGTTGCATTCAG-3') primers of Wang et al. (2018). Polymerase chain reaction (PCR) was performed in 20 µL reactions using 50 ng genomic DNA, 10 nmol of each primer, 15 nmol of each dNTP, 50 nmol additional MgCl$_2$, Taq PCR buffer (10 mmol/L Tris-HCl, pH 8.3, 50 mmol/L KCl, 1.1 mmol/L MgCl$_2$, and 0.01% gelatin), and 1 U of Taq DNA polymerase. PCR cycles included an initial denaturation step of 4 min at 94 °C and 35 cycles of denaturation for 30 s at 94 °C, primer annealing for 30 s at 48−58 °C, and extension for 1 min 30 s at 72 °C. PCR products were visualized by agarose gel electrophoresis in the presence of ethidium bromide and consequently purified using 2 µL from a 1:4 dilution of ExoSapIt (Amersham, UK) per 5 µL of PCR product prior to cycle sequencing. Sequencing was performed in both directions using the same primers as used in PCR on an ABI3730xl automated sequencer (Applied Biosystems, USA) at Evrogen Inc., Moscow (Russia). The newly obtained sequences were aligned and deposited in GenBank under the accession numbers MK095616− MK095619 and MK097271−MK097274 (Table 1). Sequences of 25 other *Tylototriton* species used for comparisons were obtained from GenBank (Table 1).

Table 1   Sequences and voucher specimens of *Tylototriton* and outgroup taxa used in this study

Sample No.	Species name	Voucher number	Locality	16S rRNA	*ND2*
	Ingroup:				
1	*Tylototriton taliangensis*	CIB GG200110183	Shimian Co., Ya'an City, Sichuan, China	KY800559	KC147819
2	*Tylototriton taliangensis*	CIB GG200110185	Shimian Co., Ya'an City, Sichuan, China	KY800560	KY800829
3	*Tylototriton taliangensis*	CIB GG200110186	Shimian Co. Ya'an City, Sichuan, China	KY800561	KY800830
4	*Tylototriton pseudoverrucosus*	CIB WCG2012003	Ningnan Co., Liangshan Yi Autonomous Prefecture, Sichuan, China	KY800597	KY800861
5	*Tylototriton pseudoverrucosus*	CIB WCG2012007	Ningnan Co., Liangshan Yi Autonomous Prefecture, Sichuan, China	KY800598	KY800862
6	*Tylototriton pseudoverrucosus*	CIB WCG2012012	Ningnan Co., Liangshan Yi Autonomous Prefecture, Sichuan, China	KY800599	KY800860
7	*Tylototriton kweichowensis*	CIB WG20080818014	Bijie City, Guizhou, China	KY800551	KY800823
8	*Tylototriton kweichowensis*	CIB WG20080818018	Bijie City, Guizhou, China	KY800552	KY800824
9	*Tylototriton kweichowensis*	CIB 20050213	Shuicheng Co., Guizhou, China	KY800557	KY800827
10	*Tylototriton kweichowensis*	CIB 20050215	Shuicheng Co., Guizhou, China	KY800558	KY800828
11	*Tylototriton shanorum* lineage 1	CAS 230933	Taunggyi Township, Shan, Myanmar	—	AB922822
12	*Tylototriton shanorum* lineage 1	CAS 230940	Taunggyi Township, Shan, Myanmar	—	AB922823
13	*Tylototriton shanorum* lineage 1	CAS 230899	Taunggyi Township, Shan, Myanmar	—	HM770087
14	*Tylototriton shanorum* lineage 2	KUHE 42348	pet trade, presumably from Myanmar	—	AB769544
15	*Tylototriton ngarsuensis*	LSUHC 13762	Ngar Su, Shan, Myanmar	—	MH836585
16	*Tylototriton ngarsuensis*	LSUHC 13763	Ngar Su, Shan, Myanmar	—	MH836584
17	*Tylototriton* sp. 1	CAS 245418	Chipwi Township, Kachin State, Myanmar	—	KT304279
18	*Tylototriton* sp. 1	CAS 245290	Lahe Township, Sagaing Region, Myanmar	—	KT304278
19	*Tylototriton himalayanus*	CIB 201406246	Mai Pokhari, Illam, Mechi, Nepal	KY800590	KT765173
20	*Tylototriton himalayanus*	CIB 201406284	Mai Pokhari, Illam, Mechi, Nepal	KY800591	KT765207
21	*Tylototriton himalayanus*	CIB 201406285	Mai Pokhari, Illam, Mechi, Nepal	KY800592	KT765208
22	*Tylototriton kachinorum* **sp. nov.**	ZMMU A5953	Ingyin Taung Mt., Indawgyi, Kachin, Myanmar	MK095618	MK097273
23	*Tylototriton kachinorum* **sp. nov.**	ZDUM-0103	Ingyin Taung Mt., Indawgyi, Kachin, Myanmar	MK095619	MK097274
24	*Tylototriton yangi*	KUHE 42282	Pingbian Co., Yunnan, China	KY800624	KY800887
25	*Tylototriton uyenoi*	ZMMU NAP-08220	Doi Inthanon, Chiang Mai, Thailand	MK095617	MK097272
26	*Tylototriton uyenoi*	KUHE 19037	Doi Inthanon, Chiang Mai, Thailand	—	AB830730
27	*Tylototriton uyenoi*	KUHE 19147	Doi Ang Khang, Chiang Mai, Thailand	—	AB830729
28	*Tylototriton uyenoi*	ITNT1	Doi Suthep, Chiang Mai, Thailand	—	AB830733
29	*Tylototriton anguliceps*	TBU PAE671	Thuan Chau, Son La, Vietnam	—	LC017833
30	*Tylototriton anguliceps*	VNMN A20143	Muong Nhe, Dien Bien, Vietnam	—	LC017832
31	*Tylototriton anguliceps*	LK003	Doi Lahnga, Chiang Mai, Thailand	—	AB830728
32	*Tylototriton podichthys*	KUHE 34399	Phu Pan, Xam Neua, Laos	—	AB830727
33	*Tylototriton podichthys*	IEBR A2014-1	Xam Neua, Huaphanh, Laos	—	LC017835
34	*Tylototriton pulcherrimus*	CIB TY 040	Lüchun Co., Yunnan, China	KY800626	KY800890
35	*Tylototriton pulcherrimus*	KUHE 46406	Pet Trade	KY800620	KY800880
36	*Tylototriton verrucosus*	CIB TSHS1	Longchuan Co., Dehong, Yunnan, China	KY800581	KY800847
37	*Tylototriton verrucosus*	CIB-TSHS2	Longchuan Co., Dehong, Yunnan, China	KY800582	KY800848
38	*Tylototriton verrucosus*	CIB TSHS3	Longchuan Co., Dehong, Yunnan, China	KY800583	KY800849

Sample No.	Species name	Voucher number	Locality	16S rRNA	*ND2*
39	*Tylototriton verrucosus*	CIB TSHS4	Longchuan Co., Dehong, Yunnan, China	KY800584	KY800850
40	*Tylototriton verrucosus*	CIB TSHS5	Longchuan Co., Dehong, Yunnan, China	KY800585	KY800851
41	*Tylototriton verrucosus*	CIB TSHS6	Longchuan Co., Dehong, Yunnan, China	KY800586	KY800852
42	*Tylototriton shanjing*	KIZ 201306081	Yongde Co., Yunnan, China	KY800593	KY800856
43	*Tylototriton shanjing*	KIZ 201306098	Yun Co., Yunnan, China	KY800594	KY800857
44	*Tylototriton shanjing*	KIZ 201306102	Jingdong Co., Yunnan, China	KY800595	KY800858
45	*Tylototriton shanjing*	KIZ 201306108	Nanjian Co., Yunnan, China	KY800596	KY800859
46	*Tylototriton shanjing*	CIB 980004	Baoshan City, Yunnan, China	KY800562	KY800831
47	*Tylototriton shanjing*	CIB 980005	Baoshan City, Yunnan, China	KY800563	KY800832
48	*Tylototriton shanjing*	CIB 980006	Baoshan City, Yunnan, China	KY800564	KY800833
49	*Tylototriton panhai*	ZMMU NAP-08217	Phu Hin Rong Kla NP, Phitsanulok, Thailand	MK095616	MK097271
50	*Tylototriton panhai*	PH019	Phu Hin Rong Kla NP, Phitsanulok, Thailand	—	AB830735
51	*Tylototriton panhai*	PL009	Phu Luang WS, Loei, Thailand	—	AB830736
52	*Tylototriton vietnamensis*	IEBR A.3674	Yen Tu, Bac Giang, Vietnam	KY800614	KY800874
53	*Tylototriton vietnamensis*	IEBR A.0702	Mauson, Lang Son, Vietnam	KY800612	KY800872
54	*Tylototriton vietnamensis*	IEBR A.0701	Mauson, Lang Son, Vietnam	KY800613	KY800873
55	*Tylototriton ziegleri*	VNMN 3389	Bao Lac, Cao Bang, Vietnam	—	KY800888
56	*Tylototriton ziegleri*	VNMN 3390	Quan Ba, Ha Giang, Vietnam	KY800625	KY800889
57	*Tylototriton ziegleri*	VNUH HG.082	Quan Ba, Ha Giang, Vietnam	KY800610	KY800870
58	*Tylototriton ziegleri*	VNUH HG.081	Quan Ba, Ha Giang, Vietnam	KY800611	KY800871
59	*Tylototriton hainanensis*	CIB 20081048	Mt. Diaoluo, Hainan, China	KY800553	KC147817
60	*Tylototriton hainanensis*	CIB 20081049	Mt. Diaoluo, Hainan, China	KY800554	KC147818
61	*Tylototriton hainanensis*	CIB 20081051	Mt. Diaoluo, Hainan, China	KY800555	KY800825
62	*Tylototriton hainanensis*	CIB 20081052	Mt. Diaoluo, Hainan, China	KY800556	KY800826
63	*Tylototriton asperrimus* lineage 2	CIB XZ20091201	Xinyi City, Guangdong, China	KY800616	KY800876
64	*Tylototriton asperrimus* lineage 2	CIB XZ20091204	Xinyi City, Guangdong, China	KY800619	KY800879
65	*Tylototriton asperrimus* lineage 2	CIB XZ20091	Xinyi City, Guangdong, China	KY800618	KY800878
66	*Tylototriton asperrimus* lineage 2	CIB XZ20092	Xinyi City, Guangdong, China	KY800617	KY800877
67	*Tylototriton notialis*	FMNH HERP271120	Boualapha Dist., Khammouan, Laos	—	HM462061
68	*Tylototriton notialis*	FMNH HERP271121	Boualapha Dist., Khammouan, Laos	—	HM462062
69	*Tylototriton notialis*	VNMN TAO1229	Pu Hoat, Nghe An, Vietnam	—	KY800883
70	*Tylototriton notialis*	VNMN TAO1235	Pu Hoat, Nghe An, Vietnam	—	KY800884
71	*Tylototriton asperrimus* lineage 1	VNMN TAO1213	Thuong Tien, Hoa Binh, Vietnam	KY800623	KY800885
72	*Tylototriton asperrimus* lineage 1	VNMN TAO1214	Thuong Tien, Hoa Binh, Vietnam	—	KY800886
73	*Tylototriton asperrimus* lineage 1	CIB 70063	Longsheng Co., Guangxi, China	KY800549	KC147816
74	*Tylototriton asperrimus* lineage 1	CIB GX20080714	Jinxiu Co., Guangxi, China	KY800546	KY800819
75	*Tylototriton asperrimus* lineage 1	CIB GX200807010	Jinxiu Co., Guangxi, China	KY800547	KY800820
76	*Tylototriton asperrimus* lineage 1	CIB GX200807012	Jinxiu Co., Guangxi, China	KY800548	KY800821
77	*Tylototriton asperrimus* lineage 1	CIB GX200807016	Jinxiu Co., Guangxi, China	KY800550	KY800822
78	*Tylototriton asperrimus* lineage 1	CIB 20070715	Jinxiu Co., Guangxi, China	KY800565	KY800834
79	*Tylototriton asperrimus* lineage 1	CIB 200807055	Jinxiu Co., Guangxi, China	KY800566	KC147815

Sample No.	Species name	Voucher number	Locality	16S rRNA	*ND2*
80	*Tylototriton liuyangensis*	CSUFT 20100108	Liuyang City, Hunan, China	KY800606	KJ205598
81	*Tylototriton liuyangensis*	CIB 110601F06	Liuyang City, Hunan, China	KY800615	KY800875
82	*Tylototriton lizhenchangi*	KUHE 42316	Yizhang Co., Hunan, China	KY800621	KY800881
83	*Tylototriton lizhenchangi*	KUHE 42317	Yizhang Co., Hunan, China	KY800622	KY800882
84	*Tylototriton dabienicus* lineage 2	CIB 08042905-2	Yuexi Co. Anhui, China	KY800587	KY800853
85	*Tylototriton dabienicus* lineage 2	CIB 08042905-3	Yuexi Co. Anhui, China	KY800588	KY800854
86	*Tylototriton dabienicus* lineage 2	CIB 08042905-4	Yuexi Co. Anhui, China	KY800589	KY800855
87	*Tylototriton broadoridgus*	CIB 200085	Sangzhi Co., Hunan, China	KY800569	KC147814
88	*Tylototriton broadoridgus*	CIB 200084	Sangzhi Co., Hunan, China	KY800570	KY800837
89	*Tylototriton dabienicus* lineage 1	HNNU 1004-015	Shangcheng Co., Anhui, China	KY800607	KC147811
90	*Tylototriton dabienicus* lineage 1	HNNU 1004-024	Shangcheng Co., Anhui, China	KY800608	KC147812
91	*Tylototriton dabienicus* lineage 1	HNNU 1004-026	Shangcheng Co., Anhui, China	KY800609	KY800869
92	*Tylototriton wenxianensis* lineage 3	CIB WH10001	Wufeng Co., Hubei, China	KY800600	KY800863
93	*Tylototriton wenxianensis* lineage 3	CIB WH10002	Wufeng Co., Hubei, China	KY800601	KY800864
94	*Tylototriton wenxianensis* lineage 3	CIB WH10003	Wufeng Co., Hubei, China	KY800602	KY800865
95	*Tylototriton wenxianensis* lineage 3	CIB WH10007	Wufeng Co., Hubei, China	KY800603	KY800866
96	*Tylototriton wenxianensis* lineage 2	CIB Wg20090730001	Libo Co., Guizhou, China	KY800575	KY800842
97	*Tylototriton wenxianensis* lineage 2	CIB Wg20090730002	Libo Co., Guizhou, China	KY800576	KY800843
98	*Tylototriton wenxianensis* lineage 2	CIB Wg20090730003	Libo Co., Guizhou, China	KY800577	KY800844
99	*Tylototriton wenxianensis* lineage 2	CIB Wg20090730005	Libo Co., Guizhou, China	KY800578	KY800845
100	*Tylototriton wenxianensis* lineage 2	CIB Wg20090730004	Libo Co., Guizhou, China	KY800580	KY800846
101	*Tylototriton wenxianensis* lineage 1	CIB WG200600019	Suiyang Co., Zunyi, Guizhou, China	KY800544	KY800817
102	*Tylototriton wenxianensis* lineage 1	CIB WG20060007	Suiyang Co., Zunyi, Guizhou, China	KY800545	KY800818
103	*Tylototriton wenxianensis* lineage 1	CIB WG20090601002	Suiyang Co., Zunyi, Guizhou, China	KY800573	KY800840
104	*Tylototriton wenxianensis* lineage 1	CIB WG20090601001	Suiyang Co., Zunyi, Guizhou, China	KY800574	KY800841
105	*Tylototriton wenxianensis* lineage 1	CIB 20090527	Wenxian Co., Gansu, China	KY800579	KC147813
106	*Tylototriton wenxianensis* lineage 1	CIB 2010123101	Pingwu Co., Gansu, China	KY800604	KY800867
107	*Tylototriton wenxianensis* lineage 1	CIB 2010123102	Pingwu Co., Gansu, China	KY800605	KY800868
108	*Tylototriton wenxianensis* lineage 1	CIB 20070639	Qingchuan Co., Sichuan, China	KY800542	KY800815

Sample No.	Species name	Voucher number	Locality	16S rRNA	*ND2*
109	*Tylototriton wenxianensis* lineage 1	CIB 20070638	Qingchuan Co., Sichuan, China	KY800543	KY800816
110	*Tylototriton wenxianensis* lineage 1	CIB 20080002	Yunyang Co., Chongqing, China	KY800540	KY800813
111	*Tylototriton wenxianensis* lineage 1	CIB 20080003	Yunyang Co., Chongqing, China	KY800541	KY800814
112	*Tylototriton wenxianensis* lineage 1	CIB 20081201	Yunyang Co., Chongqing, China	KY800567	KY800835
113	*Tylototriton wenxianensis* lineage 1	CIB 20081202	Yunyang Co., Chongqing, China	KY800568	KY800836
114	*Tylototriton wenxianensis* lineage 1	CIB WA20090601	Wangcang Co., Sichuan, China	KY800571	KY800838
115	*Tylototriton wenxianensis* lineage 1	CIB WA20090602	Wangcang Co., Sichuan, China	KY800572	KY800839
	Outgroup:				
116	*Echinotriton chinhaiensis*	CIB ZHJY1	Zhenhai Co., Zhejiang, China	KY800627	KY800891
117	*Echinotriton chinhaiensis*	CIB ZHJY2	Zhenhai Co., Zhejiang, China	KY800628	KY800892
118	*Echinotriton andersoni*	MVZ 232187	Tokunoshima, Kagoshima, Japan	EU880314	EU880314
119	*Pleurodeles waltl*	MVZ 231894	Cadiz, Andalusia, Spain	EU880330	EU880330

For sampling localities see Figure 1. Institutional abbreviations: CAS: California Academy of Sciences, Department of Herpetology, USA; CIB: Chengdu Institute of Biology, Chinese Academy of Sciences, China; CSUFT: Central South University of Forestry and Technology, China; FMNH: Field Museum, USA; HNNU: Henan Normal University, China; IEBR: Institute of Ecology and Biological Resources, Vietnam; KIZ: Kunming Institute of Zoology, Chinese Academy of Sciences, China; KUHE: Graduate School of Human and Environmental Studies of Kyoto University, Japan; LSUHC: La Sierra University, Herpetological Collection, USA; MVZ: Museum of Vertebrate Zoology, University of California, USA; TBU: Thuan Chau University, Vietnam; VNMN: Vietnam National Museum of Nature, Vietnam; VNUH: Vietnam National University Hanoi, Vietnam; ZDUM: Zoological Department, University of Mandalay, Myanmar; ZISP: Zoological Institute, Russian Academy of Sciences, Russia; ZMMU: Zoological Museum of Lomonosov Moscow State University, Russia. Co.: County. 一: Not available.

Phylogenetic analyses

Sequences of partial fragments of *ND2* and 16S rRNA mtDNA for 119 Salamandridae specimens, including 115 representatives of *Tylototriton* (26 species) and four sequences of outgroup members of Salamandridae (*Echinotriton* and *Pleurodeles*) were included in the final alignment with a total length of up to 1 665 bp. Information on voucher specimens and GenBank accession Nos. used in phylogenetic analyses is summarized in Table 1. Nucleotide sequences were initially aligned in MAFFT v. 6 (Katoh et al., 2002) with default parameters, and then checked by eye in BioEdit 7.0.5.2 (Hall, 1999) and slightly adjusted.

The dataset was divided into four partitions: three codon-partitions for the *ND2* gene and a single partition for 16S rRNA, with the optimal evolutionary models for each estimated using MODELTEST v. 3.06 (Posada & Crandall, 1998). According to the Akaike information criterion (AIC), the TVM+G model was the best fit for the 16S rRNA partition; for the *ND2* gene, however, the HKY+G model was considered the best fit for the first and second codon partitions, whereas the J2+G model was selected as the best fit for the third codon partition. Mean uncorrected genetic distances (*P*-distances) between sequences were determined with MEGA 7.0 (Kumar

et al., 2016).

The matrilineal genealogy was inferred using Bayesian inference (BI) and maximum likelihood (ML) algorithms. BI analyses were conducted in MrBayes v3.1.2 (Huelsenbeck & Ronquist, 2001; Ronquist & Huelsenbeck, 2003). Metropolis-coupled Markov chain Monte Carlo (MCMCMC) analyses were run with one cold chain and three heated chains for twenty million generations and sampled every 2 000 generations. Five independent MCMCMC runs were performed and 1 000 trees were discarded as burn-in. We checked the convergence of the runs and that the effective sample sizes (ESS) were all above 200 by exploring the likelihood plots using TRACER v1.6 (Rambaut et al., 2014). Confidence in tree topology was tested by posterior probability (PP) for the BI trees (Huelsenbeck & Ronquist, 2001). Nodes with PP values over 0.95 were *a-priori* regarded as sufficiently resolved, those between 0.95 and 0.90 were regarded as tendencies, and values below 0.90 were considered to be not supported.

We conducted ML analyses using the RAxML web server (http://embnet. vital-it. ch / raxml-bb/; Stamatakis et al., 2008) and searched ML trees using the gamma model of rate heterogeneity option. Confidence in node topology was tested

by non-parametric bootstrapping with 1 000 replicates (ML BS, see Felsenstein, 1985). We *a-priori* regarded tree nodes with bootstrap (ML BS) values of 70% or greater and BI PP values over 0.95 as sufficiently resolved; ML BS values between 70% and 50% (BI PP between 0.95 and 0.90) were treated as tendencies, and nodes with ML BS values below 50% (BI PP below 0.90) were regarded as unresolved (Felsenstein, 2004; Huelsenbeck & Hillis, 1993).

RESULTS

Phylogenetic analyses

Sequences and statistics: The final alignment of the *ND2* gene contained 1 157 aligned characters, including 712 conserved sites and 445 variable sites, of which 405 were parsimony-informative. The transition-transversion bias (R) was estimated to be 4.56 (all data for ingroup only). Nucleotide frequencies were 37.5% (A), 23.7% (T), 28.3% (C), and 10.5% (G). The final alignment of the 16S rRNA gene contained 508 aligned characters, including 424 conserved sites and 82 variable sites, of which 69 were parsimony-informative. The transition-transversion bias (R) was estimated to be 5.84 (all data for ingroup only). Nucleotide frequencies were 36.8% (A), 24.9% (T), 20.3% (C), and 18.0% (G).

Position of *Tylototriton* sp. in matrilineal genealogy: BI and ML phylogenetic analyses resulted in essentially similar topologies (Figure 2). In general, the topology of the mtDNA-based matrilineal genealogy was consistent with the phylogeny of *Tylototriton* presented by Wang et al. (2018), suggesting that the genus is divided into five clades (1−5) grouped into two major reciprocally monophyletic groups (Figure 2):

(1) The first group joined two clades with sister relationships: clade 1 (including *T. verrucosus* (type species of *Tylototriton* s. str. Anderson, 1871), *T. anguliceps*, *T. himalayanus*, *T. kweichowensis* (type species of *Qiantriton* Fei, Ye & Jiang, 2012), *T. ngarsuensis*, *T. podichthys*, *T. pulcherrimus*, *T. shanjing*, *T. shanorum*, *T. uyenoi*, *T. yangi*, and *Tylototriton* sp. 1 from the western part of the Kachin and Sagaing States of Myanmar and the newly discovered population of *Tylototriton* **sp. nov.** from the Indawgyi Lake area in the southern part of Kachin State) and clade 2 (including *T. pseudoverrucosus* and *T. taliangensis*, the latter being the type species of *Liangshantriton* Fei, Ye & Jiang, 2012).

(2) The second group joined clade 3 (including *T. broadoridgus*, *T. dabienicus*, *T. liuyangensis*, *T. lizhenchangi*, and *T. wenxianensis*), clade 4 (including *T. panhai* and *T. vietnamensis*), and clade 5 (including *T. asperrimus* (type species of *Yaotriton* Dubois & Raffaëlli, 2009), *T. hainanensis*, *T. notialis*, and *T. ziegleri*); the topological relationships between these three clades are essentially unresolved.

In accordance with the results of Wang et al. (2018) our analysis indicated deep phylogenetic structuring and paraphyly of *T. asperrimus* (consisting of two non-monophyletic lineages), *T. wenxianensis* (consisting of three lineages, not forming a monophyly), and *T. dabienicus* (consisting of two non-monophyletic lineages), suggesting that taxonomy of this group is incomplete and further taxonomic and phylogenetic research is required.

The newly discovered population of *Tylototriton* **sp. nov.** from the Indawgyi Lake area belongs to clade 1 (Figure 2), which occurs in western and northern Indochina, Himalaya, and Yunnan Province of China (Figure 1), and is grouped with *T. himalayanus* from Nepal, though not with significant node support (0.85/57, hereafter given for BI PP/ML BS, respectively). *Tylototriton* **sp. nov.** from the Indawgyi Lake area and *T. himalayanus* form a well-supported monophyletic group with *Tylototriton* species from the Shan Plateau in Myanmar (1.0/96), whereas populations of *Tylototriton* sp. 1 from the Sagaing and Kachin states in northern Myanmar, reported by Grismer et al. (2018a), are clustered with other members of *Tylototriton* clade 1 from Yunnan and northern Indochina and belong to the *T. verrucosus* species complex (Figure 2). Our analyses suggest sister relationships of closely related *T. verrucosus* and *T. shanjing* but only with support from BI (1.0/-), suggesting that the taxonomic status of *T. shanjing* might need to be reconsidered. Finally, in our tree, the recently described Myanmar species *T. ngarsuensis* is nested within differentiation of *T. shanorum*, rendering the latter paraphyletic.

Sequence divergence: The uncorrected *P*-distances among and within the studied mtDNA fragments for the examined *Tylototriton* species are shown in Table 2 (data for ingroup only). The interspecific uncorrected genetic *P*-distances between the *Tylototriton* sp. from Kachin State of Myanmar and other congeners varied from 5.3% (between *Tylototriton* sp. and its sister species *T. himalayanus*) to 14.6% (between *Tylototriton* sp. and *T. lizhenchangi*) for the *ND2* gene; and from 2.4% (between *Tylototriton* sp. and its sister species *T. himalayanus*) to 5.9% (between *Tylototriton* sp. and *T. liuyangensis* and *T. dabienicus*, lineage 1) for the 16S rRNA gene (Table 2). This degree of pairwise divergence is quite high, notably greater than the genetic divergence observed between many recognized species of *Tylototriton* (see Table 2 and Grismer et al., 2018a; Wang et al., 2018).

Taxonomy

Our mtDNA genealogy analyses based on the *ND2* and 16S rRNA genes indicated that the newly discovered population of *Tylototriton* **sp. nov.** from the Indawgyi Lake area belongs to clade 1 of the subgenus *Tylototriton* s. str. and is clustered with two other species of the genus known from Myanmar, *T. ngarsuensis* and *T. shanorum*, and with *T. himalayanus* from Nepal (Figure 2). The lineage of *Tylototriton* **sp. nov.** from Indawgyi Lake is clearly distinct and notably divergent from all other congeners with the uncorrected genetic distance for interspecific comparisons exceeding *P*=5.3% in the *ND2* gene and *P*=2.4% in the 16S rRNA gene. The observed differences in mtDNA sequences are congruent with evidence from diagnostic morphological characters (see "Comparisons"). These results support our hypothesis that the newly discovered population of *Tylototriton* **sp. nov.** from Indawgyi Lake represents a previously unknown species, which we describe herein.
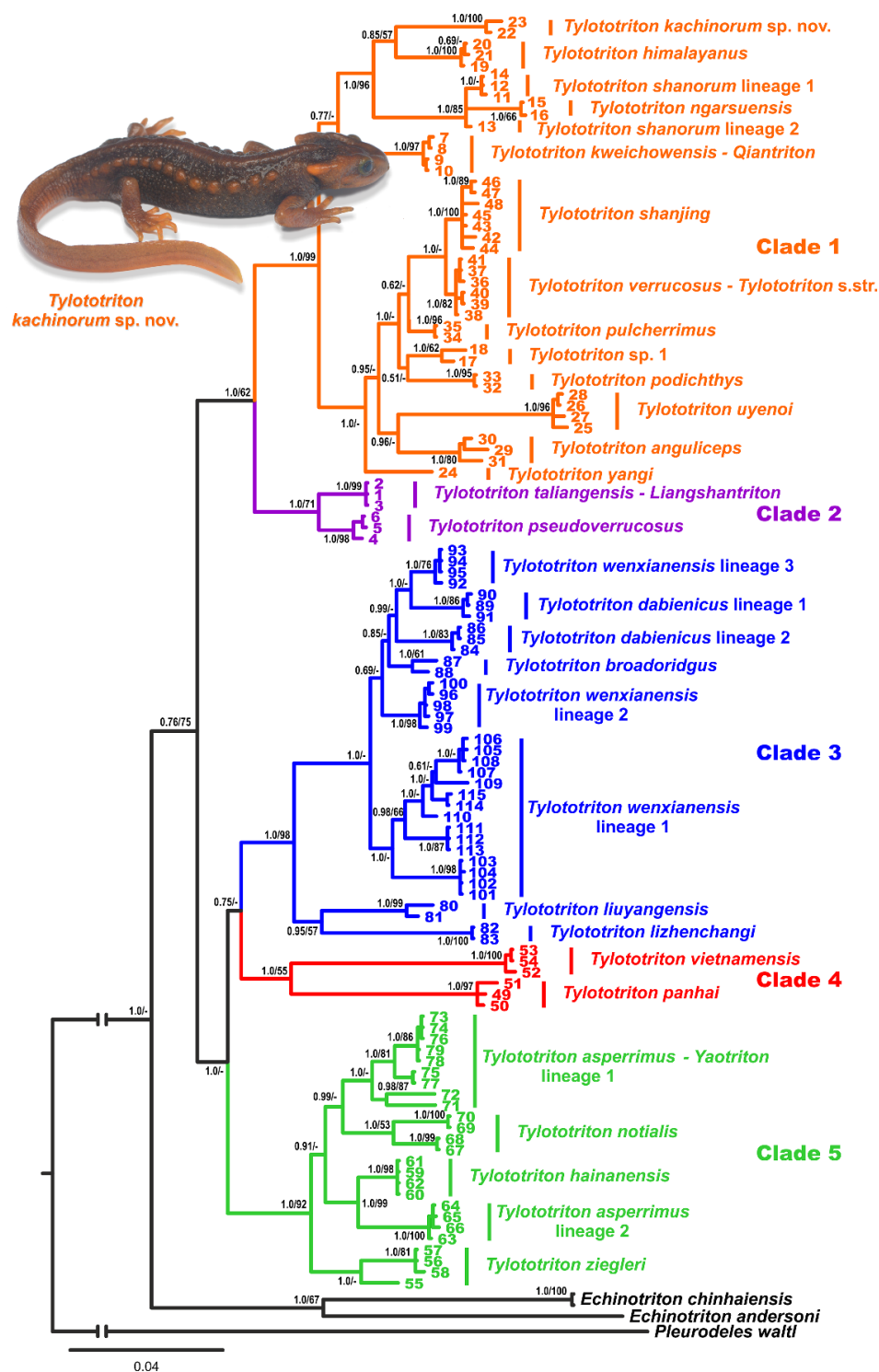
Figure 2 Bayesian inference consensus tree of genus *Tylototriton* derived from analysis of 1 157 bp *ND2* and 508 bp 16S rRNA gene fragments

Specimen numbers (1−115), corresponding voucher specimen information, and GenBank accession Nos. are given in Table 1. Color denotes five major clades revealed within genus *Tylototriton* (clades 1−5). Information on type species of subgeneric-level taxa *Tylototriton* s. str., *Qiantriton*, *Liangshantriton*, and *Yaotriton* is provided. Number at tree nodes corresponds to BI PP/ML BS support values, respectively. Photo by Nikolay A. Poyarkov.

Table 2 Uncorrected *P*-distance (percentage) between sequences of 1 157 bp *ND2* gene fragment (below diagonal) and 508 bp 16S rRNA gene fragment (above diagonal) of *Tylototriton* species included in phylogenetic analyses

Species	1	2	3	4	5	6	7	8	9	10	11	12	13	14	15	16	17	18	19	20	21	22	23	24	25	26	27	28	29	30	31
1 *T. kweichowensis*	–	–	–	–	–	–	–	–	2.8	2.4	2.7	2.5	4.0	2.4	2.8	3.8	0.0	3.4	3.8	–	4.4	4.2	4.0	3.8	3.8	4.7	3.7	3.4	3.4	–	–
2 *T. shanorum* 1	5.9	–	–	–	–	–	–	–	–	–	–	–	–	–	–	–	–	–	–	–	–	–	–	–	–	–	–	–	–	–	–
3 *T. shanorum* 2	5.6	0.6	–	–	–	–	–	–	–	–	–	–	–	–	–	–	–	–	–	–	–	–	–	–	–	–	–	–	–	–	–
4 *T. himalayanus*	5.2	5.1	4.9	–	–	–	–	–	–	–	–	–	–	–	–	–	–	–	–	–	–	–	–	–	–	–	–	–	–	–	–
5 *T. yangi*	6.1	6.6	6.4	6.5	–	–	–	–	–	–	–	–	–	–	–	–	–	–	–	–	–	–	–	–	–	–	–	–	–	–	–
6 *T. uyenoi*	8.1	9.2	9.1	8.5	7.5	–	–	–	–	–	–	–	–	–	–	–	–	–	–	–	–	–	–	–	–	–	–	–	–	–	–
7 *T. anguliceps*	6.3	7.0	6.8	7.0	4.5	7.6	–	–	–	–	–	–	–	–	–	–	–	–	–	–	–	–	–	–	–	–	–	–	–	–	–
8 *T. podichthys*	5.8	7.2	6.9	6.7	5.0	8.7	5.4	–	–	–	–	–	–	–	–	–	–	–	–	–	–	–	–	–	–	–	–	–	–	–	–
9 *T. pulcherrimus*	5.3	6.4	6.1	6.3	3.8	6.8	4.2	3.3	–	1.6	1.0	3.9	4.8	2.2	2.6	4.2	2.8	3.4	3.6	–	4.0	3.8	3.6	3.6	3.6	4.5	3.5	3.8	3.3	–	–
10 *T. verrucosus*	5.6	6.2	6.0	6.4	3.9	7.2	4.6	3.6	2.1	–	0.7	3.9	5.3	2.0	2.6	4.4	2.4	3.6	3.8	–	4.2	4.2	3.8	4.2	3.8	4.7	3.7	4.0	3.6	–	–
11 *T. shanjing*	5.9	6.6	6.4	6.2	4.5	7.2	4.8	4.0	2.6	1.1	–	3.7	5.2	2.3	2.5	4.3	2.7	3.5	3.7	–	4.1	4.0	3.7	4.0	3.7	4.5	3.6	3.9	3.5	–	–
12 *T. kachinorum* **sp. nov.**	6.5	7.6	7.1	5.3	8.2	11.6	8.3	8.0	7.7	7.3	7.9	–	5.2	4.1	4.3	4.7	2.5	5.2	5.2	–	5.5	5.9	5.0	5.0	5.0	5.9	5.0	5.2	4.9	–	–
13 *T. panhai*	10.7	12.2	12.1	11.9	12.7	12.7	13.3	13.3	12.4	11.8	12.7	13.0	–	5.1	4.8	4.4	4.0	4.4	4.8	–	4.7	4.7	4.2	4.2	4.2	4.7	3.6	4.0	3.8	–	–
14 *T. taliangensis*	6.3	8.2	8.0	7.6	7.9	9.7	8.8	7.9	7.3	7.4	7.5	7.3	10.5	–	1.2	4.2	2.4	3.2	3.6	–	4.0	3.8	3.2	4.0	3.6	4.5	3.5	3.6	3.2	–	–
15 *T. pseudoverrucosus*	5.7	7.9	7.7	7.1	7.4	9.7	8.6	7.4	6.6	7.4	7.7	7.1	10.3	2.7	–	4.0	2.8	3.2	3.6	–	3.8	3.8	3.8	4.4	4.0	4.9	3.9	3.2	3.6	–	–
16 *T. vietnamensis*	11.8	12.5	12.2	12.2	12.7	15.0	13.4	12.6	12.0	12.1	12.5	13.1	11.0	11.2	11.7	–	3.8	4.0	4.0	–	3.8	4.5	4.2	4.2	3.8	4.3	4.2	4.0	4.0	–	–
17 *T. ziegleri*	9.4	11.1	11.1	11.2	10.2	13.4	11.2	10.9	10.6	11.3	11.4	11.8	10.3	9.7	9.3	11.3	–	3.4	3.8	–	4.5	4.2	4.0	3.8	3.8	4.7	3.7	3.4	3.4	–	–
18 *T. hainanensis*	8.5	9.9	9.8	9.9	9.6	12.6	10.3	9.9	9.5	10.2	10.3	11.9	9.6	8.6	8.4	10.8	4.4	–	0.8	–	1.4	3.1	2.8	3.4	3.0	3.9	2.9	2.6	2.7	–	–
19 *T. asperrimus* 2	9.3	10.2	10.0	10.0	9.3	13.2	10.0	10.1	10.0	10.5	10.7	13.0	11.4	9.3	9.1	11.6	5.6	3.6	–	–	1.4	3.5	2.8	3.4	3.0	3.9	3.0	3.0	3.0	–	–
20 *T. notialis*	9.7	10.7	10.7	10.6	10.3	12.7	10.9	10.7	10.2	10.9	11.0	12.4	10.5	9.2	8.9	11.6	4.9	4.7	5.9	–	–	–	–	–	–	–	–	–	–	–	–
21 *T. asperrimus* 1	10.0	11.2	11.2	11.4	10.2	13.4	11.4	10.8	10.9	11.4	11.5	13.1	11.4	9.4	9.5	10.9	4.5	4.9	5.7	4.8	–	3.9	3.0	3.9	3.4	4.3	3.4	3.7	3.4	–	–
22 *T. liuyangensis*	9.4	10.3	10.3	10.3	9.5	12.7	10.4	10.5	9.9	10.3	10.7	12.3	9.5	9.1	9.0	10.9	8.5	7.8	8.5	8.6	8.6	–	2.4	1.9	1.5	2.4	2.0	1.3	1.7	–	–
23 *T. lizhenchangi*	10.7	11.9	11.8	11.5	11.1	13.2	12.6	11.9	10.9	11.5	11.7	14.6	9.8	9.5	9.8	11.7	10.0	8.7	9.6	9.7	10.4	7.1	–	2.0	1.6	2.5	2.0	1.8	1.6	–	–
24 *T. dabienicus* 2	9.7	10.8	10.8	10.9	10.1	12.7	11.1	9.9	9.9	10.6	10.5	10.9	9.7	9.0	9.4	10.8	8.3	7.9	8.8	8.2	8.1	7.3	8.3	–	0.8	1.3	0.9	1.2	1.3	–	–
25 *T. broadoridgus*	9.1	10.3	10.2	10.5	9.9	12.3	11.0	9.9	9.7	10.1	10.2	11.2	9.5	9.1	9.0	10.7	8.0	7.5	8.8	7.9	8.0	7.0	8.1	3.4	–	0.9	0.9	0.8	1.1	–	–
26 *T. dabienicus* 1	10.2	11.0	11.1	11.2	11.0	13.0	12.2	10.9	10.5	10.9	11.1	11.6	9.7	9.2	9.6	10.9	9.1	8.9	9.6	8.9	9.0	7.4	8.8	3.9	3.4	–	1.0	1.7	1.9	–	–
27 *T. wenxianensis* 3	9.1	10.2	10.2	10.3	9.9	12.0	11.2	10.0	9.6	10.3	10.4	10.8	9.2	8.8	8.9	10.7	7.8	7.5	8.5	7.8	8.2	7.0	7.8	3.2	2.2	1.0	–	1.2	1.3	–	–
28 *T. wenxianensis* 2	9.5	10.3	10.4	10.7	9.7	12.5	11.0	10.1	9.7	10.0	10.2	11.7	10.3	9.0	9.2	11.0	8.6	8.2	9.0	8.2	8.5	7.2	8.0	3.3	2.8	3.6	2.9	–	1.1	–	–
29 *T. wenxianensis* 1	9.9	11.0	11.1	10.9	10.0	12.7	11.4	10.0	9.6	10.1	10.3	11.9	10.5	9.1	9.4	10.7	9.3	8.9	9.5	8.9	9.0	7.3	8.3	4.4	4.1	4.6	4.0	4.0	–	–	–
30 *T. ngarsuensis*	6.6	1.8	1.5	6.2	6.9	9.3	7.5	6.8	2.8	6.7	7.0	8.0	12.5	9.1	8.6	13.1	11.9	10.6	10.5	11.8	11.9	11.3	12.6	11.7	11.3	12.5	11.5	11.6	11.9	–	–
31 *Tylototriton* sp. 1	5.7	6.7	6.4	6.7	4.2	7.7	4.7	3.5	2.8	2.5	3.2	6.6	12.5	7.5	7.3	12.1	10.8	10.1	10.1	10.8	10.9	10.2	11.4	10.2	10.0	10.5	10.2	10.0	10.1	6.8	–

Tylototriton kachinorum **sp. nov.**
Tables 3–4; Figures 3–6.

Holotype: ZMMU A5953 (field number NAP-08318), adult male from a swamp in a forest clearing surrounded by montane evergreen tropical forest, Ingyin Taung Mountain, Indawgyi Lake area, Mohnyin Township, Kachin State, Myanmar (approximate coordinates N25.09°, E96.28°; elevation 1 000 m a.s.l.), collected on July 18, 2018 at 2100 h by Than Zaw, Paw Lay, Parinya Pawangkhanant, Vladislav A. Gorin, and Nikolay A. Poyarkov.

Paratypes: ZMMU A5954 (field number NAP-08320), ZISP 13721 (field number NAP-08324), ZDUM-0101–0105 (field numbers NAP-08325, NAP-08322, NAP-08319, NAP-08326 and NAP-08317, respectively), seven adult males from the same locality and with the same collection information as the holotype; and ZMMU A5955–A5956 (field numbers NAP-08323 and NAP-08321, respectively), two adult females from the same locality and with the same collection information as the holotype.

Referred specimens: ZMMU A5957 (field number NAP-08305), a larva (Grosse (2013) stage 40) from the same locality and with the same collection information as the holotype.

Diagnosis: The new species is assigned to the genus *Tylototriton* based on molecular data and by the following combination of morphological attributes: (1) presence of dorsal granules, (2) dorsolateral bony ridges on head, (3) presence of dorsolateral series of knob-like warts (rib nodules); and (4) absence of quadrate spine (Figure 2). *Tylototriton kachinorum* **sp. nov.** is distinguished from all other congeners by a combination of the following morphological attributes: (1) medium body size, adult SVL 62.3–74.1 mm in males, 72.5–84.8 mm in females; (2) tail thin and long, longer than body in both sexes, lacking lateral grooves; (3) skin rough with fine granules; (4) snout truncate in dorsal view; (5) supratemporal bony ridges on head wide, protruding, beginning at anterior corner of orbit; (6) sagittal ridge on head very weak, almost indistinct; (7) limbs long and thin, tips of forelimb and hindlimb broadly overlapping when adpressed along body; (8) vertebral ridge distinct, wide, non-segmented; (9) rib nodules weakly distinct, 13–14 along each side of body; (10) background coloration brown to dark-brown; (11) labial regions, parotoids, rib nodules, whole limbs, vent, ventral tail ridge with dull orange-brown to yellowish-brown markings.

The new species is also markedly distinct from all congeners for which comparable sequences are available of *ND2* (*P*⩾5.3%) and 16S rRNA (*P*⩾2.4%) mitochondrial DNA genes.

Description of holotype: A medium-sized specimen in a good state of preservation (Figures 3–4).

Head: Head longer than wide (HW/HL ratio 89.3%) (Figure 3C), head wider than body; angularly hexagonal in shape in dorsal view, slightly depressed, gently sloping in profile (Figure 3E); snout comparatively long, three times longer than eye (UEW/

SL ratio 33.9%), sharply truncate in dorsal view (Figure 3C), slightly rounded in lateral view (Figure 3E), slightly projecting beyond lower jaw; nostrils on anterior margin of snout located notably closer to snout tip than to eye (NSD/ON ratio 58.8%), facing anterolaterally, not visible from dorsal view; labial folds absent; tongue oval, attached to anterior floor of mouth but free posteriorly and laterally; vomerine teeth arranged in inverted V-shaped almost straight series, converging and narrow anteriorly, gradually widening posteriorly, notably longer than wide (VTW/VTL ratio 77.7%), anteriorly reaching beyond level of choanae but not in contact with them, vomerine teeth 95 (47/48 in right and left branches, respectively), upper jaw teeth 93, and lower jaw teeth 110; parotoids distinct, comparatively large, crescent-shaped, notably projecting posteriorly (Figure 3E); dorsolateral supratemporal bony ridges on head wide, notably protruding, from anterior corner of orbit to anterior end of parotoid, forming medially recurved projection on its posterior end (Figure 3C); sagittal bony ridge on head very weak, almost indistinct (Figure 3C); gular fold present (Figure 3D).

Body: Body habitus comparatively slender (Figure 3A); costal folds absent; vertebral middorsal ridge wide, non-segmented, running from occiput region to anterior one fifth of tail length, separated from sagittal head ridge on head with wide gap (Figure 3C); rib nodules weakly distinct, small, forming knob-like glandular warts, arranged in two longitudinal lines on dorsolateral surfaces of dorsum, 14 on both sides of body from area posterior to axilla to level of posterior vent margin (base of tail) (Figure 3A); rib nodules almost of same size, rounded, those in posterior third of dorsum slightly oval-shaped, those on sacral area notably elongated, decreasing in size posteriorly on sacrum and tail basis. **Limbs:** Limbs comparatively long, slender (Figure 3A); forelimbs slightly shorter than hindlimbs; relative length of forelimb FLL/SVL ratio 26.2%, relative length of hindlimb ratio 28.0%; fore- and hindlimbs largely overlapping when adpressed towards each other along sides of body; fingers and toes well developed (Figure 3F–I), free of webbing; fingers four, comparative finger lengths: 1FL<4FL<2FL<3FL; toes five, comparative toe lengths: 1TL<5TL<2TL<3TL<4TL. **Tail:** Tail very long, notably exceeding body length (TAL/SVL ratio 114.9%); tail laterally compressed along entire length, tapering posteriorly, lateral grooves on tail absent; dorsal tail fin starting at anterior one fifth of tail length, more distinct posteriorly, with maximal tail height at posterior two thirds of tail length, dorsal tail fin slightly serrated; ventral tail fin smooth; tail tip pointed. **Skin texture and skin glands:** Skin rough, small granules present on dorsal surfaces of head and dorsum (Figure 3A, C), lateral sides of body and tail; on ventral surface granules become smaller, arranged in transverse striations (Figure 3B); small, sparse granules regularly arranged on throat (Figure 3D); head ridges with rough surface; skin on volar and plantar surfaces of hands and feet with tiny grooves forming reticulated pattern; metacarpal or metatarsal tubercles absent. Cloacal region notably swollen, vent as longitudinal slit (Figure 3J), vent edges with numerous transverse folds.
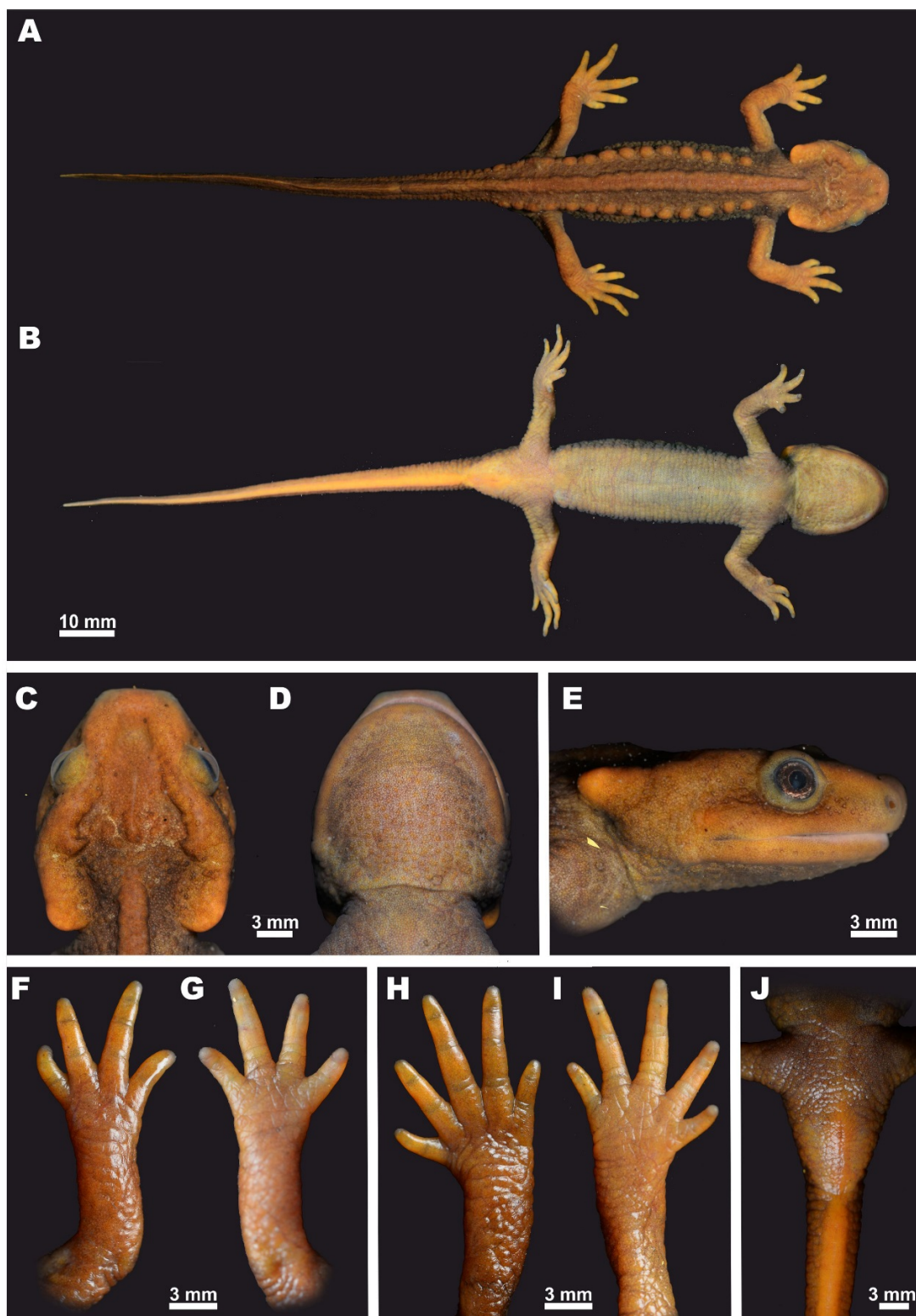
Figure 3 Holotype of *Tylototriton kachinorum* sp. nov. (ZMMU A5953, male) in life
A: Dorsal view; B: Ventral view; C: Head, dorsal view; D: Head, ventral view; E: Head, lateral view; F: Opisthenar view of right hand; G: Volar view of right hand; H: Opisthenar view of right foot; I: Plantar view of right foot; J: Ventral view of cloacal area. Photos by Nikolay A. Poyarkov.

Color of holotype in life: Dorsal ground color of dorsal surfaces of head and trunk dark brown(Figure4); dorsal surfaces of limbs and lateral surfaces of tail light yellowish-brown (Figure 3A); iris brown with tiny bronze speckles along outer margins (Figure 3E); gular region, belly, and ventral surfaces of limbs light yellowish-gray (Figure 3B); anterior parts of head and parotoids light orange-brown; rib nodules and vertebral ridge yellowish-brown to orange-brown, barely discernable from dark brown trunk coloration; upper and lower lips, posteriormost corners of parotoids, palms, and soles light-orange to yellowish.

Figure 4 Holotype of *Tylototriton kachinorum* sp. nov. (ZMMU A5953, male) *in situ* (Photo by Nikolay A. Poyarkov and Than Zaw)

Color of holotype in preservative: After preservation in ethanol for six months, coloration pattern of holotype resembles that observed in life, however yellowish and orange tints faded to light brownish-gray.

Measurements and counts of holotype: Morphometric characters (all in mm): SVL 67.2; RHL 18.1; RHW 16.2; RMXHW 16.6; RIND 5.4; RAGD 34.1; RTRL 50.4; TAL 77.3; RVL 6.3; RFLL 26.2; RHLL 28.0; RVTW 6.0; RVTL 7.7; RLJL 13.5; RSL 6.8; RIOD 7.2; RUEW 2.3; RUEL 4.4; ROL 3.3; RBTAW 9.0; RMTAW 3.2; RMXTAH 10.8; RMTAH 7.0; RON 4.6; ICD 9.6; CW 11.5; NSD 2.7; 1FL 2.9; 2FL 4.8; 3FL 5.5; 4FL 3.0; 1TL 2.5; 2TL 5.4; 3TL 7.0; 4TL 7.7; 5TL 3.6. Meristic characters: UJTN 93; LJTN 110; VTN 47/48 (right/left).

Variation: All individuals in the type series were generally similar in morphology and agreed with the holotype description in body proportions and coloration; variation of morphometric characters within the type series is shown in Table 3. The variation of dorsal coloration in seven male and two female paratypes in life is presented in Figure 5. In general, males had more robust and slender bodies than females. The males were notably smaller in body size (SVL 62.3−74.1 mm, mean 68.6 ± 2.9 mm) than the two females (SVL 72.5 − 84.8 mm) (Table 3). Body of the largest female (ZMMU A5956) was notably swollen and was wider than head width (Figure 5).

Male paratypes ZDUM-0105 and ZISP 13721 had notably shorter tails than other type specimens (Table 4) due to regeneration of tail tip after damage (Figure 5). Coloration within the type series slightly varied, from specimens lighter than the holotype, which appeared light-brown to yellowish-orange (ZDUM-0102), to darker specimens, which appeared dark-brown with duller orange-brown light markings (male ZISP 13721 and female ZMMU A5956) (Figure 5).

Eggs and clutch: The clutch size is unknown. The diameter of ripe eggs in the ovaries of a female paratype (ZMMU A5956) ranged from 1.6 to 1.7 mm (n=5, mean=1.7 mm). The animal pole was dark brown and the remaining area of ova was cream.

Larval morphology: Description of larval morphology is based on a single larval specimen (ZMMU A5957, Grosse (2013) stage 40) (see Referred specimens for details). Details of larval morphology are presented in Figure 6.

Larval measurements (all in mm): SVL 10.5; HL 3.8; HW 3.4; OL 0.8; AGD 5.9; TAL 9.7; FLL 3.6; HLL 2.8; MXTAH 2.6.

Larval external morphology: Body elongated, higher than wide. Head large, trapezoidal in shape, wide and slightly depressed with short, flattened snout, comprising 37% of snout-vent length (SVL), gently sloping in lateral view, two times wider than body in dorsal view. Snout truncate in dorsal

Figure 5 Variation of dorsal coloration in paratypes of *Tylototriton kachinorum* sp. nov.
Scale bar: 10 mm. Photos by Nikolay A. Poyarkov.

Table 3 Measurements of type series of *Tylototriton kachinorum* sp. nov. (all in mm)

Specimen	ZMMU A5953	ZMMU A5954	ZDUM-0101	ZDUM-0102	ZDUM-0103	ZDUM-0104	ZDUM-0105*	ZISP 13721*	M		ZMMU A5955	ZMMU A5956	F
Type status	Holotype	Paratype	Paratype	Paratype	Paratype	Paratype	Paratype	Paratype			Paratype	Paratype	
Sex	M	M	M	M	M	M	M	M	**Mean ±SD**	**(Min–Max)**	F	F	**Mean ±SD**
SVL	67.2	74.1	74.0	68.3	66.9	69.3	62.3	66.3	**68.6±2.9**	**(62.3–74.1)**	72.5	84.8	**78.7±6.2**
HL	18.1	20.7	20.7	18.6	19.6	19.7	16.9	17.3	**18.9±1.2**	**(16.9–20.7)**	18.1	20.3	**19.2±1.1**
HW	16.2	19.2	18.5	17.0	16.7	17.7	15.8	16.4	**17.2±1.0**	**(15.8–19.2)**	18.4	21.4	**19.9±1.5**
MXHW	16.6	19.6	18.6	17.5	17.6	18.4	16.6	16.7	**17.7±0.9**	**(16.6–19.6)**	19.4	23.0	**21.2±1.8**
IND	5.4	6.4	5.7	5.4	5.2	5.6	4.2	4.8	**5.3±0.4**	**(4.2–6.4)**	5.8	6.8	**6.3.±0.5**
AGD	34.1	36.6	36.6	34.0	33.1	33.9	30.8	33.2	**34.0±1.3**	**(30.8–36.6)**	40.5	48.2	**44.4±3.9**
TRL	50.4	56.2	55.1	51.3	50.4	52.9	47.1	49.4	**51.6±2.3**	**(47.1–56.2)**	58.4	69.0	**63.7±5.3**
TAL	77.3	89.6	96.3	79.2	79.2	85.2	57.0	67.8	**78.9±8.7**	**(57.0–96.3)**	82.7	85.2	**84.0±1.3**
VL	6.3	7.4	9.7	6.8	6.2	7.4	5.7	6.5	**7.0±0.9**	**(5.7–9.7)**	4.9	4.8	**4.9±0.1**
FLL	26.2	29.3	29.1	26.5	26.1	28.2	24.1	26.4	**27.0±1.4**	**(24.1–29.3)**	26.1	29.9	**28.0±1.9**
HLL	28.0	31.0	31.6	28.0	27.3	29.7	26.6	27.5	**28.7±1.5**	**(26.6–31.6)**	29.0	32.2	**30.6±1.6**
VTW	6.0	6.7	6.6	6.2	6.1	6.3	5.6	5.9	**6.2±0.3**	**(5.6–6.7)**	6.4	7.4	**6.9±0.5**
VTL	7.7	9.1	9.4	8.8	8.9	9.2	8.4	8.8	**8.8±0.4**	**(7.7–9.4)**	8.4	9.7	**9.1±0.6**
LJL	13.5	16.0	14.1	13.9	13.7	14.4	12.3	13.4	**13.9±0.7**	**(12.3–16.0)**	14.5	16.9	**15.7±1.2**
SL	6.8	7.6	8.1	7.3	7.0	7.5	6.2	6.5	**7.1±0.5**	**(6.2–8.1)**	7.3	8.7	**8.0±0.7**
IOD	7.2	8.4	8.1	7.3	8.0	7.9	7.2	7.3	**7.7±0.4**	**(7.2–8.4)**	7.7	8.7	**8.2±0.5**
UEW	2.3	2.5	2.6	2.4	2.4	2.4	2.2	2.2	**2.4±0.1**	**(2.2–2.6)**	2.3	2.8	**2.6±0.2**
UEL	4.4	5.0	4.9	4.6	4.4	4.6	4.1	4.4	**4.5±0.2**	**(4.1–5.0)**	4.3	5.3	**4.8±0.5**
OL	3.3	3.6	3.6	3.3	3.2	3.4	3.1	3.2	**3.3±0.1**	**(3.1–3.6)**	3.6	4.2	**3.9±0.3**
BTAW	9.0	9.7	9.5	10.0	9.7	9.6	8.8	9.6	**9.5±0.3**	**(8.8–10.0)**	8.5	9.8	**9.2±0.7**
MTAW	3.2	3.3	3.9	3.4	3.6	3.7	3.3	3.6	**3.5±0.2**	**(3.2–3.9)**	3.8	4.2	**4.0±0.2**
MXTAH	10.8	11.8	10.8	10.7	10.1	10.2	9.0	10.9	**10.5±0.6**	**(9.0–11.8)**	11.6	11.9	**11.7±0.2**
MTAH	7.0	9.0	7.3	7.5	7.8	7.7	7.7	8.4	**7.8±0.5**	**(7.0–9.0)**	9.3	9.7	**9.5±0.2**
ON	4.6	5.1	5.1	4.7	4.7	4.7	4.2	4.7	**4.7±0.2**	**(4.2–5.1)**	5.0	5.2	**5.1±0.1**

Character abbreviations: SVL: Snout-vent length; HL: Head length; HW: Head width; MXHW: Maximum head width; IND: Internarial distance; AGD: Axilla-groin distance; TRL: Trunk length; TAL: Tail length; VL: Vent length; FLL: Forelimb length; HLL: Hindlimb length; VTW: Vomerine tooth series width; VTL: Vomerine tooth series length; LJL: Lower jaw length; SL: Snout length; IOD: Interorbital distance; UEW: Upper eyelid width; UEL: Upper eyelid length; OL: Orbit length; BTAW: Basal tail width; MTAW: Tail width at mid-level of tail; MXTAH: Maximum tail height; MTAH: Tail height at mid-level of tail; ON: Orbitonarial distance. M: Male. F: Female. For other abbreviations see "Materials and Methods". Asterisk (*) denotes damaged and regenerated tail.

view (Figure 6B), rounded in lateral view (Figure 6A). Tail subequal to body length comprising 93% of SVL; myotomes on body and tail not discernable in lateral view. Nostrils rounded, small, oriented anterolaterally, located much closer to snout tip than to eye. Eyes large, rounded, with lateral orientation but still visible in dorsal view (Figure 6B). Limbs thin, forelimbs longer than hindlimbs, HLL / FLL ratio 79.1%. Forelimbs with four well-developed elongated fingers; forelimb turned, palm facing ventrally; relative finger lengths: 4FL<3FL< 1FL<2FL. Hindlimbs with knee joint already formed and four well-developed toes, fifth toe as nub; relative toe lengths: 5TL< 4TL<3TL<1TL<2TL. Orbit diameter (OL) 7.7% of SVL. Short longitudinal slit for vent. Height of tail musculature at highest portion comprises 50%−60% of tail height. Maximum height of dorsal tail fin 45%−55% of maximum tail height. Ventral tail fin two times lower than dorsal tail fin. Ventral tail fin roughly at level of vent, dorsal fin lower than head, at level of axilla and reaching maximum height mid tail. Tail tip sharply pointed (Figure 6A). Skin completely smooth; lateral line organs visible on ventral side of head; mouth open with well-developed
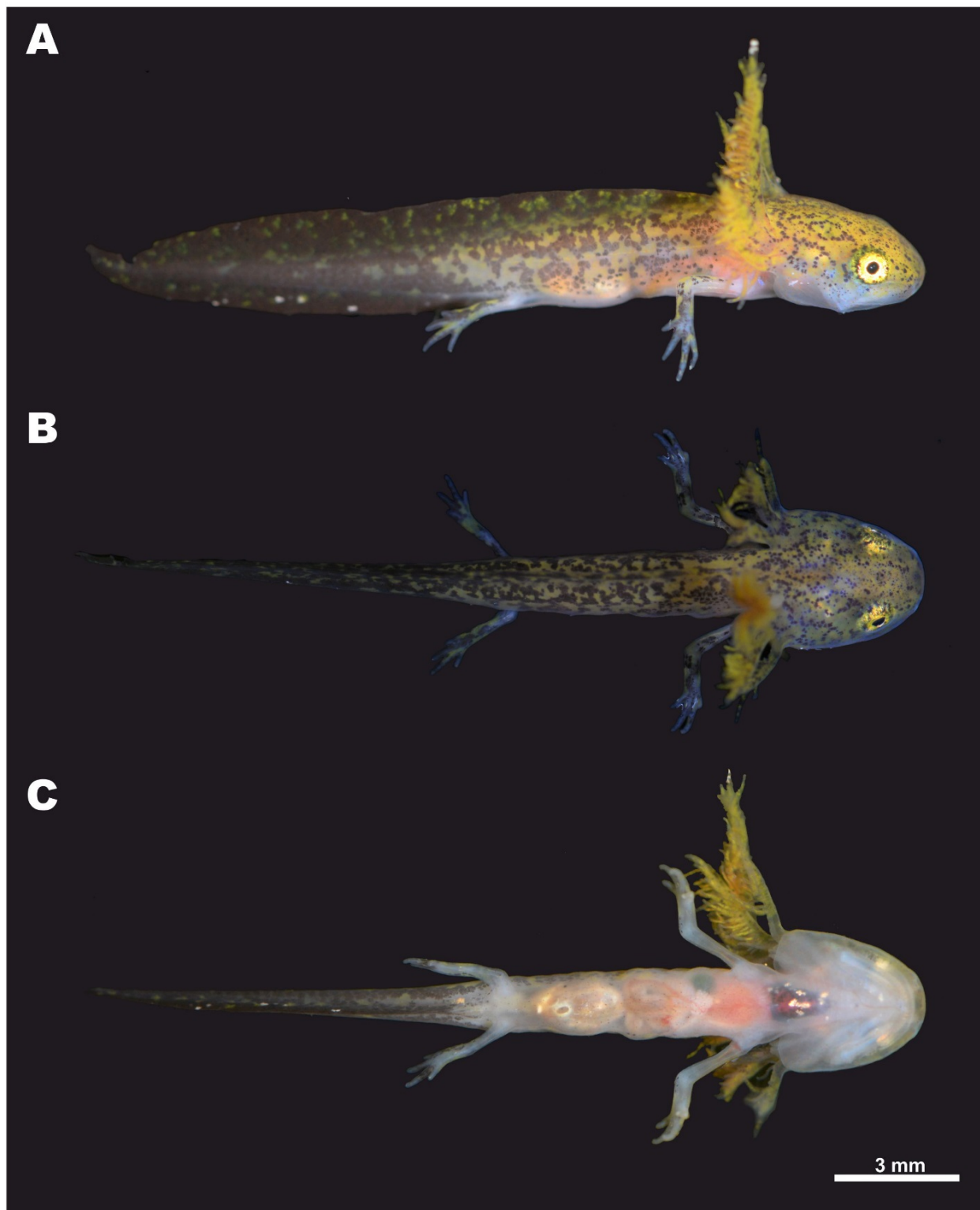
Figure 6 Lateral (A), dorsal (B), and ventral (C) views of larval specimen (ZMMU A5957; Grosse (2013) stage 40) of *Tylototriton kachinorum* sp. nov. in life
Scale bar: 3 mm. Photos by Nikolay A. Poyarkov.

teeth; no remains of yolk (Figure 6C); gills well-developed, much higher than body, with fimbriae clearly visible.

Larval coloration in life: In life body background color ochre to golden (Figure 6A, B), ventral surfaces pinkish, translucent (Figure 6C). Body, tail, and head pigmented dorsally: tail almost uniform purple-gray with rare golden speckles, pigmentation forms tortoise-shell golden−dark-gray pattern on body and dorsal fin, head pigmentation less dense, reduced to grayish spots and dots. Few dark spots on ventral fin and limbs. Eyes, except for pupil, fully pigmented, iris golden (Figure 6A).

Position in mtDNA genealogy and sequence divergence: According to our mtDNA data, *Tylototriton kachinorum* **sp. nov.** belongs to clade 1 of the subgenus *Tylototriton* s. str. (Figure 2) and is grouped with *Tylototriton* species from the Shan Plateau of Myanmar (*T. shanorum*, *T. ngarsuensis*) and Himalaya (*T. himalayanus*). Uncorrected genetic *P*-distances between *Tylototriton kachinorum* **sp. nov.**, 16S rRNA sequences, and all homologous sequences of congeners available included in our analyses varied from 5.3% (with sister species *T. himalayanus*) to 14.6% (with *T. lizhenchangi*) (Table 2).

Distribution and biogeography: To date, *Tylototriton kachinorum* **sp. nov.** is known only from a single locality on the slopes of Ingyin Taung Mountain, Kachin State, Myanmar (Figure 1) at elevations from 900 to 1 050 m a.s.l. The Ingyin Taung Mountain belongs to the southernmost part of the Kachin Hills − a heavily forested group of highlands in the extreme northeastern area of Kachin State, consisting of a series of mountain ranges running mostly in a north-to-south direction. The actual distribution of *Tylototriton kachinorum* **sp. nov.** may be wider: it is anticipated that the new species occurs in the montane forests of adjacent mountains surrounding the largest inland lake of Kachin State, Indawgyi Lake, and possibly further northwards along the Kumon Bum subrange of the Kachin Hills.

Natural history notes: Our knowledge on the biology of *Tylototriton kachinorum* **sp. nov.** is scarce. Adult animals were encountered at night after 1900 h in flooded areas of shallow slow-moving streams and artificial ponds in forest clearings, which were used by local Kachin farmers as a watering place for cattle (Figure 7). Surrounding areas were covered by secondary bamboo forest and primary mixed evergreen tropical forest. Adult male newts were observed slowly moving along the clay bottom in clear water 20−40 cm deep; both females and the larval specimen were collected in deeper areas (60−100 cm deep) from dense water vegetation using a dip-net. Courtship behavior of male newts was observed in July. Local Kachin farmers reported that they often find adult newts walking in dense vegetation far from waterbodies, especially after rain; they are also often encountered in wells they construct. The new species is known to local Kachin people as "*Lan Yan*" literally meaning "water agama" in their native language.

Other species of amphibians recorded syntopically with the new species at the type locality include *Microhyla heymonsi* Vogt, *Microhyla mukhlesuri* Hasan, Islam, Kuramoto, Kurabayashi & Sumida, *Microhyla butleri* Boulenger, *Limnonectes limborgi* (Sclater), *Limnonectes* sp., *Fejervarya* sp., *Kurixalus* sp., *Feihyla vittata* (Boulenger), *Rhacophorus bipunctatus* Ahl, *Polypedates mutus* (Smith), and *Raorchestes parvulus* (Boulenger).
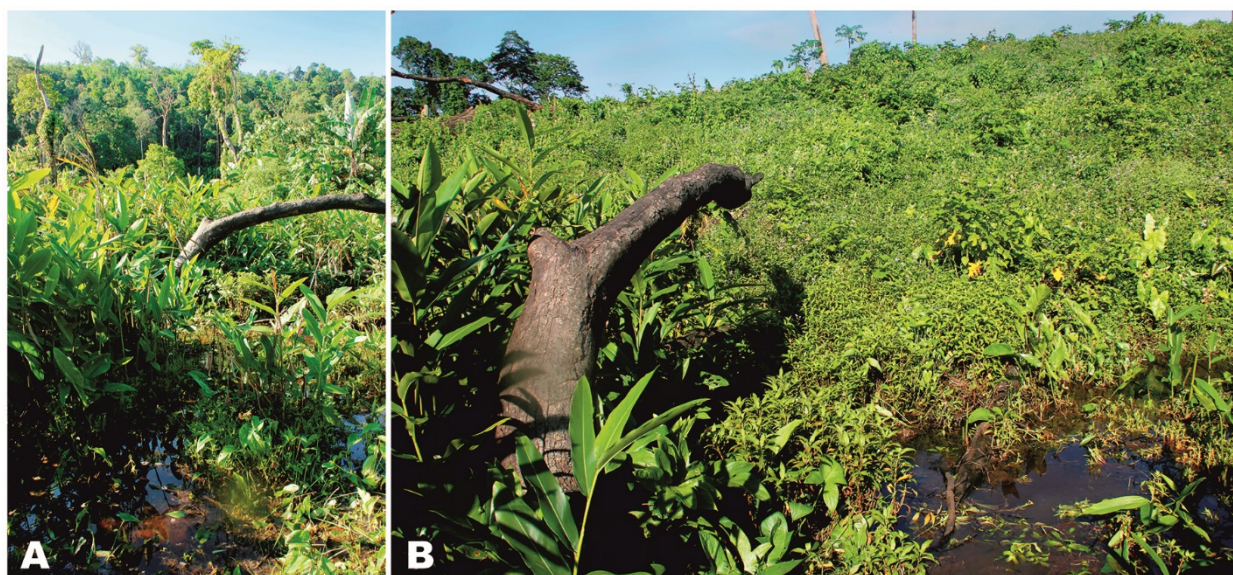

Figure 7 Breeding habitats of *Tylototriton kachinorum* sp. nov. at type locality
Temporary swamps in forest clearings within montane tropical forest on Ingyin Taung Mountain, Indawgyi Lake area, Kachin State, Myanmar, where larva and adult specimens were collected. Photos by Parinya Pawangkhanant.

Comparisons: According to phylogenetic analyses, *Tylototriton kachinorum* **sp. nov.** falls into clade 1 of the subgenus *Tylototriton* s. str. and morphological comparisons with members of this group appear to be the most pertinent. The new species can be easily distinguished from members of the subgenus *Yaotriton* (clades 3–5 in Figure 2) by having light color markings on parotoids, lips, vertebral ridge, rib nodules, limbs, and ventral tail ridge (vs. dark body coloration except for palms and soles, vent region, and ventral ridge of tail in most members of the subgenus *Yaotriton*, with the exception of *T. panhai*). The new species can be further distinguished from *T. panhai* by having light color markings on entire limbs (vs. distinct light markings only on palms, soles, and fingers).

Morphometric comparisons and morphological differences in several diagnostic characters between *Tylototriton kachinorum* **sp. nov.** and the closely related species of the subgenus *Tylototriton* are summarized in Table 4. In particular, the new species can be distinguished from *T. taliangensis* (in clade 2 of the subgenus *Tylototriton*, sometimes regarded as a separate subgenus or full genus *Liangshantriton*; see Gong et al., 2018) by having distinct rib nodules, light markings on rib nodules, lips, and parotids (vs. lack of distinct rib nodules, mostly dark charcoal-black body coloration with light orange to red markings only on posterior part of parotoids, digits, palms, soles, vent, and ventral tail ridge). From *T. pseudoverrucosus* (clade 2) and *T. kweichowensis* (clade 1 of the subgenus *Tylototriton*, sometimes regarded as a separate subgenus *Qiantriton*), *Tylototriton kachinorum* **sp. nov.** can be distinguished by having isolated light markings on rib nodules (vs. connected markings forming light dorsolateral lines).

Table 4 Morphological comparison between *Tylototriton* species found in Myanmar and adjacent territories

Species	*Tylototriton kachinorum* **sp. nov.**		*T. shanorum*		*T. ngarsuensis*	
	M	F	M	F	M	F
Character	8	2	1	2	2	1
SVL	68.6±2.9	72.5–84.8	76.0	76.5–87.9	74.9–76.4	102.3
RHL	27.6	23.9–24.9	22.4	24.3–25.7	24.0–26.0	21.5
RHW	25.1	25.3–25.4	25.4	24.8–26.3	24.5–28.2	26.6
RIND	7.7	8.0	6.7	6.0–6.3	8.0–8.8	7.7
RAGD	49.6	55.9–56.8	49.6	49.4–51.9	48.2–49.9	51.2
RTRL	75.3	80.5–81.4	77.6	74.3–75.7	74.2–75.5	77.5
RTAL	120.5	100.5–114.0	111.2	97.0–97.8	98.0–103.5	104.6
RVL	10.2	5.6–6.8	9.3	3.4–3.5	10.7–12.3	8.0
RFLL	39.3	35.3–36.0	34.7	31.7–32.5	39.7–39.9	35.5
RHLL	41.9	37.9–39.9	37.2	35.6–37.0	41.9–47.1	38.7
RMXHW	25.8	26.8–27.1	25.9	25.7–27.1	–	–
RVTW	9.0	8.7–8.8	6.1	6.1–7.5	–	–
RVTL	12.8	11.4–11.6	10.7	11.4–12.0	–	–
Snout	Truncate		Blunt to truncate		Rounded to blunt	
Supratemporal ridge	Wide, protruding, begins at anterior corner of orbit		Wide, protruding, begins in loreal region		Wide, not protruding, begins posterior to orbit	
Sagittal ridge	Very weak, indistinct		Very weak		Very weak, in males	
Surface of head ridges	Rough		Rough		Very rough	
Adpressed limbs	Overlapping		Overlapping		Overlapping	
Vertebral ridge	Wide, non-segmented		Narrow, weakly segmented		Wide, weakly segmented	
Rib nodules	Weakly distinct, 13–14		Distinct, 14		Distinct, 15	
Ground color	Brown to dark brown		Dark brown to black		Nearly black	
Color of light markings	Orange-brown to yellowish-brown		Yellow to reddish brown		Dark yellow	
Location of light markings	Parotoids, rib nodules, palms, soles, vent, ventral tail ridge		Head, vertebral ridge, rib nodules, vent, whole limbs and tail		Labial regions, palms and soles, vent, ventral tail ridge	
Lateral grooves on tail	Absent		Absent		Absent	

Species	T. himalayanus		T. verrucosus		T. shanjing	
	M	F	M	M	F	M
Character	32	13	3	32	13	3
SVL	71.92±6.1	76.06±7.5	70.7±4.7	71.92±6.1	76.06±7.5	70.7±4.7
RHL	24.5	25.9	24.3	24.5	25.9	24.3
RHW	23.0	23.6	23.7	23.0	23.6	23.7
RIND	8.4	8.2	7.0	8.4	8.2	7.0
RAGD	53.6	51.6	50.7	53.6	51.6	50.7
RTRL	79.9	77.1	75.7	79.9	77.1	75.7
RTAL	98.0	100.6	104.9	98.0	100.6	104.9
RVL	11.8	12.5	7.0	11.8	12.5	7.0
RFLL	36.2	36.1	34.3	36.2	36.1	34.3
RHLL	37.5	38.1	37.3	37.5	38.1	37.3
RMXHW	–	–	25.3	–	–	25.3
RVTW	–	–	7.7	–	–	7.7
RVTL	–	–	9.8	–	–	9.8
Snout	Blunt		Truncate		Rounded	
Supratemporal ridge	Very wide, protruding		Narrow, steep		Narrow, steep	
Sagittal ridge	Weak, glandular		Weak		Short, weak	
Surface of head ridges	Very rough		Smooth		Smooth	
Adpressed limbs	Overlapping		Overlapping		Overlapping	
Vertebral ridge	Non-segmented		Well segmented		Well segmented	
Rib nodules	Large, prominent, 16		Weakly distinct, 14–15		Distinct, 14	
Ground color	Brown to dark brown		Blackish		Blackish	
Color of light markings	Light brown		Orange		Bright to dark orange	
Location of light markings	Ventral surface of limbs, vent, ventral tail ridge		Palms, soles, vent and ventral ridge of tail		Head, vertebral ridge, rib nodules, vent, whole limbs and tail	
Lateral grooves on tail	Very distinct		Absent		Weak	
Species	T. uyenoi		T. anguliceps		T. podichthys	
	M	F	M	F	M	F
Character	9	2	2	5	2	2
SVL	68.1±3.8	69.3–78.3	61.1–62.5	70.6±3.4	56.5–60.2	73.4–78.3
RHL	24.7	25.8–26.9	26.2–29.5	23.4	32.6–34.3	28.1–29.3
RHW	25.0	23.1–24.0	22.7–23.4	22.7	26.4–28.0	24.8–25.9
RIND	7.0	7.0–7.1	6.6–7.4	6.5	8.3–8.7	7.5–7.9
RAGD	48.8	47.9–50.7	47.2–47.8	52.8	48.0–50.7	52.1–53.5
RTRL	75.3	73.1–74.2	70.5–73.8	76.6	65.7–67.4	70.7–71.9
RTAL	115.0	88.0–97.0	97.1–102.3	91.2	80.2–104.8	79.2–81.4
RVL	7.4	1.7–1.9	7.2–7.2	2.5	14.2–14.8	6.3–7.7
RFLL	34.3	30.6–32.7	32.7–34.9	30.2	39.4–40.5	34.0–36.2
RHLL	37.5	37.4–37.4	36.8–37.3	33.3	38.2–40.2	35.8–36.1
RMXHW	25.9	23.6–25.0	23.7–24.1	23.3	–	–
RVTW	7.6	6.6–7.0	6.4–7.8	6.9	–	–
RVTL	10.3	8.8–10.2	9.9–10.8	9.2	–	–

Species	T. uyenoi	T. anguliceps	T. podichthys
Snout	Rounded	Truncate	Rounded
Supratemporal ridge	Narrow, steep	Narrow, very steep	Very wide, protruding
Sagittal ridge	Short, weak	Long, protruding	Weak, glandular
Surface of head ridges	Smooth	Rough	Very rough
Adpressed limbs	Overlapping	Overlapping	Touching
Vertebral ridge	Weakly segmented	Weakly segmented	Non-segmented
Rib nodules	Prominent, 14–15	Prominent, 15	Large, prominent, 15–16
Ground color	Dark brown to black	Blackish	Blackish
Color of light markings	Dark-orange to red	Bright-orange	Orange to dark-red
Location of light markings	Head, vertebral ridge, rib nodules, vent, whole limbs and tail	Head, vertebral ridge, rib nodules, vent, whole limbs and tail	Head, vertebral ridge, rib nodules, vent, dorsal surface limbs, ventral tail ridge
Lateral grooves on tail	Absent	Absent	Absent

Character abbreviations**:** SVL: Snout-vent length; RHL: Relative head length; RHW: Relative head width; RIND: Relative internarial distance; RAGD: Relative axilla-groin distance; RTRL: Relative trunk length; RTAL: Relative tail length; RVL: Relative vent length; RFLL: Relative forelimb length; RHLL: Relative hindlimb length; RMXHW: Relative maximum head width; RVTW: Relative vomerine tooth series width; RVTL: Relative vomerine tooth series length. M: Male. F: Female. For abbreviations see "Materials and Methods".

Tylototriton kachinorum **sp. nov.** can be distinguished from *T. uyenoi*, *T. pulcherrimus*, *T. shanjing*, and *T. yangi* by having dull orange-brown to yellowish-brown light markings (vs. much brighter orange to bright-yellow light markings). In particular, *T. pulcherrimus* has a series of bright-orange glandular spots located ventrolaterally and on flanks (vs. dark-brown coloration of flanks lacking light spots in new species); *T. yangi* has contrasting charcoal-black coloration of head and lips with only posteriormost part of parotoid colored bright orange, and no light ventral markings on body and tail (vs. all head dull orange-brown with slightly lighter lips and parotoids, light markings present on ventral tail ridge and vent in new species). *Tylototriton kachinorum* **sp. nov.** can be distinguished from *T. uyenoi* by relatively longer head in males (RHL 27.6 vs. 24.7), greater internarial distance (RIND 7.7−8.0 vs. 7.0−7.1 for both sexes), and longer tail in both sexes (RTAL 120.5 vs. 115.0 for males; 100.5−114.0 vs. 88.0−97.0 for females) (Table 4). Males of the new species can be further diagnosed from males of *T. shanjing* by having comparatively wider head (RHW 25.1 vs. 22.2), longer tail (RTAL 120.5 vs. 104.4), greater internarial distance (RIND 7.7 vs. 7.1), comparatively wider (RVTW 9.0 vs. 6.7) and longer vomerine tooth series (RVTL 12.8 vs. 8.8) (Table 4). The new species can be further differentiated from *T. shanjing* by non-segmented vertebral ridge (vs. well-segmented) and brown to dark-brown background coloration of body (vs. blackish background coloration).

Tylototriton kachinorum **sp. nov.** can be distinguished from *T. verrucosus* by having light ventral markings on body and tail (vs. no ventral markings on body and tail), comparatively longer head (RHL 27.6 vs. 24.3 in males, RHL 23.9−24.9 vs. 21.7 in females), comparatively wider head in both sexes (RHW 25.1−25.4 vs. 20.5−23.7), greater internarial distance in both sexes (RIND 7.7−8.0 vs. 6.2−7.0), longer tail in both sexes (RTAL 120.5 vs. 104.9 for males; 100.5−114.0 vs. 102.5 for females) (Table 4), non-segmented vertebral ridge (vs. well-segmented), and brown to dark-brown background coloration of body (vs. blackish background coloration).

The new species can be distinguished from *T. podichthys* by having comparatively shorter head in both sexes (RHL 23.9−27.6 vs 28.1−34.3), much longer tail in both sexes (RTAL 100.5−120.5 vs. 79.2−104.8), truncate snout (vs. rounded), comparatively smoother skin on parotoids and dorsal surface of head, comparatively longer limbs (limbs widely overlap when adpressed to body in the new species vs. digit tips touch when limbs are adpressed to body in *T. podichthys*), 13−14 rib nodules (vs. 15−16 rib nodules), and duller coloration with orange-brown light markings and brown to dark-brown background (vs. orange to dark-red light markings and blackish background) (Table 4).

Tylototriton kachinorum **sp. nov.** can be distinguished from *T. anguliceps* by having larger body size in both sexes (SVL 68.6±2.9 mm in males and 72.5−84.8 mm in females of new species vs. 61.1−62.5 mm and 70.6±3.4 mm in *T. anguliceps*), comparatively wider head in both sexes (RHW 25.1−25.4 vs. 22.7−23.4), greater internarial distance in both sexes (RIND 7.7−8.0 vs. 6.5−7.4), longer tail in both sexes (RTAL 100.5−120.5 vs. 91.2−102.3), and comparatively wider (RVTW 8.8−9.0 vs. 6.4−7.8) and longer vomerine tooth series (RVTL 11.4−12.8 vs. 9.2−10.8) (Table 4). The new species can be further diagnosed from *T. anguliceps* by having wide protruding supratemporal ridges (vs. narrow and steep supratemporal ridges), very small and almost indiscernible sagittal ridge (vs.

long and notably protruding sagittal ridge), wide and non-segmented vertebral ridge (vs. narrow and weakly segmented vertebral ridge), less distinct 13–14 rib nodules (vs. rib nodules more distinct and protruding, not less than 15), and duller coloration with orange-brown light markings and brown to dark-brown background (vs. bright-orange light markings and blackish background) (Table 4).

Phylogenetically and morphologically, *Tylototriton kachinorum* **sp. nov.** is most closely related to other species of *Tylototriton* inhabiting Myanmar (e. g., *T. shanorum* and *T. ngarsuensis*) from the Shan Plateau and *T. himalayanus* from Nepalese Himalaya (Table 4). The new species can be readily distinguished from *T. shanorum* by having longer head in males (RHL 27.6 vs. 22.4), greater internarial distance in both sexes (RIND 7.7–8.0 vs. 6.0–6.7), notably longer tail in both sexes (RTAL 120.5 vs. 111.2 in males, 100.5–114.0 vs. 97.0–97.8 in females), wider vomerine tooth series in both sexes (RVTW 8.7–9.0 vs. 6.1), longer vomerine tooth series in males (RVTL 12.8 vs. 10.7) (Table 4), supratemporal bony ridges beginning at anterior corner of orbit (vs. supratemporal bony ridges beginning at loreal region), and wide, non-segmented vertebral ridge (vs. narrow, weakly segmented vertebral ridge). *Tylototriton kachinorum* **sp. nov.** has generally lighter coloration than *T. shanorum*: brownish ground color with orange-brown light markings (vs. more contrasting dark brown to black background color with yellow to reddish-brown light markings) and light markings present only on ventral tail ridge (vs. lateral sides of tail with light markings) (Table 4).

Tylototriton kachinorum **sp. nov.** can be easily distinguished from *T. ngarsuensis* by having generally smaller body size in males (SVL 68.6±2.9 mm vs. 74.9–76.4 mm) and females (SVL 72.5–84.8 mm vs. 102.3 mm), comparatively longer head in males (RHL 27.6 vs. 24.0–26.0) and females (RHL 23.9–24.9 vs. 21.5), longer tail in males (RTAL 120.5 vs. 98.0–103.5), generally longer tail in females (RTAL 100.5–114.0 vs. 104.6), and comparatively shorter vent length (in males RVL 10.2 vs. 10.7–12.3, in females 5.6–6.8 vs. 8.0) (Table 4). The new species can be further distinguished from *T. ngarsuensis* by having truncate snout (vs. rounded snout), supratemporal ridges starting at anterior corner of orbit (vs. supratemporal bony ridges beginning posterior to orbit), non-segmented vertebral ridge (vs. weakly segmented), and 13–14 weakly distinct rib nodules (vs. 15 well-distinct rib nodules) (Table 4). *Tylototriton kachinorum* **sp. nov.** also has much lighter and duller colorationthan *T. ngarsuensis*: background color brown to light brown (vs. nearly black) with light orange-brown markings on rib nodules, parotids, and whole limbs (vs. no light markings on rib nodules or parotids, dark-yellow coloration present only on palms and soles) (Table 4).

Morphologically, *Tylototriton kachinorum* **sp. nov.** most resembles its sister species, *T. himalayanus* from Nepal; however, it can be readily distinguished by the following morphological attributes: comparatively longer head in males (RHL 27.6 vs. 24.5), notably wider head in both sexes (RHW 25.1–25.4 vs. 23.0–23.6), shorter internarial distance in both sexes (RIND 7.7–8.0 vs. 8.2–8.4), and longer tail in both sexes (RTAL 100.5–120.5 vs. 98.0–100.6) (Table 4). The new

species has generally smoother skin than *T. himalayanus* and can be distinguished from the latter species by having weakly distinct 13–14 rib nodules (vs. large and prominent 16 rib nodules) and absence of lateral grooves on tail (vs. very distinct). Coloration of the new species is similar to *T. himalayanus*, but light markings are also present on labial regions, parotoids, rib nodules, and whole limbs (vs. no light markings on head and rib nodules, on limbs only on ventral surfaces) (Table 4).

Etymology: The specific name "*kachinorum*" is a Latin adjective in the genitive plural (masculine gender), derived from the name of the Kachin people who inhabit the montane areas of northern Myanmar and adjacent territories (Kachin Hills), including the type locality of the new species.

Recommended vernacular name: We recommend the following name in English: *Kachin Crocodile Newt*. Recommended vernacular name in Burmese (Myanmar) language: *Kachin Yae Poke Thin*.

Conservation status: *Tylototriton kachinorum* **sp. nov.** is, to date, known from a single locality in the southern part of the Kachin Hills of northern Myanmar; the actual range of the new species is unknown. The new species is anticipated to inhabit elevations above 900 m a. s. l. on mountains surrounding the Indawgyi Lake valley and may be found in other parts of the Kachin Hills. Further research is required to estimate the actual distribution, population trends, and possible threats to the new species. *Tylototriton kachinorum* **sp. nov.** appears to be associated with montane forests and may be affected by growing anthropogenic pressure and forest destruction observed in different areas of Kachin State in Myanmar. Given the available information, we suggest *Tylototriton kachinorum* **sp. nov.** to be tentatively considered as a Vulnerable (VU) species following IUCN's Red List categories (IUCN, 2001).

DISCUSSION

Our phylogenetic data largely confirmed the phylogeny of *Tylototriton* as presented in the earlier studies of Phimmachak et al. (2015), Khatiwada et al. (2015), Wang et al. (2018), and Grismer et al. (2018a). In particular, our data support the subdivision of *Tylototriton* into two major groups, traditionally regarded as subgenera: *Tylototriton* s. str. (clades 1 and 2) and *Yaotriton* (clades 3–5). Two other subgenera recently proposed by Fei et al. (2012), namely *Qiantriton* and *Liangshantriton* are nested within the radiation of *Tylototriton* s. str. (Figure 2) and possibly should not be regarded as independent subgenera or even genera (see Gong et al., 2018; Hernandez, 2016). Our mtDNA-based genealogy is insufficiently resolved in a number of deeper tree nodes; however, it unambiguously suggests that clade 1 of *Tylototriton* s. str. is subdivided into three main subclades with prominent geographic structuring. The northernmost member of this group – *T. kweichowensis*, occurring in the Guizhou Plateau of China (Figure 1, samples 7–10), is distant from other members

of clade 1 and its phylogenetic position is unresolved. Most other species of clade 1, which occur in northern Indochina and Yunnan Province of China, form a monophyly (including *T. verrucosus*, *T. shanjing*, *T. uyenoi*, *T. anguliceps*, *T. podichthys*, *T. pulcherrimus*, *T. yangi*, and *Tylototriton* sp. 1) (Figure 1, samples 17−18 and 24−48). Finally, four species from the northern part of Myanmar and Himalaya form a distinct monophyletic group (including *T. shanorum*, *T. ngarsuensis*, *T. himalayanus*, and *Tylototriton kachinorum* **sp. nov.**).

Studies on the taxonomic status of *Tylototriton* species in Myanmar have been delayed, even though the genus has been reported from the country for long time (see Gyi, 1969). Nishikawa et al. (2014) assigned *Tylototriton* from the Shan Plateau of eastern Myanmar to a new species, *T. shanorum*, whereas Grismer et al. (2018a) recently demonstrated the presence of divergent lineages of *Tylototriton* within different parts of the Shan Plateau and described a second species for the country − *T. ngarsuensis*. Contrary to the tree of Grismer et al. (2018a), our analysis suggests that *T. shanorum* is paraphyletic with respect to *T. ngarsuensis* and is subdivided into two lineages (Figure 2). However, it is worth noting that the second lineage of *T. shanorum* is based on data from a single specimen, reported by Nishikawa et al. (2014) (KUHE42348), which was obtained through the pet trade and presumed to come from Myanmar. Its assignment to *T. shanorum* is thus tentative and this specimen possibly represents a new lineage of *Tylototriton* from the Shan Plateau, yet undiscovered in the wild. Hence, considering the profound morphological differences between *T. ngarsuensis* and *T. shanorum* reported by Grismer et al. (2018a), though genetic divergence between these species was low (*P*=1.8% for *ND2* gene), we consider that *T. ngarsuensis* indeed represents a distinct species of *Tylototriton*.

Our description of *Tylototriton kachinorum* **sp. nov.** thus represents the third species of *Tylototriton* endemic to Myanmar. *Tylototriton kachinorum* **sp. nov.** is more closely related to *T. himalayanus* than to *T. shanorum* and *T. ngarsuensis*, occurring on the Shan Plateau in the eastern part of the country. This fact can be explained from a biogeographic viewpoint: the Kachin Hills represent the southernmost outcrop of the Great Himalaya ridge (Hadden, 2008) and are isolated from the Shan Plateau by the Irrawaddy (Ayeyarwaddy) River valley, which may serve as an important biogeographic border for forest-dwelling taxa. *Tylototritonhimalayanus*, which can be found in Nepal and possibly along the Great Himalaya Ridge, was previously reported for northern Myanmar (Hernandez, 2016, 2018), but without any information on voucher specimens or reasons for such identification. There is a possibility that these records are based on the misidentification of *Tylototriton kachinorum* **sp. nov.**

The present work indicates that *Tylototriton* diversity in Myanmar is still underestimated. Phimmachak et al. (2015) and Grismer et al. (2018a) reported sequences of *Tylototriton* cf. *verrucosus* from two regions of northern Myanmar: Sagaing Region (sample 18, see Figure 1) and the eastern part of Kachin State (sample 17, see Figure 1). Surprisingly, these populations were found to be distantly related to *Tylototriton*

kachinorum **sp. nov.**, despite the geographical proximity to the southern part of Kachin Hills where the new species occurs. Sagaing and eastern Kachin *Tylototriton* populations (indicated herein as *Tylototriton* sp. 1) were reconstructed as members of the *T. verrucosus* species complex; however, they formed an mtDNA lineage clearly distinct from all currently recognized species. These data suggest that *Tylototriton* cf. *verrucosus* from northern Myanmar might represent a currently undescribed species and further morphological and phylogenetic studies are required to evaluate its taxonomic status. In agreement with the results of Wang et al. (2018), our analysis also shows deep subdivision and the presence of several lineages of possibly full-species status within *T. asperrimus*, *T. dabienicus*, and *T. wenxianensis* of the subgenus *Yaotriton*.

Our study indicates that knowledge on amphibian diversity in montane regions of northern Myanmar is still far from complete and further diversity is likely to be revealed with additional survey efforts. A number of recent studies have shown that species diversity of amphibians and reptiles is widely underestimated across Myanmar (Grismer et al., 2017a, 2017b, 2018a, 2018b, 2018c; Mulcahy et al., 2018), and it is likely that further surveys on this geographically complex and insufficiently studied region will lead to more discoveries. Recent economic development of Myanmar has led to increasing habitat loss and modification across the country (Li & Quan, 2017). Further intensified survey efforts and biodiversity assessments are urgently required for effective conservation management of yet unrealized herpetofaunal diversity in Myanmar.

COMPETING INTERESTS

The authors declare that they have no competing interests.

AUTHORS' CONTRIBUTIONS

NOMENCLATURAL ACTS REGISTRATION

The electronic version of this article in portable document format will represent a published work according to the International Commission on Zoological Nomenclature (ICZN), and hence the new names contained in the electronic version are effectively published under that Code from the electronic edition alone (see Articles 8.5−8.6 of the Code). This published work and the nomenclatural acts it contains have been registered in ZooBank, the online registration system for the ICZN. The ZooBank LSIDs (Life Science Identifiers) can be resolved and the associated information can be viewed through any standard web browser by appending the LSID

ACKNOWLEDGEMENTS

REFERENCES

Anderson J. 1871. Description of a new genus of newts from western Yunan. *Proceedings of the Zoological Society of London*, **1871**: 423–425.

Böhme W, Schöttler T, Nguyen TQ, Köhler J. 2005. A new species of salamander, genus *Tylototriton* (Urodela: Salamandridae) from northern Vietnam. *Salamandra*, **41**(4): 215–220.

Chen XH, Wang XW, Tao J. 2010. A new subspecies of genus *Tylototriton* from China (Cudata, Salamandridae). *Acta Zootaxonomica Sinica*, **35**(3): 666–670. (in Chinese)

Fang PW, Chang MLY. 1932. Notes on *Tylototriton kweichowensis* sp. *nov. and asperrimus Unterstein. Sinensia, Nanking*, **2**: 111–122.

Fei L, Ye CY, Jiang JP. 2012. Colored Atlas of Chinese Amphibians and Their Distributions. Sichuan, China: Sichuan Publishing House of Science & Technology.

Fei L, Ye CY, Yang RS. 1984. A new species and subspecies of the genus *Tylototriton* (Caudata: Salamandridae). *Acta Zoologica Sinica*, **30**: 85−91. (in Chinese)

Felsenstein J. 1985. Confidence limits on phylogenies: an approach using the bootstrap. *Evolution*, **39**(4): 783–791.

Felsenstein J. 2004. Inferring phylogenies. Sunderland, Massachusetts: Sinauer Associates, Inc. Publishers, **2**: 465.

Gong Y, Shu G, Huang F, He L, Li C, Xie F. 2018. Courtship behaviour and male sexual competition of the Taliang crocodile newt, *Liangshantriton taliangensis*. *Amphibia-Reptilia*, **39**(3): 275–288.

Grismer LL, Wood PL Jr. , Thura MK, Zin T, Quah ESH, Murdoch ML, Grismer MS, Lin A, Kyaw H, Ngwe L. 2017a. Twelve new species of *Cyrtodactylus* Gray (Squamata: Gekkonidae) from isolated limestone habitats in east-central and southern Myanmar demonstrate high localized diversity and unprecedented microendemism. *Zoological Journal of the Linnean Society*, **182**(4): 862–959.

Grismer LL, Wood PL Jr. , Thura MK, Zin T, Quah ESH, Murdoch ML, Grismer MS, Lin A, Kyaw H, Ngwe L. 2017b. Phylogenetic taxonomy of *Hemiphyllodactylus* Bleeker, 1860 (Squamata: Gekkonidae) with descriptions of three new species from Myanmar. *Journal of Natural History*, **52**(13−16):

881–915.

Grismer LL, Wood PL Jr. , Quah ESH, Thura MK, Espinoza RE, Grismer MS, Murdoch ML, Lin A. 2018a. A new species of Crocodile Newt *Tylototriton* (Caudata: Salamandridae) from Shan State, Myanmar (Burma). *Zootaxa*, **4500**(4): 553–573.

Grismer LL, Wood PL Jr. , Thura MK, Quah ESH, Grismer MS, Murdoch ML, Espinoza RE, Lin A. 2018b. A new *Cyrtodactylus* Gray, 1827 (Squamata, Gekkonidae) from the Shan Hills and the biogeography of Bent-toed Geckos from eastern Myanmar. *Zootaxa*, **4446**(4): 477–500.

Grismer LL, Wood PL Jr. , Thura MK, Quah ESH, Murdoch ML, Grismer MS, Herr MW, Lin A, Kyaw H. 2018c. Three more new species of *Cyrtodactylus* (Squamata: Gekkonidae) from the Salween Basin of eastern Myanmar underscore the urgent need for the conservation of karst habitats. *Journal of Natural History*, **52**(19−20): 1243–1294.

Grosse WR. 2013. Kommentierte Liste zur Bestimmung der Entwicklungsstadien von Schwanzlurchen Amphibia: Urodela. *In: Schultschik G, Grosse WR. Mannheim, Gefährdete Molch - und Salamanderarten-Richtlinien für Erhaltungszuchten. Mertensiella. Chimaira, Frankfurt am Main*, 189.

Gyi KM. 1969. The occurrence of *Tylototriton verrucosus* Anderson (1871) Urodela: Salamandridae at Taunggyi, Burma, Union of Burma. *Journal of Life Sciences*, **1969**: 23–26.

Hadden RL. 2008. The Geology of Burma (Myanmar): An Annotated Bibliography of Burma's Geology, Geography and Earth Science. Alexandria, Virginia: Topographic Engineering Center, US Army Corps of Engineers, 312.

Hall TA. 1999. BioEdit: a user-friendly biological sequence alignment editor and analysis program for Windows 95 / 98 / NT. *Nuclear Acids Symposium Series*, **41**: 95–98.

Hedges SB. 1994. Molecular evidence for the origin of birds. *Proceedingsof the National Academy of Sciences of the United States of America*, **91**(7): 2621–2624.

Hernandez A. 2016. Crocodile Newts – the Primitive Salamandridae of Asia (Genera Echinotriton and Tylototriton). *Edition Chimaira, Frankfurt am Main, Germany*, 416.

Hernandez A, Escoriza D, Hou M. 2018. Patterns of niche diversification in south-east Asian crocodile newts. *Zoologischer Anzeiger*, **276**: 86–93.

Hillis DM, Moritz C, Mable BK. 1996. Molecular Systematics. 2nd edition. Sunderland, Massachusetts: Sinauer Associates, Inc.

Hou M, Li P, Lü SQ. 2012. Morphological research development of genus *Tylototriton* and primary confirmation of the status of four cryptic populations. *Journal of Huangshan University*, **14**(3): 61–65. (in Chinese)

Huelsenbeck JP, Hillis DM. 1993. Success of phylogenetic methods in the four-taxon case. *Systematic Biology*, **42**(3): 247–264.

Huelsenbeck JP, Ronquist F. 2001. MRBAYES: Bayesian inference of phylogenetic trees. *Bioinformatics*, **17**(8): 754–755.

IUCN. 2001. IUCN Red List Categories and Criteria: Version 3.

IUCN Species Survival Commission. IUCN, Gland, Switzerland and Cambridge, UK.

Katoh K, Misawa K, Kuma K, Miyata T. 2002. MAFFT: a novel method for rapid multiple sequence alignment based on fast Fourier transform. *Nucleic Acids Research*, **30**(14): 3059–3066.

Khatiwada JR, Wang B, Ghimire S, Vasudevan K, Paudel S, Jiang J-P. 2015. A new species of the genus *Tylototriton* (Amphibia: Urodela:

Salamandridae) from eastern Himalaya. *Asian Herpetological Research*, **6**(4): 245–256.

Kumar S, Stecher G, Tamura K. 2016. MEGA7: Molecular Evolutionary Genetics Analysis version7.0 for bigger datasets. *Molecular Biology and Evolution*, **33**(7): 1870–1874.

Le DT, Nguyen TT, Nishikawa K, Nguyen SLH, Pham AV, Matsui M, Bernardes M, Nguyen TQ. 2015. A new species of *Tylototriton* Anderson, 1871 (Amphibia: Salamandridae) from northern Indochina. *Current Herpetology, Kyoto*, **34**(1): 38–50.

Li SQ, Quan RC. 2017. Taxonomy is the cornerstone of biodiversity conservation-SEABRI reports on biological surveys in Southeast Asia. *Zoological Research*, **38**(5): 213–214.

Liu CC. 1950. Amphibians of western China. *Fieldiana, Zoology Memoirs*, **2**: 1–400.

Mulcahy DG, Lee JL, Miller AH, Chand M, Thura MK, Zug GR. 2018. Filling the BINs of life: Report of an amphibian and reptile survey of the Tanintharyi (Tenasserim) Region of Myanmar, with DNA barcode data. *ZooKeys*, **757**: 85–152.

Nishikawa K, Khonsue W, Pomchote P, Matsui M. 2013a. Two new species of *Tylototriton* from Thailand (Amphibia: Urodela: Salamandridae). *Zootaxa*, **3737**(3): 261–279.

Nishikawa K, Matsui M, Nguyen TT. 2013b. A new species of *Tylototriton* from northern Vietnam (Amphibia: Urodela: Salamandridae). *Current Herpetology*, **32**(1): 34–49.

Nishikawa K, Matsui M, Rao DQ. 2014. A new species of *Tylototriton* (Amphibia: Urodela: Salamandridae) from central Myanmar. *Natural History Bulletin of the Siam Society*, **60**: 9–22.

Nussbaum RA, Brodie ED Jr., Yang DT. 1995. A taxonomic review of *Tylototriton verrucosus* Anderson (Amphibia: Caudata: Salamandridae). *Herpetologica*, **51**(3): 257–268.

Okamiya H, Sugawara H, Nagano M, Poyarkov NA. 2018. An integrative taxonomic analysis reveals a new species of lotic *Hynobius* salamander from Japan. *PeerJ*, **6**: e5084.

Phimmachak S, Aowphol A, Stuart BL. 2015. Morphological and molecular variation in *Tylototriton* (Caudata: Salamandridae) in Laos, with description of a new species. *Zootaxa*, **4006**(2): 285–310.

Posada D, Crandall KA. 1998. MODELTEST: testing the model of DNA substitution. *Bioinformatics*, **14**(9): 817–818.

Poyarkov NA Jr., Che J, Min MS, Kuro-o M, Yan F, Li C, Iizuka K, Vieites DR. 2012. Review of the systematics, morphology and distribution of Asian Clawed Salamanders, genus *Onychodactylus* (Amphibia, Caudata: Hynobiidae), with the description of four new species. *Zootaxa*, **3465**: 1–106.

Qian L, Sun X, Li J, Guo W, Pan T, Kang X, Wang H, Jiang JP, Wu J, Zhang BW. 2017. A new species of the genus *Tylototriton* (Amphibia: Urodela: Salamandridae) from the southern Dabie Mountains in Anhui Province. *Asian Herpetological Research*, **8**(3): 151–164.

Rambaut A, Suchard M, Xie W, Drummond A. 2014. Tracer v. 1.6. Institute of Evolutionary Biology, University of Edinburgh. *Available at:* http://tree.bio.ed.ac.uk/software/tracer/.

Ronquist F, Huelsenbeck JP. 2003. MRBAYES 3: Bayesian phylogenetic inference under mixed models. *Bioinformatics*, **19**(12): 1572–1574.

Shen YH, Jiang JP, Mo XY. 2012. A new species of the genus *Tylototriton* (Amphibia, Salamandridae) from Hunan, China. *Asian Herpetological Research*, **3**(1): 21–30.

Stamatakis A, Hoover P, Rougemont J. 2008. A rapid bootstrap algorithm for the RAxML web servers. *Systematic Biology*, **57**(5): 758–771.

Stuart BL, Phimmachak S, Sivongxay N, Robichaud WG. 2010. A new species in the *Tylototriton asperrimus* group (Caudata: Salamandridae) from central Laos. *Zootaxa*, **2650**(1): 19–32.

Unterstein W. 1930. Beiträge zur Lurch- und Kriechtierfauna Kwangsi's. 2. Schwanzlurche. *Sitzungsberichte der Gesellschaft Naturforschender Freunde zu Berlin*, **1930**: 313–315.

Wang B, Nishikawa K, Matsui M, Nguyen TQ, Xie F, Li C, Khatiwada JR, Zhang B, Gong D, Mo Y, Wei G, Chen X, Shen Y, Yang D, Xiong R, Jiang J. 2018. Phylogenetic surveys on the newt genus *Tylototriton* sensu lato (Salamandridae, Caudata) reveal cryptic diversity and novel diversification promoted historical climatic shifts. *Peer J*, **6**: e4384.

Yang DD, Jiang JP, Shen YH, Fei DB. 2014. A new species of the genus *Tylototriton* (Urodela: Salamandridae) from northeastern Hunan Province, China. *Asian Herpetological Research*, **5**: 1–11.

Zhao YT, Rao DQ, Liu N, Li B, Yuan SQ. 2012. Molecular phylogeny analysis of *Tylototriton verrucosus* group and description of new species. *Journal of West China Forestry Science*, **41**(5): 86–89.

A new species of the endemic Himalayan genus *Liurana* (Anura, Ceratobatrachidae) from southeastern Tibet, China, with comments on the distribution, reproductive biology, and conservation of the genus

Ke Jiang[1,#], Kai Wang[1,2,#], Yu-Fan Wang[3], Cheng Li[4], Jing Che[1,5,*]

[1] *State Key Laboratory of Genetic Resources and Evolution, Kunming Institute of Zoology, Chinese Academy of Sciences, Kunming Yunnan 650223, China*
[2] *Sam Noble Oklahoma Museum of Natural History and Department of Biology, University of Oklahoma, Norman OK 73072-7029, USA*
[3] *Zhejiang Forest Resource Monitoring Center, Hangzhou Zhejiang 310020, China*
[4] *Funsome Nature Center, Shenzhen Guangdong 518067, China*
[5] *Southeast Asia Biodiversity Research Institute, Chinese Academy of Sciences, Yezin Nay Pyi Taw 05282, Myanmar*

ABSTRACT

A new species of the genus *Liurana* Dubois, 1986 is described from Medog County, Tibet, China, based on morphological and molecular data. The new species can be differentiated from all other congeners by the following combination of characters: (1) head wider than long; (2) tympanum distinct and large; (3) hindlimb long, tibiotarsal articulation beyond tip of snout when adpressed; (4) belly with flat tubercles, cloacal region with small tubercles; (5) transverse bands distinctly on dorsal limbs, four bands on thigh and three on tibia; and, (6) dark brown marbled patterns or speckles on white belly. Here, we also discuss the distribution pattern of *Liurana* in the East Himalaya region, the role of the Yarlung Tsangpo River in the speciation and genetic isolation of congeners, the direct developmental mode of reproduction, and the two different ecotypes of the genus. Lastly, we provide conservation recommendations for the genus in southeastern Tibet.

Keywords: Advertisement call; Biogeography; Ecology; Natural history; Tibet; Taxonomy

INTRODUCTION

As a wide-spread amphibian family in Southeast Asia, species of the family Ceratobatrachidae are distributed from the southern foothills of the Himalaya to the tropics of Southeast Asia (Yan et al., 2016). Members of the family are characterized as tropical specialists, with many species undergoing direct development without reliance on standing water bodies for breeding (Brown & Alcala, 1982; Brown et al., 2015). Within this family, frogs of the genus *Liurana* represent an understudied yet fascinating endemic group from the East Himalaya region.

First considered as a subgenus of *Ingerana* by Dubois (1986), *Liurana* was established based on the type species *Cornufer xizangensis* Hu, 1987, with the subgenus later elevated to full genus based on morphological evidence (Fei et al., 1997). This taxonomic elevation is supported by recent phylogenetic studies, where *Liurana* was recovered as a distinct monophyletic clade from *Ingerana*, *Platymantis*, and *Cornufer* (Yan et al., 2016). However, despite research efforts on the higher-level systematic relationships of the genus *Liurana*,

little attention has been given to the species level taxonomy of the group in the Himalaya. To date, only a few studies have focused on species level taxonomy of the genus, with just a single study conducted in the last decade (Borah et al., 2013; Fei et al., 1997; Huang & Ye, 1997; Sichuan Biological Research Institute, 1977). As a result, all recognized species of *Liurana* are known from only a few vouchered specimens, and little is understood about their morphological variation and population structure. Based on limited studies, three species have been recognized in the genus to date, including *L. alpina* Huang, Ye, 1997, *L. medogensis* Fei, Ye, Huang, 1997, and *L. xizangensis* (Hu, 1987).

During herpetological surveys in southeastern Tibet from 2012 to 2016, 20 specimens of the genus *Liurana* were collected from Bomê and Medog Counties of the Nyingchi Prefecture, Tibet, China. Combining phylogenetic and morphological datasets, we describe here a new species of the genus from the tropical rainforest of Medog County, Nyingchi Prefecture, Tibet, China. Furthermore, we comment on the evolution, ecology, natural history, and conservation of the genus *Liurana* in China.

MATERIALS AND METHODS

Taxon sampling

A total of 20 individuals of the recognized species of the genus *Liurana* were collected from different localities in the Bomê and Medog Counties, Nyingchi Prefecture, southeastern Tibet, China, and were comprised of 18 individuals of *L. alpina*, *L. medogensis*, and *L. xizangensis* and two individuals (one adult male and one adult female) of the new species (Figure 1; Appendix I). Following euthanasia, tissue samples were taken

and preserved in 95% ethanol, with the specimens then fixed in 10% buffered formalin solution and transferred to 75% ethanol after fieldwork. All specimens were deposited in the Museum of the Kunming Institute of Zoology, Chinese Academy of Sciences (KIZ) (Appendix II).

Morphological data

We confirmed the sex of each specimen by anatomical observation, with an incision made on the left side. All measurements were carried out by Ke Jiang using a digital caliper to the nearest 0.1 mm. Morphological characters and their measurement followed Fei et al. (2009) and included: snout–vent length (SVL); head length (HL), measured from posterior corner of mandible to tip of snout; head width (HW), measured at the angle of the jaw; snout length (SL), measured from tip of snout to anterior corner of eye; internarial distance (IND); interorbital distance (IOD), measured at the shortest distance between upper eyelid; maximum width of upper eyelid (UEW); eye diameter (ED), measured as the horizontal diameter of eye); tympanum diameter (TD), measured as the maximum horizontal diameter of tympanum); length of lower arm and hand (LAHL), measured from the elbow joint to the tip of the longest finger; largest diameter of lower arm (LAD); hand length (HAL), measured from the base of the outer metacarpal tubercle to the tip of finger III; femur length (FML), measured as the linear distance between the insertion of the leg to the knee joint; tibia length (TL), measured as the linear distance between the knee joint and tibiotarsal articulation; length of tarsus and foot (TFL), measured from the tibiotarsal articulation to the tip of toe IV; and foot length (FL), measured from the base of the inner metatarsal tubercle to the tip of toe IV.
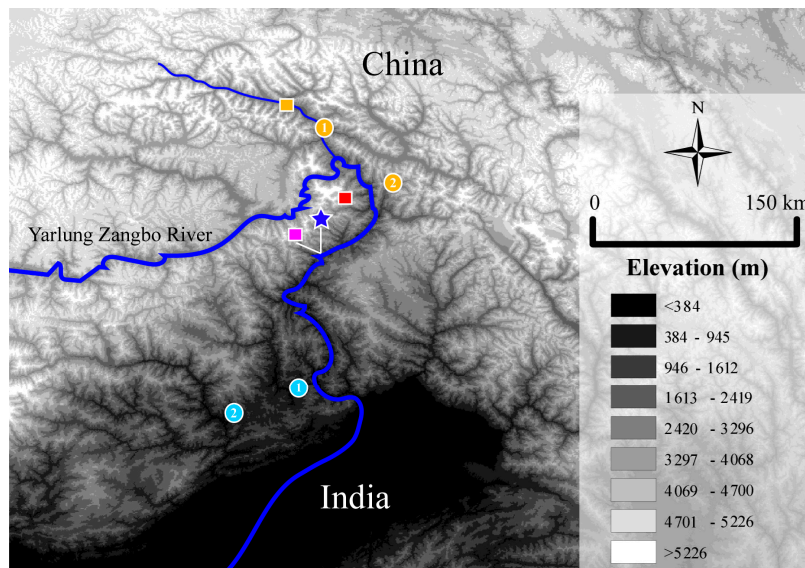
Figure 1 Distribution of *Liurana* species in the East Himalaya

Blue star represents type locality of the new species, *Liurana vallecula* **sp. nov**. Rectangles represent type localities of recognized species and circles represent additional known localities of recognized species. Different species are color-coded as follows: *L. alpina* (red), *L. medogensis* (purple), and *L. xizangensis* (yellow). For *L. xizangensis*, the two additional localities are (1) Tongmai, Bomê County, Tibet, China; and (2) 62K, Medog County, Tibet, China. The two light blue localities represent reported records of *Liurana* cf. *medogensis* from Southern Tibet (see discussion for details).

In addition to the newly obtained data, morphological data of congeners were also obtained from published literature for comparison (Borah et al., 2013; Fei et al., 1997, 2009; Huang & Ye, 1997).

Molecular analysis

Genomic DNA was extracted from tissue samples using standard phenol-chloroform protocols (Sambrook et al., 1989). Fragments of a single mitochondrial DNA locus (cytochrome c oxidase subunit I, *COI*) and three nuclear loci, including recombination activating protein 1 (Rag1), tyrosinase (Tyr), and rhodopsin (Rhod), were targeted and amplified following published primers and protocols (Che et al., 2011; Yan et al., 2016). The products were purified with a Gel Extraction Mini Kit (Watson Biotechnologies, Shanghai, China) and sequenced on an ABI 3730xl DNA automated sequencer (Applied Biosystems, UK).

Additional sequences of congeners and closely related outgroups were obtained through GenBank (Appendix II). Sequences were aligned using MUSCLE implemented in Geneious R10.0.6. Uncorrected genetic distances of the mitochondrial locus *COI* were calculated using PAUP* v4.0b10. To assess phylogenetic congruence between the mitochondrial and nuclear data, the phylogeny for each gene was inferred independently using Bayesian analyses. As no strongly supported incongruences between mitochondrial and nuclear data were observed visually, two datasets were concatenated for the final analyses.

Phylogenetic relationships were inferred using both partitioned Bayesian (MrBayes v3.2.1; Ronquist & Huelsenbeck, 2003) and maximum likelihood analyses (RAXML VI-HPC v8.2.10; Stamatakis, 2014). For Bayesian analyses, all protein-coding genes were partitioned by codon positions, and the best models of nucleotide substitution were selected for each partition by the Akaike Information Criterion (AIC), as implemented in jModelTest v2.1.10 (Darriba et al., 2012; Guindon & Gascuel, 2003). A rate multiplier model was used to allow substitution rates to vary among subsets. Default settings were used for all other model parameters. Two independent Markov chain Monte Carlo analyses were run, each with four Metropolis-coupled chains, a melting temperature of 0.02, and an exponential distribution with a rate parameter of 25 as the prior branch lengths (Marshall, 2010). All Bayesian analyses were run for 6 000 000 generations, with parameters and topologies sampled every 3 000 generations. Stationarity and convergence were assessed with TRACER v1.6.0 (Rambaut et al., 2013).

Partitioned maximum likelihood analyses were conducted on the concatenated dataset using the same partitioning strategy as for Bayesian analysis. The more complex model (GTR+Γ) was applied for all subsets (Table 1), with 1 000 replicate ML inferences. Each inference was initiated with a random starting tree, and nodal support was assessed with 1 000 bootstrap pseudoreplicates (Stamatakis et al., 2008).

The resulting phylogenetic trees were rooted using the clade containing *Ingerana* and *Limnonectes*, following recent studies on phylogenetic relationships of the focal group (Yan et al., 2016).

Table 1 Partition strategies and best evolutionary models selected for each partition

Gene	Codon	Fragment length (bp)	Model selected
COI	1st	190	GTR
	2nd	190	HKY+Γ
	3rd	190	HKY
Rag1	1st	184	F81
	2nd	184	HKY
	3rd	184	HKY
Rod	1st	105	JC
	2nd	105	F81
	3rd	105	GTR
Tyr	1st	177	GTR+Γ
	2nd	177	HKY+Γ
	3rd	177	HKY+Γ

RESULTS

Morphology

Morphometric variation of the examined *Liurana* species is summarized in Table 2. The unidentified specimens of *Liurana* were morphologically most similar to *L. medogensis* and could be differentiated from all recognized species by having a relatively wider head (HW/HL >100% vs. <100%) and longer hindlimbs, with tibiotarsal articulation reaching beyond tip of snout when adpressed (vs. reaching anterior corner of eye only). Furthermore, the unidentified *Liurana* specimens from Medog possessed distinct tubercles near the cloaca, which are absent or indistinct in all recognized congeners except for *L. xizangensis*.

Coloration and ornamentation were highly variable among the examined specimens of *L. alpina* and *L. xizangensis*, ranging from uniform bright orange reddish to brownish gray with blackish speckles (Figure 3). For *L. medogensis* and the two unidentified individuals from Medog, the coloration and ornamentation were less variable. A single individual of *L. medogensis* (KIZ05587) possessed a broad, yellowish dorsal vertebral stripe from snout to vent, whereas the other individuals of the same species exhibited a much darker vertebral stripe in light reddish brown.

Phylogeny

The phylogenetic placement of the genus *Liurana* is similar to previous results (Yan et al., 2016), with the genus recovered as monophyletic with strong support (Bayesian posterior probability (PP)=1.00; ML bootstrap support (BS)=100) (Figure 2). Within the genus, *L. xizangensis* and *L. alpina* form a monophyletic group with strong supports (PP=0.99, BS=100), which is sister to *L. medogensis* (PP=1.00, BS=100). The two unidentified individuals (*Liurana* sp.) collected from Medog County form a distinct, monophyletic clade (PP=1.00, BS=100), which is basal with respect to all other *Liurana* congeners (Figure 2).

For the obtained 570 bp fragment of *COI* data, the uncorrected genetic distance between the two unidentified *Liurana* individuals is 0.88% only, while such distance is 22.19%–22.22% to its morphologically most similar congener, *L. medogensis*, 21.67%–22.63% to *L. alpina*, and 20.19%–21.30% to *L. xizangensis* (Table 3). The observed intraspecific variation among recognized *Liurana* species is 0%–0.183% within conspecifics of *L. alpina.* For *L. xizangensis*, the greatest genetic divergence (3.12%) is observed between individuals from Tongmai, Bomê County, Tibet, China (Locality #1) and 62K, Medog County, Tibet, China (Locality #2), which are on different sides of the Yarlung Tsangpo River (Figure 1).

Because the two unidentified specimens of *Liurana* from Medog possess a suite of distinct morphological characteristics, high genetic divergence from congeners, and monophyletic and distinct phylogenetic position, we here describe them as a new species.

Taxonomy

Liurana vallecula **sp. nov.** Jiang, Wang, Wang, Li, and Che Figures 1–5.

Holotype: KIZ014083, adult female, from the side of Yarlung Zangbo River near Xirang (N29.1776°, E95.0057°, elevation 550 m a.s.l.; Figure 3), Beibeng, Medog County, southeastern Tibet, China. Collected by Cheng Li on 17 April 2016.

Table 2 Morphological comparisons for four species of the genus *Liurana*

	Liurana vallecula **sp. nov.**	*L. alpina*	*L. medogensis*	*L. xizangensis*
SVL (mm)	14.6 (1♂)	23.2–24.9 (3♂)	13.1–19.0 (3♂)	20.6–22.5 (9♂)
	20.4 (1♀)	25.5 (1♀)		29.4–30.5 (2♀)
HL/HW	<100%	>100%	>100%	>100%
Tibiotarsal articulation	Beyond tip of snout	Reaching anterior corner of eye	Reaching anterior corner of eye	Reaching anterior corner of eye
Flat tubercles on belly	Absent	Absent	Absent	Present
Tubercles around cloaca	Present	Absent	Indistinct	Present
Ventral pattern	Thin, marbled-patterns	Thin, marbled-patterns	Thick, vermiculated stripes	Thin, marbled-patterns

Morphological abbreviations are listed in the methods.

Table 3 Uncorrected genetic distances of the *COI* fragment obtained (570 bp) among *Liurana* species

1	*L.* **sp. nov.** YPX47504	–													
2	*L.* **sp. nov.** YPX47527	0.00877	–												
3	*L. medogensis* KIZ 010955	0.22191	0.222	–											
4	*L. alpina* KIZ 07357	0.22029	0.21666	0.13394	–										
5	*L. alpina* KIZ 011140	0.22632	0.22281	0.13207	0.00178	–									
6	*L. alpina* KIZ 011141	0.22216	0.21853	0.13211	0.00183	0	–								
7	*L. xizangensis* KIZ 06707 (Locality #2)	0.2129	0.21297	0.14312	0.09541	0.09345	0.09358	–							
8	*L. xizangensis* KIZ 09956 (Locality #2)	0.2129	0.21297	0.14312	0.09541	0.09345	0.09358	0	–						
9	*L. xizangensis* KIZ 012705 (Locality #2)	0.2129	0.21297	0.14312	0.09541	0.09345	0.09358	0	0	–					
10	*L. xizangensis* KIZ 012706 (Locality #2)	0.2129	0.21297	0.14312	0.09541	0.09345	0.09358	0	0	0	–				
11	*L. xizangensis* KIZ 011104 (Locality #2)	0.2129	0.21297	0.14312	0.09541	0.09345	0.09358	0	0	0	0	–			
12	*L. xizangensis* KIZ 012707 (Locality #2)	0.21107	0.21114	0.14495	0.09725	0.09535	0.09541	0.00183	0.00183	0.00183	0.00183	0.00183	–		
13	*L. xizangensis* KIZ 012704 (Topotype)	0.20372	0.20379	0.12661	0.08624	0.08436	0.0844	0.02752	0.02752	0.02752	0.02752	0.02752	0.02936	–	
14	*L. xizangensis* KIZ 014046 (Locality #1)	0.20187	0.20195	0.12844	0.08807	0.0862	0.08624	0.02936	0.02936	0.02936	0.02936	0.02936	0.03119	0.00183	–

Paratype: KIZ014106, adult male, from the side of Baimaxilu River (a tributary of the Yarlung Zangbo River) near Maniweng (N29.2667°, E95.1667°, elevation 850 m a.s.l.), Beibeng, Medog County, southeastern Tibet, China. Collected by Ke Jiang and Yu-Fan Wang on 29 April 2016.

Diagnosis: *Liurana vallecula* **sp. nov.** is assigned to the genus *Liurana* by its phylogenetic position and the following morphological characters: (1) body size small (SVL 14.6–20.4 mm, *n*=2); (2) tips of fingers and toes not expanded, (3) grooves absent on tips of fingers and toes; (4) webbing absent on all digits; (5) metacarpal tubercles and metatarsal tubercles absent; (6) tarsal fold absent; and (7) vocal sac and vocal sac openings absent.

Liurana vallecula **sp. nov.** can be distinguished from all currently recognized congeners by a combination of the following morphological characters: (1) head wider than long HW/HL 108%–113%; (2) tympanum distinct, large; (3) hind limbs long, with tibiotarsal articulation reaching beyond tip of snout when adpressed; (4) flat tubercles present on ventral surface of body; (5) small tubercles present on cloacal region; and (6) dark brown marbled pattern present on ventral surface of body.

Description of holotype: Body size small, SVL 20.4 mm. Head wider than long (HW/HL=108%); snout rounded, slightly projecting over lower jaw; canthus rostralis distinct, relatively sharp; nostril closer to tip of snout than to eye; loreal region slightly concave and oblique; eye relatively large (ED/HL=40%); internarial distance larger than interorbital distance and width of upper eyelid; tympanum oval, concealed under skin, with distinct, elevated rim, slightly less than half of eye diameter (TD/ED=45%); supratympanic fold distinct, extending posterior-inferiorly to area above forelimb insertion; pair of distinct skin folds present on head from posterior orbit dorsally to pectoral region, symmetrical along vertebral line, extending toward medial line posteriorly.
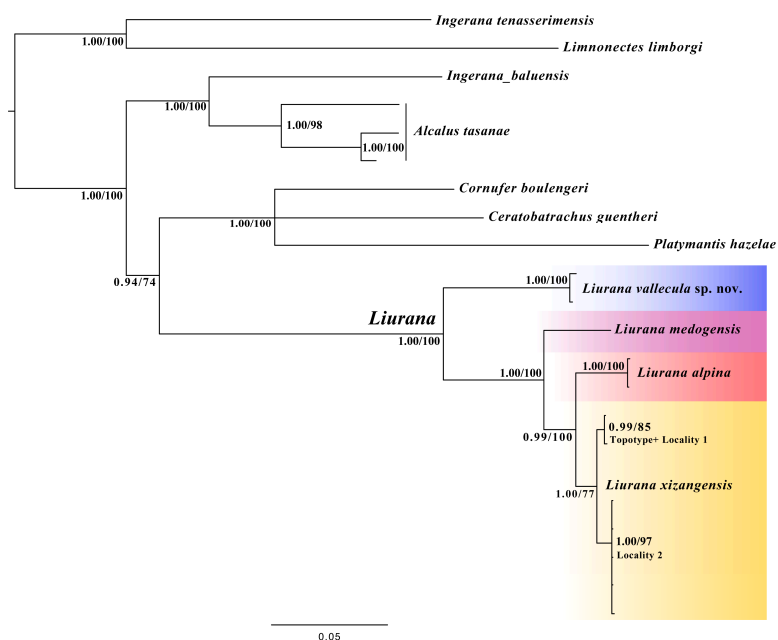
Figure 2 Phylogenetic relationships among *Liurana* species based on maximum likelihood and Bayesian analyses of one mitochondrial gene (*COI*) and three nuclear genes (*Rag1*, *Rod*, and *Tyr*)

Maximum likelihood bootstrap and Bayesian posterior probability values are given at all nodes (in such order respectively), except the internal nodes within *L. xizangensis* from Locality #2, which have short branch lengths and resemble polytomy.

Figure 3 Holotype of *Liurana vallecula* sp. nov. in life (adult female, KIZ014083)

A: Dorsolateral view; B: Ventral view; C: Ventral close-up of hand; D: Ventral close-up of feet. Photos by Yu-Fan Wang.

Forelimb slender; forearm and hand length less than half of body length (LAHD/SVL=44%); fingers compressed vertically, tips rounded but not expanded, transverse grooves absent, relative finger lengths I<II<IV<III; subarticular tubercles absent; three metacarpal tubercles present, flat and indistinct. Hind limb slender, tibiotarsal articulation reaching beyond tip of snout when adpressed; heels overlapped when flexed and held perpendicular to body; tibia length larger than half of body length (TL/SVL=58%); toes compressed vertically, tips slightly expanded, transverse grooves absent; relative toe lengths I<II<V<III<IV; toe webbing absent; subarticular tubercles indistinct; inner metatarsal tubercle oval, indistinct; outer metatarsal tubercle indistinct; tarsal fold absent.

Relatively weak, discontinuous folds present on dorsolateral body from shoulder to about two thirds of trunk on each side of body; single skin fold present along vertebrate from snout to vent, much weaker than discontinuous folds laterally; dorsal surface relatively rough, tubercles randomly scattered on dorsal and lateral head, body, and limbs as well as around cloaca; tubercles much finer on ventrolateral region of body. Ventral head, body, and limbs mostly smooth, except several flat tubercles on base of ventral thigh and small tubercles on ventral surface of tarsus and metatarsus. Vomerine teeth absent; tongue large, elongated oval, deeply notched posteriorly, small papillae scattered on tongue.

Coloration of holotype in life: The dorsal surfaces of the head and body are reddish brown. Dark brown streaks and marble patterns are present on dorsal head, body, and limbs, including a transverse streak between orbit on dorsal surface of head, a X-shaped pattern on pectoral region of dorsum, irregular marble patterns on lateral body, and transverse streaks across dorsal limbs (more distinct on the dorsal hind limbs). The lower parts of canthus rostralis and supratympanic fold are blackish brown. The ventrolateral surface of the body is dark brown, with small white spots scattered across. Ventral surfaces of limbs, head, and body are light grayish brown; white marble patterns are present on ventral surfaces of head, body, and ventral forelimbs, and ventrolateral surfaces of thigh. The white marble patterns are finer and much smaller on ventral head comparing to ventral body, giving a speckle impression; white marble patterns on ventral body are mostly interconnected. A few smaller white spots are also present on ventral thigh, tibia, and femur.

Coloration of holotype in preservative: Ornamentation patterns remain after preservation. However, coloration changes after preservation, include: (1) dorsal surfaces of head, limbs, and body become grayish brown, with dark gray patches; (2) lower parts of canthus rostralis and supratympanic fold, transverse bands on dorsal limbs, as well as lower part of lateral body become dark gray; (3) ventral surfaces of throat and limbs become brown, with grayish white spots.

Variation: Morphometric variations of the type series are shown in Table 4. Most external morphological characters are identical between the two individuals, but the paratype is smaller than the holotype (SVL 14.6 mm in paratype male vs.

20.4 mm in holotye female), as well as in having rather paler dorsal coloration and more dense spots on ventral body. No secondary sexual characters, such as vocal sac or nuptial pad, are observed in the paratype male, but a single black testicle was observed on the left side of the male paratype, which is oval shaped and relatively large, with a longitudinal length of about 1.5 mm.

Ecological and natural history notes: *Liurana vallecula* **sp. nov.** is a terrestrial, leaf-litter specialist, inhabiting the forest floor of tropical broad-leaf forest at low elevations (below 1 000 m a.s.l.) near Yarlung Zangbo River and its immediate tributaries. The female holotype had about five immature eggs in the left ovary, which were well developed and relatively large.

Distribution: Currently the new species is known only from the type localities of Xirang and Maniweng of Beibeng, Medog County, Nyingchi Prefecture, Tibet, China. The new species likely inhabits other nearby regions in southern Tibet (see Discussion below).

Etymology: The specific epithet of the new species, "*vallecula*" means "valley inhabitor", in reference to the habitat of this species in the lower river valley of Yarlung Zangbo Grand Canyon. We suggest Valley Papilla-tongued Frog as its English common name and He Gu She Tu Wa (河谷舌突蛙) as its Chinese common name.

Comparisons: *Liurana vallecula* **sp. nov.** differs from the three congeners by having a much wider head (HW/HL >100% vs. <100%) and longer hindlimbs (tibiotarsal articulation reaching beyond tip of snout when adpressed vs. reaching only anterior corner of eye when adpressed). In addition, *Liurana vallecula* **sp. nov.** can be further distinguished from *L. alpina* and *L. xizangensis* by having a smaller body size (SVL 14.6 mm in male, 20.4 mm in female vs. SVL 23.2–24.9 mm in males, 25.5 mm in female for *L. alpina*; 20.6–24.5 mm in males, 29.4–30.5 mm in females for *L. xizangensis*); and from *L. medogensis* by its different ventral pattern (small, marbled patterns or speckles vs. broad, vermiculated stripes).

DISCUSSION

Liurana medogensis from Southern Tibet

Recently, Borah et al. (2013) reported *L. medogensis* from the eastern part of Southern Tibet, which they recognized as *Limnonectes* (*Taylorana*) *medogensis* in the study (localities 1 and 2 in light blue; Figure 1) (all abbreviations of "*L.*" in this paragraph refer to *Liurana*, not *Limnonectes*). Although one of the reported specimens (ZSI a11549) resembles the external appearance of *L. medogensis* based on the figure in the manuscript (Borah et al., 2013; Figure 1), according to the description, it possesses morphological characteristics that differ from the diagnosis of the genus *Liurana*, including having a distinct vomerine ridge, prominent vomerine teeth, and rudimentary webbing on toes (vs. vomerine ridge, vomerine teeth, and toe webs absent in *Liurana*) (Fei et al., 2009, 2010; Yan et al., 2016). Furthermore, this specimen was collected at a much higher elevation (2 000–2 500 m a.s.l.) than the known

range for *L. medogensis* (about 1 400 m a.s.l.). For the second reported specimen of *L.* cf. *medogensis* (BMHE a0081), based on the description provided by the authors, it matches the morphological diagnosis of our new species, *Liurana vallecula*, including having a wide head (HW/HL>100%), but lacks the broad, vermiculate patterns on the ventral surface of the body (Borah et al., 2013). As we cannot examine these specimens or obtain their genetic data, we cannot confirm the taxonomic status of these two specimens reported by Borah et al. (2013). Future taxonomic studies are needed to gain a better understanding of *Liurana* diversity in this region.

Table 4 Measurements (in mm) of type series of *Liurana vallecula* sp. nov.

Number	Status	Sex	SVL	HL	HW	SL	IND	IOD	UEW
KIZ014083	Holotype	Female	20.4	7.3	7.9	3.2	3.0	2.2	2.0
Ratio to SVL (%)			–	37.2	38.7	15.6	14.5	10.7	9.8
KIZ014106	Paratype	Male	14.6	5.6	6.3	2.5	2.3	1.5	1.5
Ratio to SVL (%)			–	38.1	43.2	17.5	15.7	10.4	10.0

Number	ED	TD	LAHL	LAD	HAL	FML	TL	TFL	FL
KIZ014083	2.9	1.3	9.0	1.5	5.1	10.9	11.8	17.4	11.6
Ratio to SVL (%)	14.1	6.4	44.1	7.3	24.7	53.3	57.6	85.3	57.0
KIZ014106	2.0	1.0	6.3	1.1	3.3	7.7	8.5	11.2	7.1
Ratio to SVL (%)	13.7	43.6	7.4	22.4	52.7	58.4	76.8	49.0	43.6

See methods section for abbreviations. –: Not applicable.

Ecotypes

Liurana diversity can be divided into two major ecotypes: the alpine ecotype that inhabits cool, moist mixed forests at 2 000–3 000 m a.s.l. (including *L. alpina* and *L. xizangensis*), and the tropical ecotype that inhabits low-elevation tropical rainforest below 2 000 m a.s.l. (including *L. medogensis* and *Liurana vallecula*). For the first ecotype, coloration of individuals is highly variable, ranging from uniform bright reddish orange to marbled purplish gray. Frogs of this ecotype live under thick layers of moss on fallen tree trunks or rocks along the forest edge. The second ecotype consists of leaf litter specialists that inhabit the forest floor under pristine tropical rainforest. Coloration of this ecotype is much more cryptic, ranging from a single, wide, brownish orange dorsal stripe to dark brown with darker marbling (Figures 4, 5).

Even though *L. medogensis* and *Liurana vallecula* both belong to the second ecotype, they do not form a monophyletic group according to our genetic data (Figure 2). Future ecological studies are needed to further differentiate the ecological niche of each species and investigate the evolution of ecotypes in the genus *Liurana*.

Reproductive biology

Although the reproductive biology, particularly the direct developing reproductive mode, has long been documented within the family Ceratobatrachidae (Brown & Alcala, 1982; Siler et al., 2010), little is known about the reproductive biology of *Liurana* specifically. Considering the Tibetan *Liurana* species as *Platymantis* at that time, Hu et al. (1987) first commented on the reproductive mode of the Tibetan species and suggested

that they may go through direct development, similar to other *Platymantis* species. It was only until 2010 when the eggs of *Liurana* species in the alpine ecotype from Tibet were first collected (Li et al., 2010). According to Li et al. (2010), eggs of the unidentified *Liurana* species from 62K in the Medog County (confirmed as *L. xizangensis* according to Yan et al. (2016) and the present study) were large (with a diameter of about 3.5 mm) and the clutch size was small. These egg characteristics are similar to those of direct development in the same family (Siler et al., 2010). Similar to Li et al. (2010), we also observed eggs in a female *L. xizangensis* (KIZ014153) from the same locality, where the female displayed 14 and 16 yellowish white eggs in the left and right oviduct, respectively, though not all were fully developed (Figure 6).

More recently, Borah et al. (2013) provided information regarding the reproductive biology of the tropical ecotype of *Liurana* from Southern Tibet. Embryos displayed characteristics of the direct developing species in the family Ceratobatrachidae, including having a few embryos, large individual embryo size, and whitish coloration (Borah et al., 2013). Based on these similarities, the authors claim that this *Liurana* species reproduces through direct development without the larval stage (Borah et al., 2013). However, such conclusions on direct development in *Liurana* are still based on indirect inferences of egg characteristics. Therefore, we recommend future studies focus on the reproductive biology of the genus to clarify the reproductive mode of *Liurana*.

Acoustic signals

In addition to the differences in general habitat preferences and external morphology, the two ecotypes of *Liurana* also differ in their acoustic signals. In fact, extensive acoustic signals have been observed in the alpine ecotype only (Fei et al., 2009; Hu et al., 1987; present study). Such differences in acoustic signals may be explained by the relative cost-benefit ratios of calling in each specific environment (Ryan, 1988). Future ecological and behavioral studies are needed to confirm this hypothesis in the field and investigate the communication strategies of the tropical ecotype.

Evolution

Frogs of the genus *Liurana* are endemic to eastern Himalaya, and all are found in the Yarlung Zangbo Drainage in Southern Tibet (Figure 1). Based on the available distribution data, *L. xizangensis* is distributed on the eastern side of the Yarlung Zangbo River, whereas *L. alpina* is found on the western side of the river. As the two species are found in cool environments at high elevation only (>2 000 m a.s.l.), the hot tropical valley of the Yarlung Zangbo River may serve as a dispersal barrier, thereby shaping the genetic diversity and facilitating the speciation processes of the two congeners. This hypothesis is partly supported by our genetic data, where closely distributed populations from two sides of the river possessed higher genetic divergence than further distributed populations from the same side (Table 3). Future studies should expand population sampling of the two species along both sides of Yarlung Zangbo River to examine its role in the evolution of *Liurana*.

Figure 4 Comparisons of dorsal (1) and ventral (2) views of live individuals of *Liurana xizangensis* (A and B), *L. alpina* (C and D), *L. medogensis* (E), and *Liurana vallecula* sp. nov. (F). Photos by Ke Jiang, Kai Wang, and Yu-Fan Wang

Figure 5 Habitat of *Liurana vallecula* sp. nov. (A) (Xirang, elevation 550 m a.s.l.), *L. medogensis* (B) (Xigong Lake, elevation 1 300 m a.s.l.), *L. alpina* (C) (Dayandong, elevation 3 000 m a.s.l.), and *L. xizangensis* (D) (62K, elevation 2 800 m a.s.l.) in Medog County, southeastern Tibet, China, respectively. Photos by Ke Jiang, Kai Wang, and Shuai Wang

Figure 6 Gravid female (A) and developing eggs through transparent abdomen (B) of *Liurana xizangensis* from 62K, Medog County, Tibet, China. Photos by Ke Jiang

Conservation

As micro-endemic habitat specialists, *Liurana* species are threatened by habitat destruction in southern Tibet. Based on our continuous field surveys since 2012, considerable habitat destruction has been observed at 62K in Medog County, which is one of only three known localities for *L. xizangensis*. Unregulated infrastructure developments have destroyed the mossy fields along the forest edges, streams, and wetlands, which constitute the core habitats not only for *L. xizangensis*, but also other micro-endemic anuran species such as *Scutiger wuguanfui* and *S. spinosus* (Jiang et al., 2016). Similarly, continuous tourist development and road construction along the hiking trail of Medog pose serious threats to habitat at the only known locality of *L. alpina*. Therefore, we recommend that local authorities and regional governments take habitat conservation into account when making developmental decisions, and we urge law enforcement agencies to enforce the existing environmental regulations of construction projects in the region, particularly in Medog County.

COMPETING INTERESTS

The authors declare that they have no competing interests.

AUTHORS' CONTRIBUTIONS

K.W., K.J., Y.W., and C.L. conducted fieldworks in Tibet. K.J. and K.W. collected data and conducted the analyses. J.C. supervised the analyses. K.J. and K.W. wrote the manuscript with the other authors' inputs. K.W. submitted molecular data to GenBank. K.J., K.W., and J.C. revised the manuscript. All authors read and approved the final version of the manuscript.

NOMENCLATURAL ACTS REGISTRATION

The electronic version of this article in portable document format will represent a published work according to the International Commission on Zoological Nomenclature (ICZN), and hence the new names contained in the electronic version are effectively published under that Code from the electronic edition alone (see Articles 8.5–8.6 of the Code). This published work and the nomenclatural acts it contains have been registered in ZooBank, the online registration system for the ICZN. The ZooBank LSIDs (Life Science Identifiers) can be resolved and the associated information can be viewed through any standard web browser by appending the LSID to the prefix http://zoobank.org/.

Publication LSID:

urn:lsid:zoobank.org:pub: 8D6905B9-0AEA-4091-BCA6-A7C849BD1848.

Liurana vallecula LSID:

urn:lsid:zoobank.org:act: 2AD61C3A-E263-46CC-A919-399992A558C8.

REFERENCES

Borah MM, Bordoloi S, Purkayastha J, Das M, Dubois A, Ohler A. 2013. *Limnonectes* (*Taylorana*) *medogensis* from Arunachal Pradesh (India), and on the identity of some diminutive ranoid frogs (Anura: Dicroglossidae, Occidozygidae). *Herpetozoa*, **26**(1/2): 39–48.

Brown WC, Alcala AC. 1982. Modes of reproduction of Philippine anurans. *In*: Rodin AGJ, Miyata A. Advances in Herpetology and Evolutionary Biology. Cambridge, MA: Museum of Comparative Biology, 416–428.

Brown RM, Siler CD, Richards SJ, Diesmos CA, Cannatella DC. 2015. Multilocus phylogeny and a new classification for Southeast Asian and Melanesian forest frogs (family Ceratobatrachidae). *Zoological Journal of the Linnean Society*, **174**(1): 130–168.

Che J, Chen HM, Yang JX, Jin JQ, Jiang K, Yuan ZY, Murphy RW, Zhang YP. 2011. Universal COI primers for DNA barcoding amphibians. *Molecular Ecology,* **12**(2): 247–258.

Darriba D, Taboada GL, Doallo R, Posada D. 2012. jModelTest 2: more models, new heuristics and parallel computing. *Nature Methods*, **9**(8): 772.

Dubois A. 1986. Miscellanea taxinomica batrachologica (I). *Alytes*, **5**(1–2): 7–95.

Fei L, Hu SQ, Ye CY, Tian WS, Jiang JP, Wu GF, Li J, Wang YZ. 2009. Fauna Sinica Amphibia. Vol. 2: Anura. Beijing: Science Press, 1–958. (in Chinese)

Fei L, Ye CY, Huang YZ. 1997. Taxonomic studies of the genus *Liurana* of China including descriptions of a new species (Amphibia: Ranidae). *Cultum Herpetologica Sinica*, **6–7**: 75–80.

Fei L, Ye CY, Jiang JP. 2010. Phylogenetic systematic of Ranidae. *Herpetologica*, **12**: 1–43. (in Chinese)

Guindon S, Gascuel O. 2003. A simple, fast and accurate method to estimate large phylogenies by maximum-likelihood. *Systematic Biology*, **52**(5): 698–704.

Hu S, Zhao E, Jiang Y, Fei L, Ye C, Hu Q, Huang Q, Huang Y, Tian W. 1987. *Amphibia-Reptilia of Xizang*. Beijing: Science Press (in Chinese).

Huang YZ, Ye CY. 1997. A new species of the genus *Liurana* (Amphibia: Ranidae) from Xizang, China. *Cultum Herpetologica Sinica*, **6–7**: 112–115.

Jiang K, Wang K, Zou DH, Yan F, Li PP, Che J. 2016. A new species of the genus *Scutiger* (Anura: Megophryidae) from Medog of southeastern Tibet, China. *Zoological Research*, **37**(1): 21–30.

Li P, Zhao E, Dong B. 2010. *Amphibians and Reptiles of Tibet*. Beijing: Science Press. (in Chinese).

Marshall DC. 2010. Cryptic failure of partitioned Bayesian phylogenetic analyses: lost in the land of long trees. *Systematic Biology*, **59**(1): 108–117.

Rambaut A, Suchard M, Drummond A. 2013. Tracer v1.6. Available at: http://tree.bio.ed.ac.uk/software/tracer.

Ronquist F, Huelsenbeck JP. 2003. MrBayes 3: Bayesian phylogenetic inference under mixed models. *Bioinformatics*, **19**(12): 1572–1574.

Ryan MJ. Constrains and patterns in the evolution of anuran acoustic communication. 1988. *In*: Fritzsch B, Ryan M, Wilczynski W, Walkowiak W,

Hetherington T. The Evolution of the Amphibian Auditory System. New York: John Wiley and Sons Incs, 637–677.

Sambrook J, Fritsch E, Maniatis T. 1989. Molecular Cloning: A Laboratory Manual (2nd ed.). New York: Cold Spring Harbor Laboratory Press, 1–1546.

Sichuan Biological Research Institute. 1977. A survey of amphibians in Xizang (Tibet). *Acta Zoologica Sinica*, **23**(1): 54–63.

Siler CD, Diesmos AC, Linkem CW, Diesmos ML, Brown RM. 2010. A new species of limestone-forest frog, genus *Platymantis* (Amphibia: Anura: Ceratobatrachidae) from central Luzon Island, Philippines. *Zootaxa*, **2482**: 49–63.

Stamatakis A. 2014. RAxML version 8: a tool for phylogenetic analysis and post analysis of large phylogenies. *Bioinformatics*, **30**(9): 1312–1313.

Stamatakis A, Hoover P, Rougemont J. 2008. A rapid bootstrap algorithm for the RAxML Web servers. *Systematic Biology*, **57**(5): 758–771.

Yan F, Jiang K, Wang K, Jin JQ, Suwannapoom C, Li C, Vindum JV, Brown RM, Che J. 2016. The Australasian frog family Ceratobatrachidae in China, Myanmar and Thailand: discovery of a new Himalayan forest frog clade. *Zoological Research*, **37**(1): 7–14.

APPENDIX I

Specimens examined for comparison. Museum abbreviations follow those from the methods section.

Liurana alpina (*n*=4): KIZ011140–42 (males), KIZ07358 (Dayandong (type locality)) Medog County, Tibet, China.

Liurana medogensis (*n*=3): KIZ010955, 05886, 05587 (males), (Xigong Lake (type locality)) Medog County, Tibet, China.

Liurana xizangensis (*n*=11): KIZ012704, 014046 (males), (Tongmai (close to type locality "Yi'ong", =Yigong)) Bomê, Tibet, China; KIZ06707, 09954–56, 011105–06, 012706 (males); KIZ09953, 014153 (females), 62K, Medog County, Tibet, China.

APPENDIX II GenBank sequences used and accession Nos. of novel sequences

				Gene and GenBank accession No.			
Genus	Species	Voucher or tissue number	Locality	COI	Rag1	Rod	Tyr
Alcalus	*tasanae*	CAS232349	Myanmar	–	KU243096	KU243106	KU243116
Alcalus	*tasanae*	CAS247243	Myanmar	–	KU243097	KU243107	KU243117
Alcalus	*tasanae*	THNHM20534	Myanmar	–	KU243098	KU243108	KU243118
Ceratobatrachus	*guentheri*	VUB1017(SR5543)	Solomon Islands	AY883979	DQ347272	DQ347391	DQ347179
Cornufer	*boulengeri*	BPBM22329	Papua New Guinea	HQ844999	KP298309	–	KP298385
Ingerana	*tenasserimensis*	CAS205064/ TADP918	Myanmar/Thailand	KR087736	DQ347258	AY322236	KP298327
Limnonectes	*limgorgi*	VUB1218	Laos	–	DQ347286	DQ347407	DQ347194
Liurana	*alpina*	KIZ011140	Medog, Tibet, China	MK462138	KU243094	KU243104	KU243114
Liurana	*alpina*	KIZ011141	Medog, Tibet, China	MK462139	KU243095	KU243105	KU243115
Liurana	*alpina*	KIZ07357	Medog, Tibet, China	MK462137	–	–	–
Liurana	*medogensis*	KIZ010955	Medog, Tibet, China	MK462136	–	KU243103	KU243113
Liurana	*vallecula*	KIZ014083	Medog, Tibet, China	MK462134	MK315115	MK462150	MK462155
Liurana	*vallecula*	KIZ014106	Medog, Tibet, China	MK462135	–	MK462151	MK462156
Liurana	*xizangensis*	KIZ06707	Medog, Tibet, China	MK462140	KU243092	KU243101	KU243111
Liurana	*xizangensis*	KIZ09956	Medog, Tibet, China	MK462141	–	–	–
Liurana	*xizangensis*	KIZ011104	Medog, Tibet, China	MK462144	–	–	–
Liurana	*xizangensis*	KIZ012705	Medog, Tibet, China	MK462142	–	–	–
Liurana	*xizangensis*	KIZ012706	Medog, Tibet, China	MK462143	–	–	–
Liurana	*xizangensis*	KIZ012707	Medog, Tibet, China	MK462145	–	–	–
Liurana	*xizangensis*	KIZ012704	Medog, Tibet, China	MK462146	–	–	–
Liurana	*xizangensis*	KIZ014046	Medog, Tibet, China	MK462147	–	–	–
Platymantis	*hazelae*	TNHC62160 & CMNH-RSK3918	Phillipines	–	DQ347248	DQ347369	DQ347153

–: Not available.

Duplication and diversification of insulin genes in ray-finned fish

David M. Irwin[1,2,*]

[1] *Department of Laboratory Medicine and Pathobiology, University of Toronto, Toronto Ontario* M5S 1A8, *Canada*
[2] *Banting and Best Diabetes Centre, University of Toronto, Toronto Ontario* M5S 1A8, *Canada*

ABSTRACT

Insulin is a key hormone for the regulation of metabolism in vertebrates. Insulin is produced by pancreatic islet cells in response to elevated glucose levels and leads to the uptake of glucose by tissues such as liver and adipose tissue to store energy. Insulin also has additional functions in regulating development. Previous work has shown that the proglucagon gene, which encodes hormones counter regulating insulin, is duplicated in teleost fish, and that the peptide hormones encoded by these genes have diversified in function. I sought to determine whether similar processes have occurred to insulin genes in these species. Searches of fish genomes revealed an unexpected diversity of insulin genes. A triplication of the insulin gene occurred at the origin of teleost fish, however one of these three genes, *insc*, has been lost in most teleost fish lineages. The two other insulin genes, *insa* and *insb*, have been retained but show differing levels of selective constraint suggesting that they might have diversified in function. Intriguingly, a duplicate copy of the *insa* gene, which I named *insab*, is found in many fish. The coding sequence encoded by *insab* genes is under weak selective constraint, with its predicted protein sequences losing their potential to be processed into a two-peptide hormone. However, these sequences have retained perfectly conserved cystine residues, suggesting that they maintain insulin's three-dimensional structure and therefore might modulate the processing and secretion of insulin produced by the other genes.

Keywords: Insulin; Teleost fish; Gene duplication; Adaptive evolution; Gene loss

INTRODUCTION

Fish have been important contributors to our understanding of human biology and disease (Lieschke & Currie, 2007; MacRae & Peterson, 2015), especially in endocrinology (Conlon, 2000a). In vertebrates, insulin is a hormone produced by the beta-cells of pancreatic islets in response to increased levels of blood glucose, which induces the uptake of glucose by tissues such as liver and adipose tissue for storage, and thus is a key regulator of glucose metabolism (Röder et al., 2016). Deficiencies in insulin production and/or signaling leads to diabetes in humans and other animals (Röder et al., 2016; Weiss, 2009). Many aspects of insulin function have been learned from extensive studies in diverse species of fish (Caruso & Sheridan, 2011; Conlon, 2000b; Polakof et al., 2012). Fish have also been explored in the development of potential treatments for diabetes. Xenotransplantation of fish islets, using both wild-type and humanized insulin, has been considered due to the relative ease of isolation of islets from pancreatic tissue in fish (e.g., tilapia, *Oreochromis niloticus*) compared to mammalian sources (Wright et al., 2014). Insulin, however, in addition to its role in the regulation of metabolism, also has other roles in vertebrate biology, including some in development (Chan & Steiner, 2000; Hernández-Sánchez et al., 2006).

Insulin is a polypeptide hormone composed of two peptides, A- and B-chains of about 20 and 30 amino acids, respectively, which are held together by disulfide bridges (Conlon, 2001; Steiner et al., 1985, 2009; Weiss, 2009). Insulin sequences have been characterized, mostly at the protein level, in a large number of vertebrate and fish species (Caruso & Sheridan, 2011; Conlon, 2000b, 2001). Typically, vertebrate species have a single copy of the insulin gene in their genomes (Nishi & Nanjo, 2011; Steiner et al., 1985), however, multiple insulin genes have been characterized in some species, such as

rodents (Long et al., 2013; Soares et al., 1985; Wentworth et al., 1986) and some fish (Caruso et al., 2008; Caruso & Sheridan, 2011, 2014; Irwin, 2004). Within fish, it appears that only one of these insulin genes, which produces the hormone that regulates blood glucose levels, is expressed in the pancreas (Caruso & Sheridan, 2011; Irwin, 2004), with the exception of the multiple insulin genes produced by the very recent genome duplication in salmonid fish (Caruso et al., 2008; Caruso & Sheridan, 2014). While the origin of the two insulin genes found in some fish (e.g., zebrafish) was shown to be early in teleost fish evolution, whether this *ins2* gene has been retained in the genomes of diverse fish is unclear (Caruso & Sheridan, 2011; Irwin, 2004). The fish *ins2* gene has been poorly characterized. The initial identification of this gene in zebrafish (*Danio rerio*) and takifugu (*Takifugu rubripes*) only showed expression in the embryo of zebrafish (Irwin, 2004). A subsequence study of the expression of the two insulin genes in zebrafish suggested that *ins2* potentially has a function as a growth and neurotrophic factor during development (Papasani et al., 2006). More recently, studies of the tilapia (*O. niloticus*) *ins2* gene showed that it had negligible expression in the pancreas, thus likely is not a major contributor to the regulation of glucose metabolism and would not need to be silenced to allow the xenotransplantation of tilapia islets as a treatment for diabetes in humans (Hrytsenko et al., 2016).

Changes in the function of insulin can be paralleled by changes in the function of glucagon, the hormone that counters the action of insulin (Seino et al., 1988). Recently it has been shown that duplicated proglucagon genes are widespread in teleost fish, and that the functions of the proglucagon-derived peptides encoded by these genes have diversified (Irwin & Mojsov, 2018). Here I have taken advantage of the large number of fish genomes that have been characterized in the past few years (Ravi & Venkatesh, 2018) to determine the distribution of insulin genes in the genomes of ray-finned fish. Analysis of these sequences allows us to begin to understand the origin of these genes, including the measurement of the selective forces acting upon them, which might provide evidence for differences in function. Surprisingly, I found a greater diversity in the numbers of insulin genes than expected, with the identification of a third insulin paralog, as well as lineage-specific duplicates of some of these paralogs. My analyses suggest that all three fish insulin paralogs encode functional protein products.

MATERIALS AND METHODS

Data collection

Genome sequences databases maintained by the National Center for Biotechnology Information (NCBI: https://www.ncbi.nlm.nih.gov/genome/gdv/) and Ensembl (http://www.ensembl.org) were searched in March/April 2018, for sequences that were predicted to encode proteins similar to proinsulin. Initial searches used the *tBLASTn* algorithm (Gertz et al., 2006) using previously characterized zebrafish (*Danio rerio*) proinsulin protein sequences (Irwin, 2004; Milewski et al., 1988) as queries. Subsequent *tBLASTn*, *BLASTn*, and *BLASTp*

searches used our putative proinsulin sequences as queries. Genome sequences of 55 fish (52 ray-finned (Superclass Actinopterygii), 2 cartilaginous (Superclass Chondrichthyes), and one lobe-finned (Class Sarcopterygii)) were examined, with 52 of these contained in the NCBI Genome Data Viewer, and three (Atlantic cod, *Gadus morhua*; three-spined stickleback, *Gasterosteus aculeatus*; and the spotted green pufferfish, *Tetraodon nigroviridis*) only in the Ensembl database (9 were in both NCBI and Ensembl). A list of species with genomes used here, and their phylogenetic relationships, is presented in Figure 1. All sequences with E-scores below 0.001 were examined. As an initial step to assess homology and orthology, reciprocal BLASTp searches of the zebrafish proteome were conducted to examine the similarity of the putative proinsulin sequences. Sequences that were not more obviously similar to insulin-like growth factor-I (*igf1*) or insulin-like growth factor-II (*igf2*) were used for the following analyses. Here I suggest a standardized set of names for fish *ins* genes, based on the analysis described below, with *insa*, *insb*, and *insc* representing the three *ins* paralogs that originated early in teleost fish evolution, and *insaa* and *insab* representing duplicates of the *insa* gene shared by multiple species. Arabic numerals are used for recent lineage-specific duplicates and do not indicate necessarily indicate orthology.

Phylogenetic analysis

Prior to phylogenetic analysis, proinsulin (*ins*) coding sequences were aligned using the MAFFT algorithm (Katoh et al., 2001) as implemented at the Guidance2 server (http://guidance.tau.ac.il/ver2/; Penn et al., 2010). Phylogenetic relationships were established using both maximum likelihood and Bayesian methods. PhyML 3.0 (http://www.atgc-montpellier.fr/phyml/; Guindon et al., 2010) was used to generate maximum likelihood trees, with 500 bootstrap replications, where the Smart Model Selection (SMS) (Lefort et al., 2017) option was used to identify the best fitting evolutionary model. Bayesian trees were constructed using MrBayes 3.2.6 (Huelsenbeck et al., 2001; Ronquist et al., 2012), with 5 000 000 generations and four simultaneous Metropolis-coupled Monte Carlo Markov chains sampled every 100 generations under the same evolutionary model used for maximum likelihood. The first 25% of the trees were discarded as burn-in with the remaining samples used to generate consensus trees. Insulin coding sequences from cartilaginous (*Callorhinchus milli* (Elephant shark) and *Rhincodon typus* (Whale shark)) and lobe-finned fish (*Latimeria chalumnae* (Coelacanth)) were used as outgroups to root the trees for all insulin coding sequences. Subsequent analyses, using subsets of the sequence data, were conducted with similar approaches, and used sequences identified in our initial analyses as outgroups.

Evolutionary analysis

Genes adjacent to insulin genes in fish genomes were identified by examining genomic contigs in the NCBI and Ensembl databases using methods that I have previously used (Irwin, 2002, 2012; Irwin & Mojsov, 2018). Briefly, the identity and orientation of genes neighboring insulin genes were identified

from the genomic databases. The orthology of the genes adjacent to insulin genes was assessed (or confirmed if annotated) using *BLASTp* searches of the zebrafish and human proteomes (Kuraku & Meyer, 2012).
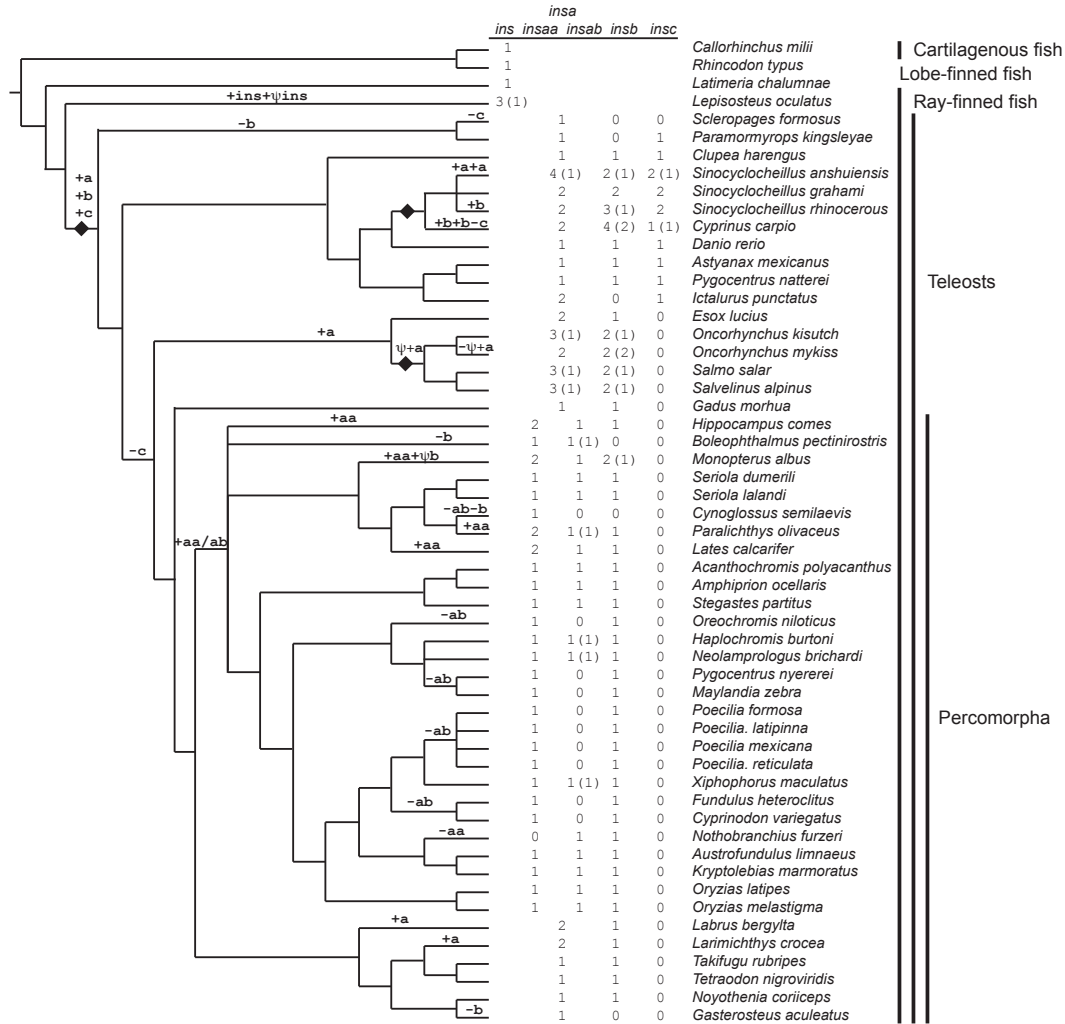

Figure 1 Diversity and evolution of fish insulin genes

Summary of the evolution of insulin genes in ray finned fish. Phylogenetic relationships of species with genome sequences is based on Betancur-R et al. (2017), with modifications in an area that is not confidently resolved to minimize the number of gene duplications or deletions. Some phylogenetic relationships are not resolved. Branches are not proportional to evolutionary time. Classification of fish is shown to the right. Solid diamonds indicate genome duplications. The numbers of different types of insulin gene found in each genome is listed, with numbers in brackets indicating incomplete sequences. Gene additions or gene losses are indicated by plus (+) and minus (−) before an a, b, or c, representing the *insa*, *insb*, and *insc* paralogs, respectively. The *insa*, *insb*, and *insc* paralogs originated near the genome duplication in the ancestor of teleosts and are indicated as +a, +b, and +c to refer to the two gene duplications. The duplication to generate the *insaa* and *insab* genes is indicated by +aa/ab. +ins indicated the gene duplication on the *Lepisosteus oculatus* lineage. +ψins, +ψa, and +ψb indicates retroposition events that generated processed pseudogenes.

The strength of selective pressure acting upon the insulin coding sequences can be measured by comparing the relative rates of nonsynonymous (d_N) and synonymous substitutions (d_S). Sequences under stronger selective pressure for protein function will have lower nonsynonymous to synonymous (d_N/d_S) ratios. d_N/d_S rate ratios were obtained from analyses using RELAX (Wertheim et al., 2014) as implemented on the Datamonkey Adaptive Evolution server (http://datamonkey.org/; Weaver et al., 2018), which also tested for intensification or relaxation of the levels of selection on tested lineages.

Evidence for positive selection on branches of the phylogenetic tree was tested using aBSREL (Smith et al., 2015) on the Datamonkey Adaptive Evolution server (Weaver et al., 2018).

Prediction of protein processing sites and alignment of peptide sequences

Signal peptidase cleavage sites in the proinsulin protein sequences were predicted using SignalP 4.1 (http://www.cbs.dtu.dk/services/SignalP/; Petersen et al., 2011). I used two prediction programs to identify potential prohormone protease processing sites in the proinsulin sequences, NeuroPred (http://neuroproteomics.scs.illinois.edu/neuropred.htm; Southey et al., 2006) and ProP 1.0 (http://www.cbs.dtu.dk/services/ProP/; Duckert et al., 2004), with "general PC prediction" selected. To visual the conservation of the processing sites and insulin peptide sequences, the proinsulin protein sequences were aligned using Clustal Omega (https://www.ebi.ac.uk/Tools/msa/clustalo/; Sievers et al., 2011). Consensus proinsulin A- and B-chain peptide sequences were generated from the alignments using WebLogo 3 (http://weblogo.threeplusone.com/; Crooks et al., 2004).

RESULTS

Numbers of insulin genes in fish genomes

Searches of genome databases maintained by NCBI and Ensembl resulted in the identification of 168 insulin genes from the genomes of 55 species examined, with 141 of these predicted to be intact full-length coding sequences (Figure 1 and Supplementary Table S1). While only single copy insulin genes were found in the genomes of cartilaginous and lobe-finned fish, multiple genes were found in the genomes of most ray-finned fish. Within ray-finned fish, the number of identified insulin genes ranged from 1 (*Sclerophages fromosus*) to 8 (*Sinocyclocheilus anshuiensis*). As expected, fish species that experienced recent genome duplications, i.e., carp (*Cyprinus carpio*; Xu et al., 2014), members of the genus *Sinocyclocheilus* (Yang et al., 2016), and salmonids (*Oncorhynchus kisutch*, *O. mykiss*, *Salmo salar*, and *Salvelinus alpinus*; Lien et al., 2016) have the largest numbers of insulin genes. Phylogenetic analysis (see below) suggested the presence of three insulin paralogs in teleost fish: *insa*, *insb*, and *insc*. Of the 162 insulin genes identified in the 51 species of teleost fish (infraclass Teleostei), 92 were classified as *insa* (which includes *insaa* and *insab* genes), 57 as *insb*, and 13 as *insc*, with 11, 12, and 3 of the sequences found to be incomplete, respectively, for these three paralogs (Figure 1 and Supplementary Table S1). All 51 species of teleost fish possessed at least one *insa* gene, with 45 having *insb* genes, and 10 with *insc* genes (Figure 1 and Supplementary Table S1). The 6 species of teleost fish where I failed to identify *insb* genes are distributed across the accepted phylogeny of fish (Figure 1; Betancur-R et al., 2017; Near et al., 2012), suggesting they were lost independently several times (or are missing from these genome assemblies). In contrast, almost all of the species lacking *insc* genes share a common ancestor (Figure 1, clade Euteleostei), suggesting a single gene loss event

explains the absence of *insc* genes in most teleost fish. The coding sequences of the insulin (*ins*) genes used in our analysis described below are presented in Supplementary Figure S1.

Phylogeny of fish insulin genes

To better understand the origin and evolution of the multiple insulin (*ins*) genes found in the genomes of ray-finned fish, their phylogenetic relationships, rooted using *ins* gene sequences from cartilaginous and lobe-finned fish, were inferred using maximum likelihood (Figure 2) and Bayesian (Supplementary Figure S2) methods. Both analyses generated similar phylogenies with independent duplications of the insulin gene on the spotted gar (*Lepisosteus oculatus*; infraorder Holostei) and teleost (infraorder Teleostei) fish lineages. While duplicated *insa* and *insb* genes were previously identified in teleost fish (Caruso & Sheridan, 2014; Hrytsenko et al., 2016; Irwin, 2004), here I find that these species have a third insulin paralog, which I named *insc*. The species relationships within each paralog of insulin genes, given its limited power at resolving species relationships, is in general agreement with the accepted phylogeny of teleost fish (Betancur-R et al., 2017; Near et al., 2012). This observation suggests that the triplication of the insulin gene occurred in an early teleost. The relationships among the *insa*, *insb*, and *insc* paralogs is poorly resolved in our phylogenetic analyses, with the maximum likelihood analysis suggesting a closer relationship between *insa* and *insb*, while the Bayesian analysis suggesting that *insb* and *insc* are most closely related.

Most teleost species that possess *insb* and *insc* genes have a single copy of each gene, except those species that have experienced additional genome duplications (i.e., *Cyprinus carpio*, salmonids (*O. mykiss*, *O. kisutch*, *Salmo salar*, and *Salvelinus aplinus*), and the genera *Sinocyclocheilus*)). In contrast, a large number (30 of 51) of teleosts have multiple *insa* genes (Figure 1 and Supplementary Table S1). While some of these appear to be due to lineage-specific genome duplications (i.e., *Cyprinus carpio*, salmonids, and the genera *Sinocyclocheilus*) or single-gene duplications (e.g., *Labrus bergylta* and *Larimichthys crocea*), many are due to a duplication event that occurred on an early Percomorpha lineage (Figures 1, 2, and Supplementary Figure S2). The genomes of many Percomorpha fish contain two (or more) *insa* genes that form monophyletic clades that are largely in accord with the accepted species phylogeny (Betancur-R et al., 2017; Near et al., 2012). This observation suggests that a duplication of the *insa* gene, generating *insaa* and *insab* genes, occurred in an early lineage of Percomorpha fish (see Figure 1). In species that are inferred to be descendants of this Percomorpha-specific *ins* gene duplication, all but *Nothobranchius furzeri* possess an *insaa* gene, however, a larger number of species, such as tilapia (*Oreochromis niloticus*), some cichlids (e.g., *Pundamilia nyererei* and *Maylandia zebra*), and species of the genus *Poecilia* do not have an *insab* gene (Figures 1, 2 and Supplementary Figure S2 and Table S1). This suggests that the *insab* gene was lost in parallel in a number of species of Percomorpha (see Figure 1).
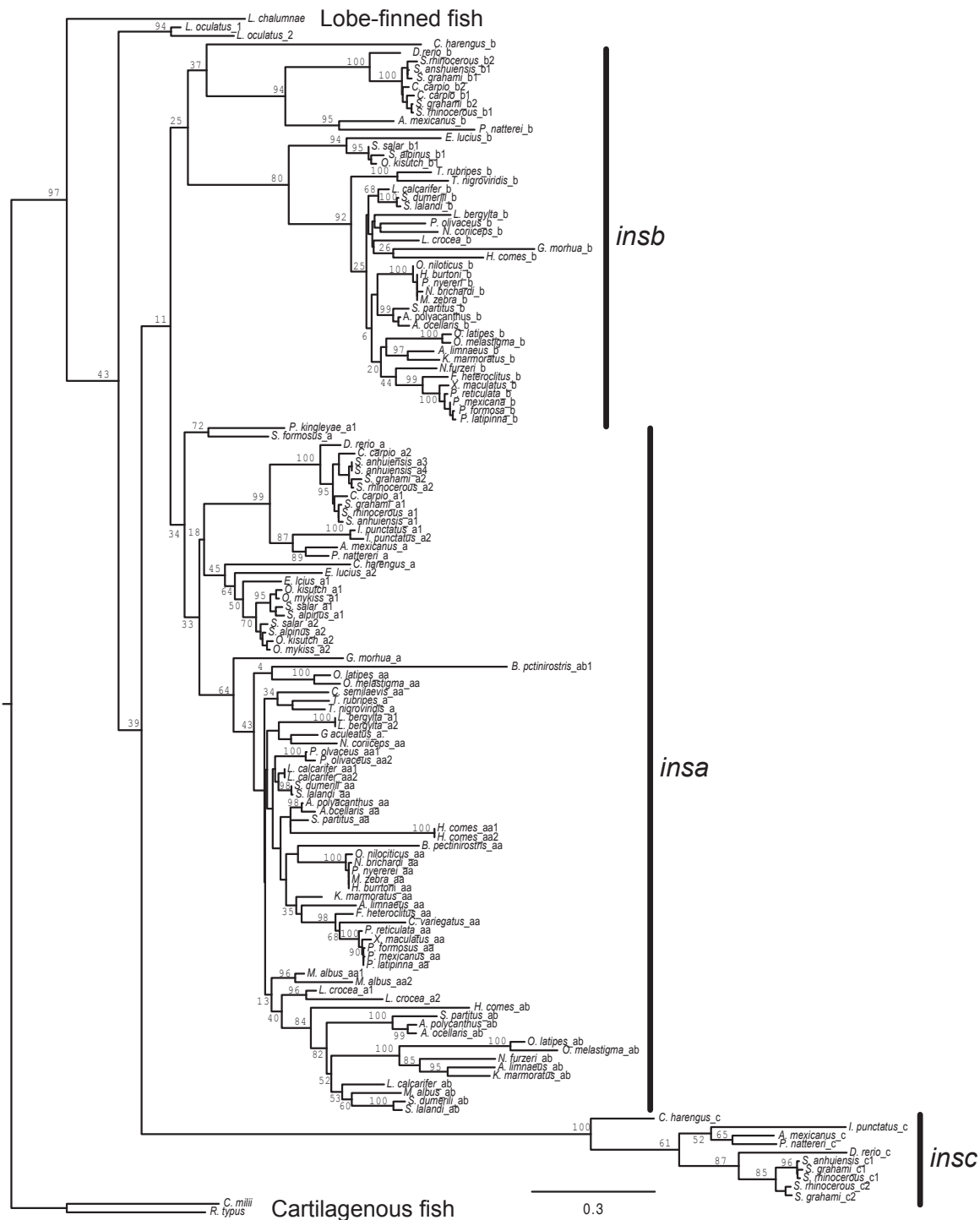
Figure 2 Phylogeny of fish insulin genes

Phylogenetic relationship of insulin coding sequences was inferred using maximum likelihood with the best fitting evolutional model GTR+G+I (GTR with gamma distribution and invariant sites) and bootstrapped with 500 replications. A similar phylogeny was generated using Bayesian methods (Supplementary Figure S2). Percent bootstrap support for lineages are shown. The tree in Newick format, with all branch lengths and support values, is presented in Supplementary Figure S3. The phylogeny was rooted with sequences from cartilaginous (*Callorhinisus milli* and *Rhincodon typus*) and lobe-finned (*Latimeria chalumnae*) fish. Full species names are listed in Figure 1. *insa*, *insb*, and *insc* indicate the three clades of insulin genes found in teleost fish.

Duplications of fish insulin genes

To aid in the assessment of the orthology of insulin genes, and to gain insight into the gene duplication events, I identified genes flanking the insulin genes in the genomic sequences of 55 species of fish (Supplementary Table S2, examples given in Figure 3). A genome duplication occurred in the ancestor of teleost fish, the teleost fish-specific genome duplication (Glasauer & Neuhauss, 2014; Meyer & Van de Peer, 2005). Our phylogenetic analyses (Figure 2 and Supplementary S2) suggests that the three insulin paralogs found in teleost fish (*insa*, *insb*, and *insc*) originated on this lineage. If duplicate genes originated through a genome duplication, then one might expect similar genomic neighborhoods for these genes (i.e., similar genes found adjacent to different *ins* genes), as observed for the duplicated proglucagon (*gcg*) and glucagon receptor (*gcgr*) genes of teleost fish (Irwin, 2014; Irwin & Mojsov, 2018). For the three insulin paralogs examined here, only very limited similarity was seen in the genomic neighborhoods (longer genomic regions were examined, with immediate neighborhoods summarized in Supplementary Table S2). A gene similar to *tenm2* (teneurin transmembrane protein 2) was found adjacent to *insa* genes in *Exox lucius*, *O. kisutch*, *O. mykiss*, *Paramormyrops kingsleyae*, *Salmo salar*, and *Sclerophages formosus*, and *insb* genes in *Pygocentrus nattereri*, *Salvelinus alpinus*, and *Sinocyclocheilus rhinocerous* (Supplementary Table S2). This might suggest that the *insa* and *insb* genes originated via the teleost-fish specific genome duplication. However, as the linkage between the *tenm2* and *ins* genes was only observed in a small number of species, this would require large number of independent losses (or genomic rearrangements) of *tenm2*-like genes to yield the absence of a linked *tenm2*-like with most *ins* genes, therefore the evidence for the origin of *insa* and *insb* by a genome duplication event is not strong. No genes near *insc* were similar to those adjacent to *insa* or *insb*, thus it more likely originated as a single gene duplication event rather than through a genome duplication. If the *insa* and *insb* genes originated via a genome duplication, an addition single-gene duplication would still be needed to explain the origin of *insc*. The gene neighborhood data does not help resolve the relationships among the three *ins* genes. Intriguingly, the genomic neighborhoods of none of the insulin gene paralogs in teleost fish is similar to the typical vertebrate insulin gene neighborhood, where insulin is flanked by insulin-like growth factor 2 (*igf2*) and tyrosine hydroxylase (*th*) genes (Patton et al., 1998), although similar neighborhoods were found for the insulin genes in cartilaginous and lobe-finned fish (Supplementary Table S2). This suggests that the insulin genomic neighborhood was rearranged on the ancestral ray-finned fish lineage.

Orthologous genes often have similar genomic neighborhoods, thus can these neighborhoods can be used to assess orthology when gene sequence similarity is limited (Kurokawa et al., 2005). When the genomic neighborhoods surrounding *insb* and *insc* genes were examined (Figure 3 and Supplementary Table S2) shared features were identified for each gene. All *insb* genes are adjacent to a *hmmr*

(hyaluronan mediated motility receptor)-like gene, while all *insc* genes are flanked by *prr12* (proline rich 12) and *scaf1* (SR-related CTD associated factor 1)-like genes (as shown for the *Clupea harengus insb* and *Danio rerio insc* genes in Figure 3), suggesting that their genomic neighborhoods are largely conserved since they originated in the early teleost. In contrast, several different genomic neighborhoods were observed for the *insa* genes (Supplementary Table S2, examples shown in Figure 3). The most phylogenetically widespread genomic neighborhood has a *nipal* (magnesium transporter NIPA3-like)-like gene adjacent to the *insa* gene (Supplementary Table S2) and is found in species representing Osteoglossomorpha (e.g., *Sclerophages formosus*, shown in Figure 3), Protacanthopterygii (e.g. *Esox lucius* and *Salmo salar*), Paracanthopterygii (e.g., *Gadus morhua*), and Percomorpha (e.g., *Takifugu rubripes* and *Oryzias latipes*). The only major group of teleost fish that does not have an *insa* gene adjacent to *nipal* are those of Otomorpha (e.g., *Danio rerio*, shown in Figure 3), suggesting a change in the gene order occurred in this group and that the linkage of *insa* with *nipal* is ancestral. Within Percomorpha (Supplementary Table S2), the *insaa* genes are found adjacent to *nipal*-like genes (as in *Sclerophages formosus*, Figure 3), while the *insab* genes are near a *sh3pxd2b* (SH3 and PX domains 2B)-like genes (e.g., *Haplochromis burtoni*, Figure 3). The linkage of the *insab* genes with *sh3pxd2b* strengthens the conclusion that all *insab* genes are orthologous and indicates that *insaa* is located at the ancestral genomic location and was the source (locus-of-origin) for the *insab* gene that was inserted into a new genomic locus.
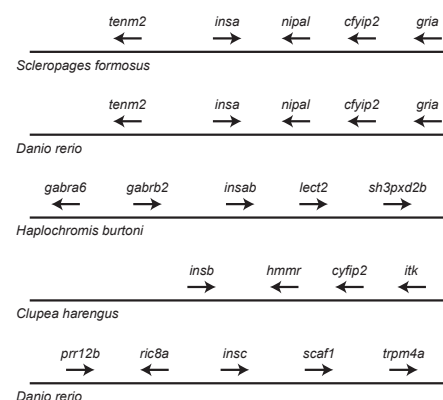

Figure 3 Genomic neighborhoods surrounding fish insulin genes

Examples of genomic neighborhoods found for insulin paralogs in ray-finned fish. Genomic neighborhoods are listed in Supplementary Table S2. A: Typical genomic neighborhood for *insa* and *insaa* genes as illustrated from *Scleropages formosus*. B: Genomic neighborhood for *insa* genes in *Danio rerio* and close relatives. C: Typical genomic neighborhood for *insab* genes as illustrated from *Haplochromis burtoni*. D: Typical genomic neighborhood for *insb* genes as illustrated from *Clupea harengus*. E: Typical genomic neighborhood for *insc* genes as illustrated from *D. rerio*. See Supplementary Table S2 for full gene names.

Lineage-specific changes in insulin gene number

The gene duplication events described above explain most, but not all, of the insulin genes identified (Figure 1 and Supplementary Table S1). Many of the additional genes can be explained by tandem gene duplication, which lead to two insulin genes arranged head-to-tail in the genome (see Supplementary Tables S1, S2) and includes the *insa1* and *insa2* genes in *Parmormyrops kingsleyae* and in *Larmichthys crocea*, the *insaa1* and *insaa2* genes in *Hippocampus comes*, and the *insab1* and *insab2* genes in *Boleopththalmus pectinirostris*. Both *Cyprinus carpio* and *Sinocyclocheilus rhinocerous* have tandemly arranged *insb* genes (*insb3* and *insb4* in *C. carpio* and *insb2* and *insb3* in *S. rhinocerous*, Supplementary Table S2) that might have originated prior to the divergence of these two species (although, they would then have to be lost in the two other *Sinocyclocheilus* species). *Sinocyclocheilus anshuiensis* has two pairs of tandemly arranged genes, *insa1/insa2* and *insa3/insa4*, which either originated prior to this species genome duplication (and then were lost in the closely related species that share this genome duplication), had parallel tandem duplications, or is an assembly error (the tandemly arranged genes are identical in sequence). The *ins1* and *ins2* genes of *Lepisosteus oculatus* might also have originated via a tandem duplication, which was then followed by rearrangements so that these lineage-specific gene duplicates are now found in opposite orientations on either side of a *hmmr*-like gene (see Supplementary Table S2). More complex duplication events, resulting in genes moving to new locations are need to explain the remaining genes, with some being extremely recent (e.g., the identical *insaa1* and *insaa2* genes in *Labrus bergylta*) or more ancient (e.g., *insa1* and *insa2* gene of *Esox lucius*).

While duplication of genomic DNA is a frequent mechanism for the origin of duplicate genes, they can also be generated by retroposition of cDNA generated from mRNA transcripts (Long et al., 2013). Indeed, the well-characterized duplicate *ins1* gene in mice was generated from an incompletely processed mRNA transcript (Shiao et al., 2008; Soares et al., 1985). Typically, insulin genes contain two coding exons that must be spliced together to create an intact coding sequence. Here I identified 6 insulin genes that are likely generated by reverse-transcribed mRNAs, as these genomic sequences do not have an intron interrupting the coding sequence (see Supplementary Figure S4 for an example). The 6 retro-processed insulin genes can be explained by three integration events: (1) between *ankrd6* (ankyrin repeat domain 6) and *lyrm2* (LYR motif containing 2)-like genes on the *Lepisosteus oculatus* lineage to generate ψ*ins*; (2) within an *apbb3* (amyloid beta precursor protein binding family 8 member 3)-like gene on the *Monopterus albus* lineage to generate ψ*insb*; and (3) within a *psd3* (PH and SEC7 domain containing protein 3)-like gene on the ancestral lineage for salmonids (*Oncorhynchus mykiss*, *O. kisutch*, *Salmo salar*, and *Salvelinus aplinus*) and the Northern pike (*Esox lucius*) that generated ψ*insa* in *O. kisutch*, *S. salar*, and *S. alpinus* (but was not found in *O. mykiss*) and an intact coding sequence (*insa2*) in

Esox lucius (Figure 1 and Supplementary Figure S4 and Table S2). The maintenance of an intact open reading frame in *Exox lucius insa2* (Supplementary Figure S4) suggests that this retropositioned sequence, like the mouse *ins1* gene (Soares et al., 1985), is still functional. However, this sequence has lost its coding potential in salmonid fish and is a pseudogene (Figure 1 and Supplementary Table S1). Additional processed genes might also exist, as several incomplete genes (e.g., *insb4* from *Cyprinus carpio* and *insa3* from *Paramormyrops kingsleyae*) were identified (see Supplementary Table S1) that were located at unique location of the genome (see Supplementary Table S2) consistent with being inserted processed cDNAs, but the sequences were similar to either exon 1 or 2 (and not both), thus cannot be distinguished from a sequence generated by an DNA-mediated incomplete gene duplication event.

Gene for insulin a (*insa*) is evolving under greater evolutionary constraint

Our genomic and phylogenetic analyses of fish genome sequences demonstrated that teleost fish have three paralogous insulin genes. In contrast, most other vertebrate species only have one (Chan & Steiner, 2000; Conlon, 2000b). The increased number of insulin genes in teleost fish raises the possibility that they have been diversified to: (1) subfunctionalize distinct functions of insulin, (2) neofunctionalize to acquire novel functions, or (3) lose function (pseudogenize). As a first step to explore possible changes in the biological roles of these distinct insulin genes I assessed the selective pressures acting upon the sequences. This can be done by comparing the rates of nonsynonymous (d_N) to synonymous (d_S) substitutions (Yang & Bielawski, 2000). If the protein encoded by a gene has lost its function, then it would be expected that there would be no selection against nonsynonymous substitutions, and that rates of nonsynonymous and synonymous substitutions would be the same rate (i.e., d_N/d_S=1, neutral evolution). If the protein encoded by these genes still had a function, then selection should act against a subset of nonsynonymous substitutions (the deleterious mutations) and be lower than the synonymous rate (i.e., d_N/d_S<1, purifying selection). Rarely, one might see d_N/d_S>1, which would indicate positive selection for change in amino acid sequence (Yang & Bielawski, 2000). If protein coding sequences of genes are being maintained for different functions, with different parts of the sequence being important for these functions, then one might see differing levels of selective constraint.

I used the program RELAX (Wertheim et al., 2014) to assess the levels of selective pressure (d_N/d_S) for each of the three insulin gene paralogs, and to determine whether the selective pressure was intensified or relaxed compared to the other insulin genes, with sequences from a non-teleost ray-finned fish, *Lepisosteus oculatus*, used as outgroup. When all sequences were analyzed, *insa* genes showed the stronger levels of purifying selection (d_N/d_S=0.266 6, 0.333 2, and 0.325 8 for *insa*, *insb*, and *insc*, respectively; Table 1). If I restricted these analyses to either species that have all

three paralogs, or species that only have a single copy of these paralogs, to attempt to minimize species-specific effects (changes seen in species that only have some of the genes) or due to differences in gene number, the difference in the selective constraints acting on *insa* vs. *insb* and *insc* became even more pronounced (Table 1). The results from RELAX also indicated that selection intensification, compared to the other insulin sequences, occurred on *insa*, while selection relaxation occurred for *insb* (Table 1). No significant change in selection intensity was seen for *insc* vs. all other insulin sequences. Similar results, with *insa* showing greater constraint, were seen in comparisons of *insa* and *insb* genes in species that had both of these genes (Table 1). These results suggest that the *insa* paralog is under greater purifying selective constraint than either the *insb* or *insc* paralog, but also importantly demonstrate that both *insb* and *insc* are continuing to experience purifying selection. Thus, it can be concluded that the protein coding sequence of *insa* is under the greatest level of selective constraint, however, the coding sequences of both *insb* and *insc* are also experiencing selective constraints consistent with their protein products having essential biological functions.

Table 1 Differences in the selective pressure (d_N/d_S) acting on insulin paralogs in teleosts

Sequences tested[a]	*insa*	*insb*	*insc*
All	0.2666[b] (80)	0.3332[c] (44)	0.3258 (10)
Species with *insa*, *insb*, and *insc*	0.2120[b] (11)	0.3309[c] (9)	0.3406 (9)
Species with single copy *insa*, *insb*, and *insc*	0.1911 (4)	0.3164 (4)	0.3129 (4)
Species with single copy *insa* and *insb*	0.1664[b] (17)	0.3171[c] (17)	N/A
Species with single copy *insa* and *insb*, but no *insc*	0.1366[b] (13)	0.3191[c] (13)	N/A

Numbers in brackets is the numbers of sequences used. [a]: The two complete *Lepisosteus acaulatus ins* sequences were used as outgroups. [b]: Test for selection intensification was significant. [c]: Test for selection relaxation was significant. N/A: Not applicable.

Adaptive evolution of insulin genes

While the protein products of the three insulin genes are being maintained for function, they might not be the same function. To examine whether any of the sequences might have gained new functions I tested for evidence of positive selection on lineages using aBSREL (Smith et al., 2015). Only one lineage showed significant evidence for episodic diversifying selection, the ancestral lineage for the *insc* genes. Inspection of the phylogenetic tree generated from all of the insulin coding sequences suggest that the ancestral branch for the *insc* genes is longer than for the *insa* and *insb* genes (Figure 2 and Supplementary Figure S2), consistent with a

greater number of nonsynonymous substitutions driven by positive selection. No evidence for positive selection was found on the ancestral lineages for the *insa* or *insb* genes. These results might suggest that *insc* has acquired a new function (neofunctionalization) driven by positive selection, while *insa* and *insb* have been retained due to subfunctionalization of insulin functions between the two genes.

Relaxed selection on the *insab* duplicate of the insulin a (*insa*) gene

An intriguing observation from our analysis of the selective constrains acting upon *insa*, *insb*, and *insc* paralogs was that the calculated value for the selective constraint acting on *insa* varied considerably depending upon which sequences were used for the analysis (Table 1). The ratio of the nonsynonymous to synonymous rates was higher when all *insa* sequences were used than if sequences were used only from species that had all three paralogs or had only single copies of the *insa* and *insb* paralogs (Table 1). These observations suggest that inclusion of *insa* sequences from species that have multiple *insa* sequences yields higher estimates of the d_N/d_S ratio due to some of these sequences having lower levels of sequence constraint. As the duplication to generate the *insaa* and *insab* genes is a major source of the multiple *insa* genes in teleost fish (see Figures 1, 2 and Supplementary Figure S2 and Table S1), I compared the selective constraints acting upon *insaa* and *insab* genes (Table 2). The *insaa* coding sequences were found to be under selective constrains (Table 2) similar to those of other *insa* sequences, and especially those from species that had single copy *insa*, while the *insab* sequences displayed the lowest levels of constrains seen for any fish *ins* sequence (Tables 1, 2). Test for intensification or relaxation of selective constraint showed that *insaa* was under significant intensification of selective constraint, while *insab* was significant relaxation of selective constraint was demonstrated for *insab* (Table 2). These results suggest that *insaa* retains the function of *insa*, which would be consistent with it being at the locus of origin, while *insab* is evolving with far less constraint, to the extent that it has been lost on a number of lineages (e.g., *Oreochromis niloticus*, *Pundamilia nyererei*, *M. zebra*, and species of the genus *Poecilia*, see Figure 1). This might suggest that *insab* is not essential.

Table 2 Differences in the selective pressure (d_N/d_S) acting on insaa and insab genes

Sequences tested[a]	*insaa*	*insbb*
All *insa*	0.1691[b] (18)	0.4766[c] (14)
Species with one copy of each	0.1251[b] (9)	0.5139[c] (9)

Numbers in brackets is the numbers of sequences used. [a]: The two complete *Lepisosteus acaulatus ins* sequences were used as outgroups. [b]: Test for selection intensification was significant. [c]: Test for selection relaxation was significant.

Processing of proinsulin sequences

To be functional, the protein product encoded by insulin genes need to be proteolytically processed and secreted to generate two-peptide chain insulin molecules (Steiner et al., 1996, 2009). Our analysis was initially only focused on sequences that showed similarity to previously characterized proinsulin sequences and had intact coding sequences, i.e., had an initiation codon, a termination codon and intact open reading frame with greater similarity to proinsulin than to other insulin-like sequences (e.g., insulin-like growth factors). To determine whether the encoded protein sequences could be secreted and properly processed I searched for potential signal peptidases and proprotein processing sites using programs that predict these sites (Duckert et al., 2004; Petersen et al., 2011; Southey et al., 2006).

The coding sequences of intact proinsulin open reading frames from all ray-finned fish identified here are predicted to have functional signal peptides (Table 3 and Supplementary Table S3 and Figure S6), thus should be able to be secreted. In addition, all of the proinsulin protein sequences encoded by the *insa*, *insab*, *insb*, and *insc* genes have potential prohormone protease cleavage sites that could yield typical two-chain insulin hormone molecules (Table 3 and Supplementary Table S3 and Figure S6). In contrast, however, only one of the 14 proteins encoded by *insab* genes is predicted to potentially produce a two-chain insulin (Table 3). For the insab sequences, only 2 have potential B-chain/C-peptide processing site and 9 have potential C-peptide/A-chain processing sites (Table 3 and Supplementary Table S3 and Figure S6), indicating that neither site is conserved. Both NeuroPred (Southey et al., 2006) and ProP (Duckert et al., 2004) predicted similar sites, but ProP also provided a list of other potential processing sites that did not score well enough to be predicted sites (see Supplementary Table S3). The alternative potential sites identified by ProP in the insab proteins still would not generate 2-chain insulin molecules similar to functionally characterized insulin molecules (Steiner et al., 1996, 2009) as they would generate very short B-chains, often missing residues essential for function.

Table 3 Secretion and processing of fish proinsulin proteins

Gene	Signal peptide[a]	B-C junction[b]	C-A junction[b]	2-chain insulin[c]
insa	35/35[d]	35/35	35/35	35/35
insaa	32/32	32/32	32/32	32/32
insab	14/14	2/14	9/14	1/14
insb	45/45	44/45	45/45	44/45
insc	10/10	10/10	10/10	10/10

[a]: Sequences with signal peptidase processing sites. [b]: Sequences with proprotein processing sites for the B-chain/C-peptide and C-peptide/A-chain processing sites. [c]: Number that can be secreted and properly processed to yield two-chain polypeptides. [d]: Number with the site/total number of sequences.

The hormone insulin is a two-chain peptide molecule held together by disulfide bridges (Steiner et al., 1996, 2009). To confirm that two-chain molecules could be produced from the proinsulin protein sequences I generated consensus sequences for the A- and B-chains for the different types of insulins (Figure 4). The lengths of the predicted A- and B-chains were similar between the different types of insulins, with more variation, at both the N- and C-termini, within proteins encoded by a type of gene than between types of genes (Figure 4 and Supplementary Figure S6). When cysteine residues were examined one of the two insc sequences from *Sinocyclocheilus grahami* (*insc2*) had a cystine replaced by an arginine residue. It is possible that the *S. graham insc2* gene does not encode a functional insulin, but this is compensated by the presence of an *insc1* gene that encodes an insulin that can be secreted processed and has all six cysteine residues. Surprisingly, when I examined A- and B-chain sequences homologous to those of other insulins in the protein encoded by *insab* genes, all of the cysteine residues were perfectly conserved, however much of the rest of the sequence showed greater variation than within other types of insulins (Figure 4 and Supplementary Figure S6). This raises the possibility that insab could still fold in a similar fashion as typical insulin, thus be transported to insulin secretory granules, but then not be processed into an active hormone (Liu et al., 2015).

DISCUSSION

Searches of diverse fish genomes, including in the extensively characterized zebrafish (*Danio rerio*) genome, unexpectedly revealed the existence of three insulin gene paralogs (Figure 1 and Supplementary Figure S1 and Table S1). Previously, two paralogous insulin genes, *insa* and *insb*, had been found in the zebrafish genome that have distinct expression patterns (Irwin, 2004; Papasani et al., 2006). Here I found *insa* genes in the genomes of all teleost fish (Figure 1 and Supplementary Figure S1 and Table S1), which encode the previously isolated insulin hormone sequences (Caruso & Sheridan, 2011; Conlon, 2000b) that regulate glucose metabolism. Given the central role of insulin in the regulation of metabolism (Caruso & Sheridan, 2011; Röder et al., 2016; Weiss, 2009), it is not surprising that this gene was found in all fish. The presence of a high selective constraint (Tables 1, 2) on the protein sequences encoded by *insa* and *insaa* genes supports the conclusion that this sequence is essential. A surprising discovery was the presence of a duplicate of the *insa* gene, the *insaa* and *insab* genes, in a large number of teleost fish (Figure 1 and Supplementary Table S1). The protein coding sequence encoded by *insab* genes have the highest nonsynonymous substitution rate (Table 2), and thus least selective constraint, yet the consensus sequences of the potential A- and B-chains of insulin predicted from these genes have perfectly conserved cystine residues (Figure 4). This suggests that these genes might encode proinsulin-like proteins that could properly fold but would not be properly processed in secretory granules to produce active insulin molecules (Liu et al., 2015). Thus, insab proteins might compete with insaa proteins for processing enzymes and modulate the release of functional insulin molecules in these species.
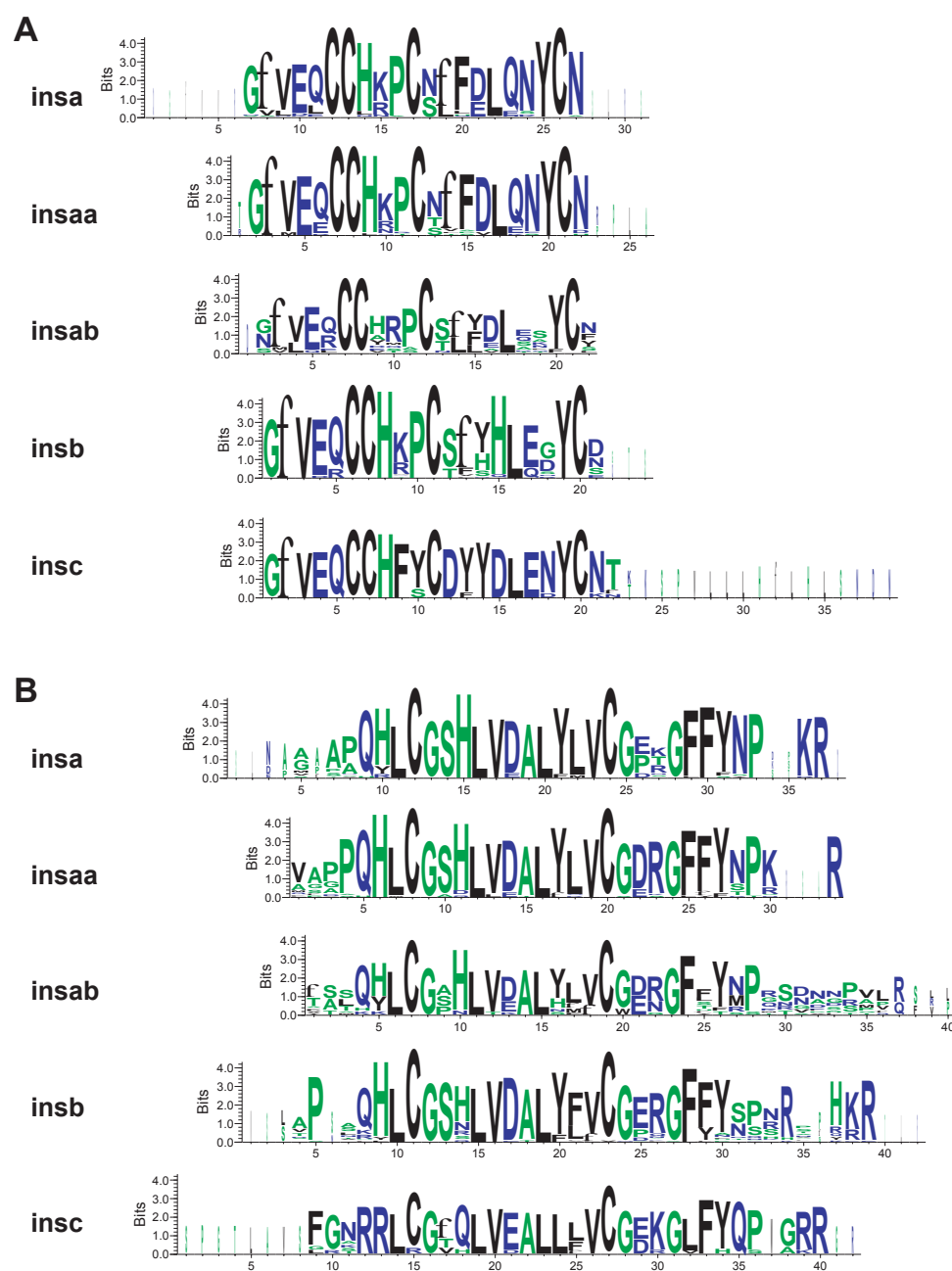
Figure 4 Consensus fish insulin peptide sequences

Consensus sequences for the A-chain (A) and B-chain peptides (B) for insulin encoded by *insa*, *insaa*, *insab*, *insb*, and *insc* genes. Consensus sequences were generated from aligned predicted protein sequences (see Supplementary Figure S5) of genes with complete open reading frames (*Larimichthys crocea insa2* was removed as it may not be functional). Hight of the residue is proportional to representation among the compared sequences, while residue width represents proportion of sequences without a gap (thin residues are gaps in many sequences).

The *insb* gene was found in the genomes of almost all teleost fish species examined, demonstrating that it is conserved in these fish (Figure 1 and Supplementary Figure S1 and Table S1). The selective forces acting on *insb* are weaker than those acting on *insa* (Table 1) suggesting that these two genes have different functions. Previous work indicates

that *insb* is not appreciably expressed in the pancreas, and instead is more predominantly expressed in early development (Hrytsenko et al., 2016; Irwin, 2004; Papasani et al., 2006). The analysis of selective constraints and these expression results are consistent with speculation that *insb* is not primarily involved in the regulation of blood glucose level, but instead has a role in development (Hrytsenko et al., 2016; Papasani et al., 2006). Given the conservation of the *insb* gene across teleost fish, it likely acquired this role soon after its origin and has been conserved.

Unexpectedly I found an *insc* paralog, and it was present in the well characterized zebrafish (*D. rerio*) genome (Figure 1 and Supplementary Figure S1 and Table S1). Upon closer examination, the *insc* gene in both the Ensembl (gene ID: ENSDARG00000096862) and NCBI (GenBank accession No.: 100534937) zebrafish genomes fail to predict an intact open reading frame, with the intact *insc* coding sequence only coming from the linked mRNA sequence (XM_009299616.3) in the NCBI database (see Supplementary Table S1). I could find no raw sequence data (e.g., ESTs) that supports the existence of an intact open reading frame for zebrafish *insc*, as all mRNA derived sequences (GenBank accession Nos. EH533807.1 and EH507658.1, forward and reverse sequences of the same EST clone) also contained the deletion found in the genomic sequence. This suggests that the zebrafish *insc* gene does not encode an intact protein product. However, our analysis of the selective forces acting upon the *insc* coding sequences indicate that the nonsynonymous rate of substitutions (d_N) is much lower than the rate of synonymous substitutions (d_S) consistent with selection to maintain a protein coding sequence (Table 1) in most, if not all, species that have intact *insc* genes. The *insc* gene, in contrast to *insa* and *insb*, is restricted to the genomes of only a few lineages, with this gene been lost from the genome of most teleost fish (Figure 1 and Supplementary Table S1). This distribution of the gene among fish suggests that it does not encode a function that is essential in most species, and its loss might have been compensated by the presence of paralogs of insulin in the fish genomes. Expression of *insc*, based on a single EST clone (with sequences from both ends) that was identified in zebrafish, is found in the "gut and internal organs" of adults, thus potentially it could be expressed in the pancreas and be replaced by *insa*. Further studies on the expression of *insc* in other fish are needed to identify its role in physiology.

CONCLUSION

Searches of ray-finned fish genomes have demonstrated that they contain more insulin genes than previously appreciated and suggest that the roles of these genes have diversified. The diversification of the functions of insulin parallels the diversification of the proglucagon-encoded peptides found in fish (Irwin & Mojsov, 2018). Similarly, parallel changes in the biological functions of insulin and proglucagon-derived peptides have been observed in hystricomorph rodents (i.e., guinea pig and relatives), where changes in sequence and action of insulin have compensating changes in glucagon

(Seino et al., 1988).

REFERENCES

Betancur-R R, Wiley EO, Arratia G, Acero A, Bailly N, Miya M, Lecointre G, Ortí G. 2017. Phylogenetic classification of bony fishes. *BMC Evolutionary Biology*, **17**(1): 162.

Caruso MA, Sheridan MA. 2011. New insights into the signaling system and function of insulin in fish. *General and Comparative Endocrinology*, **173**(2): 227–247.

Caruso MA, Sheridan MA. 2014. Differential regulation of the multiple insulin and insulin receptor mRNAs by somatostatin. *Molecular and Cellular Endocrinology*, **384**(1–2): 126–133.

Caruso MA, Kittilson JD, Raine J, Sheridan MA. 2008. Rainbow trout (*Oncorhynchus mykiss*) possess two insulin-encoding mRNAs that are differentially expressed. *General and Comparative Endocrinology*, **155**(3): 695–704.

Chan SJ, Steiner DF. 2000. Insulin through the ages: Phylogeny of a growth promoting and metabolic regulatory hormone. *American Zoologist*, **40**(2): 213–222.

Conlon JM. 2000a. Singular contributions of fish neuroendocrinology to mammalian regulatory peptide research. *Regulatory Peptides*, **93**(1–3): 3–12.

Conlon JM. 2000b. Molecular evolution of insulin in non-mammalian vertebrates. *American Zoologist*, **40**(2): 200–212.

Conlon JM. 2001. Evolution of the insulin molecule: insights into structure-activity and phylogenetic relationships. *Peptides*, **22**(7): 1183–1193.

Crooks GE, Hon G, Chandonia JM, Brenner SE. 2004. WebLogo: A sequence logo generator. *Genome Research*, **14**(6): 1188–1190.

Duckert P, Brunak S, Blom N. 2004. Prediction of proprotein convertase cleavage sites. *Protein Engineering, Design and Selection*, **17**(1): 107–112.

Gertz EM, Yu YK, Agarwala R, Schäffer AA, Altschul SF. 2006. Composition-based statistics and translated nucleotide searches: improving the TBLASTN module of BLAST. *BMC Biology*, **4**: 41.

Glasauer SM, Neuhauss SCF. 2014. Whole-genome duplication in teleost fishes and its evolutionary consequences. *Molecular Genetics and Genomics*, **289**(6): 1045–1060.

Guindon S, Dufayard JF, Lefort V, Anisimova M, Hordijk W, Gascuel O. 2010. New algorithms and methods to estimate maximum-likelihood phylogenies: assessing the performance of PhyML 3.0. *Systematic Biology*, **59**(3): 307–321.

Hernández-Sánchez C, Mansilla A, de la Rosa EJ, de Pablo F. 2006. Proinsulin in development: New roles for an ancient prohormone. *Diabetologia*, **49**(6): 1142–1150.

Hrytsenko O, Pohajdak B, Wright JR, Jr. 2016. Ancestral genomic duplication

of the insulin gene in tilapia: An analysis of possible implications for clinical islet xenotransplantation using donor islets from transgenic tilapia expressing a humanized insulin gene. *Islets*, **8**(4): e1187352.

Huelsenbeck JP, Ronquist F, Nielsen R, Bollback JP. 2001. Bayesian inference of phylogeny and its impact on evolutionary biology. *Science*, **294**(5550): 2310–2314.

Irwin DM. 2002. Ancient duplications of the human proglucagon gene. *Genomics*, **79**(5): 741–746.

Irwin DM. 2004. A second insulin gene in fish genomes. *General and Comparative Endocrinology*, **135**(1): 150–158.

Irwin DM. 2012. Origin and convergent evolution of exendin genes. *General and Comparative Endocrinology*, **175**(1): 27–33.

Irwin DM. 2014. Evolution of receptors for peptides similar to glucagon. *General and Comparative Endocrinology*, **209**: 50–60.

Irwin DM, Mojsov S. 2018. Diversification of the functions of proglucagon and glucagon receptor genes in fish. *General and Comparative Endocrinology*, **261**(5): 148–165.

Katoh K, Misawa K, Kuma K, Miyata T. 2001. MAFFT: a novel method for rapid multiple sequence alignment based on fast Fourier transform. *Nucleic Acids Research*, **30**(14): 3059–3066.

Kuraku S, Meyer A. 2012. Detection and phylogenetic assessment of conserved synteny derived from whole genome duplications. *Methods in Molecular Biology*, **855**: 385–395.

Kurokawa T, Uji S, Suzuki T. 2005. Identification of cDNA coding for a homologue to mammalian leptin from pufferfish, *Takifugu rubripes. Peptides*, **26**(5): 745–750.

Lefort V, Longueville JE, Gascuel O. 2017. SMS: Smart Model Selection in PhyML. *Molecular Biology and Evolution*, **34**(9): 2422–2424.

Lien S, Koop BF, Sandve SR, Miller JR, Kent MP, Nome T, Hvidsten TR, Leong JS, Minkley DR, Zimin A, Grammes F, Grove H, Gjuvsland A, Walenz B, Hermansen RA, von Schalburg K, Rondeau EB, Di Genova A, Samy JK, Olav Vik J, Vigeland MD, Caler L, Grimholt U, Jentoft S, Våge DI, de Jong P, Moen T, Baranski M, Palti Y, Smith DR, Yorke JA, Nederbragt AJ, Tooming-Klunderud A, Jakobsen KS, Jiang X, Fan D, Hu Y, Liberles DA, Vidal R, Iturra P, Jones SJ, Jonassen I, Maass A, Omholt SW, Davidson WS. 2016. The Atlantic salmon genome provides insights into rediploidization. *Nature*, **533**(7602): 200–205.

Lieschke GJ, Currie PD. 2007. Animal models of human disease: zebrafish swim into view. *Nature Reviews Genetics*, **8**(5): 353–367.

Liu M, Sun J, Cui J, Chen W, Guo H, Barbetti F, Arvan P. 2015. INS-gene mutations: from genetics and beta cell biology to clinical disease. *Molecular Aspects of Medicine*, **42**: 3–18.

Long M, VanKuren NW, Chen S, Vibranovski MD. 2013. New gene evolution: little did we know. *Annual Review of Genetics*, **47**: 307–333.

MacRae CA, Peterson RT. 2015. Zebrafish as tools for drug discovery. *Nature Reviews Drug Discovery*, **14**(10): 721–731.

Meyer A, Van de Peer Y. 2005. From 2R to 3R: evidence for a fish-specific genome duplication (FSGD). *Bioessays*, **27**(9): 937–945.

Milewski WM, Dugay SJ, Chan SJ, Steiner DF. 1988. Conservation of PDX-1 structure, function and expression in zebrafish. *Endocrinology*, **139**(3): 1440–1449.

Near TJ, Eytan RI, Dornburg A, Kuhn KL, Moore JA, Davis MP, Wainwright PC, Friedman M, Smith WL. 2012. Resolution of ray-finned fish phylogeny and timing of diversification. *Proceedings of the National Academy of Sciences of the United States of America*, **109**(34): 13698–13703.

Nishi M, Nanjo K. 2011. Insulin gene mutations and diabetes. *Journal of Diabetes Investigation*, **2**(2): 92–100.

Papasani MR, Robison BD, Hardy RW, Hill RA. 2006. Early developmental expression of two insulins in zebrafish (*Danio rerio*). *Physiological Genomics*, **27**(1): 79–85.

Patton SJ, Luke GN, Holland PW. 1998. Complex history of a chromosomal paralogy region: insights from amphioxus aromatic amino acid hydroxylase genes and insulin-related genes. *Molecular Biology and Evolution*, **15**(11): 1373–1380.

Penn O, Privman E, Ashkenazy H, Landan G, Graur D, Pupko T. 2010. GUIDANCE: a web server for assessing alignment confidence scores. *Nucleic Acids Research*, **38**(14): W23–28.

Petersen TN, Brunak S, von Heijne G, Nielsen H. 2011. SignalP 4.0: discriminating signal peptides from transmembrane regions. *Nature Methods*, **8**(10): 785–786.

Polakof S, Panserat S, Soengas JL, Moon TW. 2012. Glucose metabolism in fish: a review. *Journal of Comparative Physiology*, **182**(8): 1015–1045.

Ravi V, Venkatesh B. 2018. The divergent genomes of teleosts. *Annual Review of Animal Bioscience*, **6**: 47–68.

Röder PV, Wu B, Liu Y, Han W. 2016. Pancreatic regulation of glucose homeostasis. *Experimental & Molecular Medicine*, **48**: e219.

Ronquist F, Teslenko M, van der Mark P, Ayres DL, Darling A, Höhna S, Larget B, Liu L, Suchard MA, Huelsenbeck JP. 2012. MrBayes 3.2: efficient Bayesian phylogenetic inference and model choice across a large model space. *Systematic Biology*, **61**(3): 539–542.

Seino S, Blackstone CD, Chan SJ, Whittaker J, Bell GI, Steiner DF. 1988. Appalachian spring: variations on ancient gastro-entero-pancreatic themes in New World mammals. *Hormone and Metabolic Research*, **20**(7): 430–435.

Shiao MS, Liao BY, Long M, Yu HT. 2008. Adaptive evolution of the insulin two-gene system in mouse. *Genetics*, **178**(3): 1683–1691.

Sievers F, Wilm A, Dineen D, Gibson TJ, Karplus K, Li W, Lopez R, McWilliam H, Remmert M, Söding J, Thompson JD, Higgins DG. 2011. Fast, scalable generation of high-quality protein multiple sequence alignments using Clustal Omega. *Molecular Systems Biology*, **7**: 539.

Smith MD, Wertheim JO, Weaver S, Murrell B, Scheffler K, Kosakovsky Pond SL. 2015. Less is more: an adaptive branch-site random effects model for efficient detection of episodic diversifying selection. *Molecular Biology and Evolution*, **32**(5): 1342–1353.

Soares MB, Schon E, Henderson A, Karathanasis SK, Cate R, Zeitlin S, Chirgwin J, Efstratiadis A. 1985. RNA-mediated gene duplication: the rat preproinsulin I gene is a functional retroposon. *Molecular and Cellular Biology*, **5**(8): 2090–2103.

Southey BR, Amare A, Zimmerman TA, Rodriguez-Zas SL, Sweedler JV. 2006. NeuroPred: a tool to predict cleavage sites in neuropeptide precursors and provide the masses of the resulting peptides. *Nucleic Acids Research*, **34**(Web Server issue): W267–272.

Steiner DF, Chan SJ, Welsh JM, Kwok SC. 1985. Structure and evolution of the insulin gene. *Annual Reviews Genetics*, **19**: 463–484.

Steiner DF, Rouillé Y, Gong Q, Martin S, Carroll R, Chan SJ. 1996.

The role of prohormone convertases in insulin biosynthesis: evidence for inherited defects in their action in man and experimental animals. *Diabetes & Metabolism*, **22**(2): 94–104.

Steiner DF, Park SY, Støy J, Philipson LH, Bell GI. 2009. A brief perspective on insulin production. *Diabetes, Obesity and Metabolism*, **11**(S4): 189–196.

Weaver S, Shank SD, Spielman SJ, Li M, Muse SV, Kosakovsky Pond SL. 2018. Datamonkey 2.0: a modern web application for characterizing selective and other evolutionary processes. *Molecular Biology and Evolution*, **35**(3): 773–777.

Weiss MA. 2009. Proinsulin and the genetics of diabetes mellitus. *Journal of Biological Chemistry*, **284**(29): 19159–19163.

Wentworth BM, Schaefer IM, Villa-Komaroff L, Chirgwin JM. 1986. Characterization of the two nonallelic genes encoding mouse preproinsulin. *Journal of Molecular Evolution*, **23**(4):305–312.

Wertheim JO, Murrell B, Smith MD, Kosakovsky Pond SL, Scheffler K. 2014. RELAX: detecting relaxed selection in a phylogenetic framework. *Molecular Biology and Evolution*, **32**(3): 820–832.

Wright JR Jr, Yang H, Hyrtsenko O, Xu BY, Yu W, Pohajdak B. 2014. A review of piscine islet xenotransplantation using wild-type tilapia donors and the production of transgenic tilapia expressing a "humanized" tilapia insulin. *Xenotransplantation*, **21**(6): 485–495.

Xu P, Zhang X, Wang X, Li J, Liu G, Kuang Y, Xu J, Zheng X, Ren L, Wang G, Zhang Y, Huo L, Zhao Z, Cao D, Lu C, Li C, Zhou Y, Liu Z, Fan Z, Shan G, Li X, Wu S, Song L, Hou G, Jiang Y, Jeney Z, Yu D, Wang L, Shao C, Song L, Sun J, Ji P, Wang J, Li Q, Xu L, Sun F, Feng J, Wang C, Wang S, Wang B, Li Y, Zhu Y, Xue W, Zhao L, Wang J, Gu Y, Lv W, Wu K, Xiao J, Wu J, Zhang Z, Yu J, Sun X. 2014. Genome sequence and genetic diversity of the common carp, *Cyprinus carpio*. *Nature Genetics*, **46**(11): 1212–2129.

Yang J, Chen X, Bai J, Fang D, Qiu Y, Jiang W, Yuan H, Bian C, Lu J, He S, Pan X, Zhang Y, Wang X, You X, Wang Y, Sun Y, Mao D, Liu Y, Fan G, Zhang H, Chen X, Zhang X, Zheng L, Wang J, Cheng L, Chen J, Ruan Z, Li J, Yu H, Peng C, Ma X, Xu J, He Y, Xu Z, Xu P, Wang J, Yang H, Wang J, Whitten T, Xu X, Shi Q. 2016. The *Sinocyclocheilus* cavefish genome provides insights into cave adaptation. *BMC Biology*, **14**: 1.

Yang Z, Bielawski JP. 2000. Statistical methods for detecting molecular adaptation. *Trends in Ecology and Evolution*, **15**(12): 496–503.

Effects of C-terminal amidation and heptapeptide ring on the biological activities and advanced structure of amurin-9KY, a novel antimicrobial peptide identified from the brown frog, *Rana kunyuensis*

Fen Zhang[1,#], Zhi-Lai Guo[3,#], Yan Chen[1], Li Li[3], Hai-Ning Yu[2,*], Yi-Peng Wang[1,*]

[1] *Department of Pharmaceutical Sciences, College of Pharmaceutical Sciences, Soochow University, Suzhou Jiangsu* 215123, *China*
[2] *Department of Bioscience and Biotechnology, Dalian University of Technology, Dalian Liaoning* 116023, *China*
[3] *School of Life Sciences, Guizhou Normal University, Guiyang Guizhou* 550001, *China*

ABSTRACT

Rana kunyuensis is a species of brown frog that lives exclusively on Kunyu Mountain, Yantai, China. In the current study, a 279-bp cDNA sequence encoding a novel antimicrobial peptide (AMP), designated as amurin-9KY, was cloned from synthesized double-strand skin cDNA of *R. kunyuensis*. The amurin-9KY precursor was composed of 62 amino acid (aa) residues, whereas the mature peptide was composed of 14 aa and contained two cysteines forming a C-terminal heptapeptide ring (Rana box domain) and an amidated C-terminus. These structural characters represent a novel amphibian AMP family. Although amurin-9KY exhibited high similarity to the already identified amurin-9AM from *R. amurensis*, little is known about the structures and activities of amurin-9 family AMPs so far. Therefore, amurin-9KY and its three derivatives (amurin-9KY1–3) were designed and synthesized. The structures and activities were examined to evaluate the influence of C-terminal amidation and the heptapeptide ring on the activities and structure of amurin-9KY. Results indicated that C-terminal amidation was essential for antimicrobial activity, whereas both C-terminal amidation and the heptapeptide ring played roles in the low hemolytic activity. Circular dichroism (CD) spectra showed that the four peptides adopted an α-helical conformation in THF/H$_2$O (v/v 1:1) solution, but a random coil in aqueous solution. Elimination of the C-terminal heptapeptide ring generated two free cysteine residues with unpaired thiol groups, which greatly increased the concentration-dependent anti-oxidant activity. Scanning electron microscopy (SEM) was also performed to determine the possible bactericidal mechanisms.

INTRODUCTION

Antimicrobial peptides (AMPs), which are small, cationic and amphipathic peptides widely distributed throughout organisms, are evolutionarily ancient weapons against environmental pathogens (Zasloff, 2002). They are important components of innate immune systems and play key roles in the anti-infective immune responses of organisms (Radek & Gallo, 2007). According to previous studies, AMPs possess strong and diverse antimicrobial activities against bacteria, fungi, viruses and even

protozoa. The activities and specificities of AMPs can be affected by various factors such as molecular weight, sequence, charge, conformation, hydrophobicity and amphipathicity (Brogden, 2005). The antimicrobial mechanisms are diverse among different AMPs. However, most AMPs are thought to function by forming pores in the membranes of target microorganisms, ultimately leading to disruption of cellular integrity (Nicolas, 2009).

Frogs belonging to the family Ranidae are widely distributed around the world, except for the Polar Regions, southern South America and most of Australia (Conlon et al., 2004). So far, 347 ranid species have been identified worldwide, with most living in moist environments surrounded by diverse pathogens. As a result, they are continuously threatened by pathogenic invasions and have therefore evolved effective immune systems (Conlon et al., 2004; Zasloff, 2002). Among these systems, AMPs play key roles in the anti-infective immune response of ranid frogs (Kreil, 1994). To date, hundreds of AMPs have been characterized from various ranid species. According to their primary structures, they are divided into dozens of different families, including gaegurins, brevinins (1 and 2), ranalexins, ranatuerins (1 and 2), esculentins (1 and 2), palustrins, japonicins (1 and 2), nigrocin-2, tigerinins, temporins and odorranains (A–W) (Conlon, 2004; Duda et al., 2002; He et al., 2012; Li et al., 2007; Matutte et al., 2000).

Brown frogs, also known as wood frogs, are a group of ranid species belonging to *Rana*. Currently, there are 14 recognized brown frogs in China distributed in 30 provinces. *Rana kunyuensis*, an endemic brown frog species in China, exclusively lives on Kunyu Mountain, Yantai, Shandong Province. In the present study, we identified a novel AMP family member, named amurin-9KY, from the skin secretions of *R. kunyuensis*. The structure-function relationship of amurin-9KY was clarified to establish the effect of C-terminal amidation and the heptapeptide ring on the biological activities and advanced structures of amphibian AMPs.

MATERIALS AND METHODS

Frog collection
Adult specimens of *R. kunyuensis* (*n*=5, weight range 5–10 g) were captured on Kunyu Mountain, Yantai, Shandong Province, China. The frogs were housed in plastic box and fed with yellow mealworms in the lab for one week until the experiment.

Total RNA extraction, cDNA synthesis and amurin-9KY-encoding cDNA screening
An individual frog (female, 8 g) was washed with distilled water twice and anaesthetized with ice before being euthanized with a needle. The dorsal skin was quickly removed with a small pair of scissors and placed into a pre-cooling homogenizer. The skin was then immediately homogenized into powder in liquid nitrogen and mixed with Trizol reagent (Invitrogen, CA, USA). The subsequent procedures were carried out according to the manufacturer's instructions and the extracted total RNA was preserved in liquid nitrogen until use. All animal experimental protocols in the present study were approved by the Animal Care and Use Ethics Committee of Soochow University.

Double-strand cDNA was synthesized using an In-Fusion SMARTer™ Directional cDNA Library Construction Kit (Clontech, USA). The primers used for first strand synthesis were 3′ In-Fusion SMARTer CDS Primer, 5′-CGGGGTACG ATGAGACACCA(T)$_{20}$VN-3′ (N=A, C, G, or T; V=A, G, or C) and SMARTer V Oligonucleotide, 5′-AAGCAGTGGTATCAA CGCAGAGTACXXXXX-3′ (X=undisclosed base in the proprietary SMARTer oligo sequence). The enzyme used for first strand synthesis was SMARTScribe™ Reverse Transcriptase and was supplied by the kit. The second strand was amplified by 50× Advantage 2 Polymerase Mix using 5′ PCR Primer II A and 3′ In-Fusion SMARTer PCR Primer, 5′-CGGGGTACGATGAGACACCA-3′. The synthesized double-strand cDNA was stored at –80 °C until use.

The synthesized double-strand cDNA was used as a template to screen the cDNAs encoding the AMPs of *R. kunyuensis*. A sense degenerate oligonucleotide primer (RanaAMP, 5′-CCAAAGATGTTSMCCWYGAAG-3′, M=A or C; W=A or T; Y=C or T), designed according to the conserved signal peptide domain sequences of previously characterized AMPs from the skin of ranid frogs, and a 3′-antisense primer (3′-PCR, 5′-CGGGGTACGATGAGACACCAT-3′) were used for PCR analysis. The PCR procedure was as follows: 4 min of denaturation at 95 °C; 30 cycles: denaturation at 95 °C for 30 s, annealing at 57 °C for 30 s, extension at 72 °C for 1 min; final extension at 72 °C for 10 min. The PCR product was purified by agarose gel electrophoresis, cloned into pMD™19-T vector (Takara, Dalian, China) and transformed into *E. coli* for sequencing.

Peptide synthesis
Amurin-9KY and its derivatives (amurin-9KY1–3) were chemically synthesized on an Applied Biosystems model 433A peptide synthesizer (ABI, USA) according to the manufacturer's standard protocols. The crude peptides were purified by reversed-phase high performance liquid chromatography (RP-HPLC) to a final purity higher than 95% and their identities were confirmed by automated Edman degradation and matrix-assisted laser desorption/ionization–time-of-flight mass spectrometry (MALDI-TOF-MS). The intra-peptide disulfide bridge and N-terminal amidation were accurately formed in the synthesis process.

Antimicrobial assay
In total, eight microbial strains, including gram-positive bacteria, gram-negative bacteria and fungi, were used for the antimicrobial assay. The assays included inhibition zone examination and minimum inhibitory concentration (MIC) determination and were conducted as described in our previous papers (He et al., 2012; Lu et al., 2010). Briefly, microbes were inoculated in Mueller-Hinton broth (MH) and incubated at 37 °C to the exponential phase. The inoculum was then diluted with fresh MH broth to 10^6 CFU/mL, and 50-μL bacterial dilutions were mixed with serial dilutions of peptides (50 μL) in 96-well microtiter plates. The plates were incubated at 37 °C for 18 h and the minimum concentrations at which no visible growth of bacteria occurred were recorded as MIC values.

Hemolytic assay

Hemolytic assay was conducted as previously reported (Wang et al., 2011). Fresh human erythrocytes were collected from a healthy donor and washed with 0.9% saline. The erythrocytes were re-suspended with 0.9% saline and incubated with serial peptide dilutions at 37 °C for 30 min. The mixtures were then centrifuged at 2 000 r/min at room temperature for 5 min, after which the supernatants were removed and their absorbance was measured at 540 nm. We used 1% (v/v) Triton X-100 to determine the 100% hemolysis, with 0.9% saline used as the negative control.

Anti-oxidant assay

As a stable nitrogen radical, 2, 2-diphenyl-1-picrylhydrazyl (DPPH, Sigma, USA) has been widely used to examine the anti-oxidant activities of biological samples, drugs and foods. In the present study, the DPPH radical scavenging activities of the peptides were determined according to our previously described method (Zhang et al., 2012). Briefly, 92 μL of 6×10^{-5} mol/L DPPH radical dissolved in methanol was mixed with 8 μL of peptide solution (2 mg/mL, mass ratio of peptide to DPPH of ~3:1). The mixture was kept in the dark for 30 min at room temperature and then the amount of reduced DPPH was quantified by measuring the decrease in absorbance at 520 nm. The DPPH radical scavenging percentage (S%) of the peptides was calculated according to the formula: $S\% = (A_{blank} - A_{sample}) \times 100/A_{blank}$. Deionized water was used as the negative control.

Circular dichroism (CD) spectroscopy

To investigate the secondary structure of amurin-9KY and its derivatives (amurin-9KY1–3), CD spectroscopy was performed using a Jasco J-810 spectrophotometer (JASCO, Japan). Samples with a constant peptide concentration of 0.12 mg/mL were prepared in two different solvents, i.e., water and 50% (v/v) trifluoroethanol (TFE)-water, and added to a quartz optical cell with a path length of 0.1 cm at 25 °C. The spectra were averaged over three consecutive scans, followed by subtraction of the CD signal of the solvent.

Scanning electron microscopy (SEM)

The surface morphologies of the AMP-treated microbes were observed by SEM, which can partly reveal the antimicrobial mechanisms of AMPs. In the present study, *S. aureus* ATCC25923 was used to evaluate the potential antimicrobial mechanism of amurin-9KY. The experiment was carried out according to the method described by Lu et al. (2010). The concentration of amurin-9KY used in the experiment was 1×MIC. The treatment conditions of the bacterial and amurin-9KY mixture were 37 °C for 30 min. After that, samples were prepared, and photographs were taken. Ampicillin was used as the positive control in the experiment.

RESULTS

cDNA cloning and characterization of amurin-9KY

A 279-bp cDNA sequence (GenBank accession No.: JX421759) encoding a 62-aa precursor was cloned from the constructed skin cDNA library of *R. kunyuensis*. The nucleotide sequence of the cDNA and the deduced amino acid sequence are shown in Figure 1. To confirm the existence and accuracy of the cloned cDNA sequence, two antisense specific primers, that is, RKAMP-R1 (5′-GCCAAGACACCCGATGTGTATTTAG-3′) and RKAMP-R2 (5′-CCCTTTTCCACATTTTCTGGTAATT-3′), were designed according to the cloned cDNA sequence and coupled with the sense specific primer RanaAMP for PCR (synthesized skin cDNA library of *R. kunyuensis* was used as a template). The PCR products were sequenced and verified the identity of the cDNA sequence above (data not shown).

```
atgttcaccttgaagaaatccctgttgcttcttttcttccttgggatcatcaacgtatct   60
 M  F  T  L  K  K  S  L  L  L  L  L  F  F  L  G  I  I  N  V  S   20
ctctgtgaggaagagagaaatgccgaggaagaaagaagagatgatcccgaagaaagggcc  120
 L  C  E  E  E  R  N  A  E  E  E  R  R  D  D  P  E  E  R  A     40
gttgaggtggaaaaagatttttaccattttttgcagcatgtgcaattaccagaaaatgt   180
 V  E  V  E  K  R [ F  L  P  F  F  A  A  C  A  I  T  R  K  C    60
ggaaaatgattttctaaatacacatcgggtgtcttataaaaaataaagatgaagcctac  240
 G  K ] *                                                       62
aaaaaaaaaaaaaaaaaaaaaaaaaaaaaaaaaaaaaaaaaaa                    279
```

Figure 1 Nucleic acid sequence of cDNA encoding the precursor of amurin-9KY

The signal peptide domain is indicated in italics, the putative mature peptide is boxed and the stop codon is indicated by an asterisk (*).

The 62-aa AMP precursor deduced from the cDNA sequence included an N-terminal signal peptide domain of 22 aa, an acidic amino acid residue-rich (Asp and Glu) spacer peptide domain and a mature peptide domain of 16 aa residues. There was a conserved dibasic cleavage site Lys-Arg (K-R) between the spacer peptide domain and mature peptide domain, which was likely cleaved by trypsin-like proteases followed by mature peptide release. Sequence alignment of the mature peptide with the NCBI protein database revealed that it possessed highest primary structure similarity with amurin-9AM (GenBank accession No.: AEP84587). Hence, it was designated amurin-9KY according to the origin of *R. kunyuensis*.

Amurin-9KY was also found to possess high sequence similarity to the temporin AMP family, especially the C-terminal Gly-Lys (G-K) di-residue, which is regarded as an amidation site (Figure 2). However, unlike the temporin family, amurin-9KY exhibited two cysteine residues forming an intra-molecular disulfide bridge, which appeared as a C-terminal heptapeptide ring (Rana box domain). The physical and chemical parameters of amurin-9KY were computed by ProtParam (http://web.expasy.org/protparam/), demonstrating a molecular weight of 1 584.97, theoretical pI of 8.96 and net charge of +2.

To evaluate the influence of C-terminal amidation and the heptapeptide ring on the biological activities of the peptide *in vitro*, three derivatives (amurin-9KY1–3) were designed and chemically synthesized, with their biological functions then examined (Table 1).

Antimicrobial and hemolytic assays

As listed in Table 2, amurin-9KY was active against the tested

gram-positive bacteria *S. aureus* ATCC25923, S. *aureus* 090223+ (IS) and *N. asteroids* 090312+ (IS), and showed the strongest potency against *S. aureus* ATCC25923, with an MIC of 4.68 μg/mL. However, amurin-9KY did not show any antimicrobial activity against the tested gram-negative bacteria or fungi, consistent with the features of the temporin family (Conlon, 2004). The derivative amurin-9KY1 exhibited less potent activities against all three gram-positive bacteria. Interestingly, unlike amurin-9KY, amurin-9KY1 was able to kill the eukaryotic microbe *Slime mold* 090413 (IS) with an MIC value of 75 μg/mL. However, derivatives amurin-9KY2 and amurin-9KY3 exhibited no activities against any of the tested microbes.

The hemolytic activities of amurin-9KY and the three derivatives were also examined. All four peptides showed slight hemolytic activity against fresh human erythrocytes at concentrations of 100 μg/mL, with hemolytic rates of 2%, 15.4%, 17.9% and 20.8%, respectively.

Kunyuenin	--FLPFFAACAITRKCGK	16	*R. kunyuensis*
Temporin-SHe	FLPALAGIAGLLGKIFGK	18	*R. saharica*
Temporin-LTd	---FLPGLIAGIAKMLGK	15	*R. latouchii*
Temporin-1Ja	---ILPLVGNLLNDLLGK	15	*R. japonica*
Temporin-1V	---FLPLVGKILSGLIGK	15	*R. versabilis*
Temporin-G	---FFPVIGRILNGILGK	15	*R. temporaria*
Temporin-10a1	---FLPLLASLFSRLLGK	15	*R. ornativentris*
Temporin-CDYb	---ILPILAPLIGGLLGK	15	*R. dybowskii*
	**		

Figure 2 Amino acid sequence comparison of amurin-9KY with amurin-9AM from *R. amurensis* and temporin family AMPs from other ranid frogs

All AMP sequences used were derived from the NCBI protein database. The two cysteine residues of amurin-9KY are indicated in gray shadow. The length of the AMPs is shown and species from which the AMPs are derived are on the right. Asterisks (*) indicate identical residues.

Table 1 Structural parameters of amurin-9KY and its derivatives

Sample	Amino acid sequence	Molecular weight	Structure characteristics
Amurin-9KY	FLPFFAACAITRKC-NH$_2$	1 584.96	C-terminal amidation and C-terminal heptapeptide ring C8-C14
Amurin-9KY1	FLPFFAACAITRKC-NH$_2$	1 586.96	C-terminal amidation
Amurin-9KY2	FLPFFAACAITRKC	1 585.96	C-terminal heptapeptide ring C8-C14
Amurin-9KY3	FLPFFAACAITRKC	1 587.96	None

Table 2 Antimicrobial activities of amurin-9KY and its derivatives

Microorganism	MIC (μg/mL)			
	Amurin-9KY	Amurin-9KY1	Amurin-9KY2	Amurin-9KY3
Gram-positive				
Staphylococcus aureus ATCC25923	4.68	37.5	ND	ND
Staphylococcus aureus 090223+ (IS)	37.5	75	ND	ND
Nocardia asteroids 090312+ (IS)	37.5	75	ND	ND
Gram-negative				
Escherichia coli ATCC25922	ND	ND	ND	ND
Klebsiella pneumonia 1368 (IS)	ND	ND	ND	ND
Pseudomonas aeruginosa ATCC27853	ND	ND	ND	ND
Fungi				
Candida albicans ATCC2002	ND	ND	ND	ND
Slime mold 090413 (IS)	ND	75	ND	ND

MIC: Minimum inhibitory concentration. These concentrations represent mean values of three independent experiments performed in duplicate. IS: Clinically isolated strain. ND: No detectable activity in inhibition zone assay at a dose of 2 mg/mL.

Anti-oxidant activity

To date, many peptides exhibiting anti-oxidant activity have been identified from several species of ranid frogs, which constitute the excellent skin anti-radiation defense system of ranid frogs (He et al., 2012; Liu et al., 2010; Lu et al., 2010; Yang et al., 2009). Most are dual-functional peptides, possessing both anti-oxidant and antimicrobial activities (He et

al., 2012; Liu et al., 2010; Lu et al., 2010; Yang et al., 2009). In the present study, the anti-oxidant activities of amurin-9KY and the three derivatives were also evaluated (Figure 3). Amurin-9KY exhibited slight concentration-dependent DPPH radical scavenging activity, with an optimal S% value of 30.6% at a concentration of 400 μg/mL. In contrast, the derivatives amurin-9KY1 and amurin-9KY3 exhibited strong anti-oxidant activities, with S% values exceeding 60% at concentrations as low as 50 μg/mL. Compared to the other three peptides, amurin-9KY2 exhibited the lowest anti-oxidant activity, with an S% value of 20% at a concentration of 400 μg/mL.

Solution structures of amurin-9KYs

The CD spectra of amurin-9KY in water showed a negative band at 200 nm, indicating a random-coil conformation. In the membrane-mimetic solvent (50% TFE-water) the presence of one positive band (190 nm) and two large negative dichroic bands at 208 and 222 nm (–50 mdeg) in amurin-9KY was consistent with the α-helical conformations (Figure 4A). For amurin-9KY1–3, the negative dichroic bands at 208 and 222 nm were much smaller, about –10 mdeg. The α-helical structure of most active AMPs is thought to be responsible for the formation of pores in the membranes of target organisms, thus disrupting metabolic activity (Brogden, 2005). The CD results support the concept that amurin-9KY most likely killed the bacteria through membrane disruption. In addition, the much smaller negative 208 and 222 nm dichroic bands were in good agreement with the antimicrobial activity data for amurin-9KY1–3.

Effects of amurin-9KY on microbial membrane morphology by SEM

Previous studies have demonstrated that AMPs achieve antimicrobial activity by disrupting various key microorganism cell processes, with some AMPs possessing multiple mechanisms (Brogden, 2005; Nguyen et al., 2011). There are many specific targets in microbial cells for AMPs, including external proteins, outer surface lipids, outer membrane proteins (gram-negative bacteria), inner membrane, integral membrane proteins, nucleic acids and intracellular proteins (Liu et al., 2017, 2018; Nguyen et al., 2011). Among them, disrupting the integrity of the microbial inner membrane is the most common mode for AMPs (Liu et al., 2017, 2018; Nguyen et al., 2011), the disruption of which results in obvious morphological alteration. Here, the antimicrobial results showed that *S. aureus* ATCC25923 was most sensitive to amurin-9KY, and therefore it was selected to examine the induced membrane morphological alterations by SEM. As illustrated in Figure 5, the untreated *S. aureus* cells exhibited normal shape and smooth surfaces (Figure 5A). In contrast, after treatment with amurin-9KY for 30 min, the cellular shape and surface of *S. aureus* exhibited obvious alterations (Figure 5B). The bacterial cells showed rough surfaces, prevalent membrane vesicles, and cellular fragments, implying that amurin-9KY might act on the bacterial membrane and induce disruption of membrane integrity. Ampicillin-treated *S. aureus* exhibited no significant morphological alteration compared with the untreated bacteria (Figure 5C), except for the appearance of many granules on the surfaces. Ampicillin usually kills bacteria by disturbing the synthesis of the cell wall.
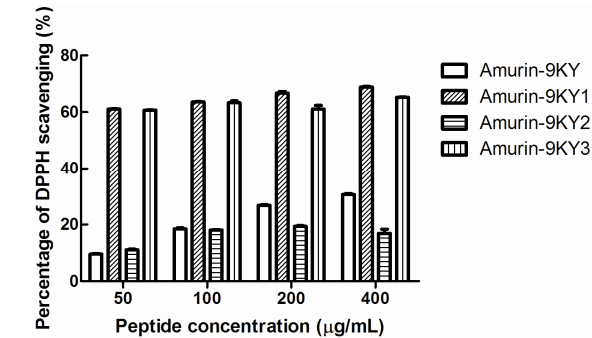
Figure 3 Anti-oxidant activity of amurin-9KY and derivatives (amurin-9KY1–3)

Different concentrations of peptides were incubated with DPPH solution at room temperature for 30 min, and then the amount of reduced DPPH was quantified by measuring the decrease in absorbance at 520 nm. Results represent mean values of three independent experiments.
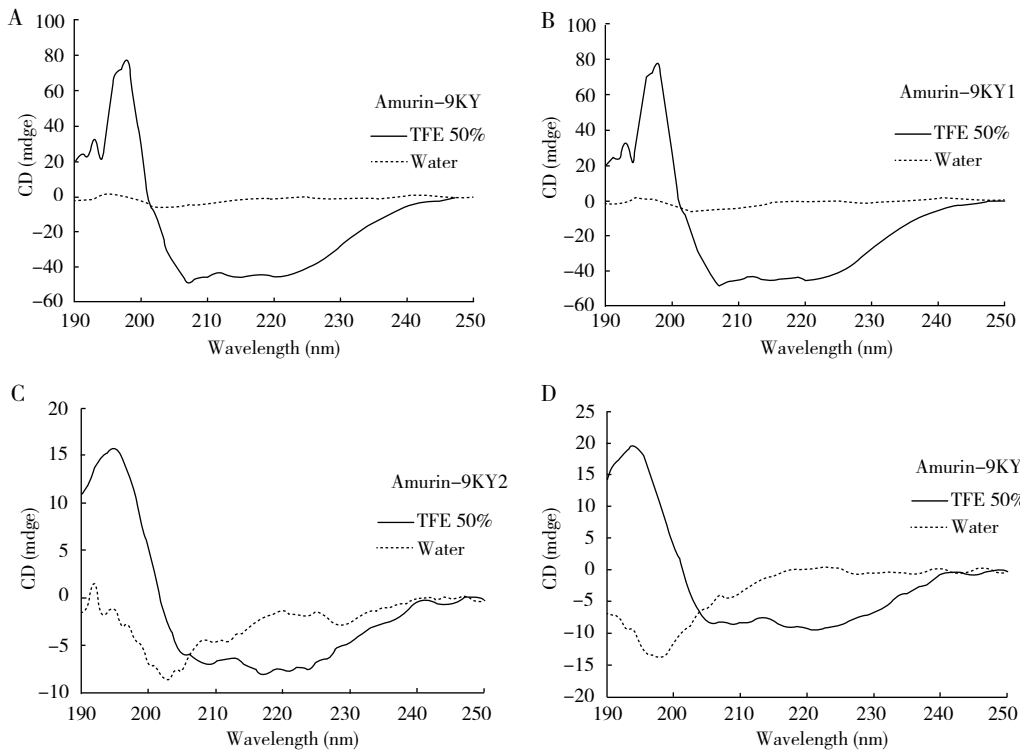
Figure 4 CD spectra of the four peptides in different solutions

A: Amurin-9KY; B–D: Amurin-9KY1–3.
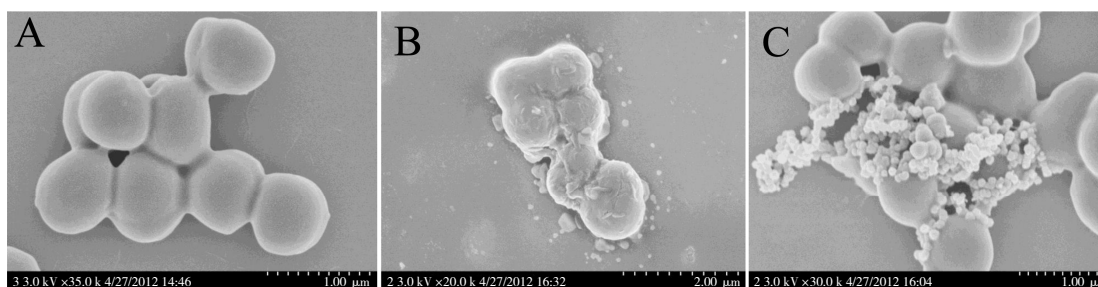
Figure 5 Scanning electron micrographs of *S. aureus* treated with amurin-9KY

A: *S. aureus* ATCC25923 control; B: Amurin-9KY-treated *S. aureus* ATCC25923; C: Ampicillin-treated *S. aureus* ATCC25923.

DISCUSSION

Among the AMP families identified from ranid species, the C-terminal heptapeptide ring (Rana box domain, two cysteine residues connected by a disulfide bridge) is a common structural feature, which broadly exists in families such as brevinin-1, brevinin-2, esculentin-1, esculentin-2, ranatuerin-1, ranalexin, japonicin-1, nigrocin-2, odorranain-C, odorranain-D, odorranain-F, odorranain-G, odorranain-H, odorranain-P1 and hainanenin (Conlon, 2004; Duda et al., 2002; He et al., 2012; Li et al., 2007; Matutte et al., 2000). In addition, other cyclic ranid AMPs have also been identified, including those with a C-terminal octapeptide ring (japonicin-2), C-terminal hexapeptide ring (ranatuerin-2, amolopin-6), middle heptapeptide ring (palustrin-2) or ring formed by more than seven amino acids (odorranain-A, odorranain-B, odorranain-J, odorranain-P2, odorranain-T, odorranain-U and ranacyclins) (Conlon, 2004; Duda et al., 2002; He et al., 2012; Li et al., 2007; Matutte et al., 2000). To date, three AMP families characterized with C-terminal amidation have been identified from ranid frogs, including temporins, ranacyclins and tiannanenin (Conlon, 2004; He et al., 2012; Li et al., 2007). Among the AMP families identified from ranid frogs so far, ranacyclin is a unique family possessing both a disulfide bridge-formed ring and amidated C-terminus (Mangoni et al., 2003). The ring structure of ranacyclins is composed of 11 residues and is located in the middle of the sequences. Comparatively, the novel AMP in the present study (amurin-9KY) is the first reported to have both a C-terminal heptapeptide ring and amidated C-terminus.

The three derivatives (amurin-9KY1–3) were designed here to evaluate the influence of C-terminal amidation and the C-terminal heptapeptide ring on the biological activities of amurin-9KY. The four peptides were chemically synthesized and their *in vitro* functions were subsequently examined. The antimicrobial assay results indicated that C-terminal amidation played an important role in the antimicrobial activity of amurin-9KY, whereas the heptapeptide ring contributed no obvious influence. SEM demonstrated that amurin-9KY induced obvious bacterial membrane morphological alteration, indicating that it might act through the disruption of bacterial membrane integrity.

Amurin-9KY possessed strong antimicrobial activity against gram-positive bacteria and low hemolytic activity, consistent with the features of temporin family AMPs. Previous study of temporin-1Od from the Japanese mountain brown frog *R. ornativentris* demonstrated that it possessed high antimicrobial potency towards *S. aureus* due to a positive charge associated with the free N-terminal amino group (Kim et al., 2001). The current study further confirmed that the free amino group is essential for the antimicrobial activity of AMPs, no matter at which terminus (N or C) it is located. Previous structure-activity analysis of brevinin 1E, a brevinin-1 family AMP identified from *R. esculenta*, demonstrated that the elimination of the intra-disulfide bridge did not greatly affect the antimicrobial activity (Kwon et al., 1998), which was further verified in the present result.

Regarding hemolytic activity, both C-terminal amidation and the heptapeptide ring significantly reduced the hemolytic activity of amurin-9KY compared with the derivatives without these two structural features. Elimination of the C-terminal heptapeptide ring greatly increased the anti-oxidant activity of amurin-9KY, whereas elimination of C-terminal amidation did not affect it at all. These results are likely because the unpaired thiol group of cysteine generated after elimination of the heptapeptide ring acted as an electron donor to the radical, which is crucial for the anti-oxidant activity of peptides (Akerström et al., 2007; Liu et al., 2010).

COMPETING INTERESTS

The authors declare that they have no competing interests.

AUTHORS' CONTRIBUTIONS

F.Z. and Z.L.G. performed the experiments. Y.C. performed the CD and SEM analyses. Y.P.W. and L.L. designed the study and analyzed the data. Y.P.W. and H.N.Y. wrote and revised the paper. All authors read and approved the final version of the manuscript.

REFERENCES

Akerström B, Maghzal GJ, Winterbourn CC, Kettle AJ. 2007. The lipocalin alphal microglobulin has radical scavenging activity. *Journal of Biological Chemistry*, **282**(43): 31493–31503.

Brogden KA. 2005. Antimicrobial peptides: pore formers or metabolic inhibitors in bacteria?. *Nature Reviews Microbiology*, **3**(3): 238–250.

Conlon JM. 2004. The therapeutic potential of antimicrobial peptides from frog skin. *Reviews in Medical Microbiology*, **15**(1): 17–25.

Conlon JM, Kolodziejek J, Nowotny N. 2004. Antimicrobial peptides from ranid frog: taxonomic and phylogenetic markers and a potential source of new therapeutic agents. *Biochimica et Biophysica Acta*, **1696**(1): 1–14.

Duda TF, Vanhoye D, Nicolas P. 2002. Roles of diversifying selection and coordinated evolution in the evolution of amphibian antimicrobial peptides. *Molecular Biology and Evolution*, **19**(6): 858–864.

He W, Feng F, Huang Y, Guo H, Zhang S, Li Z, Liu J, Wang Y, Yu H. 2012. Host defense peptides in skin secretions of *Odorrana tiannanensis*: Proof for other survival strategy of the frog than merely anti-microbial. *Biochimie*, **94**(3): 649–655.

Kim JB, Iwamuro S, Knoop FC, Conlon JM. 2001. Antimicrobial peptides from the skin of the Japanese mountain brown frog, *Rana ornativentris*. *Journal of Peptide Research*, **58**(5): 349–356.

Kreil G. 1994. Antimicrobial peptides from amphibian skin - an overview. *Ciba Foundation Symposium*, **186**: 77–85.

Kwon MY, Hong SY, Lee KH. 1998. Structure-activity analysis of brevinin 1E amide, an antimicrobial peptide from *Rana esculenta*. *Biochimica et Biophysica Acta*, **1387**(1–2): 239–248.

Li J, Xu X, Xu C, Zhou W, Zhang K, Yu H, Zhang Y, Zheng Y, Rees HH, Lai R, Yang D, Wu J. 2007. Anti-infection peptidomics of amphibian skin. *Molecular and Cellular Proteomics*, **6**(5): 882–894.

Liu CB, Hong J, Yang HL, Wu J, Ma DY, Li DS, Lin DH, Lai R. 2010. Frog skins keep redox homeostasis by antioxidant peptides with rapid radical scavenging ability. *Free Radical Biology and Medicine*, **48**(9): 1173–1181.

Liu C, Qi J, Shan B, Ma Y. 2018. Tachyplesin causes membrane instability that kills multidrug-resistant bacteria by inhibiting the 3-ketoacyl carrier protein reductase FabG. *Frontiers in Microbiology*, **9**: 825.

Liu C, Shan B, Qi J, Ma Y. 2017. Systemic responses of multidrug-resistant *Pseudomonas aeruginosa* and Acinetobacter baumannii following exposure to the antimicrobial peptide cathelicidin-BF imply multiple intracellular targets. *Frontiers in Cellular and Infection Microbiology*, **7**: 466.

Lu Z, Zhai L, Wang H, Che Q, Wang D, Feng F, Zhao Z, Yu H. 2010. Novel families of antimicrobial peptides with multiple functions from skin of Xizang plateau frog, *Nanorana parkeri*. *Biochimie*, **92**(5): 475–481.

Mangoni ML, Papo N, Mignogna G, Andreu D, Shai Y, Barra D, Simmaco M. 2003. Ranacyclins, a new family of short cyclic antimicrobial peptides: biological function, mode of action, and parameters involved in target specificity. *Biochemistry*, **42**(47): 14023–14035.

Matutte B, Storey KB, Knoop FC, Conlon JM. 2000. Induction of synthesis of an antimicrobial peptide in the skin of the freeze-tolerant frog, *Rana sylvatica*, in response to environmental stimuli. *FEBS Letter*, **483**(2–3): 135–138.

Nguyen LT, Haney EF, Vogel HJ. 2011. The expanding scope of antimicrobial peptide structures and their modes of action. *Trends in Biotechnology*, **29**(9): 464–472.

Nicolas P. 2009. Multifunctional host defense peptides: intracellular-targeting antimicrobial peptides. *FEBS Journal*, **276**(22): 6483–6496.

Radek K, Gallo R. 2007. Antimicrobial peptides: natural effectors of the innate immune system. *Seminars in Immunopathology*, **29**(1): 27–43.

Wang Y, Lu Z, Feng F, Zhu W, Guang H, Liu J, He W, Chi L, Li Z, Yu H. 2011. Molecular cloning and characterization of novel cathelicidin-derived myeloid antimicrobial peptide from *Phasianus colchicus*. *Developmental and Comparative Immunology*, **35**(3): 314–322.

Yang H, Wang X, Liu X, Wu J, Liu C, Gong W, Zhao Z, Hong J, Lin D, Wang, Lai R. 2009. Antioxidant peptidomics reveals novel skin antioxidant system. *Molecular and Cellular Proteomics*, **8**(3): 571–583.

Zasloff M. 2002. Antimicrobial peptides of multicellular organisms. *Nature*, **415**(6870): 389–395.

Zhang S, Guo H, Shi F, Wang H, Li L, Jiao X, Wang Y, Yu H. 2012. Hainanenins: a novel family of antimicrobial peptides with strong activity from Hainan cascade-frog, *Amolops hainanensis*. *Peptides*, **33**(2): 251–257.

Purification and characterization of a novel anti-coagulant from the leech *Hirudinaria manillensis*

Ruo-Mei Cheng[1,#], Xiao-Peng Tang[2,3,#], Ai-Lin Long[2,3,#], James Mwangi[2], Ren Lai[2], Rui-Pu Sun[4], Cheng-Bo Long[2,*], Zhen-Qing Zhang[1,*]

[1] *Department of Pharmaceutical Sciences*, *College of Pharmaceutical Sciences*, *Soochow University*, *Suzhou Jiangsu* 215123, *China*

[2] *Key Laboratory of Animal Models and Human Disease Mechanisms of Chinese Academy of Sciences ∕ Key Laboratory of Bioactive Peptides of Yunnan Province*, *Kunming Institute of Zoology*, *Kunming Yunnan* 650223, *China*

[3] *Kunming College of Life Science*, *University of Chinese Academy of Sciences*, *Kunming Yunnan* 650204, *China*

[4] *Jiangxi Medical College*, *Nanchang University*, *Nanchang Jiangxi* 330006, *China*

ABSTRACT

Protease inhibitors have been reported rarely from the leech *Hirudinaria manillensis*. In this study, we purified a novel protease inhibitor (bdellin-HM-2) with anticoagulant properties from *H. manillensis*. With a molecular weight of 1.4×10^4, bdellin-HM-2 was also characterized with three intra-molecular disulfide bridges at the N-terminus and multiple HHXDD and HXDD motifs at the C-terminus. cDNA cloning revealed that the putative nucleotide-encoding protein of bdellin-HM-2 contained 132 amino acids and was encoded by a 399 bp open reading frame (ORF). Sequence alignment showed that bdellin-HM-2 shared similarity with the "non-classical" Kazal-type serine protease inhibitors, but had no inhibitory effect on trypsin, elastase, chymotrypsin, kallikrein, factor XIIa (FXIIa), factor XIa (FXIa), factor Xa (FXa), thrombin, or plasmin. Bdellin-HM-2 showed anticoagulant effects by prolonging the activated partial thromboplastin time (aPTT), indicating a role in enabling *H. manillensis* to obtain a blood meal from its host. Our results suggest that bdellin-HM-2 may play a crucial role in blood-sucking in this leech species and may be a potential candidate for the development of clinical anti-thrombotic drugs.

Keywords: *Hirudinaria manillensis*; Bdellin-HM-2; "Non-classical" Kazal inhibitors; Blood sucking; Anticoagulant; Anti-thrombotic drugs

INTRODUCTION

Protease inhibitors occur naturally in living organisms, including animals (Shadrin et al., 2015; Vicuna et al., 2015; Wang et al., 2005; Zhang, 2006), plants (Kim et al., 2009; Ryan, 1990), fungi (Sabotic & Kos, 2012), and bacteria (Supuran et al., 2002). They have multifunctional roles in many physiological processes and play an important role in biological functions of venomous animals, such as in predation (Birrell et al., 2007) and defense (Ali et al., 2002). To prevent clotting during blood feeding from a host, hematophagous animals have developed various mechanisms to interfere with blood coagulation (Markwardt, 1996). Among the inhibitors involved in coagulation, protease inhibitors are the most prominent anticoagulants currently described and characterized from leeches (Dodt, 1995) and insects (De Marco et al., 2010; Mende et al., 1999).

There are at least four types of protease inhibitors, including serine, cysteine, aspartic, and metalloprotease inhibitors (Leung et al., 2000). The Kazal family is one of the best-known groups of serine protease inhibitors (Rimphanitchayakit & Tassanakajon, 2010). Kazal-type inhibitory can be sorted into classical and non-classical Kazal domains. The classical Kazal domain has two residues between cys4 and cys5, whereas the non-classical Kazal inhibitor has a spacer region between cys4 and cys5, ranging from three to seven residues

(Moser et al., 1998). There are highly homologous three-dimensional structures in the Kazal-type serine proteinase inhibitors regardless of length of amino acid sequences between the cysteines and amino acid sequence variation (Eigenbrot et al., 2012). The P1 residue, located in the second amino acid downstream of the second conserved cysteine residue, is inserted into the S1 specificity pocket of the protease in a substrate-like way (Bode & Huber, 1992; Laskowski & Kato, 1980).

Several Kazal-type serine protease inhibitors have been characterized from leeches. A few "non-classical" Kazal inhibitors have been reported from different leeches, including bdellin-B-3 (Fink et al., 1986), bdellin-KL (Kim et al., 2001), and bdellin-HM (Lai et al., 2016). In this study, bdellin-HM-2 was purified and characterized from the leech *H. manillensis*. To the best of our knowledge, bdellin-HM-2 is the first Kazal-type serine protease inhibitor displaying anticoagulant properties identified from *H. manillensis*.

MATERIALS AND METHODS

Collection of crude extracts
The *H. manillensis* leeches were purchased from Jinbian aquafarm, Qinzhou City, Guangxi Province in China. The leeches were still alive when transported to the laboratory. We prepared the crude extracts from the leech heads as described previously (Lai et al., 2016). In short, leech heads were separated from the bodies, washed in 0.9% saline, quickly frozen, and then ground in liquid nitrogen.

Purification of bdellin-HM-2
Purification of bdellin-HM2 followed similar methods described in our previous published article (Lai et al., 2016). Briefly, crude extracts were dissolved in 50 mmol/L Tris-HCl buffer (pH 8.9) and subsequently separated by a DEAE Sephadex A-50 column (5 cm diameter, 60 cm length, GE, USA). Elution was performed at a flow rate of 15 mL/h at 4 °C and 3.0 mL fractions were collected in separate tubes. The absorbance of the fractions was monitored at both 215 and 280 nm. Fractions that could prolong the activated partial thromboplastin time (aPTT) were pooled and lyophilized prior to further purification. The powder from the previous step was dissolved and loaded for reverse-phase high-performance liquid chromatography (RP-HPLC) on a C_{18} column (Waters, Milford, MA, USA, 5 μm particle size, 250 mm×4.6 mm). Elution was carried out with a linear gradient of 10%−60% solution B (99.9% acetonitrile, 0.1% TFA) for 60 min at a flow rate of 1 mL/min. The eluted fraction that prolonged aPTT was collected.

Mass spectrometric analysis and peptide sequencing
The molecular weight of the collected fraction was analyzed by matrix-assisted laser desorption ionization time-of-flight mass spectrometry (MALDI-TOF-MS, Autoflex speed TOF/TOF, Bruker Daltonik GmbH, Bruker Corporation, Germany) using positive ion and linear mode, with specific operating parameters including a 20 kV ion acceleration voltage, 50-time accumulation for single scanning, and 0.1% accuracy of mass determinations. The partial peptide sequence of the N-terminal was determined by automatic Edman degradation on a pulsed liquid-phase sequencer (PPSQ-31A, Shimadzu Corporation, Japan).

RNA extraction and cDNA library construction
Total RNA from the head of *H. manillensis* was extracted using Trizol reagent (Life Technologies, Carlsbad, CA, USA) according to the manufacturer's instructions and was dissolved in RNase-Free water. A SMART™ PCR cDNA construction kit (Clontech, Palo Alto, CA, USA) was used for synthesizing cDNA, as described previously (Lai et al., 2016).

Screening of cDNA encoding bdellin-HM-2
To screen the cDNA encoding the precursor of bdellin-HM-2, synthesized cDNA was used as the template for PCR, following previously described methods (Lai et al., 2016). Briefly, two pairs of oligonucleotide primers (Table 1) were used in PCR reactions, where primers 1 and 3 were designed according to the partial N-terminal sequence of bdellin-HM-2 and primers 2 and 4 were from the SMART™ PCR cDNA construction kit. The PCR conditions were as described previously (Lai et al., 2016).

Table 1   Primers used for cDNA cloning of bdellin-HM-2

Primer	Sequence (5'–3')
1	AACAGGTTTGCGGAAGT
2	AAGCAGTGGTATCAACGCAGAGT
3	AATTCCAGGGTACAGACG
4	ATTCTAGAGGCCGAGGCGGCCGA

Primers 1 and 2 for signal peptide cloning; primers 3 and 4 for mature peptide cloning.

Effects of bdellin-HM-2 on blood coagulation
For aPTT assay, the aPTT reagent (50 μL, F008-1, Nanjing Jiancheng Bioengineering Institute, China) was incubated with 50 μL of plasma and different concentrations of bdellin-HM-2 (0.7 and 1.4 μmol/L). After 3-min incubation, $CaCl_2$ (50 μL, 25 mmol/L) preheated at 37 °C for 5 min was added, and the clotting curve was monitored at 650 nm using an enzyme-labeled instrument (Epoch BioTek, USA) for 2 min. To test the prothrombin time (PT), plasma (50 μL) was incubated with different concentrations of bdellin-HM-2 (0.7 and 1.4 μmol/L) for 3 min at 37 °C, after which the PT reagent (100 μL, F007, Nanjing Jiancheng Bioengineering Institute, China) preheated at 37 °C for 15 min was added and the clotting curve was monitored at 650 nm using the enzyme-labeled instrument for 30 s.

Effects of bdellin-HM-2 on proteases
Effects of bdellin-HM-2 on proteases, including trypsin, elastase, chymotrypsin, kallikrein, factor XIIa (FXIIa), factor XIa (FXIa), factor Xa (FXa), thrombin, and plasmin were tested using the corresponding chromogenic substrates. The testing enzyme was incubated with different concentrations (0, 0.7, 1.4, 2.8, and 5.6 μmol/L) of bdellin-HM-2 in 60 μL of 50 mmol/L Tris buffer (pH 7.4) for 5 min, with a certain concentration of

chromogenic substrate then added. Absorbance at 405 nm was monitored immediately and the kinetic curve was recorded using the enzyme-labeled instrument for 30 min. Bovine pancreas trypsin, elastase, chymotrypsin, and plasmin were all obtained from Sigma (USA) and the enzyme concentrations used were 800, 400, 400, and 20 nmol/L, respectively. The corresponding chromogenic substrates (Sigma, USA) were Gly-Arg-p-nitroanilide dihydrochloride for trypsin, N-methoxysuccinyl-Ala-Ala-Pro-Val-p-nitroanilide for elastase, N-succinyl-Gly-Gly-Phe-p-nitroanilide for chymotrypsin, and Gly-Arg-p-nitroanilide dihydrochloride for plasmin. The concentration of all substrates in the reactions was 0.2 mmol/L. The concentrations used for kallikrein, FXIa, and FXa (Enzyme Research Laboratory, USA) were 400, 400, and 20 nmol/L, respectively, and the corresponding chromogenic substrates were H-D-Pro-Phe-Arg-pNA · 2HCl (Hyphen Biomed, France), H-D-Pro-Phe-Arg-pNA · 2HCl (Hyphen Biomed, France), and CH$_3$OCO-D-CHA-Gly-Arg-pNA-AcOH (Sigma, USA), respectively. The concentration of all three substrates in the reaction was 0.2 mmol/L. Human thrombin (Sigma, USA, 10 nmol/L) and FXIIa (Enzyme Research Laboratories, USA, 10 nmol/L) were reacted with 0.2 mmol/L chromogenic substrate of H-D-Phe-Pip-Arg-pNa · 2HCl (Hyphen Biomed, France) and H-D-Pro-Phe-Arg-pNA · 2HCl (Hyphen Biomed, France), respectively.

RESULTS

Purification of bdellin-HM-2
The crude extracts from *H. manillensis* were resolved into several fractions by DEAE Sephadex A-50 column. The fraction that prolonged the aPTT was indicated by a bar (Figure 1A). We then obtained the purified peptide exerting an aPTT inhibitory effect, named bdellin-HM-2 (indicated by an arrow in Figure 1B), using a C$_{18}$ RP-HPLC column. MALDI-TOF-MS showed that bdellin-HM-2 had a molecular weight (MW) of 14141.5 (Figure 1C).

Primary structure of bdellin-HM-2
Based on automatic Edman degradation, the partial N-terminal sequence of bdellin-HM-2 was determined to be ETECVCTLELKQVCGS. According to the N-terminal sequence, degenerate primers were designed (Table 1) to clone the cDNA encoding the precursor of bdellin-HM-2 from the cDNA library. A 399 bp cDNA encoding the precursor of bdellin-HM-2 was obtained. The cDNA had an open reading frame (ORF) of 396 nucleotides coding a pro-protein of 132 amino acids, including a signal peptide of 18 residues (indicated by box) and mature bdellin-HM-2 of 114 residues (Figure 2A). The theoretical MW of mature bdellin-HM-2 was 13144.78, which was not consistent with the observed mass by mass spectrometry analysis (Figure 1C). This inconsistency may be due to post-translational modification of the protein. Sequence alignment showed similarity to bdellin-KL (Kim et al., 2001), bdellin-B-3 (Fink et al., 1986), and bdellin-HM (Lai et al., 2016), which are 'non-classical' Kazal serine protease inhibitors (Figure 2B). Multiple sequence alignment showed that the six
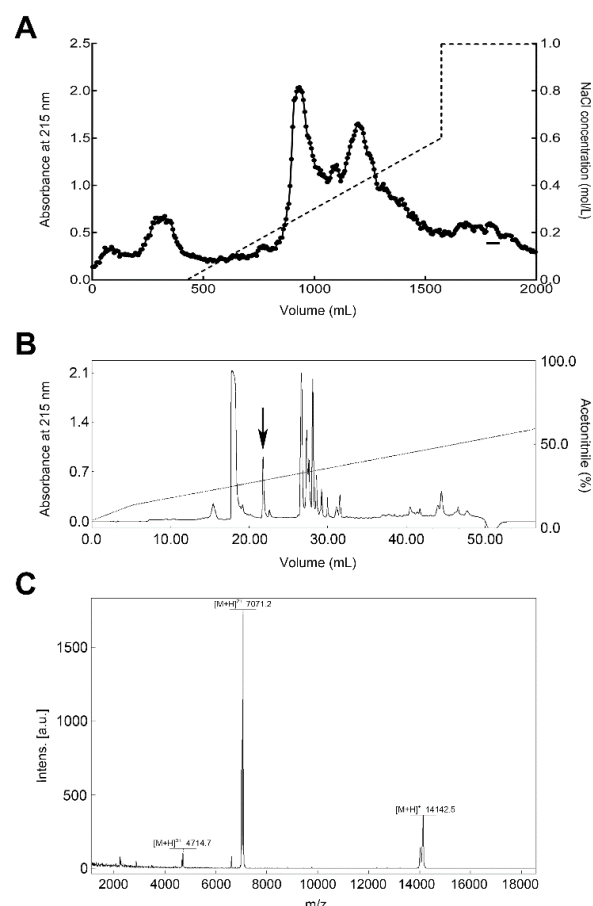

Figure 1 Purification of bdellin-HM-2 from *H. manillensis*

A: Crude extracts were fractionated using DEAE Sephadex A-50 ion exchange. Fraction exerting inhibitory activity on aPTT is indicated by a bar (−). B: Fraction exerting inhibitory activity on aPTT was further purified by C$_{18}$ reverse-phase high-performance liquid chromatography (RP-HPLC). Protein peak exerting inhibitory activity on the aPTT is marked by an arrow. C: Matrix-assisted laser desorption ionization time-of-flight (MALDI-TOF) analysis of purified native bdellin-HM-2.

cysteine residues and threonine-tyrosine residues were highly conserved among different species (Figure 2C). There were multiple HHXDD and HXDD motifs at the C-terminus of bdellin-HM-2.

Anticoagulant activity of bdellin-HM-2
Under the assay conditions, bdellin-HM-2 exerted anticoagulatory activity by inhibiting aPTT (Figure 3A), whereas no inhibitory activity was observed on PT (Figure 3B). Compared with the control with an aPTT of ~60 s, the aPTT was prolonged to ~100 s after 0.7 and 1.4 µmol/L bdellin-HM-2 treatment, suggesting that bdellin-HM-2 acts on the intrinsic pathway. Bdellin-HM-2 had no effect on trypsin, elastase, chymotrypsin, kallikrein, FXIIa, FXIa, FXa, thrombin, or plasmin (Figure 3C). All enzyme activity test results were plotted (Figure 4).
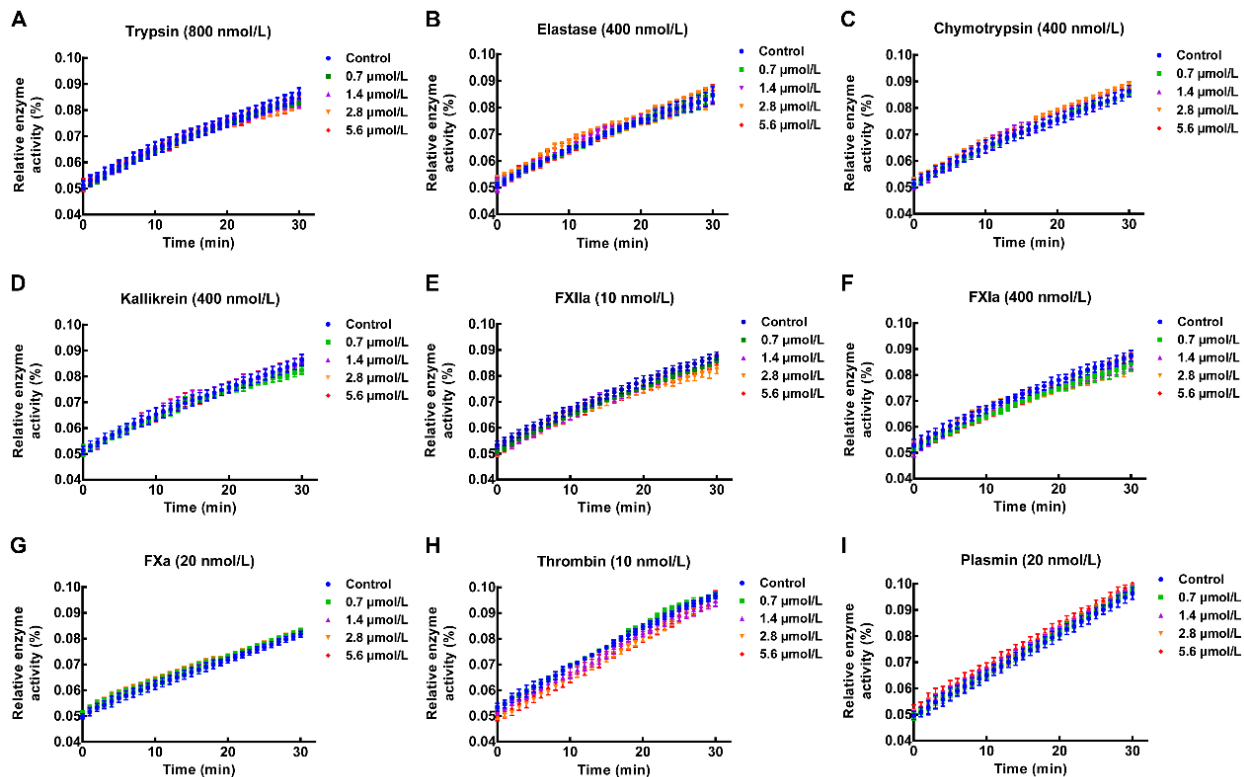
A

```
atgaagtttttgatcgctcttctctttctctgctctctggtcagcatcgaggctgagaca
 M  K  F  L  I  A  L  L  F  L  C  S  L  V  S  I  E  A  E  T      20
gaatgcgtctgtaccctggaattgaaacaggtttgcggaagtgatggtgtcacatatgac
 E  C  V  C  T  L  E  L  K  Q  V  C  G  S  D  G  V  T  Y  D      40
aacccgtgcctagcaacctgccacggggcatcggttgtaaacgaacacgcctgcgaacat
 N  P  C  L  A  T  C  H  G  A  S  V  V  N  E  H  A  C  E  H      60
cacggcgatgaccatcacgatgacgatcatgatgaccatgatgacgatcacaaagacgat
 H  G  D  D  H  H  D  D  D  H  D  D  H  D  D  D  H  K  D  D      80
caccatggcgacgatcaccatgatgacgatcaccatgacgaccacaaggacgatcatcac
 H  H  G  D  D  H  H  D  D  D  H  H  D  D  H  K  D  D  H  H     100
gatgatcaccatgacgataataacaaccacgacgacgaccatgatgatgatgatggtgat
 D  D  H  H  D  D  N  N  N  H  D  D  D  H  D  D  D  H  D  D  D  D  G  D  120
gaccacaaggacgaccatcacgaggaagatgacgactag
 D  H  K  D  D  H  H  E  E  D  D  D  -                          132
```

B

```
                  10          20          30          40          50
              P1
Bdellin-HM-2  ETECVCTLELKQVCGSDGVTYDNPCLATCHGASVVNEHACEHHGDDHHDD
Bdellin-HM    DSECVCTKELNQVCGSDGHTYDNPCLATCHGASVAHEHACEGHEEEHHEE
Bdellin-KL    DTECVCTKELLRVCGEDGVTYDNSCLATCHGTSVAHEHACEG-FVEHHED
Bdellin B-3   DTECVCTKELHRVCGSDGVTYDNECLATCHGASVAHDHACEG-HEEHHVD
              ***** ** * ***  *** ****  ****** **   ****   **

                  60          70          80          90         100
Bdellin-HM-2  DHDD-----------------HDDDHKDDHHGDDHHDD-DHHDDHKDDH
Bdellin-HM    DHHDGEHNNGDHHEGEHNNGEHHDDEHKDDHDEDGEHNEEHKDDHHED
Bdellin-KL    EHHEGEEHKEEGHEGHD---DHHDDGHEEHHEGEEHKD--EHHEEGHDDH
Bdellin B-3   EHGEDHD-----------------------------------------
              *

                 110         120         130         140
Bdellin-HM-2  HDDHHDDNN--------NHDDDHDDDDG--DDHKDDHHEEDDD------
Bdellin-HM    HDDGHDDHHNNGDHKDDHHEEEHHEEHHEGDHHEEEHHEEEHKDDHHHD
Bdellin-KL    HEEGHDDHH------DDEHKEDHHDDEHKEDDDHHDDEHKDDDHHEEHHD
Bdellin B-3   ------------------------------------------------
```

C

```
                 10          20          30          40          50
Bdellin-HM-2  CV-----CTLELKQVCGSDGVTYDNPCLAT-----CH-----GAS------VVNEHAC
AaKPI         CA-----CPRIYMPVCGSNLKTYNNDCLLR-----CEINSDLGRANNLRK--IADQAC
AsEI          CP--L--ICTMQYDPVCGSDGITYGNACMLLGAS--CRS-DTP-------IELVHKGRC
LDTI          CA-----CPKILKPVCGSDGRTYANSCIAR-----CN-----GVS------IKSEGSC
```

Figure 2 cDNA sequence encoding bdellin-HM-2 precursor and sequence alignment with other protease inhibitors

A: Nucleotide sequence encoding bdellin-HM-2 precursor and deduced amino acid sequence. Signal peptide is boxed. Bar (−) indicates stop codon. B: Sequence comparison of bdellin-HM-2 with bdellin-HM, bdellin-KL, and bdellin-B-3. Identical amino acid residues are indicated by an asterisk (*). C: Multiple sequence alignment of Kazal domain from *H. manillensis* (bdellin-HM-2), *Aedes aegypti* (AaKPI ABF18209), *Anemonia sulcata* (AsEI 1Y1B), and *H. medicinalis* (LDTI P80424). Conserved threonine-tyrosine residues between cysteine 3 and 4 are indicated. Conserved cysteine motifs are also indicated.

DISCUSSION

Several protease inhibitors exerting anticoagulant effects have been found from leeches (Hong & Kang, 1999; Markwardt, 2002; Salzet et al., 2000; Salzet, 2001; Strube et al., 1993; Tuszynski et al., 1987). In this report, a novel protease inhibitor (bdellin-HM-2) with anticoagulant effects was purified and further characterized from *H. manillensis* for the first time. The cDNA encoding bdellin-HM-2 precursor was cloned from the cDNA library, and the mature bdellin-HM-2 consisted of 114 amino acid residues. MALDI-TOF-MS showed that the MW of bdellin-HM-2 was 14141.5, compared to the theoretical molecular weight of 13144.78, a difference of 996.72, which is not consistent with the theoretical value. Research shows glycosylation influences the function of protein, governs physiology, and contributes to disease (Ohtsubo & Marth,

Figure 3 Effects of bdellin-HM-2 on aPTT

Bdellin-HM-2 action on aPTT (A) and PT (B). C: Bdellin-HM-2 effects on trypsin, elastase, chymotrypsin, kallikrein, FXIIa, FXIa, FXa, thrombin, and plasmin were analyzed by hydrolysis of chromogenic substrates. Data are means±*SD* of six independent experiments.

2006). We speculated that bdellin-HM-2 was O-glycosylated at Thr-20, Thr-25, Ser-34, Thr-38, and Thr-46. (Gupta & Brunak, 2002), although further research on these O-glycosylation sites should be performed in the future.

Kazal-type inhibitors with one or more Kazal domains are characterized by multiple HHXDD and HXDD motifs in their amino acid sequences (Laskowski & Kato, 1980) and by their highly homologous three-dimensional structures (Van et al., 1995). Each Kazal domain usually contains six conserved cysteine residues forming three intra-molecular disulfide

Figure 4 Bdellin-HM-2 had no effect on proteases
Bdellin-HM-2 effects on trypsin (A), elastase (B), chymotrypsin (C), kallikrein (D), FXIIa (E), FXIa (F), FXa (G), thrombin (H), and plasmin (I). Data represent at least six independent experiments and are presented as means±*SD*.

bridges (Laskowski & Kato, 1980; Magert et al., 1999). P1 residue, which contributes to the inhibitory specificity, is located at the second position after the second cysteine residue of the Kazal domain (Bode & Huber, 1992). Although bdellin-HM-2 showed high similarity to bdellin-HM and bdellin-KL by sequence analysis and belongs to the family of non-classical Kazal domains, enzyme activity tests showed that bdellin-HM-2 had no inhibitory effects on trypsin, elastase, chymotrypsin, kallikrein, FXIIa, FXIa, FXa, thrombin, or plasmin under the assay conditions. Sequence alignment showed that the P1 residue of bdellin-HM-2 was different from bdellin-HM, bdellin-KL, and bdellin-B-3. The difference in P1 residue was considered the cause of the enzyme activity test results.

Bdellin-HM-2 prolonged the aPTT, implying that bdellin-HM-2 functioned to help *H. manillensis* obtain a blood meal by inhibiting blood coagulation. Results showed that the activity was dose-independent. Further work to identify the target of bdellin-HM-2 in blood is necessary. Blood-sucking animals obtain a blood meal by overcoming the host's natural blood coagulation (De Marco et al., 2010; Dodt, 1995; Markwardt, 1996; Mende et al., 1999). The anticoagulant peptide obtained from *H. manillensis* not only facilitates our understanding of the mechanism of blood feeding for *H. manillensis*, but also provides a new candidate for the development of clinical anticoagulant drugs.

In conclusion, bdellin-HM-2 identified from *H. manillensis* prolonged the aPTT but exhibited no influence on PT and no inhibitory activity on trypsin, elastase, chymotrypsin, kallikrein, FXIIa, FXIa, FXa, thrombin, or plasmin under the assay conditions. Further research on O-glycosylation sites will be performed in the future. Bdellin-HM-2 is the first identified Kazal-type serine protease inhibitor from *H. manillensis* that shows a potent anticoagulant effect.

COMPETING INTERESTS

The authors declare that they have no competing interests.

AUTHORS' CONTRIBUTIONS

R.M.C., X.P.T., and A.L.L. performed the experiments and data analysis. J. M. and R.P.S. assisted in collection and purification. R.L., C.B.L., and Z.Q. Z. conceived and designed the study. R.M.C., X.P.T., and C.B.L. conceived and supervised the project and prepared the manuscript. All authors read and approved the final version of the manuscript.

ACKNOWLEDGMENTS

Chinese Academy of Sciences) for help in the analysis of mass spectrometry results.

REFERENCES

Ali MF, Lips KR, Knoop FC, Fritzsch B, Miller C, Conlon JM. 2002. Antimicrobial peptides and protease inhibitors in the skin secretions of the crawfish frog, *Rana areolata*. *Biochimica et Biophysica Acta-Proteins and Proteomics*, **1601**(1): 55–63.

Birrell GW, Earl STH, Wallis TP, Masci PP, De Jersey J, Gorman JJ, Lavin MF. 2007. The diversity of bioactive proteins in Australian snake venoms. *Molecular & Cellular Proteomics*, **6**(6): 973–986.

Bode W, Huber R. 1992. Natural protein proteinase inhibitors and their interaction with proteinases. *European Journal of Biochemistry*, **204**(2): 433–451.

De Marco R, Lovato DV, Torquato RJS, Clara RO, Buarque DS, Tanaka AS. 2010. The first pacifastin elastase inhibitor characterized from a blood sucking animal. *Peptides*, **31**(7): 1280–1286.

Dodt J. 1995. Anticoagulatory substances of bloodsucking animals: from hirudin to hirudin mimetics. *Angewandte Chemie-International Edition*, **34**(8): 867–880.

Eigenbrot C, Ultsch M, Lipari MT, Moran P, Lin SJ, Ganesan R, Quan C, Tom J, Sandoval W, Van Lookeren Campagne M, Kirchhofer D. 2012. Structural and functional analysis of HtrA1 and its subdomains. *Structure*, **20**(6): 1040–1050.

Fink E, Rehm H, Gippner C, Bode W, Eulitz M, Machleidt W, Fritz H. 1986. The primary structure of Bdellin B-3 from the leech Hirudo Medicinalis - Bdellin B-3 is a compact proteinase inhibitor of a "Non-classical" Kazal Type - It is present in the leech in a high molecular mass form. *Biological Chemistry Hoppe-Seyler*, **367**(12): 1235–1242.

Gupta R, Brunak S. 2002. Prediction of glycosylation across the human proteome and the correlation to protein function. *Pacific Symposium on Biocomputing*, **7**(3): 310–322.

Hong SJ, Kang KW. 1999. Purification of granulin-like polypeptide from the blood-sucking leech, *Hirudo nipponia*. *Protein Expression and Purification*, **16**(2): 340–346.

Kim YH, Choi JG, Lee GM, Kang KW. 2001. Domain and genomic sequence analysis of bdellin-KL, a leech-derived trypsin-plasmin inhibitor. *Journal of Biochemistry*, **130**(3): 431–438.

Kim JY, Park SC, Hwang I, Cheong H, Nah JW, Hahm KS, Park Y. 2009. Protease inhibitors from plants with antimicrobial activity. *International Journal of Molecular Sciences*, **10**(6): 2860–2872.

Lai Y, Li B, Liu W, Wang G, Du C, Ombati R, Lai R, Long C, Li H. 2016. Purification and characterization of a novel Kazal-type trypsin inhibitor from the leech of *Hirudinaria manillensis*. *Toxins*, **8**(8): 229–239.

Laskowski M, Jr, Kato I. 1980. Protein inhibitors of proteinases. *Annual Review of Biochemistry*, **49**: 593–626.

Leung D, Abbenante G, Fairlie DP. 2000. Protease inhibitors: current status and future prospects. *Journal of Medicinal Chemistry*, **43**(3): 305–341.

Mägert HJ, Ständker L, Kreutzmann P, Zucht HD, Reinecke M, Sommerhoff CP, Fritz H, Forssmann WG. 1999. LEKTI, a novel 15-domain type of human serine proteinase inhibitor. *Journal of Biological Chemistry*, **274**(31): 21499–21502.

Markwardt F. 1996. State-of-the-Art Review: Antithrombotic agents from hematophagous animals. *Clinical and Applied Thrombosis-Hemostasis*, **2**(2): 75–82.

Markwardt F. 2002. Hirudin as alternative anticoagulant-a historical review. *Seminarsin Thrombosis and Hemostasis*, **28**(5): 405–413.

Mende K, Petoukhova O, Koulitchkova V, Schaub GA, Lange U, Kaufmann R, Nowak G. 1999. Dipetalogastin, a potent thrombin inhibitor from the blood-sucking insect Dipetalogaster maximus-cDNA cloning, expression and characterization. *European Journal of Biochemistry*, **266**(2): 583–590.

Moser M, Auerswald E, Mentele R, Eckerskorn C, Fritz H, Fink E. 1998. Bdellastasin, a serine protease inhibitor of the antistasin family from the medical leech (*Hirudo medicinalis*) - primary structure, expression in yeast, and characterisation of native and recombinant inhibitor. *European Journal of Biochemistry*, **253**(1): 212–220.

Ohtsubo K, Marth JD. 2006. Glycosylation in cellular mechanisms of health and disease. *Cell*, **126**(5): 855–867.

Rimphanitchayakit V, Tassanakajon A. 2010. Structure and function of invertebrate Kazal-type serine proteinase inhibitors. *Developmental & Comparative Immunology*, **34**(4): 377–386.

Ryan CA. 1990. Protease inhibitors in plants-genes for improving defenses against insects and pathogens. *Annual Review of Phytopathology*, **28**: 425–449.

Sabotic J, Kos J. 2012. Microbial and fungal protease inhibitors-current and potential applications. *Applied Microbiology and Biotechnology*, **93**(4): 1351–1375.

Salzet M. 2001. Anticoagulants and inhibitors of platelet aggregation derived from leeches. *FEBS Letters*, **492**(3): 187–192.

Salzet M, Chopin V, Baert JL, Matias I, Malecha J. 2000. Theromin, a novel leech thrombin inhibitor. *Journal of Biological Chemistry*, **275**(40): 30774–30780.

Shadrin N, Shapira MG, Khalfin B, Uppalapati L, Parola AH, Nathan I. 2015. Serine protease inhibitors interact with IFN-γ through up-regulation of FasR; a novel therapeutic strategy against cancer. *Experimental Cell Research*, **330**(2): 233–239.

Strube KH, Kröger B, Bialojan S, Otte M, Dodt J. 1993. Isolation, sequence-analysis, and cloning of Haemadin - an anticoagulant peptide from the Indian leech. *Journal of Biological Chemistry*, **268**(12): 8590–8595.

Supuran CT, Scozzafava A, Clare BW. 2002. Bacterial protease inhibitors. *Medicinal Research Reviews*, **22**(4): 329–372.

Tuszynski GP, Gasic TB, Gasic GJ. 1987. Isolation and characterization of antistasin - an inhibitor of metastasis and coagulation. *Journal of Biological Chemistry*, **262**(20): 9718–9723.

Van De Locht A, Lamba D, Bauer M, Huber R, Friedrich T, Kröger B, Höffken W, Bode W. 1995. Two heads are better than one: crystal structure of the insect derived double domain Kazal inhibitor rhodniin in complex with thrombin. *EMBO Journal*, **14**(21): 5149–5157.

Vicuña L, Strochlic DE, Latremoliere A, Bali KK, Simonetti M, Husainie D, Prokosch S, Riva P, Griffin RS, Njoo C, Gehrig S, Mall MA, Arnold B, Devor M, Woolf CJ, Liberles SD, Costigan M, Kuner R. 2015. The serine protease inhibitor SerpinA3N attenuates neuropathic pain by inhibiting T cell-derived leukocyte elastase. *Nature Medicine*, **21**(5): 518–523.

Wang LJ, Gao GF, Bai SP, Liu ZG, Liang JG, Zhang KY, Lai R. 2005. A thrombin inhibitor from ixodid tick, *Ixodide sinesis*. *Zoological Research*, **26**(3): 328–331.

Zhang Y. 2006. Amphibian skin secretions and bio-adaptive significance - implications from *Bombina maxima* skin secretion proteome. *Zoological Research*, **27**(1): 101–112.

Passive eye movements induced by electromagnetic force (EMF) in rats

Yue Yu[1,#], Jun Huang[1,#], Chun-Ming Zhang[2], Tian-Wen Chen[1], David S. Sandlin[3], Shao-Xun Wang[1,4], Alberto A. Arteaga[1], Jerome Allison[5], Yang Ou[1], Susan Warren[5], Paul May[5], Hong Zhu[1,5,*], Wu Zhou[1,5,6,*]

[1] *Departments of Otolaryngology and Communicative Sciences, University of Mississippi Medical Center, Jackson MS 39216, USA*

[2] *Department of Otolaryngology, First Affiliated Hospital, Shanxi Medical University, Taiyuan Shanxi 030001, China*

[3] *MD/PhD Program, University of Mississippi Medical Center, Jackson MS 39216, USA*

[4] *Pharmacology and Toxicology, University of Mississippi Medical Center, Jackson MS 39216, USA*

[5] *Neurobiology and Anatomical Sciences, University of Mississippi Medical Center, Jackson MS 39216, USA*

[6] *Neurology, University of Mississippi Medical Center, Jackson MS 39216, USA*

ABSTRACT

Accurate information on eye position in the orbit is available from visual feedback, efference copy of the oculomotor commands and proprioceptive signals from the extraocular muscles (EOM). Whereas visual feedback and oculomotor commands have been extensively studied, central processing of EOM proprioceptive signals remains to be elucidated. A challenge to the field is to develop an approach to induce passive eye movements without physically contacting the eyes. A novel method was developed to generate passive eye movements in rats. A small rare-earth magnet disk (0.7 mm diameter, 0.5 mm thickness) was attached to the surface of a rat's eyeball. A metal rod (5 mm diameter) wrapped with an electromagnetic (EM) coil was placed near the magnet (8–15 mm). By passing currents to the EM coil, electromagnetic force (EMF) was generated and acted upon the magnet and induced passive eye movements. The EMF induced well-defined passive eye movements, whose directions were dependent on current polarity and amplitudes and peak velocities were dependent on current intensity and duration. Peak velocities of the EMF-induced eye movements were linearly related to amplitudes, exhibiting main sequence relationships similar to that of saccades in awake rats and eye movements induced by electrical microstimulation of the abducens nucleus in anesthetized rats. Histological examination showed that repetitive EMF stimulations did not appear to result in damages in the EOM fibers. These results validated the EMF approach as a novel tool to investigate EOM proprioceptive signals and their roles in visual localization and gaze control.

Keywords: Eye movement; Proprioception; Extraocular muscles; Stretch reflex

INTRODUCTION

An important issue in modeling visual localization and gaze control is to determine whether the central nervous system (CNS) obtains eye position information in the orbit via efference copy (or corollary discharge) of ocular motor commands or proprioception signals from the extraocular muscles (EOM) or the orbital connective tissues. Whereas Helmholtz (1925) emphasized the roles of efference copy, Sherrington (1918) emphasized the roles of EOM proprioception. The two camps have been debating this issue over the past century. On one hand, earlier studies showed that humans are aware of the passive displacements of the eyes in darkness (Skavenski, 1972) and altering this proprioceptive information consistently leads to errors in visual localization (Allin et al., 1996; Balslev & Miall, 2008; Bridgeman & Stark, 1991; Campos, 1986; Campos et al., 1989; Gauthier et al., 1990; Lennerstrand et al., 1997). Recent finding of EOM proprioceptive signals

in the somatosensory cortex (Wang et al., 2007) and its roles in computing spatial maps (Xu et al., 2012) provided compelling evidence that the CNS utilizes the proprioceptive eye position signals. On the other hand, bilateral section of the monkey trigeminal nerves did not reduce accuracy of open-loop pointing (Lewis et al., 1994) and memory-guided saccades (Guthrie et al., 1983). Based on the assumption that the trigeminal nerves carry eye proprioceptive information to the brain (Porter et al., 1983), these results suggested that eye proprioception signal is not necessary for visual localization and gaze control because efference copy of the oculomotor motor commands is sufficient to implement these tasks.

The lack of understanding of the EOM proprioceptive signals is partially attributable to the fact that location of the peripheral sensors and their connections to the brain are still a matter of debate (Billig et al., 1997; Lienbacher et al., 2011a, 2011b; Zimmermann et al., 2011, 2013). However, it is also attributable to limitations of the three types of methods that have been used to induce passive eye movements. One method is to eliminate the EOM proprioceptive signals by use of surgical (Guthrie et al., 1983; Lewis et al., 1998) or pharmacological approaches (O'Keefe & Berkley, 1991). The second method is to mechanically displace an eye with a suction lens (Keller & Robinson, 1971) or by having the subject manually press on one of their eyes. The third method is to perturb the proprioceptive representation by vibrating the extraocular muscle tendon or electrically stimulating extraocular muscles (Han & Lennerstrand, 1999). These approaches suffer from the fact they may disrupt ongoing behaviors and create other sensory or motor signals. In the present study, we described a novel approach, which employs electromagnetic force (EMF) to induce passive eye movements in rats. The goal of the experiments was to demonstrate that the EMF approach is an effective tool for producing eye movements without inducing motor or non-proprioceptive somatosensory signals. Consequently, it can be used to determine the roles of eye position proprioceptive signals in visual localization and gaze control.

MATERIALS AND METHODS

Animals

A total of nine pigmented, female Long-Evans rats (Harlan Labs, Indianapolis, IN, USA) weighing 250–300 g were used in this study. Six of them were for EMF-induced eye movement experiments and three of them were for histological experiments. All procedures were carried out in accordance with NIH guidelines and approved by the Institutional Animal Care and Use Committee at the University of Mississippi Medical Center.

Surgical procedures

All surgical procedures were performed aseptically, as described before (Zhu et al., 2011). Briefly, a rat was implanted with a small head holder on the skull and allowed 7 days for recovery before eye movement tests. On the day of testing, the rat was first anesthetized with 5% isoflurane-O_2 (2 L/min). Once the rat was sedated, the isoflurane level was maintained at 2.5% throughout the rest of the procedure. A drop of

ophthalmic solution (Proparacaine Hydrochloride Ophthalmic Solution, USP 0.5%, Valeant Pharmaceuticals North America LLC, NJ, USA) was applied on the top of corneal surface for local anesthesia. Next, a small magnetic disk ~0.7 mm in diameter and 0.5 mm in thickness was attached by 3 mol/L Vetbond (n-butyl-cyanoacrylate) tissue adhesive (St Paul, MN, USA) to the surface of the eyeball nasal to the pupil (Figure 1A). The line connecting the magnet poles was tangential to eye surface. A small soft iron core rod (5 mm diameter) was placed within 8–15 mm of the magnet and aligned with the line connecting the magnet poles. The end of the rod away from the magnet was inside of an electromagnetic coil (Figures 1, 2), which generated magnetic field to magnetize the rod when current passed through the coil. The magnet field amplitude and onset were monitored by recording the EM coil current signal. The larger the activation current intensity (0.1–0.6 A), the stronger the electromagnetic field it generates. Based on the specifications of the EM coil (Figure 2), we used the following equation to estimate the magnetic flux (B) generated by activation current.

$$B = n \times I/(L_{core}/\mu + L_{gap}/\mu_0) \tag{1}$$

Where B is magnetic flux in Teslas, n is number of turns, I is activation current in Amperes, L_{core} is the length of the core in meters, L_{gap} is the distance from the core, μ is permeability of soft iron and μ_0 is permeability of air. At 10 mm from the core, an activation current of 0.6 A generated a magnetic flux of about 0.2 Teslas.

Eye movement recording

Horizontal and vertical eye position signals were recorded using a video-based ISCAN ETS-200 eye tracking system (ISCAN, Burlington, MA, USA). An infrared camera equipped with a zoom lens (Computar Optics Group, Japan) was attached to the platform of the rotator/sled and was focused on the left eye of the rat, which was secured to platform via the head holder. The rat's eye was illuminated by a standard ISCAN multiple infrared LED illuminator attached to the camera to produce a reference of corneal reflection (CR) for measuring eye position in the orbit. The eye tracker tracks the pupil center and the CR at a speed of 240 frames per second with a spatial resolution of 0.1 degrees. The differences of the two signals provided real-time signals related to eye position. Calibration was achieved by rotating the camera from left 10 degrees to right 10 degrees around the vertical axis of the recorded eye (de Jeu & de Zeeuw, 2012).

Electrical stimulation of abducens nucleus

Rats were anesthetized by isoflurane with their heads fixed on the stereotaxic frame through the use of surgically implanted head holder. The right occipital bone was opened and the cerebellum exposed. A microelectrode pulled from a thin glass pipette (OD: 1.2 mm; ID: 0.9 mm; Sutter Instruments, Novato, CA, USA) was filled with 3 mol/L sodium chloride (10–20 MΩ) and was advanced to the abducens nucleus using coordinates in the atlas of Paxinos & Watson (2009). The abducens nucleus was identified as the site where abducting eye movements

were evoked by low intensity electrical stimulation (10 mA, 200 ms duration, 100 Hz, pulse duration 0.2 ms) delivered through the recording electrode. Stimulation-evoked eye movement was recorded by the eye tracker. By varying current intensity, electrical stimulation evoked eye movements with varying amplitudes were produced. After completion of the experiments, the recording sites were marked by ejecting fast green with a negative 7 mA current for 10 min, and their locations were subsequently verified histologically.
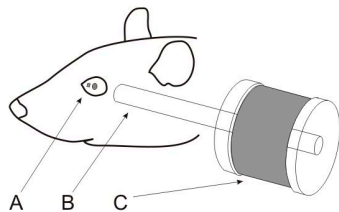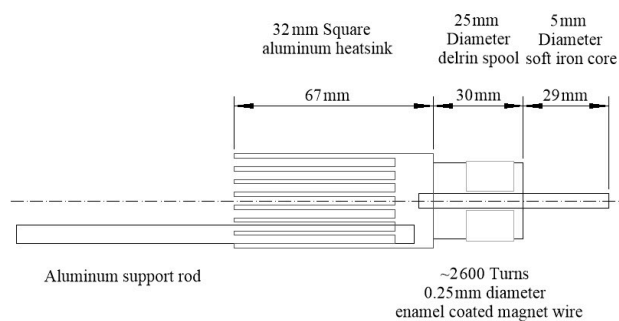

Figure 1 Schematic illustration of the experimental setup
After anesthesia, a small magnet was attached to the surface of the rat's left eyeball nasal to the pupil (A). The line connecting the poles of the magnet was in the direction tangent to the eye surface. A small metal rod (B) was placed within 8–15 mm of the magnet and aligned with the line connecting its poles. The end of the metal rod away from the magnet was surrounded by an electromagnetic coil (C), which generated magnetic field to magnetize the metal rod when current passed through the coil.

Figure 2 Schematic illustration of the electromagnetic device
It has a 59 mm soft iron core rod wrapped with ~2 600 turns of enamel coated magnet wire (0.25 mm diameter). The rod is attached to an aluminum heatsink and an aluminum support rod.

Data acquisition and analysis
Signals related to horizontal and vertical eye position and detecting coil voltage were sampled at 1 kHz at 16 bits resolution by a CED Power 1401 system (Cambridge Electronics Devices, Cambridge, UK). Eye movement responses were analyzed using Spike2 (Cambridge Electronics Devices, Cambridge, UK). Raw eye position data were filtered and differentiated with a band-pass of DC to 50 Hz to obtain eye velocity data. Trials in which there was no pupil tracking within 50 ms of the onset of the EMF onset were rejected (less than 5%). Trials in the data stream were aligned with the EMF onset and averaged (~100 trials per condition) to obtain low-noise estimates of eye position and velocity as a function of time. The EMF induced a displacement of eye position, whose direction was dependent on the EMF polarity (attractive or repulsive). After the EMF was turned off, the eye returned to

its initial position with an exponential time course, which was fitted by a sum of two exponentials (Anderson et al., 2009).

$$A(t) = A_1 e^{-(t/T1)} + A_2 e^{-(t/T2)} \qquad (2)$$

Examination of extraocular muscle morphology
In order to determine whether repetitive EMF-induced movements of the eye damaged the orbital contents, the eyes of three rats were examined histologically. Following completion of >3 000 EMF-induced eye movements toward the ear (i.e., stretching the medial rectus), rats were sacrificed via intracardiac perfusion with 4% paraformaldehyde in pH7.2, 0.1 mol/L phosphate-buffered saline (PBS). The orbit and its contents (bone, globe, extraocular muscles and glands) were harvested. The globe and extraocular muscles were placed in 30% sucrose in pH 7.2, 0.1 mol/L phosphate buffer (PB) solution. They were then cryoprotected by moving them through increasingly concentrated solutions of Cryomatrix embedding medium (Shandon Cryomatrix, Thermo Fisher Scientific Inc., DE, USA). The globe was then oriented in a disposable mold containing Cryomatrix and frozen. Once the specimen was cooled to −19 ℃, individual sections containing the globe and extraocular muscles were cut serially at 35 μm on a cryostat (Thermo Shandon Cryotome E cryostat, Thermo Fisher Scientific Inc., DE, USA). Sections were secured to cold, gelatin coated glass slides. They were then stained using Masson Trichrome stain, cleared and cover slipped. Digital photographs were taken using NIS-Elements AR and a Nikon Eclipse E600 light microscope equipped with a 1.5 megapixel Nikon DS-Ri1 high resolution camera. When necessary, images were adjusted for brightness, contrast and color using Adobe Photoshop CS5 to replicate the image as it appeared when visualized under the microscope.

RESULTS

Passive eye movement induced by EMF
The EMF induced well-defined eye movements in both horizontal and vertical directions. In the example shown in Figure 3, negative current pulses (20 ms, −0.55 A) generated attractive EMF to the magnet at a distance of 10 mm, which rotated the left eye toward the left ear with a latency of ~5 ms, resulting in a passive eye movement of 11.4 deg in the leftward horizontal direction and 2.2 deg in the upward direction (Figure 3A). About 11 ms after the EMF was turned off, the elasticity of the eye plant drove the eye toward its initial position with exponential a time course. Plots of this movement could be fitted with two time constants (8.5 ms and 557 ms, R^2=0.99, Figure 3A, blue dotted line). Positive current pulses (20 ms, 0.55 A) generated repulsive EMF to the magnet, which rotated the left eye away from the left ear with a latency of ~5 ms, resulting in a passive eye movement of 7.4 deg in the rightward horizontal direction and 1.0 deg in the downward direction (Figure 3B). About 9 ms after the EMF was turned off, the elasticity of the eye plant drove the eye back to its initial position with an exponential time course, which could be fitted with two time constants (6.7 ms and 228.1 ms, R^2=0.99, Figure 3B, blue dotted line).
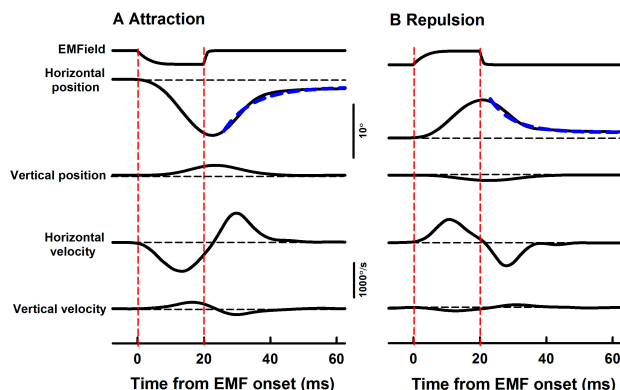
Figure 3 Averaged eye position and velocity responses to EMF (Rat1)

A: Attractive EMF induced passive eye movements of the left eye toward the left ear. B: Repulsive EMF induced passive eye movements of the left eye away from the left ear. The vertical dashed lines indicate EMF onset (current pulse: 0.55 A; 20 ms). Horizontal dashed lines indicate initial eye position and baseline eye velocity (zero). Upward traces indicate eye movements away from the left ear. Downward traces indicate eye movements toward the left ear.

To assess the effectiveness of using EMF to induce passive eye movements, we examined effects of EM coil current intensity (0.1 A–0.6 A) on amplitudes of EMF-induced eye movement. Figure 4A shows representative eye responses (Rat2) at two EM coil current intensities (0.3 A and 0.4 A) and two polarities (repulsion and retraction) at a distance of 10 mm. EM coil currents with higher intensities induced eye movements with larger amplitudes. Figure 3B summarizes eye movement responses from four rats with attraction EMF (black symbols and lines) and three rats with repulsion EMF (grey symbols and lines). Eye movement amplitudes increased linearly with EM coil intensity. For the four cases with attraction EMF (Figure 4B, black lines), the slopes of eye movement-current intensity are 23.6±0.9 deg/A, 24.3±3.6 deg/A, 10.2±1.1 deg/A and 3.9±1.4 deg/A, respectively. For the three cases with repulsion EMF (Figure 4B, grey lines), the slopes of eye movement-current intensity are 12.2±0.9 deg/A, 9.4±0.8 deg/A and 3.2±0.2 deg/A, respectively.

We also examined effects of EM coil current duration (5–30 ms) on amplitudes of the EMF-induced eye movement. Figure 5A shows representative eye responses at three EM coil current durations (15 ms, 20 ms and 25 ms, 0.55 A intensity) and two polarities (repulsion and retraction) at a distance of 10 mm. EM coil currents with longer durations induced eye movements with larger amplitudes. Figure 5B summarizes eye movement responses from 2 rats with attraction EMF (black symbols and lines) and repulsion EMF (grey symbols and lines). Eye movement amplitude increased linearly with EM coil current duration. For attraction EMF, the slopes of eye movement-current duration are 0.59±0.03 deg/ms and 0.26±0.04 deg/ms for Rat1 and Rat5, respectively. For repulsion EMF, the slopes of eye movement-current duration are 0.44±0.05 deg/ms and 0.1±0.03 deg/ms for Rat1 and Rat5, respectively.
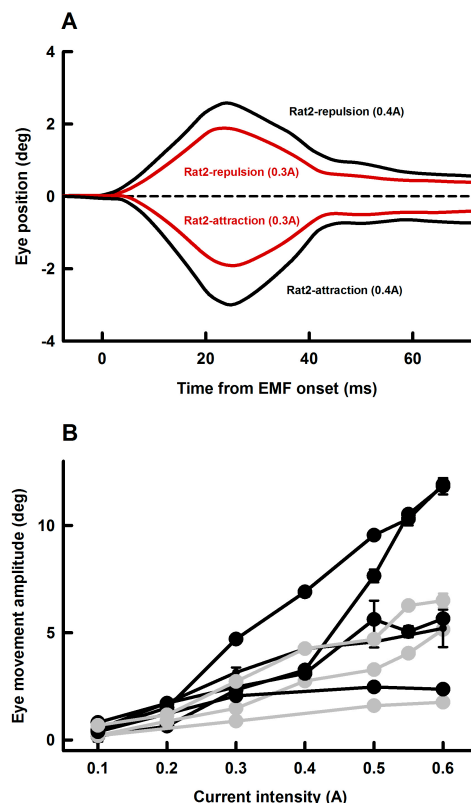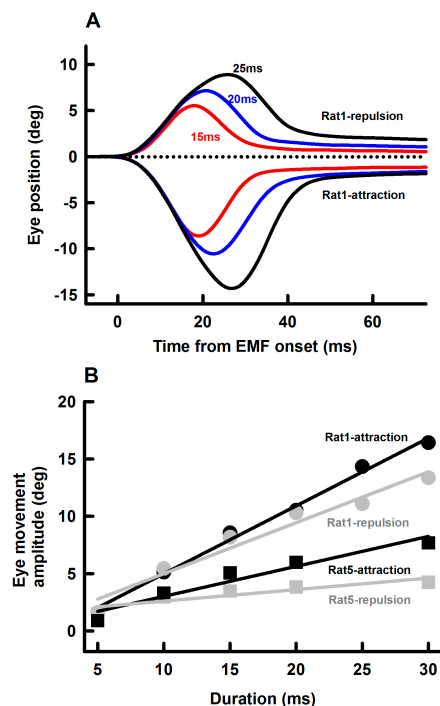
Figure 4 Effect of EM coil current intensity on EMF-induced eye movements

A: Representative averaged eye movement responses of Rat2 at two current intensities for the two polarities. Error bars indicating standard error are within the thickness of the lines. B: Summary of amplitudes of EMF-induced eye movements as functions of current intensity from 4 rats with attraction EMF (black symbols and lines) and 3 rats with repulsion EMF (grey symbols and lines). EM distance from the magnet on the rat eye (10 mm) and EM duration (20 ms) remained unchanged throughout the measurements. Error bars indicating standard errors are within the thickness of the symbols.

Effects of the magnet-metal rod distance on the EMF-induced eye movement

Since the EMF is inversely related to square of distance between the magnet and the magnetized metal rod, the amplitudes of the EMF-induced eye movements were expected to be inversely related to square of the distance. Figure 6 plotted the amplitudes of EMF-induced eye movements as a function of the distance for two rats. The two solid lines show that the following equations provide excellent fits of the data.

$$E = 1424.9/D^2 \qquad (3)$$
$$(R^2 = 0.99, \mathrm{Rat1})$$

$$E = 786.7/D^2 \qquad (4)$$
$$(R^2 = 0.99, \mathrm{Rat2})$$

Where E is the amplitude of EMF-induced eye movement and D is the distance between the magnet and the metal rod (Figure 1).

Main sequence of EMF-induced eye movement

To assess the dynamics of the EMF-induced eye movements, we compared their main sequences to that of saccades in awake rats and the eye movements evoked by microstimulation of the abducens nucleus in anesthetized rats. Peak velocities of the EMF-induced eye movement were plotted against their amplitudes for three rats (Figure 7, green/blue/red symbols). Data from the three animals fell on a single straight line with a slope of 89±1 deg/s/deg (R^2=0.98), indicating a well-defined main sequence for this condition. However, since EMF had a much more rapid onset than the muscle forces generated during saccade and abducens nucleus stimulation, the main sequence of the EMF-induced eye movements exhibited a steeper slope than that of the awake saccade (Figure 7, black symbols, slope of 65±10 deg/s/deg, R^2=0.62), as well as eye movements induced by abducens nucleus stimulation in anesthetized rats (Figure 7, grey symbols, slope of 36±2 deg/s/deg, R^2=0.9) (P<0.01).

Figure 5 Effect of EM current duration on EMF-induced eye movements

A: Representative averaged eye movement responses (Rat1) at three current durations for the two polarities. Error bars indicating standard error are within the thickness of the lines. B: Amplitudes of EMF-induced eye movements as functions of current duration from Rat1 and Rat5. Other parameters (EM distance from the magnet on the rat eye: 10 mm; EM current: 0.55 A) remained unchanged throughout the measurements. Error bars indicating standard errors are within the symbols.

Effects of passive stretching on the extraocular muscle morphology

The eyes used in these experiments were stained with Masson trichrome stain to evaluate whether repeated FMF-induced eye

movements resulted in morphological changes. Since the EMF-induced eye movements were always in the abduction direction for this experiment, any strain was presumed to be induced on the medial rectus muscle, which was stretched without the tonic eye position motor commands being suppressed. The lateral rectus, would be shortened under these procedures. Figure 8 shows photomicrographs of a section taken through a left globe containing both the stretched medial rectus muscle (Figure 8A, B) and the compressed lateral rectus muscle (Figure 8C, D). The EMF-induced eye movements did not appear to displace the medial rectus muscle from its normal location between lobes of the Harderian gland (Figure 8A). The medial rectus muscle scleral insertion appeared intact. No obvious tearing or separation of the muscle insertion were noted. The morphology of the neurovascular bundles (not illustrated) in the stretched medial rectus muscle was similar to the control lateral rectus muscle. Medial rectus and lateral rectus muscle structure (boxes in Figure 8A, C) are shown at high magnification (Figure 8B, D). The stain revealed similar striation patterns for the medial rectus (Figure 8B) and lateral rectus (Figure 8D) muscles. No obvious structural changes were seen when viewed at higher magnification. Taken together, the medial rectus muscle morphology, as determined by this qualitative assessment, appeared unchanged by this perturbation. We hypothesized that damage to the medial rectus muscle structure might manifest as increases in local inflammatory response including an increase in inflammatory cells or extravasation of blood into the surrounding connective tissue. However, no obvious increase in the inflammatory cells or accumulation of blood within the muscle or surrounding connective tissue was observed in the orbit. Thus, based on the qualitative light microscopic analysis, the EMF-induced eye movements observed in this study did not appear to produce gross changes to the EOM morphology.
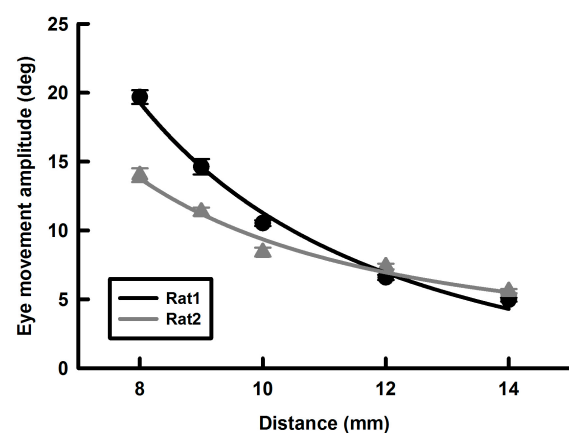
Figure 6 Effect of the distance between the tip of the metal rod (C in Figure 1) and the magnet on the rat eye (B in Figure 1) on EMF-induced eye movements

Red dots are for Rat1 and blue dots are for Rat2. EM current was 0.55 A and EM duration was 20 ms. Error bars indicate standard errors are within the symbols.
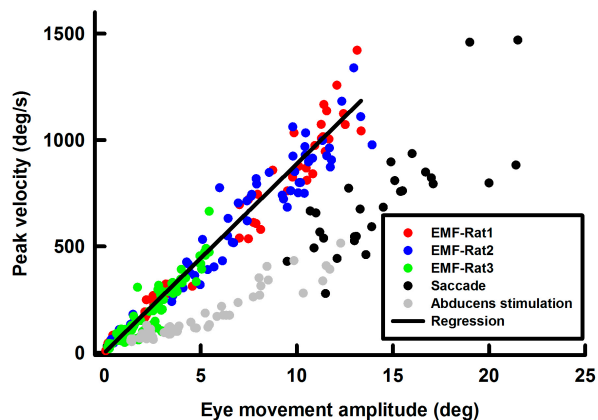
Figure 7 Main sequence of EMF-induced eye movements (each rat is indicated by different colored symbols)
The grey symbols and the black symbols are for abducens stimulation-induced eye movements in anesthetized rats and saccades in awake rats, respectively.
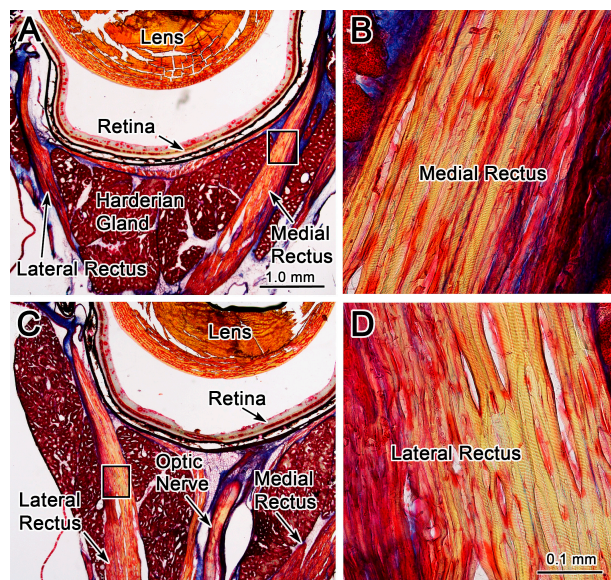

Figure 8 Morphologic evidence against EMF-induced damage in extraocular muscle fibers
Photomicrographs of Mason trichrome stained sections through the left globe at the level of the medial rectus (stretched) and the lateral rectus (compressed) muscles. Low power photomicrographs show the organization of the medial rectus (A) and lateral rectus (C) muscles. When the medial rectus muscle (box in A) and the lateral rectus muscle (box in C) are viewed at higher magnification in B and D respectively, they appear the same. Scale bars: 1.0 mm for A and C; 0.1 mm for B and D.

DISCUSSION

The feasibility of using EMF to generate eye movement was first demonstrated by Bohlen & Chen (2016) in a ping-pong ball model. In the present study, we presented further evidence in a rat model that the EMF induced well-defined passive eye movements over a range of amplitudes (up to 15 deg) and peak velocities (up to ~1 500 deg/s) without causing damages to the extraocular muscles. The EMF approach

offers important features that make it an excellent tool to study neural processing of EOM proprioception signals in awake animal models. First, the EMF generates passive eye movement without physically contacting the eye. This feature is essential for perturbing fixation or ongoing eye movements in awake and behaving subjects. Second, the EMF induces eye movement with a very short latency (<5 ms). Since a typical saccadic eye movement lasts only 20–50 ms, the rapid activation and deactivation of the electromagnet minimizes potential biases of subjects' attention and anticipation. Third, by selecting appropriate current parameters (polarity, intensity and duration), passive eye movements can be generated with desired direction, amplitude and duration. This feature allows generation of a wide range of passive movements to fully characterize neural encoding of the EOM proprioceptive signals. Fourth, by varying magnet and rod positions, it is possible to perturb different EOMs and generate passive eye movements in different directions. This would overcome the limitations of the vibratory method, which primarily activates the inferior rectus muscle, as the tendons of other EOMs are difficult to reach via this technique (Han & Lennerstrand, 1999; Velay et al., 1997).

Previous studies on proprioceptive signals of the EOMs
There is a long history of eye muscle proprioception investigation (for review see Donaldson, 2000). Since it is difficult to access the primary trigeminal afferent neurons under chronic conditions, early studies of extraocular proprioceptors primarily relied on examining the effects of sectioning the ophthalmic branch of the trigeminal nerve (Guthrie et al., 1983; Lewis et al., 1998) or surgically altering EOM insertions to alter the position of an eye in the orbit (Steinbach & Smith, 1981). Although important insights have been gained in these studies, their approaches were invasive, irreversible, and the results may have been confounded by central nervous system compensation. Investigators have also tried to directly manipulate proprioceptive sensory signals while subjects performing visuo-motor tasks, by pulling on the eye via sutures or suction, or by tugging or vibrating eye muscles. For example, Keller & Robinson (1971) trained monkeys to fixate a visual target with one eye while the other eye was passively pulled by force applied to a contact lens. Abducens neurons on the side of the pulled eye were recorded. They found that the abducens neuron activity exhibited no change in response to the passively generated eye movements, suggesting that there was no stretch reflex in the lateral rectus muscle. While these results were widely interpreted as evidence against a role of the EOM afferent signals in eye movement control, it is important to note the study's limitation, i.e., it only generated slow passive eye movements and the eye was not moving. It did not rule out the possibility that stretch reflexes may be present if the eye was moving at high velocity. Indeed, another study using contact lenses to impede the movements of an eye during saccades showed changes in the contralateral eye (Knox et al., 2000). Furthermore, in a recent study in anesthetized rats and squirrel monkeys, Dancause et al. (2007) manually rotated the eye, while measuring the EMG activity

in the lateral rectus muscle. By producing passive eye movements of ~25 deg within about 100 ms (eye velocity of 200 deg/s), they observed typical stretch reflexes in these muscles.

In addition to using surgical and mechanical approaches to manipulate the proprioceptive EOM signal, pharmacological approaches have also been used to investigate the functional roles of EOM proprioceptive signals. For example, O'Keefe & Berkley (1991) injected dibucaine (a high-potency paralytic agent) in one eye of anesthetized cats to block sensory nerve transmission in the eye.   They found that the injection reduced frequency and amplitude of spontaneous eye movement in both the treated and non-treated eyes and concluded that proprioceptive sensory signals from one eye are used to modulate movements of the other eye. This is consistent with the fact that the unilateral trigeminal inputs are distributed bilaterally by trigemino-trigeminal projections (Warren & May, 2013).

In contrast to the extensive studies on the behavioral effects of manipulating EOM proprioceptive signals, few studies have examined the neural substrates of the EOM proprioceptive signals. In an earlier study, Fuchs & Kornhuber (1969) reported evoked potential responses in cat cerebellum while their eyes being rotated at saccade velocities. In an important recent study, Goldberg and colleagues discovered a representation of proprioceptive eye position signals in the somatosensory cortex of behaving monkeys (Wang et al., 2007). To elucidate the nature of these eye position-related signals, they injected lidocaine into the retro-orbital space of an eye in awake behaving monkeys to block all sensory inputs from the eye. The injection substantially reduced eye position-sensitive neuronal activity in the somatosensory cortex. Their subsequent studies of gain fields in parietal cortex suggest that while corollary discharge is used for guiding the initial saccades in a memory guided series, proprioception plays the more important role in subsequent saccades in the series (Sun & Goldberg, 2016; Xu et al., 2012).

Future studies

In comparison with neural processing of corollary discharge signals related to oculomotor commands (Sommer & Wurtz, 2008), neural processing of EOM proprioceptive signals has received much less attention. However, understanding the EOM feedback signals and their interactions with the feedforward efference copy signals has important functional and clinical implications.   It was the finding of EOM proprioceptive signals in the somatosensory cortex (Wang et al., 2007) that reignited interest in elucidating the role that EOM proprioceptive signals play for gaze control and spatial perception at different levels of the oculomotor system. The present study was an effort to develop the EMF approach for effective manipulation of proprioceptive signals without changing ongoing motor commands. The results demonstrate the feasibility of using EMF approach in other species, including monkeys. Ongoing studies are directed at improving the EMF approach in two ways. One is to develop a ferrous metal ring that can be implanted under the conjunctiva of the eyes. The other one is to further develop the EM coil and control

of the activation current so that both we can either generate an eye movement with desired speeds and amplitudes or hold the eye at any desired position for a period of time. This approach will offer an important technical advancement to facilitate behavioral and neurophysiological studies in awake and behaving subjects.

COMPETING INTERESTS

AUTHORS' CONTRIBUTIONS

Y.Y., J.H., C.Z., H.Z. and W.Z. designed the study.   Y.Y., J.H., C.Z., T.C., D.S.S., S.W., A.A.A., J.A., Y.O., S.W., H.Z. and W.Z. performed the experiments and data analyses. Y.Y., J.H., C.Z., D.S.S., S.W., P.M., H.Z. and W.Z. revised the manuscript. All authors read and approved the final version of the manuscript.

REFERENCES

Allin F, Velay JL, Bouquerel A. 1996. Shift in saccadic direction induced in humans by proprioceptive manipulation: a comparison between memory-guided and visually guided saccades. *Experimental Brain Research*, **110**(3): 473–481.

Anderson SR, Porrill J, Sklavos S, Gandhi NJ, Sparks DL, Dean P. 2009. Dynamics of primate oculomotor plant revealed by effects of abducens microstimulation. *Journal of Neurophysiology*, **101**(6): 2907–2923.

Balslev D, Miall RC. 2008. Eye position representation in human anterior parietal cortex. *The Journal of Neuroscience*, **28**(36): 8968–8972.

Billig I, Buisseret DC, Buisseret, P. 1997. Identification of nerve endings in cat extraocular muscles. *The Anatomical Record*, **248**(4): 566–575.

Bohlen MO, Chen LL. 2016. A noninvasive electromagnetic perturbation approach to probe extraocular proprioception. *Journal of AAPO*, **20**(1): 12–18.

Bridgeman B, Stark L. 1991. Ocular proprioception and efference copy in registering visual direction. *Vision Research*, **31**(11): 1903–1913.

Campos EC. 1986. Sensory and sensori-motor adaptations in strabismus: Their role in space perception. *Acta Psychologica*, **63**(3): 281–295.

Campos EC, Bolzani R, Schiavi C, Fanti MR, Cavallini GM. 1989. Further evidence for the role of proprioception in space perception. *Documenta Ophthalmologica*, **72**(2): 155–160.

Donaldson IM. 2000. The functions of the proprioceptors of the eye muscles. *Philosophical Transactions of the Royal Society of London. Series B, Biological Sciences*, **355**(1404): 1685–1754.

Dancause N, Taylor MD, Plautz EJ, Radel JD, Whittaker T, Nudo RJ, Feldman AG. 2007. A stretch reflex in extraocular muscles of species purportedly lacking muscle spindles. *Experimental Brain Research*, **180**(1): 15–21.

de Jeu M, de Zeeuw CI. 2012. Video-oculography in mice. *Journal of Visualized Experiments*, **65**: e3971, doi: 10.3791/3971.

Fuchs AF, Kornhuber HH. 1969. Extraocular muscle afferents to the cerebellum of the cat. *The Journal of Physiology*, **200**(3): 713–722.

Gauthier GM, Nommay D, Vercher JL. 1990. Ocular muscle proprioception and visual localization of targets in man. *Brain*, **113**(Pt 6): 1857–1871.

Guthrie BL, Porter JD, Sparks DL. 1983. Corollary discharge provides accurate eye position information to the oculomotor system. *Science*, **221**(4616): 1193–1195.

Han Y, Lennerstrand G. 1999. Changes of visual localization induced by eye and neck muscle vibration in normal and strabismic subjects. *Graefe's Archive for Clinical and Experimental Ophthalmology*, **237**(10): 815–823.

Helmholtz VH. 1925. Treatise on Physiological Optics, Volume III. Mineola, NY: Dover Publication Inc.

Keller EL, Robinson DA. 1971. Absence of a stretch reflex in extraocular muscles of the monkey. *Journal of Neurophysiology*, **34**(5): 908–919.

Knox PC, Weir CR, Murphy PJ. 2000. Modification of visually guided saccades by a nonvisual afferent feedback signal. *Investigative Ophthalmology & Visual Science*, **41**(9): 2561–2565.

Lennerstrand G, Tian S, Han Y. 1997. Effects of eye muscle proprioceptive activation on eye position in normal and exotropic subjects. *Graefe's Archive for Clinical and Experimental Ophthalmology*, **235**(2): 63–69.

Lewis RF, Gaymard BM, Tamargo RJ. 1998. Efference copy provides the eye position information required for visually guided reaching. *Journal of Neurophysiology*, **80**(3): 1605–1608.

Lewis RF, Zee DS, Gaymard BM, Guthrie BL. 1994. Extraocular muscle proprioception functions in the control of ocular alignment and eye movement conjugacy. *Journal of Neurophysiology,* **72**(2): 1028–1031.

Lienbacher K, Mustari M, Ying HS, Büttner-Ennever JA, Horn AK. 2011a. Do palisade endings in extraocular muscles arise from neurons in the motor nuclei? *Investigative Ophthalmology & Visual Science*, **52**(5): 2510–2519.

Lienbacher K, Mustari M, Hess B, Büttner-Ennever J, Horn AK. 2011b. Is there any sense in the Palisade endings of eye muscles? *Annals of the New York Academy of Sciences*, **1233**: 1–7.

O'Keefe LP, Berkley MA. 1991. Binocular immobilization induced by paralysis of the extraocular muscles of one eye: evidence for an interocular proprioceptive mechanism. *Journal of Neurophysiology*, **66**(6): 2022–2033.

Paxinos G, Watson C. 2009. The Rat Brain in Stereotaxic Coordinates. Cambridge, MA: Academic Press.

Porter JD, Guthrie BL, Sparks DL. 1983. Innervation of monkey extraocular muscles: localization of sensory and motor neurons by retrograde transport of horseradish peroxidase. *The Journal of Comparative Neurology*, **218**(2):

208–219.

Sherrington CS. 1918. Observations on the sensual role of the proprioceptive nerve-supply of the extrinsic ocular muscles. *Brain*, **41**(3–4): 332–342.

Skavenski AA. 1972. Inflow as a source of extraretinal eye position information. *Vision Research*, **12**(2): 221–229.

Sommer MA, Wurtz RH. 2008. Brain circuits for the internal monitoring of movements. *Annual Review of Neuroscience*, **31**: 317–338.

Steinbach MJ, Smith DR. 1981. Spatial localization after strabismus surgery: evidence for inflow. *Science*, **213**(4514): 1407–1409.

Sun LD, Goldberg ME. 2016. Corollary discharge and oculomotor proprioception: cortical mechanisms for spatially accurate vision. *Annual Review of Vision Science*, **2**: 61–84.

Velay JL, Allin F, Bouquerel A. 1997. Motor and perceptual responses to horizontal and vertical eye vibration in humans. *Vision Research*, **37**(18): 2631–2638.

Wang X, Zhang M, Cohen IS, Goldberg ME. 2007. The proprioceptive representation of eye position in monkey primary somatosensory cortex. *Nature Neuroscience*, **10**(5): 640–646.

Warren S, May PJ. 2013. Morphology and connections of intratrigeminal cells and axons in the macaque monkey. *Frontiers in Neuroanatomy*, **7**: 11.

Xu BY, Karachi C, Goldberg ME. 2012. The postsaccadic unreliability of gain fields renders it unlikely that the motor system can use them to calculate target position in space. *Neuron*, **76**(6): 1201–1209.

Zhu H, Tang X, Wei W, Mustain W, Xu Y, Zhou W. 2011. Click-evoked responses in vestibular afferents in rats. *Journal of Neurophysiology*, **106**(2): 754–763.

Zimmermann L, May PJ, Pastor AM, Streicher J, Blumer R. 2011. Evidence that the extraocular motor nuclei innervate monkey palisade endings. *Neuroscience Letters*, **489**(2–4): 89–93.

Zimmermann L, Morado-Díaz CJ, Davis-López de Carrizosa MA, de la Cruz RR, May PJ, Streicher J, Pastor ÁM, Blumer R. 2013. Axons giving rise to the palisade endings of feline extraocular muscles display motor features. *The Journal of Neuroscience*, **33**(7): 2784–2793.

Depressed female cynomolgus monkeys (*Macaca fascicularis*) display a higher second-to-fourth (2D:4D) digit ratio

Wei Li[1,2,3,#], Ling-Yun Luo[4,#], Xun Yang[2,3], Yong He[2,3], Bin Lian[2,3], Chao-Hua Qu[2,3], Qing-Yuan Wu[2,3], Jian-Guo Zhang[2,3], Peng Xie[2,3,*]

[1] *Department of Neurology, Army Medical Center of PLA, Chongqing* 400042, *China*

[2] *Institute of Neuroscience, Chongqing Medical University, Chongqing* 400016, *China*

[3] *Chongqing Key Laboratory of Neurobiology of Chongqing Medical University, Chongqing* 400016, *China*

[4] *Department of Neurology, the Third Affiliated Hospital of Sun Yat-Sen Universlty Yuedong Hospital, Guangzhou Guangdong* 514700, *China*

ABSTRACT

This research aimed to provide evidence of a relationship between digit ratio and depression status in the cynomolgus monkey (*Macaca fascicularis*). In stable cynomolgus monkey social groups, we selected 15 depressed monkeys based on depressive-like behavioral criteria and 16 normal control monkeys. All animals were video recorded for two weeks, with the duration and frequency of the core depressive behaviors and 58 other behaviors in 12 behavioral categories then evaluated via behavioral analysis. Finger lengths from the right and left forelimb hands of both groups were measured by X-ray imaging. Finger length and digit ratio comparisons between the two groups were conducted using Student's *t*-test. In terms of the duration of each behavior, significant differences emerged in "Huddling" and five other behavioral categories, including Ingestive, Amicable, Parental, Locomotive, and Resting. In addition to the above five behavioral categories, we found that depressed monkeys spent less time in parental and rubbing back and forth behaviors than the control group. Furthermore, the 4th fingers were significantly longer in the left and right hands in the control group relative to the depressed monkeys. The second-to-fourth (2D:4D) digit ratio in the left and right forelimb hands was significantly lower in the control group than that in the depressed group. Our findings revealed significant differences in finger lengths and digit ratios between depressed monkeys and healthy controls, which concords with our view that relatively high fetal testosterone exposure may be a protective factor against developing depressive symptoms (or that low fetal testosterone exposure is a risk factor).

INTRODUCTION

Major depressive disorder (MDD) is a debilitating psychiatric mood disorder that affects millions of individuals globally (Gelenberg, 2010). Our understanding of the biological basis of MDD is poor, and current treatments are ineffective in a significant proportion of cases. This likely relates to the lack of human and non-human primate research models compared with the dominant rodent models of depression, which possess translational limitations due to limited homologies with humans. Therefore, a more homologous primate model of depression is needed to advance our understanding of the pathophysiological mechanisms underlying depression and to provide a sound basis for conducting pre-clinical therapeutic trials.

Social stress plays a major role in the pathogenesis of depression (Krishnan & Nestler, 2008). In human research, depressive patients, especially women, are more likely to experience depression after prolonged stress (Sherrill et al., 1997). The diagnosis of depression in humans is based on various scales. In line with the DSM-V (Diagnostic and

Statistical Manual of Mental Disorders, fifth edition) diagnostic criteria, MDD is characterized by five (or more) of the following symptoms: depressed mood, loss of interest, weight change, sleep disturbance, psychomotor agitation or retardation, loss of energy, feelings of worthlessness, difficulty concentrating, and recurrent thoughts of death. These symptoms must persist for at least two weeks and must include depressed mood and / or loss of interest (Gnanavel & Robert, 2013). In determination of primate depressive behavior, the most reliable method is through behavioral phenotypes. Because of the inability to transfer pressure after being the subject of aggression, depressed female cynomolgus monkeys (*Macaca fascicularis*) can experience long-term social pressure. Shively et al. (2005) indicated that socially-subordinate female cynomolgus monkeys, who are likely weak competitors in social environments due to long-term attack and suppression, can exhibit similar pathogenetic processes as depression in humans. Female cynomolgus monkeys have several behavioral and physiological characteristics in common with human depression. They tend to spend more time alone than their dominant counterparts, exhibit greater vigilance, display slumped or collapsed body posture, show diminished interest in feeding and sex, and subdued communication and reciprocal grooming with others for at least two weeks (Shively et al., 2005). Huddling, which is defined as a slumped body posture with the head at or below the shoulders during the awake state (i. e., when the monkey's eyes are opened) accompanied by a relative lack in responsiveness to environmental stimuli, is used as a behavioral indicator of depression and is a core posture reflecting depressed mood in monkeys (Felger et al., 2007). Based on these well-established criteria, we successfully constructed a naturally occurring depression model in macaques (Xu et al., 2015). Because of the similarities in complex behavioral and psychological processes between macaques and humans, the development of naturally occurring animal models of disease, whether physical or psychological, is a valuable approach for translational research between human studies and induced primate models, especially for depression (Capitanio, 2017).

The ratio of the index to ring finger length is a commonly used measure. The male ring finger is longer than the index finger, whereas the index finger of the female is basically equal to that of the ring finger. The second-to-fourth (2D:4D) digit ratio was first proposed by Manning et al. (1998) to predict estrogen and sperm number and prenatal sex hormones. Under regulation of the Hox gene, hormone levels during embryonic development, especially the level of androgen, affect finger development (Goodman & Scamble, 2001). The 2D:4D ratio is present in a human embryo by the seventh week of pregnancy (Lutchmaya et al., 2004). Additionally, evidence suggests that in both males and females, the digit ratio can act as an indicator of the level of testosterone the developing fetus was exposed to, making it a useful indirect measure of organizational prenatal hormone exposure. Some research indicates that the 2D:4D ratio may also be an indicator of perinatal androgen action, whereby lower digit ratios predict greater androgen sensitivity (Smedley

et al., 2014). Thus, given that depression is a strongly sexually dimorphic trait, it is reasonable to expect that the 2D:4D ratio may be related to depression (Evardone & Alexander, 2009). Furthermore, previous investigations have confirmed that the 2D:4D ratio is associated with human behavior, such as aggression, cooperation, left-handedness, and human disease, including breast cancer, dyslexia, infertility, myocardial infarction, and autism (Ronalds et al., 2002). For instance, Bailey & Hurd (2005) reported that the 2D:4D ratio is related to individual aggressiveness, confidence, and competitive ability. Furthermore, other developmental disorders, emotional behaviors, and negative and affective symptoms in schizophrenia are reported to be related to the 2D:4D ratio (Carre et al., 2015). Previous studies have also shown that individuals with a higher 2D:4D ratio are more likely to suffer from depression. For instance, Smedley et al. (2014) found that a higher digit ratio is correlated with higher depression scores in females, but not males. To date, however, results have been inconsistent. For example, using a large sample comprised of 298 college students (149 males and 149 females), Bailey & Hurd (2005) found that more feminine ratios were associated with higher depression in men, but found no correlation between the 2D: 4D ratio and depression in women. Bailey & Hurd (2005) produced the unusual finding of no sex differences in depression, although digit ratios did differ in the expected direction. As such, it remains unclear to what degree depression and the 2D: 4D ratio, both characterized by marked sex differences, are related (Smedley et al., 2014).

Females are more susceptible to depression in social groups and depression is approximately twice more common among women than men (Trivers et al., 2006). Therefore, we chose female cynomolgus monkeys as our research targets. Based on our previous method (Xu et al., 2015), a total of 15 depressed female monkeys were selected across 52 enclosures, with 16 healthy subjects selected as controls from the original population (*n*=6 012). A strict radiographic procedure was used to measure index and ring finger lengths in both forelimb hands. This investigation aimed to provide evidence of a relationship between the digit ratio and depression status in the cynomolgus monkey.

MATERIALS AND METHODS

Ethics statement

Behavioral data acquisition was observational under normal circumstances and did not involve physical manipulation of the subjects or changes to their environment or diet. Animal care and housing procedures followed Chinese regulatory requirements and the Association for Assessment and Accreditation of Laboratory Animal Care International. In brief, complete animal husbandry and veterinary care were provided daily. Animals were fed a nutritious standardized diet, supplemented daily with fresh fruits and vegetables. Animals had unrestricted access to potable water and their enclosures were cleaned each day. Animals were observed daily by trained care-takers. Any observed abnormality, disease, or

injury was reported to the veterinary staff for diagnosis and treatment; this veterinary support was documented in both hard copy and electronic formats. In addition, this study was performed in strict accordance with the recommendations in the Guide for the Care and Use of Laboratory Animals of the Institute of Neuroscience of Chongqing Medical University (Approval No.: 20100031). Prior to implementation, the experimental protocol was approved by the Committee on the Ethics of Animal Experiments at Chongqing Medical University and was in accordance with state regulations.

Observation site

The *M. fascicularis* Feeding Base of Zhongke Experimental Animal Co., Ltd. is in Suzhou, China, at E31º07′03″ to E31º 07′06″, N120º19′08″ to N120º19′15″. The company imported the *M. fascicularis* subjects from Guangdong Province, China and from Vietnam in 1990, from which they established a domestication and breeding base for these monkeys.

Subjects

We scanned a total population of 6 012 adult female cynomolgus monkeys across all 52 enclosures. Depressive behavior was identified using the operational definition according to Shively's criteria: slumped or collapsed body posture (Figure 1), diminished interest in feeding and sex, and diminished communication and reciprocal grooming with others (Xu et al., 2015). Sixteen healthy adult female *M. fascicularis* subjects (aged 9−13 years) were randomly selected from the pool of 6 012 monkeys. A total of 15 depressed female monkeys (aged 10−12 years) were selected from the 52 enclosures based on the above-mentioned depression phenotypes lasting for at least two weeks. All subjects were reared in socially-stable colonies with negligible rates of conflict (Willard & Shively, 2012). Staff veterinarians ruled out disease in the subjects. Each colony was housed in an indoor free enclosure measuring 8.0 m×3.0 m×3.0 m (L× W×H) with continuous daylight exposure. Every colony was composed of two males, 16−22 adult females, and their offspring of less than six months of age. To reflect wild populations, the male:female ratio was maintained at 1:(7−10).
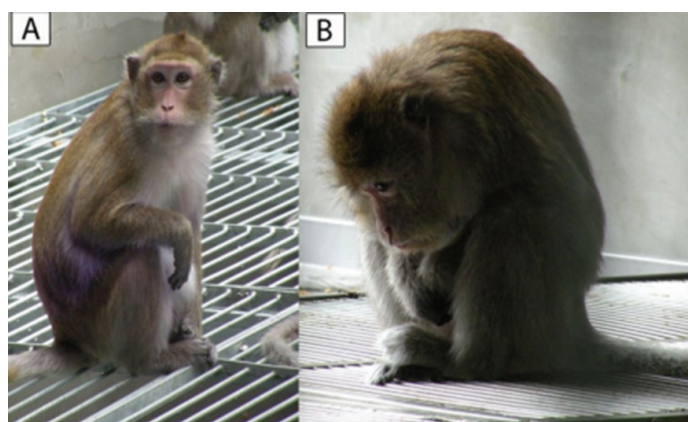
Figure 1 Core depressive behavior ("Huddling") in a cynomolgus monkey
A: Normal cynomolgus monkey; B: Depressed cynomolgus monkey exhibiting "Huddling" behavior.

Behavioral recording methods and scored behavioral items are described in our previous work (Xu et al., 2012). The duration and frequency of the core depressive behavior "Huddling" (Figure 1) and 58 other behaviors in 12 categories (Ingestive, Thermoregulatory, Rutting and estrous, Mating, Resting, Parental, Amicable, Conflict, Vigilance, Communication, Locomotive, Miscellaneous behaviors) were video recorded by three well-trained observers blind to the behavioral definition using NOLDUS Observer XT software (v10.0, Noldus Information Technology, Leesburg, PA, USA) during two consecutive weeks with four phases per day (A1 0900−0930 h; A2 0930−1000 h; P1 1500−1530 h; P2 1530−1600 h). Behavioral data were coded as duration (in seconds) and frequency (in count) for each discreet behavioral item per 30 min observational phase and presented as means±*SD*.

Finger length measurement with radiography

We measured index and ring finger lengths from the right and left forelimb hands in both groups after the last day of behavioral data acquisition using a digital radiography unit with a flat-panel digital detector (PLX8200, Perlove, Nanjing, China) (Kalichman et al., 2017). The digital detector was exposed to X-ray at 60 kVp, with an approximate detector-to-tube distance of 1 m. Exposure times were no greater than 0.1 s, resulting in 4.0 mA exposure. Three qualified staff performed this process in cooperation: one undertook anesthesia and hand-position adjustment, one operated the machine to acquire finger length, and one recorded the data and was blind to the experiment. Ketamine (10 mL / kg) anesthetic was administered intramuscularly (I.M.) in the distal hind limb at 0900 h (Nelson & Voracek, 2010). Approximately 10 min after ketamine injection, the finger length ratio was measured at an accuracy of 0.01 mm using X-ray imaging (Choi et al., 2011) (Figure 2).

Statistical methods

To assess the behavioral differences between depressed subjects and healthy controls, Student's *t*-test was performed
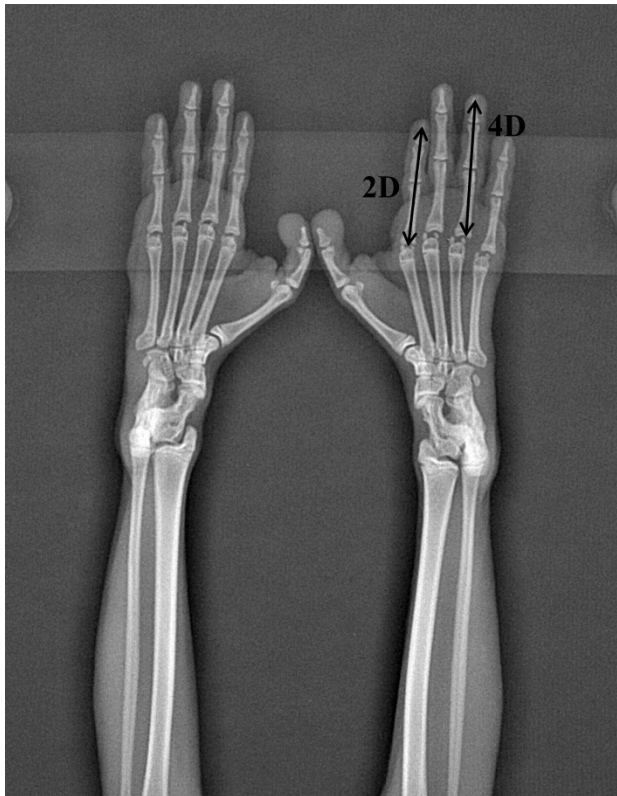
Figure 2 Forelimb hand X-ray image
2D: Index finger; 4D: Ring finger.

if the data were normally distributed; otherwise, the Mann-Whitney *U* test was applied. As there were 58 behavioral items in total, Bonferroni correction was used to reduce type I errors for multiple comparisons. Primate fingers are termed 1 through 5 from the thumb to the smallest digit, respectively. In this investigation, the 2D:4D digit ratio was used (Kyriakidis et al., 2010). To minimize error, all finger length data were presented as means±*SD*. Finger length and digit ratio comparisons between the two groups were conducted using Student's *t*-test. *P* values of less than 0.05 were deemed significant for all data. Data management and statistical analysis were performed using SPSS 21.0.

RESULTS

Differences in behavioral phenotype between depressed and control monkeys

In terms of the duration of behavior, depressed monkeys spent more time "Huddling" (*P*<0.001), in which the target displayed a fetal-like, self-enclosed posture with a lowered head during the awake state (i.e., when the monkey's eyes were opened). The increased duration of "Huddling" indicated that the depressed subjects recursively stayed in the depressed mood condition. For Ingestive behavior, the control subjects preferred to "feed while sitting" (*P*<0.05), whereas

the depressed subjects displayed more vigilance and preferred "feeding while hanging" to avoid potential threats and attacks. They also spent more time "licking food residue off the cage" (*P*<0.05) due to the pressure of other monkeys during normal food intake. In accordance with the depression criteria, depressed monkeys also spent less time drinking. The impact of pressure on both groups was further reflected in resting behavior, with the depressed group more reluctant to "hang on iron chain rest" (*P*<0.001) compared to the control group, but more willing to choose a remote area for resting, namely, "hanging on skylight rest" (*P*<0.001). Regarding locomotive behavior, depressed individuals exhibited less vitality in walking and standing and spent relatively less time performing "quadrupedal walking on floor" (*P*<0.001), "walking on iron chain" (*P*<0.001), and "standing" (*P*<0.05). Indicative of a friendly relationship among others, the control group received more amicable grooming (i.e., "being groomed" (*P*<0.001)) and groomed others more often (i. e., "mutual grooming" (*P*<0.001)) than exhibited by the depressed group, suggesting reduced interaction in depression. Furthermore, there was a reduction in the duration of "nursing" (*P*<0.05) parental behavior. For mating behavior, which is a sign of sexual interest, the duration of "copulation" (*P*<0.05) was higher in the control monkeys in comparison to the depressed females, with a significant difference in the frequency of mating behavior also observed (Table 2). In the end, except the frequency of behaviors matched with the duration of behaviors, a lower frequency of miscellaneous behavior (i.e., "rub hand back and forth" (*P*<0.001)) existed in depressed individuals, suggesting that depressed monkeys may be less imposing and lacking in confidence.

Finger length data
Finger length was measured in the 16 control and 15 depressed animals (Table 3). For both the left and right hand, the ring finger was significantly longer in the control group than that in the depressed group.

Digit ratio comparison
The digit ratio was significantly lower in the control group than in the depressed monkeys (Table 4), including the 2D:4D ratio in the right and left forelimb hands of depressed and control subjects.

DISCUSSION

With respect to primate finger length investigations, the 2D:4D ratio is strongly related to social behavior and physical aggression. Nelson & Shultz (2010) reported that a low 2D:4D ratio is associated with more competitive social systems, which is in accordance with our previous observation (Zhou et al., 2014) that depressed monkeys face greater competition for social resources–including feeding opportunities, comfortable resting places, and mating opportunities–and display significant deficits in social interactions. Thus, the cynomolgus monkey population is a suitable choice to study the relationship between the 2D:4D ratio and depression.

Table 1 Duration of behaviors observed in depressed and control subjects

Behavior		Duration			
Behavioral category	Behavior	Depressed group	Control subjects	P value	Adjusted P value
Core behavior	Huddling***	365.44±514.14	159.00±355.08	P<0.001	P<0.001
Ingestive behavior	Drinking***	2.51±13.09	5.92±21.59	P<0.001	P<0.001
	Feeding while hanging*	6.16±33.19	3.56±24.14	P=0.0004	P=0.0243
	Lick food residue off cage*	1.29±13.78	0.44±3.24	P=0.0007	P=0.0419
	Feeding while sitting***	29.73±89.06	63.29±171.94	P<0.001	P<0.001
Amicable behavior	Mutual grooming***	51.96±153.61	114.13±226.53	P<0.001	P<0.001
	Being groomed***	51.75±120.17	97.94±198.63	P<0.001	P<0.001
Parental behavior	Nursing*	7.33±36.69	11.75±57.42	P=0.0006	P=0.0334
Locomotive behavior	Quadrupedal walking on floor***	62.82±58.99	82.03±75.68	P<0.001	P<0.001
	Walking along iron chain***	0.13±1.26	0.85±5.62	P<0.001	P<0.001
	Standing*	9.75±25.35	13.94±29.95	P=0.0006	P=0.0378
Resting behavior	Hanging on iron chain rest***	5.85±71.70	45.35±176.59	P<0.001	P<0.001
	Hanging on skylight rest***	23.18±143.93	8.88±81.59	P<0.001	P<0.001

Data are means±SD. Bonferroni correction was used to reduce type I errors for multiple comparisons. Mann-Whitney U test, *: P<0.05; **: P<0.01; ***: P<0.001.

Table 2 Frequency of behaviors observed in depressed and control subjects

Behavior		Frequency			
Behavioral category	Behavior	Depressed group	Control subjects	P value	Adjusted P value
Core behavior	Huddling***	1.53±2.17	0.51±1.25	P<0.001	P<0.001
Ingestive behavior	Feeding while hanging***	0.11±0.63	0.05±0.28	P<0.001	P<0.001
	Feeding while sitting**	0.85±2.15	1.11±2.47	P<0.001	P<0.01
	Drinking***	0.20±0.86	0.51±1.59	P<0.001	P<0.001
Amicable behavior	Mutual grooming***	0.74±1.83	1.33±2.40	P<0.001	P<0.001
Mating behavior	Copulation*	0.08±0.35	0.12±0.53	P=0.0007	P=0.0418
Parental behavior	Nursing*	0.28±1.01	0.40±1.44	P=0.0002	P=0.0129
Resting behavior	Hanging on iron chain rest***	0.02±0.22	0.23±0.80	P<0.001	P<0.001
	Hanging on skylight rest***	0.29±1.63	0.10±0.62	P<0.001	P<0.001
Locomotive behavior	Walking along iron chain***	0.03±0.21	0.10±0.53	P<0.001	P<0.001
Miscellaneous behavior	Rub hand back and forth***	0.02±0.15	0.06±0.43	P<0.001	P<0.001

Data are means±SD. Bonferroni correction was used to reduce type I errors for multiple comparisons. Mann-Whitney U test, *: P<0.05; **: P<0.01; ***: P<0.001.

Table 3 Digit length in right and left forelimbs of depressed and control subjects (cm)

Left/Right	Digit†	Control (n=16)		Depressed (n=15)	
		Mean	SD	Mean	SD
Left	2	29.76	2.46	29.28	2.62
	4*	37.75	2.60	35.45	3.17
Right	2	30.25	2.67	29.04	2.78
	4*	37.14	2.64	35.09	3.24

†: Fingers are numbered 1 to 5 from thumb to smallest digit. Data are means±SD. Student's t-test, *: P<0.05.

Table 4 2D:4D ratio in the right and left forelimb hands of depressed and control subjects

Left/Right	Digit Ratio	Control			Depressed			P value
		n	Mean	SD	n	Mean	SD	
Left	2D:4D	16	0.79	0.04	15	0.83	0.03	0.002**
Right	2D:4D	16	0.81	0.03	15	0.84	0.05	0.0372*

Data are means±SD. Student's t-test, *: P<0.05; **: P<0.01; ***: P<0.001.

In the present study, we employed a reliable naturally occurring primate depression model to identify depressed cynomolgus monkeys. Our data disclosed that the ring fingers in both the left and right forelimb hands were longer in healthy

female monkeys than in depressed female monkeys. In terms of the finger length data, we found that the digit ratios were significantly higher in depressed monkeys, including the 2D:4D ratios in the left and right forelimb hands. Depression can occur due to long-term social pressures, especially in females (Sherrill et al., 1997). In a competitive environment, the dorsal anterior cingulate cortex (dACC) region in the brain controls support, emotion regulation, conflict monitoring, and behavioral inhibition (Dedovic et al., 2016). Gorka et al. (2015) revealed a significant positive correlation between the 2D:4D ratio and gray matter volume of the dACC in women but not in men. Interestingly, maturation of the dACC influences the development of MDD (Ho et al., 2017). The critical hippocampal brain area, which is strongly associated with the pathogenesis of depression, is also related to the 2D:4D ratio (Kallai et al., 2005). These studies provide a possible intrinsic link in the brain tissue between 2D:4D ratio and depression.

Previous investigations have shown that the digit ratio persists in a stable range during embryogenesis and increases in accordance with personal growth (Goodman & Scamble, 2001; Herault et al., 1997). Interestingly, Williams et al. (2000) used the 2D:4D ratio to reflect the degree of prenatal androgen exposure in humans. However, a growing body of evidence indicates that the 2D:4D ratio is unrelated to adult sex hormone (e. g., estrogen and androgen) concentrations (Muller et al., 2011). The 2D:4D ratio appears to be relatively stable, although it does increase somewhat throughout childhood (Trivers et al., 2006). Thus, there is a general consensus that the 2D:4D ratio is a relatively stable biomarker for the balance between fetal testosterone (FT) and fetal estrogen (FE), with low FT and high FE linked to high 2D:4D (Manning et al., 2014). Based on these findings, we hypothesize that the 2D and 4D finger length ratios are primarily determined by prenatal sex hormone exposure, and that the effects of this prenatal hormone on the 2D:4D ratio are not presented as estrogen or androgen concentrations differences in a later period. However, the prenatal sex hormon affect the subject's neural development and biochemistry (Honekopp et al., 2007). Those with longer finger lengths tend to possess poor aggression tendencies and emotion regulation function. This is also consistent with our findings. In a competitive environment, high 2D:4D female individuals exhibited a high correlation with depression. Thus, our findings provide a novel way in which to select depressed monkeys according to comparison of the 2D:4D ratio. Future work should examine the relationship between the 2D:4D ratio and the severity of depression in larger samples that report a wider range of depression symptoms. Measurement of the 2D:4D ratio may provide a predictive tool for the diagnosis of depression and strong support for indications of depression risk to proceed early intervention.

CONCLUSIONS

Most previous primate digit ratio studies have been examined in regard to social behaviors and rank. However, few have investigated the relationship between digit ratios and depression in primates. This is the first study to reveal significant differences in finger lengths and digit ratios between depressed monkeys and healthy controls. We discovered that depressed monkeys presented with shorter 4th fingers and a higher 2D:4D ratio in both forelimbs. These metrics show promise as gross biological indicators to facilitate screening for depressed monkeys in large population-based studies. However, whether this conclusion can be applied to screen for human depression requires further investigation.

REFERENCES

Bailey AA, Hurd PL. 2005. Finger length ratio (2D:4D) correlates with physical aggression in men but not in women. *Biological Psychology*, **68**: 215–222.

Capitanio JP. 2017. Naturally occurring nonhuman primate models of psychosocial processes. *ILAR Journal*, **58**(2): 226–234.

Carre JM, Ortiz TL, Labine B, Moreau BJ, Viding E, Neumann CS, Goldfarb B. 2015. Digit ratio (2D:4D) and psychopathic traits moderate the effect of exogenous testosterone on socio-cognitive processes in men. *Psychoneuroendocrinology*, **62**: 319–326.

Choi IH, Kim KH, Jung H, Yoon SJ, Kim SW, Kim TB. 2011. Second to fourth digit ratio: a predictor of adult penile length. *Asian Journal of Andrology*, **13**(5): 710–714.

Dedovic K, Slavich GM, Muscatell KA, Irwin MR, Eisenberger NI. 2016. Dorsal anterior cingulate cortex responses to repeated social evaluative feedback in young women with and without a history of depression. *Frontiers in Behavioral Neuroscience*, **10**: 64

Evardone M, Alexander GM. 2009. Anxiety, sex-linked behaviors, and digit ratios (2D:4D). *Archives of Sexual Behavior*, **38**(3): 442–455

Felger JC, Alagbe O, Hu F, Mook D, Freeman AA, Sanchez MM, Kalin NH, Ratti E, Nemeroff CB, Miller AH. 2007. Effects of interferon-alpha on rhesus monkeys: a nonhuman primate model of cytokine-induced depression. *Biological Psychiatry*, **62**(11):1324–1333.

Gelenberg AJ. 2010. The prevalence and impact of depression. *The Journal of Clinical Psychiatry*, **71**(3): e06.

Gnanavel S, Robert RS. 2013. Diagnostic and statistical manual of mental disorders, fifth edition, and the impact of events scale-revised. *Chest*, **144**(6):1974.

Goodman FR, Scambler PJ. 2001. Human HOX gene mutations. *Clinical Genetics*, **59**(1):1–11.

Gorka AX, Norman RE, Radtke SR, Carre JM, Hariri AR. 2015. Anterior cingulate cortex gray matter volume mediates an association between 2D:4D ratio and trait aggression in women but not men. *Psychoneuroendocrinology*, **56**:148–156.

Hérault Y, Fraudeau N, Zákány J, Duboule D. 1997. Ulnaless(Ul), a regulatory mutation inducing both loss-of-function and gain-of-function of posterior Hoxd genes. *Development*, **124**(18): 3493–3500.

Ho TC, Sacchet MD, Connolly CG, Margulies DS, Tymofiyeva O, Paulus MP, Simmons AN, Gotlib IH, Yang TT. 2017. Inflexible functional connectivity of the dorsal anterior cingulate cortex in adolescent major depressive disorder. *Neuropsychopharmacology*, **42**(12):2434–2445.

Hönekopp J, Bartholdt L, Beier L, Liebert A. 2007. Second to fourth digit length ratio (2D:4D) and adult sex hormone levels: new data and a meta-analytic review. *Psychoneuroendocrinology*, **32**(4):313–321.

Kallai J, Csathó A, Kövér F, Makány T, Nemes J, Horváth K, Kovács N, Manning JT, Nadel L, Nagy F. 2005. MRI-assessed volume of left and right hippocampi in females correlates with the relative length of the second and fourth fingers (the 2D:4D ratio). *Psychiatry Research*, **140**(2):199–210.

Kalichman L, Batsevich V, Kobyliansky E. 2017. 2 D4D finger length ratio and radiographic hand osteoarthritis. *Rheumatology International*, **38**(5): 865–870.

Krishnan V, Nestler EJ. 2008. The molecular neurobiology of depression. *Nature*, **455**(7215): 894–902.

Kyriakidis I, Papaioannidou P, Pantelidou V, Kalles V, Gemitzis K. 2010. Digit ratios and relation to myocardial infarction in Greek men and women. *Gender Medicine*, **7**(6): 628–636.

*Lutchmaya S*1, Baron-Cohen S, Raggatt P, Knickmeyer R, Manning JT. 2004. 2nd to 4th digit ratios, fetal testosterone and estradiol. *Early Human Development*, **77**(1–2): 23–28.

Manning J, Kilduff L, Cook C, Crewther B, Fink B. 2014. Digit Ratio (2D:4D): A biomarker for prenatal sex steroids and adult sex steroids in challenge situations. *Frontiers in Endocrinology*, **5**:9.

Manning JT, Scutt D, Wilson J, Lewis-Jones DI. 1998. The ratio of 2nd to 4th digit length: a predictor of sperm numbers and concentrations of testosterone, luteinizing hormone and oestrogen. *Human Reproduction*, **13**(11):3000–3004.

Muller DC, Giles GG, Bassett J, Morris HA, Manning JT, Hopper JL, English DR, Severi G. 2011. Second to fourth digit ratio (2D:4D) and concentrations of circulating sex hormones in adulthood. *Reproductive Biology and Endocrinology*, **9**: 57.

Nelson E, Shultz S. 2010. Finger length ratios (2D: 4D) in anthropoids implicate reduced prenatal androgens in social bonding. *American Journal of Physical Anthropology*, **141**(3): 395–405.

Nelson E, Voracek M. 2010. Heritability of digit ratio (2D: 4D) in rhesus macaques (*Macaca mulatta*). *Primates*, **51**(1):1–5.

Ronalds G, Phillips DIW, Godfrey KM, Manning JT. 2002. The ratio of second to fourth digit lengths: a marker of impaired fetal growth. *Early Human Development*, **68**(1): 21–26.

Sherrill JT, Anderson B, Frank E, Reynolds CF, Tu XM, Patterson D, Ritenour A, Kupfer DJ. 1997. Is life stress more likely to provoke depressive episodes in women than in men? *Depress Anxity*, **6**(3): 95–105

Shively CA, Register TC, Friedman DP, Morgan TM, Thompson J, Lanier T. 2005. Social stress-associated depression in adult female cynomolgus monkeys (*Macaca fascicularis*). *Biological Psychology*, **69**(1): 67–84.

Smedley KD, Mckain KJ, Mckain DN. 2014. **2** D4D digit ratio predicts depression severity for females but not for males. *Personality and Individual Differences*. **70** (11):136–139.

Trivers R, Manning J, Jacobson A. 2006. A longitudinal study of digit ratio (2D: 4D) and other finger ratios in Jamaican children. *Hormones and Behavior*. **49** (2):150–156.

Willard SL, Shively CA. 2012. Modeling depression in adult female cynomolgus monkeys (*Macaca fascicularis*). *American Journal of Primatology*, **74**(6): 528–542.

Williams TJ, Pepitone ME, Christensen SE. 2000. Finger length ratios and sexual orientation. *Nature*, **404**: 455–456.

Xu F, Wu Q, Xie L, Gong W, Zhang J, Zheng P, Zhou Q, Ji Y, Wang T, Li X, Fang L, Li Q, Yang D, Li J, Melgiri ND, Shively C, Xie P. 2015. Macaques exhibit a naturally-occurring depression similar to humans. *Scientific Reports*, **5**: 9220.

Xu F, Xie L, Li X, Li Q, Wang T, Ji YJ, Kong F, Zhan QL, Cheng K, Fang L, Xie P. 2012. Construction and validation of a systematic ethogram of *Macaca fascicularis* in a free enclosure. *PLoS One*, **7**: e37486.

Zhou Q, Xu F, Wu Q, Gong W, Xie L, Wang T, Fang L, Yang D, Melgiri ND, Xie P. 2014. The mutual influences between depressed *Macaca fascicularis* mothers and their infants. *PLoS One*, **9**: e89931.

High egg rejection rate in a Chinese population of grey-backed thrush (*Turdus hortulorum*)

DEAR EDITOR,

Several previous studies have indicated that nest sanitation behavior is a general adaptation in altricial birds, with egg recognition capacity evolving as a specific response to interspecific brood parasitism (IBP). However, a recent study suggested an alternative hypothesis, concluding that conspecific brood parasitism (CBP) selects for egg rejection in thrushes, with IBP as a by-product. In the present study, we used a spectrophotometer to quantify egg coloration and egg mimicry and performed artificial parasitism experiments in the grey-backed thrush (*Turdus hortulorum*). We showed that individuals of this species rejected 100% of 12 foreign eggs, without IBP or CBP detected. In a review of previous studies, we also discuss possible explanations for the high egg rejection rate in the grey-backed thrush and suggest areas for future study.

Altricial birds have evolved advanced reproductive behavior to increase the fitness of their offspring by building elaborate structures (i. e., nests), in which they lay eggs and rear their nestlings (Hansell, 2000). Bird nests not only provide a suitable place for nestling development, but also act as a concealed location for safety from predators. Furthermore, bird parents have evolved nest sanitation behavior to clean foreign objects from their nests, including feces, eggshells, branches, and leaves, because they induce predation, facilitate microorganism growth, damage eggs, or hurt nestlings during brooding (Guigueno & Sealy, 2012). Therefore, nest sanitation has evolved as a general behavior in altricial birds for distinguishing between egg-shaped and non-egg-shaped objects. This recognition capacity has further improved in some species to facilitate detection of differences within eggs (i. e., egg recognition) as a specific adaptation to avian brood parasitism, where other birds lay parasitic eggs in nests that are not their own, thereby reducing reproductive output of the hosts (Davies, 2011; Yang et al., 2015a). Avian brood parasitism can be classified as either interspecific brood (IBP) or conspecific brood parasitism (CBP). Numerous empirical studies have shown that IBP selects for the capacity of hosts to recognize and reject foreign eggs (Davies, 2000; Liang et al., 2016; Moksnes et al., 1991; Rothstein & Robinson, 1998; Yang et al., 2010). Alternatively, the "collateral damage" hypothesis states that CBP is responsible for egg rejection in birds, with rejection due to IBP constituting a by-product of host adaptations against CBP (Jackson, 1998). However, this hypothesis failed to explain egg recognition by hosts because

it was tested and supported in a single non-passerine bird species (Lyon & Eadie, 2004, 2008). Recently, new research re-examined this hypothesis and drew supportive conclusions by testing it in two passerine species of thrush, that is, the song thrush (*Turdus philomelos*) and European blackbird (*Turdus merula*) (Samas et al., 2014a). However, Soler (2014a) stated that, to date, there is no evidence of CBP causing egg rejection in thrushes *per se*, though Samas et al. (2014b) subsequently supported their conclusion with empirical evidence. Similarly, Ruiz-Raya et al. (2016) investigated recognition of conspecific or heterospecific eggs in European blackbirds by manipulating the risk of CBP and IBP, respectively. They found that blackbirds presented low recognition of conspecific eggs even under high risk of CBP, and thus their results supported the IBP hypothesis that egg recognition has evolved and is maintained in blackbirds as a response to previous cuckoo parasitism.

Here we performed an empirical study to test egg recognition capacity in the grey-backed thrush. The main purpose of this study was to provide initial information on egg recognition in this species, which may facilitate further study. According to previous studies on *Turdus* spp., we predicted that the grey-backed thrush would not show egg recognition capacity because no CBP or IBP has been found in this population. An alternate prediction was also considered, that the grey-backed thrush may also display egg recognition due to previous IBP by cuckoos, which still affects host behavior.

This study was performed in Fusong County, Jilin Province, China (N42º 19' 382", E127º 15' 107"), an area of secondary forest fragmented by corn (*Zea mays*) crop farmland and scattered plantations (dominated by larch *Larix* spp.), from May to June 2013. This region is in the temperate zone at an elevation of 481 m, with a continental monsoon climate characterized by cold and snowy winters with an average annual temperature of 4 ºC. The grey-backed thrush belongs to the Turdidae family and is mainly distributed in East Asia (MacKinnon & Phillipps, 1999), where it chooses nest sites

with short ground cover and a high density of small trees and shrubs (Zhou et al., 2011). In our study site, open-cup nests were built in trees (Figure 1A), and pale green eggs with reddish markings were laid in these nests. (Figure 1B), with an average clutch size of 4.42 eggs±0.51 (range 4–5 eggs, n=12).

Figure 1 Nest site, nest, incubating female, and eggs of the grey-backed thrush (Photos by Long-Wu Wang)

All experiments complied with the current laws of China. Experimental procedures were in accordance with the Animal Research Ethics Committee of Hainan Provincial Education Centre for Ecology and Environment, Hainan Normal University (permit No. HNECEE-2012-004).

The appearances of the thrush and model eggs were quantified with a spectrophotometer (Avantes-2048, Avantes, Apeldoorn, The Netherlands). Six reflectance spectra were measured in each egg and averaged to represent the color of the egg. Model eggs were immaculate blue, a common coloration of cuckoo eggs in China (Yang et al., 2010, 2012). Thrush eggs are pale green with reddish markings and thus their egg ground color and markings were measured, respectively. Subsequently, egg spectra were loaded into AvaSoft 7.3, at which the wavelength range of spectra varied from 300 to 700 nm. The spectral range of 300−400 nm and 400−700 nm refers to ultraviolet (UV) light and visible light (VIS), respectively (for details, see Yang et al., 2010, 2013).

Nests of the grey-backed thrush were found by searching potential nest sites and monitoring the activity of reproductive adults. Nests were then randomly sorted into two groups: (1) manipulated group into which one immaculate blue model egg was introduced just after clutch completion (n=12) (Figure 2); and (2) control group in which nests were visited by the same procedure to control for human disturbance, but no manipulation was made (n=10). Manipulation was performed in these circumstances without observing hosts to avoid potential effects of host observations on recognition (Hanley et al., 2015). Observed nests were monitored for 6 d after manipulation and the responses of thrushes to foreign eggs were classified as rejection, if foreign eggs were ejected, pecked, or deserted, or accepted if foreign eggs were intact and incubated (Yang et al., 2010, 2014b). Model eggs were made by polymer clay and their sizes were standardized to 25 mm×19.5 mm, similar to thrush eggs (25.07±0.42 mm×19.74±0.71 mm, n=10).

Figure 2 Experimental nest of the grey-backed thrush with a blue model egg (Photo by Long-Wu Wang)

The grey-backed thrushes laid pale green eggs with dense reddish markings (Figure 1B). Egg reflectance analysis illustrated that egg ground color was consistent with human eye assessment, with a reflectance peak in the range of green light (475−550 nm) (Figure 3). Similarly, the reddish markings had a reflectance peak in the range 550−620 to 620−700 nm, which represents yellow and red light, respectively (Figure 3). The blue model egg had a reflectance peak in the range of blue light (400−475 nm) (Figure 3). The reflectance contrast between trough and peak reflects chroma (or color saturation). Therefore, blue model eggs were more saturated in color than the thrush egg. In brief, the model egg was very different from thrush eggs according to vision based on human eyes and spectral reflectance. Experimental parasitism indicated that the grey-backed thrush rejected all non-mimetic model eggs, with a rejection rate of 100% (n=12). All rejections occurred within a day (i. e., 24 h) and were all performed by ejection without any recognition error. No rejection was found in the control group (n=10).

This Chinese population of grey-backed thrush possessed high recognition capacity, rapidly rejecting 100% of non-mimetic foreign eggs. This contradicted our expectation that
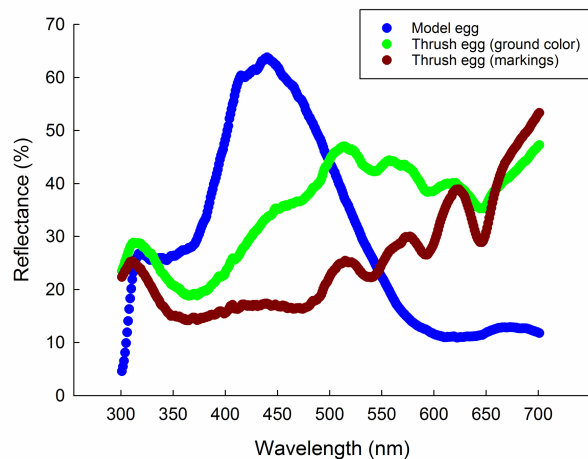
Figure 3 Egg reflectance of the grey-backed thrush and model eggs
Reflectance of thrush eggs was averaged from three eggs from the nest in Figure 2.

grey-backed thrush should have no or low-level egg recognition capacity because no CBP or IBP was detected in our study population. Thus, this egg rejection ability of the grey-backed thrush needs further investigation.

A recent study on artificial parasitism in song thrushes and European blackbirds found unusually high rejection rates of CBP (up to 60%) and positive co-variance with conspecific population densities without risk of IBP (Samas et al., 2014). Because IBP rejection rates did not covary geographically with IBP risk (Grim & Stokke, 2016) and thus contradicted the IBP hypothesis that egg recognition has evolved as a response to IBP, Samas et al. (2014) concluded that egg recognition in *Turdus* spp. has evolved as a response to CBP, not to IBP. However, if egg rejection abilities can be maintained in the absence of IBP, high egg rejection rates can still be retained without geographic co-variation. Therefore, Soler (2014a) criticized the conclusion of Samas et al. (2014) and argued they made an invalid conclusion due to an out-of-date theoretical background and a biased selection of references. However, Samas et al. (2014b) argued that a theory is never out of date and addressed the theoretical objections by empirical evidence. Recently, Ruiz-Raya et al. (2016) further tested egg recognition in blackbirds by manipulating the risk of CBP and IBP and concluded that selection from IBP likely accounts for egg recognition in blackbirds.

In our study population, grey-backed thrushes displayed high recognition capacity of foreign eggs. It is generally accepted that IBP rather than CBP contributes to egg recognition in hosts. Firstly, egg recognition capacity is much more unlikely to evolve in response to CBP than IBP because IBP gives rise to dramatic fitness costs, which are much lower than those from CBP (Petrie & Møller, 1991). Parasites and hosts with CBP are conspecific and share the same gene pool and thus constitute much weaker selection than IBP (Ruiz-Raya et al., 2016; Soler, 2014b). Furthermore, conspecific egg phenotypes in CBP are too similar to initiate evolution of egg

recognition (Soler et al., 2011). However, intraspecific variation in egg coloration is high for some host species, and CBP may account for the evolution of egg recognition (Cassey et al., 2008a, 2008b; Hanley et al., 2017; Samas et al., 2014a). Secondly, in order to select for conspecific egg rejection, the level of CBP must be high. However, in our study population, no CBP was detected. Similarly, Samas et al. (2014) described that the rates of CBP were only 0%−2.2% and 0%−3.1% for the song thrush and blackbird, respectively. However, current parasitism rates may not represent actual selection pressure from IBP and CBP without considering other factors, such as recognition error and rejection cost. Furthermore, because egg rejection capacity has evolved in response to IBP, and it can be maintained in the absence of IBP, this may also occur in response to CBP but in its absence. Many currently unparasitized potential host species exhibit a rejection rate of nearly 100% (Lahti, 2006; Peer & Sealy, 2004; Yang et al., 2014a, 2015b). For example, blackbirds were introduced in the nineteenth century to New Zealand, where a high rejection rate of non-mimetic eggs has been reported (62%, Samas et al., 2014; 83.9%, Hale & Briskie, 2007), similar to the rejection rate of 90% in Europe (Grim et al., 2014; Martín-Vivaldi et al., 2012; Moskát et al., 2003). Moreover, a recent review concluded that it is not correct to formulate predictions that assume that rejection behavior of hosts must be lost in the absence of obligate brood parasites (Soler, 2014b). Finally, aggressive behavior towards adult cuckoos and reluctance to feed cuckoo chicks has been empirically shown in thrushes (Grim et al., 2011), providing evidence for contact with IBP in the past, resulting in successful resistance against interspecific brood parasitism (Ruiz-Raya et al., 2016). However, Samas et al. (2014b) argued that aggression in blackbirds did not specifically evolve in response to IBP because they are aggressive not only to cuckoo dummies but also to any intruders near their nests, including harmless pigeons (*Columba livia*). Thus, switching to new types of food is an unlikely defense against brood parasite chicks because such changes would not prevent most costs from IBP (Grim et al., 2011; Samas et al., 2014b). However, Ruiz-Raya et al. (2016) found that blackbirds were able to recognize and eject heterospecific eggs at high rates, whereas most conspecifics eggs were not recognized. Moreover, ejection rates of conspecific eggs did not exceed 13%, even in the presence of a high risk of CBP, whereas ejection rates of experimental eggs simulating IBP were much higher (80%−100%). Female blackbirds were also found to be more aggressive towards cuckoos than towards blackbird dummies (Ruiz-Raya et al., 2016). Additionally, Ruiz-Raya et al. (2016) estimated that the level of CBP necessary to select for evolution of host response against conspecific eggs would range from 55% to 65%. Because the grey-backed thrush has retained a high level of egg recognition, the rejection costs, which would contradict such maintenance, should be negligible. According to our results, no rejection cost was detected. Like blackbirds, the grey-backed thrush also has a large bill to grasp foreign eggs for rejection. Therefore, rejection costs should not prevent grey-backed thrushes from retaining egg rejection capacity.

In summary, previous studies on thrush hosts have provided inconsistent conclusions. This situation is complicated by the explanation for one species not being suitable for another. Our study provides preliminary information, and thus cannot offer sufficient evidence to support either the IBP or CBP hypothesis. However, considering that previous studies have provided strong evidence that hosts affected by IBP can retain egg recognition capacities after long-term escape from cuckoo parasitism (Lahti, 2006), egg rejection capacity in grey-backed thrushes may be maintained because parasitic cuckoos have exploited this potential host in the past. Although theoretically hosts may also retain egg recognition due to previous CBP, like IBP, empirical studies are currently insufficient to clarify this assumption. Furthermore, recent studies have revealed that egg accepters can become rejecters after stimulation, in all cases switching from acceptance to rejection, implying that historical cases of IBP or CBP are considerably underestimated in currently non-parasitized potential host species (Molina-Morales et al., 2014; Yang et al., 2015b). Further studies referring to egg color variation and recognition with different degrees of egg mimicry are necessary in the grey-backed thrush and even other species of *Turdus*. Such studies will help us better understand the origin of egg recognition in thrushes.

COMPETING INTERESTS

The authors declare that they have no competing interests.

AUTHORS' CONTRIBUTIONS

W.L. designed the study. L.W.W. collected data and conducted experiments in the field. C.C.Y. analysed the data and drafted the manuscript. W.L. and A. P. M. discussed and revised the manuscript. All authors read and approved the final version of the manuscript.

ACKNOWLEDGMENTS

We are grateful to Dr. Tomas Grim, one anonymous reviewer, and the editors for their constructive comments.

Can-Chao Yang[1], Long-Wu Wang[2],
Wei Liang[1,*], Anders Pape Møller[3]

[1] *Ministry of Education Key Laboratory for Ecology of Tropical Islands*, *College of Life Sciences, Hainan Normal University, Haikou Hainan 571158*, *China*
[2] *State Forestry Administration of China Key Laboratory for Biodiversity Conservation in Mountainous Areas of Southwest Karst*, *School of Life Sciences*, *Guizhou Normal University*, *Guiyang Guizhou 550001*, *China*
[3] *Ecologie Systématique Evolution*, *Université Paris-Sud*, *CNRS*, *AgroParisTech*, *Université Paris-Saclay*, *F-91405 Orsay Cedex*, *France*
*Corresponding author, E-mail: liangwei@hainnu.edu.cn

REFERENCES

Cassey P, Ewen JG, Blackburn TM, Hauber ME, Vorobyev M, Marshall NJ. 2008a. Eggshell colour does not predict measures of maternal investment in eggs of *Turdus* thrushes. *Naturwissenschaften*, **95**(8): 713–721.

Cassey P, Honza M, Grim T, Hauber ME. 2008b. The modelling of avian visual perception predicts behavioural rejection responses to foreign egg colours. *Biology Letters*, **4**(5): 515–517.

Davies NB. 2000. Cuckoos, Cowbirds and Other Cheats. London: T. & A. D. Poyser.

Davies NB. 2011. Cuckoo adaptations: trickery and tuning. *Journal of Zoology*, **284**(1): 1–14.

Grim T, Stokke BG. 2016. In the light of introduction: Importance of introduced populations for the study of brood parasite-host coevolution. *In*: Weis JS, Sol D. Biological Invasions and Animal Behaviour. Cambridge, UK: Cambridge University Press, 133–157.

Grim T, Samaš P, Hauber ME. 2014. The repeatability of avian egg ejection behaviors across different temporal scales, breeding stages, female ages and experiences. *Behavioral Ecology and Sociobiology*, **68**(5): 749–759.

Grim T, Samaš P, Moskát C, Kleven O, Honza M, Moksnes A, Røskaft E, Stokke BG. 2011. Constraints on host choice: why do parasitic birds rarely exploit some common potential hosts?. *Journal of Animal Ecology*, **80**(3): 508–518.

Guigueno MF, Sealy SG. 2012. Nest sanitation in passerine birds: implications for egg rejection in hosts of brood parasites. *Journal of Ornithology*, **153**(1): 35–52.

Hale K, Briskie JV. 2007. Response of introduced European birds in New Zealand to experimental brood parasitism. *Journal of Avianal Biology*, **38**(2): 198–204.

Hanley D, Grim T, Igic B, Samaš P, López AV, Shawkey MD, Hauber ME. 2017. Egg discrimination along a gradient of natural variation in eggshell coloration. *Proceedings of the Royal Society B*, **284**(1848): 20162592.

Hanley D, Samaš P, Heryán J, Hauber ME, Grim T. 2015. Now you see it, now you don't: flushing hosts prior to experimentation can predict their responses to brood parasitism. *Scientific Reports*, **5**: 9060.

Hansell M. 2000. Bird Nests and Construction Behaviour. Cambridge, UK: Cambridge University Press.

Jackson WM. 1998. Egg discrimination and egg-color variability in the northern masked weaver: the importance of conspecific versus interspecific parasitism. *In*: Rothstein SI, Robinson SK. Parasitic Birds and Their Hosts: Studies in Coevolution. New York: Oxford University Press, 407–418.

Lahti DC. 2006. Persistence of egg recognition in the absence of cuckoo brood parasitism: pattern and mechanism. *Evolution*, **60**(1): 157–168.

Liang W, Møller AP, Stokke BG, Yang C, Kovařík P, Wang H, Yao CT, Ding P, Lu X, Moksnes A, Røskaft E, Grim T. 2016. Geographic variation in egg ejection rate by great tits across 2 continents. *Behavioral Ecology*, **27**(5): 1405–1412.

Lyon BE, Eadie JMcA . 2004. An obligate brood parasite trapped in the intraspecific arms race of its hosts. *Nature*, **432**(7015): 390–393.

Lyon BE, Eadie JMcA . 2008. Conspecific brood parasitism in birds: A life-history perspective. *The Annual Review of Ecoloyg Evolution and Systematics*, **39**: 343–363.

MacKinnon J, Phillipps K. 1999. A Field Guide to the Birds of China. Oxford: Oxford University Press.

Martín-Vivaldi M, Soler JJ, Møller AP, Pérez-Contreras T, Soler M. 2012. The importance of nest-site and habitat in egg recognition ability of potential hosts of the common cuckoo *Cuculus canorus*. *Ibis*, **155**(1): 140–155.

Moksnes A, Røskaft E, Braa AT. 1991. Rejection behavior by common cuckoo hosts towards artificial brood parasite eggs. *The Auk*, **108**: 348–354.

Molina-Morales M, Martínez JG, Martín-Gálvez D, Dawson DA, Burke T, Avilés JM. 2014. Cuckoo hosts shift from accepting to rejecting parasitic eggs across their lifetime. *Evolution*, **68**(10): 3020–3029.

Moskát C, Karcza Z, Csörgő T. 2003. Egg rejection in European blackbirds (*Turdus merula*): the effect of mimicry. *Ornis Fennica*, **80**: 86–91.

Peer BD, Sealy SG. 2004. Fate of grackle (*Quiscalus* spp.) defenses in the absence of brood parasitism: implications for long-term parasite–host coevolution. The Auk, **121**(4): 1172–1186.

Petrie M, Møller AP. 1991. Laying eggs in others' nests: intraspecific brood parasitism in birds. *Trends Ecology & Evolution*, **6**(10): 315–320.

Rothstein SI, Robinson SK. 1998. Parasitic Birds and Their Hosts: Studies in Coevolution. New York: Oxford University Press.

Ruiz-Raya F, Soler M, Roncalli G, Abaurrea T, Ibáñez-Álamo JD. 2016. Egg rejection in blackbirds *Turdus merula*: a by-product of conspecific parasitism or successful resistance against interspecific brood parasites?. *Frontiers in Zoology*, **13**: 16.

Samas P, Hauber ME, Cassey P, Grim T. 2014a. Host responses to interspecific brood parasitism: a by-product of adaptations to conspecific parasitism?. *Frontiers in Zoology*, **11**: 34.

Samas P, Hauber ME, Cassey P, Grim T. 2014b. The evolutionary causes of egg rejection in European thrushes (*Turdus* spp.): a reply to M. Soler. Frontiers in Zoology, **11**: 72.

Soler M. 2014a. No evidence of conspecific brood parasitism provoking egg rejection in thrushes. *Frontiers in Zoology*, **11**: 68.

Soler M. 2014b. Long-term coevolution between avian brood parasites and their hosts. *Biological Reviews*, **89**(3): 688–704.

Soler M, Ruiz-Castellano C, Fernández-Pinos MC, Rösler A, Ontanilla J, Pérez-Contreras T. 2011. House sparrows selectively eject parasitic conspecific eggs and incur very low rejection costs. *Behavioral Ecology and Sociobiology*, **65** (10): 1997–2005.

Yang C, Liu Y, Zeng L, Liang W. 2014a. Egg color variation, but not egg rejection behavior, changes in a cuckoo host breeding in the absence of brood parasitism. *Ecology and Evolution*, **4**(11): 2239–2246.

Yang C, Wang L, Liang W, Møller AP. 2015a. Nest sanitation behavior in hirundines as a pre-adaptation to egg rejection to counter brood parasitism. *Animal Cognition*, **18**(1): 355–360.

Yang C, Wang L, Cheng S-J, Hsu YC, Liang W, Møller AP. 2014b. Nest defenses and egg recognition of yellow-bellied prinia against cuckoo parasitism. *Naturwissenschaften*, **101**(9): 727–734.

Yang C, Antonov A, Cai Y, Stokke BG, Moksnes A, Røskaft E, Liang W. 2012. Large hawk-cuckoo *Hierococcyx sparveroides* parasitism on the Chinese babax *Babax lanceolatus* may be an evolutionarily recent host–parasite system. *Ibis*, **154**(1): 200–204.

Yang C, Wang L, Hsu YC, Antonov A, Moksens A, Røskaft E, Liang W, Stokke BG. 2013. UV reflectance as a cue in egg discrimination in two Prinia species exploited differently by brood parasites in Taiwan. *Ibis*, **155**(3): 571–575.

Yang C, Wang L, Cheng SJ, Hsu YC, Stokke BG, Røskaft E, Moksnes A, Liang W, Møller AP. 2015b. Deficiency in egg rejection in a host species as a response to the absence of brood parasitism. *Behavioral Ecology*, **26** (2): 406–415.

Yang C, Liang W, Cai Y, Shi S, Takasu F, Møller AP, Antonov A, Fossøy F, Moksnes A, Røskaft E, Stokke BG. 2010. Coevolution in action: disruptive selection on egg colour in an avian brood parasite and its host. *PLoS One*, **5**(5): e10816.

Zhou D, Zhou C, Kong X, Deng W. 2011. Nest-site selection and nesting success of grey-backed thrushes in northeast China. *Wilson Journal of Ornithology*, **123**(3): 492–501.

Threshold for maximal electroshock seizures (MEST) at three developmental stages in young mice

DEAR EDITOR,

Early brain development after birth is extremely dynamic, suggesting that potential functional changes occur during this period. In this study, the maximal electroshock seizure threshold (MEST) was used to explore the electrophysiological variation among three developmental stages in young mice (no more than 5 weeks old). The induced electroshock seizure (ES) behavior of early postnatal mice (1−2-weeks old) differed from that during weaning (3 weeks old) and early puberty (4−5-weeks old). Thus, we further explored their respective characteristic responses to the ES parameters. When the stimulation current (SC) was limited to 4.0 mA, only the 1−2-week-old mice were induced to exhibit ES behavior at voltages of 30 V and 40 V, indicating they were more sensitive to maximal electroshock seizure (MES) (response to lower voltage). Surprisingly, however, they showed substantially lower mortality than the older groups under higher voltage conditions (60, 100, 160, and 200 V), suggesting better tolerance to the SC. We also found that when the current limit decreased to 3.5 mA, the 4−5-week-olds mice exhibited stable ES behavior with low mortality, while for 3-week-olds mice, the SC limit required to be reduced to 1.5 mA. In conclusion, our findings showed that neural sensitivity to MES was significantly different in young mice before puberty. Thus, greater attention should be given to distinguishing the developmental period of mice, especially in electrophysiological examination.

While the macroscopic layout of the brain is nearly complete by the end of pregnancy, it develops continuously at a high speed until prepuberty (Stiles & Jernigan, 2010). Recent magnetic resonance imaging studies have depicted structural change processes by brain volume (Gogtay et al., 2004; Knickmeyer et al., 2008) and fiber connection (Chen et al., 2016; Li et al., 2015) growth curves, suggesting that early brain development after birth is extremely dynamic (Li et al., 2013). In addition, many developmental mental disorders likely originate from developmental problems in preadolescents (Chen et al., 2017; Li et al., 2016). For example, it is estimated that 10.5 million children under 15 have active pediatric epilepsy, which is more than 10 times greater than that found in adults (Keezer et al., 2016).

Maximal electroshock seizure (MES) is an experimental paradigm that induces synchronous neural discharges in the brain through artificial current input (Kamei et al., 1978), and is used to induce acute epileptic behaviors (Fischer & Muller,

1988). However, there are limited reports on the application of MES in young mice to mimic childhood epilepsy. In this study, a MES threshold paradigm was applied to investigate electrophysiological variations in young mice less than five weeks old. Group information was summarized in Table 1. Behavioral expression in the mice included electroshock seizure (ES), death, and no response, which reflected their brain network states. Young mice less than 5 weeks old were divided into three groups: 1−2-week-, 3-week-, and 4−5-week-old groups, based on their physical features and activities. These groups corresponded to three critical developmental stages: i.e., early postnatal, weaning, and early puberty (Miao, 1997; Xu et al., 2011).

Usually, an electrical stimulus of the MES paradigm is delivered to adult mice (more than 6–week old) and is about 3−10 times higher than the individual electrical seizure threshold of the animal (Kamei et al., 1978; Murakami et al., 2007). The typical MES behaviors are: hind-limb extension, fall, and back rigidity, followed by foaming at the mouth and urinary incontinence (Ferraro et al., 1998, 2002)(Figure 1A). We found that seizure in 3–week-old and 4−5-week-old mice induced typical MES behavior as Figure 1A shown. Under the same conditions (i.e., SC limited to 3.5 mA and voltage of 80 V), the induced seizures of early postnatal mice (1−2 weeks old) were different; although urinary incontinence and mouth foaming were also observed, the seizures of 1−2-week-old mice did not include hind-limb extension and fall, with most limbs bending and convulsing (Figure 1B).

These behavioral differences may be due to the sensitivity differences in nerves. Therefore, the mice were subjected to electrical stimuli with elevated parameters. Surprisingly, when the SC was limited to 4.0 mA and the voltage was 160−200 V, all 1−2-week-old mice survived the elicited ES behaviors. Under the above parameters, all behaviors exhibited by 1−2-week-old mice were consistent with typical opisthotonus,

Table 1 Animals were grouped based on age and current limit in the MEST test

	Current limited to 4.0 mA	Current limited to 3.5 mA	Current limited to 1.5 mA	Total (n)
1–2 weeks	85	10	10	105
3 weeks	36	25	52	113
4–5 weeks	39	70	23	132
Total (n)	160	105	85	350
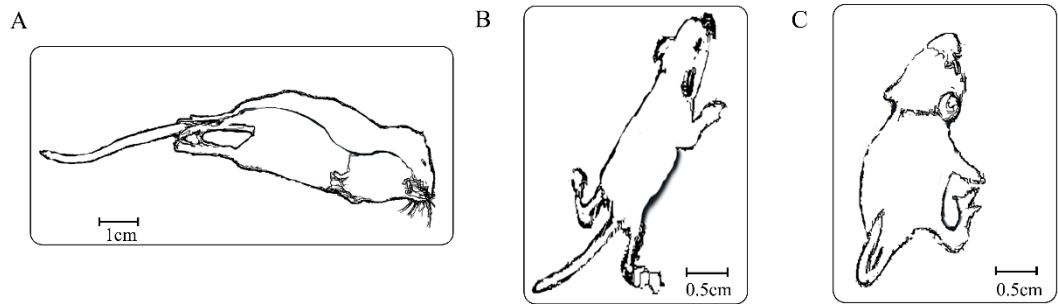
Figure 1 Electroshock seizure (ES) behavior at different developmental stages in mice

A: ES behavior of 3-week-old and 4–5-week-old mice. B: Typical ES behavior patterns of 1–2-week-old mice at low voltage (30−100 V, 4.0 mA); C: ES behavior patterns of 1–2-week-old mice at high voltage (120–200 V, 4.0 mA).

which differs from the previous stimulus conditions. The MES behaviors in 1–2-week-old mice included bilateral forelimb clonus, tail stiffness, and bending (Figure 1C). In contrast, under the same conditions (i.e., 4.0 mA and 160−200 V), all but one of the 3−week-old and 4−5-week-old mice died after rigidity seizures (Figure 2).
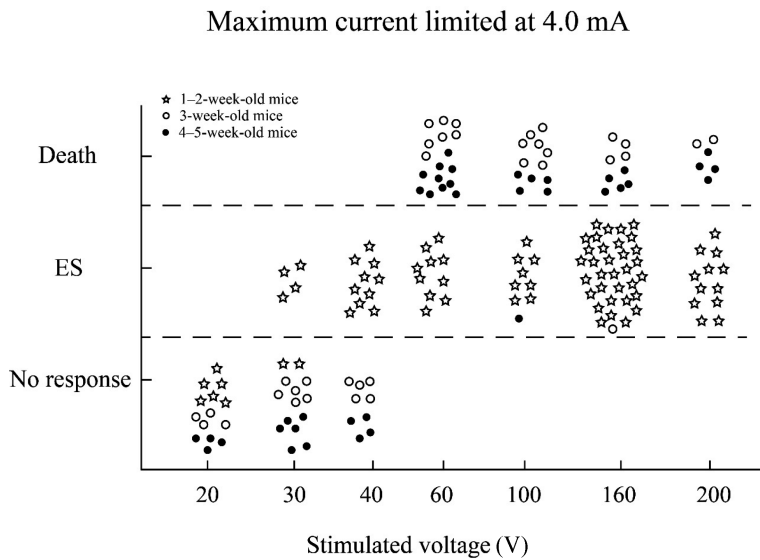
Figure 2 Maximal electroshock seizure (MES) occurrence, no-response, and death voltage range of 1−2-week-old, 3-week-old, and 4−5-week-old mice at 4.0 mA

When the maximum output current was limited to 4.0 mA, death, MES, and no response were in response to constant voltage electrical stimulation. ES: Electroshock seizure.

Based on the above results, a series of stimuli was given to the three groups of young mice to determine the optimal range of parameters for inducing ES behavior.

As shown in Figure 2, when the SC was limited at 4.0 mA and the voltages were 30 V and 40 V, ES behavior was observed in 1−2-week-old mice (87.5%, n=16) but not in the

other groups, indicating that the 1−2-week-old mice were more susceptible to electrical stimulation than the older groups (Figure 2). This age is equivalent to the human breastfeeding stage before 2 years old. Furthermore, this result is consistent with the clinical epidemic status of epilepsy, a brain disease with abnormal synchronous neural discharge of the cerebral cortex, thus indicating that the early postnatal brain is more sensitive to electrical stimulations.

Interestingly, at voltages of 60, 100, 160, and 200 V (Table 2), 100% of 1−2-week-old mice survived after ES behavior occurrence (63/63). In contrast, 95.6% of 3-week-old and 4−5-week-old mice died (44 / 46), demonstrating a substantially higher mortality than the youngest group (P<0.000 1). This indicated that early postnatal mice better endured electrical stimulation than early puberty mice, which has not been reported previously.

Electrical stimuli with reduced current were applied to explore the appropriate stimulus range for 3-week-old and 4−5-week-old mice. As shown in Figure 3A, when the SC was limited to 3.5 mA, 72% (38 in 53) of 4−5-week-old mice elicited ES at voltages of 80 V and 100 V. This was a relatively safe stimulation range in which to induce ES behavior of 4−5-week-old mice. For 3-week-old mice, however, only 50% (4 in

Table 2   Responses of 1 − 2-week-old and 3 − 5-week-old mice under 4.0 mA and 60−200 V

Age	Number (n)	ES	Death	*Chi*-square test
1–2 weeks	63	100%	0	
3–5 weeks	46	4.3%	95.6%	P<0.000 1

Statistics were analyzed by *Chi*-square test. ES: Electroshock seizure.

8) exhibited successful induction of ES behavior at 60 V. Furthermore, when the voltage increased to 80, 100, and 120 V, all 3-week-old mice died. When the SC was limited to 1.5 mA, 3-week-old mice exhibited ES behavior within a broad range of voltages (100 − 140 V). This was therefore considered a suitable range of the stimulus parameters, although 4−5-week-old mice demonstrated no responses under these conditions. Comparing the three groups, we determined that the behavioral responses of young mice in different periods under a MEST paradigm were different due to the different intensities of brain network connections. The stimulated parameter ranges eliciting MES for different groups of young mice were not continuous. Thus, based on our results, it appears that 3 weeks of age may be a turning point in nervous system development in mice.
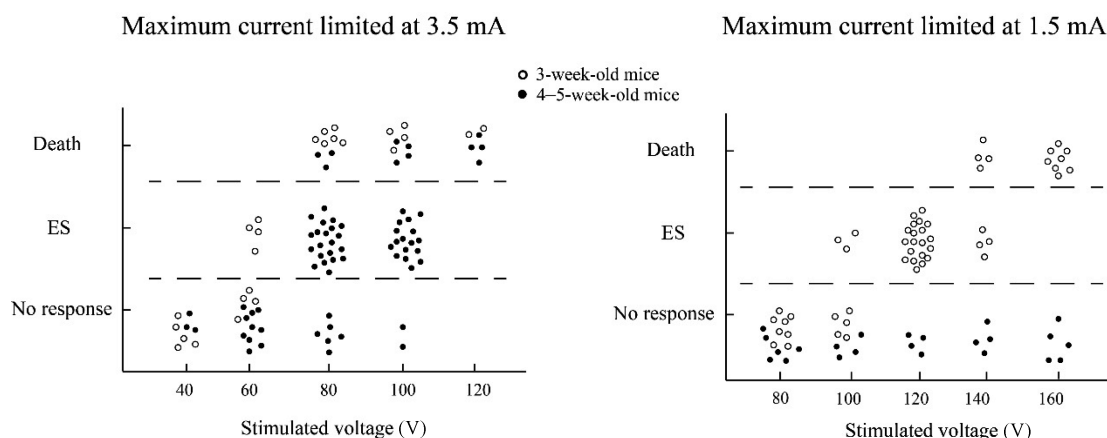

Figure 3 Voltage range of 3-week-old and 4−5-week-old mice showing successful maximal electroshock seizure (MES), no-response, and death with current limited to 3.5 mA or 1.5 mA

When the maximum output current was limited to 3.5 mA (left) or 1.5 mA (right), death, MES, and no response of 3-week-old (circle) and 4−5-week-old mice (solid circle) were in response to constant voltage electrical stimulation. ES: Electroshock seizure.

To validate that the behaviors induced by electrical stimulation in all young mice were the same as epileptic seizures, an antiepileptic positive drug inhibitory experiment was conducted. Phenobarbital sodium, which is a commonly used treatment for epilepsy, was used here to inhibit the epidemiology of MES under an adult median effective dose (ED_{50}) of 2.0 mg/kg. Results showed that it significantly inhibited the onset of ES behavior in 1−2-week-old (10/16), 3-week-old (7 / 13), and 4−5-week-old mice (4 / 8), as shown in Table 3. These results suggest that although the behavior and ranges of voltage and current that induced ES in young mice differed from that observed in adults (Ferraro et al., 2002),

they were still indicative of epileptic episode and could be inhibited by antiepileptic drugs.

The present study used the MEST paradigm to explore neurophysiological differences in three developmental stages before puberty in mice. We found that seizure was induced in all three groups of young mice (less than 5 weeks of age) soon after electrical stimulation. The 1−2-week-old mice exhibited both forelimb and tail stiffness with mild convulsions, whereas the other two groups displayed hind-limb extension, fall, and back rigidity. All young mice foamed at the mouth during seizure and experienced urinary incontinence, but recovered to normal activity after 2−5 s. In addition to

Table 3 Inhibition of phenobarbital sodium on MES behavior

Group	Treatment	Total (MES/Anti-convulsant)	Inhibition (%)
1–2 weeks	ES	9 (9/0)	62.5 ($P^{\#}$=0.008 8)
	ES+PB	16(6/10)	
3 weeks	ES	12(12/0)	53.8 (P=0.005 2)
	ES+PB	13(6/7)	
4–5 weeks	ES	16(16/0)	50 (P=0.006 6)
	ES+PB	8(4/4)	

ES: Electroshock seizure. PB: Phenobarbital sodium, which was administered via intraperitoneal injection at a dose of 2.0 mg / kg. $^{\#}$: Statistics were analyzed by *Chi*-square test.

differences in seizure behavior, the three age groups demonstrated different behavioral outcomes under electrical stimulation. For example, 3-week-old mice showed significantly higher mortality when the SC was 4.0 and 3.5 mA. Only when the current was limited to 1.5 mA could they survive after induction of MES, whereas, the mice in the 4-5-week group showed no responses to electrical stimulations. The optimal MES stimulation conditions in 4–5-week-old mice in this study are similar to those of adult rats in previous studies (Ferraro et al., 2002). Unexpectedly, we found that not only did 1–2-week-old mice experience induced seizures at lower voltage, but they also survived at higher voltage stimulation.

Seizures induced by electroshock are one of the two most widely studied animal models of generalized epilepsy, the other being pentylenetetrazol (PTZ) administration (Loscher, 2011). Accumulated evidence implicates structures of the brainstem as being involved in both kinds of experimental seizures. Stimulation of the midbrain reticular formation induces motor seizures in cats, rats, and rabbits (Kreindler et al., 1958). The substantia nigra also seems to play an important role in mediating seizure discharge release. The seizures (tonic hindlimb extension behaviors of 3 - and 4 – 5-week-old mice in the present study) induced by MES can be prevented by lesions of the substantia nigra in rats (Garant & Gale, 1983). Furthermore, injections of GABA agonist muscimol and opiates into the same region can also prevent MES-induced seizures (Iadarola & Gale, 1982). However, lesions in the mesencephalic reticular formation can antagonize the production of PTZ-induced convulsions (Jinnai et al., 1969). Moreover, seizures induced by PTZ administration rather than MES can be protect by bilateral diencephalic lesions. (Mirski & Ferrendelli, 1986). It is not yet clear whether the diencephalon and substantia nigra are parts of a single complex neuroanatomical network mediating experimental seizures or whether they belong to two separate independent pathways for propagation of different types of seizures. As mice reach sexual maturity at 6–7 weeks of age, these young mice possibly correspond to different human developmental periods: 1–2 weeks corresponds to a breastfeeding infant period, 3 weeks corresponds to the childhood weaning period, and 4–5 weeks corresponds to early puberty (Miao, 1997). In the new postnatal brain, the neural fiber connection is involved in rapid synaptic formation and redundant cutting. For 1–2-week-old mice, the connection state of the diencephalic and mesencephalic structures differs from that of the older group, which may be the cause of specific seizure phenotypes and greater resilience to electrical stimulation. Previous investigations have found that adult mice die from MES due to respiratory arrest (Buchanan et al., 2014). The high mortality of the 3-week-old mice may also be due to changes in the state of connection in the brainstem, resulting in increased susceptibility to inhibition of the respiratory center.

As pediatric epilepsy is one of the most vulnerable diseases in children (Keezer et al., 2016), the MEST paradigm was used to explore the physiological variation in the prepuberty brain. Animal epilepsy models of ES are useful for investigating pathophysiological mechanisms and developing or evaluating new antiepileptic treatments. However, the development of pediatric epilepsy models is still challenging due to dynamic development in the immature brain. Yet, MES and intravenous pentylenetetrazol tests can be used to demonstrate the anticonvulsant properties of anti-epileptic drugs. The former acts as an acute seizure model (Castel-Branco et al., 2009; Murakami et al., 2007), whereas the latter is a chronic model (Loyens et al., 2012). They can help to identify the effects of compounds on seizure spread and increase the seizure threshold, respectively. In this study, phenobarbital, an antiepileptic positive drug, was used to determine if the induced behaviors in 1–2-week-old mice were the same as epileptic seizures. The MES reactions were compared between mice with prior injection of phenobarbital (2.0 mg / kg) and the blank solvent control. Results showed that all MES behaviors in tested mice at the three developmental stages were significantly inhibited at similar intensity with phenobarbital, indicating that the MES behaviors of the mice were the same as those experienced during epileptic seizures.

Thus, physiological variation in the prepubertal brain to electrical stimulation at different developmental stages was found using the MEST paradigm, with the three age groups exhibiting different behavioral outcomes. The results from this study will improve our knowledge regarding early brain development and provide new evidence that neural pathology in children differs from that in adults, suggesting that the development of the brain from birth to adolescence is extremely dynamic. Thus, it is necessary to strictly divide the developmental stages of youth to obtain an appropriate animal model.

COMPETING INTERESTS

AUTHORS' CONTRIBUTIONS

Cheng Xiang[1,#], Zhi-Na Li[1,#], Tian-Zhuang Huang[1],
Jing-Hui Li[2], Lei Yang[3], Jing-Kuan Wei[1,*]

[1] *Faculty of Life Science and Technology, Kunming University of
Science and Technology, Kunming Yunnan* 650500, *China*
[2] *First Affiliated Hospital of Kunming Medical University, Kunming
Yunnan* 650032, *China*
[3] *Department of Neurosurgery, Kunming Children's Hospital,
Kunming Yunnan* 650021, *China*
[#]Authors contributed equally to this work
[*]Corresponding author, E-mail: weijingkuan@163.com

REFERENCES

Buchanan GF, Murray NM, Hajek MA, Richerson GB. 2014. Serotonin neurones have anti-convulsant effects and reduce seizure-induced mortality. *The Journal of Physiology*, **592**(19): 4395–4410.

Castel-Branco MM, Alves GL, Figueiredo IV, Falcao AC, Caramona MM. 2009. The maximal electroshock seizure (MES) model in the preclinical assessment of potential new antiepileptic drugs. *Methods and Findings in Experimental and Clinical Pharmacology*, **31**(2): 101–106.

Chen XB, Zhang H, Gao Y, Wee CY, Li G, Shen DG.. Alzheimer's Disease Neuroimaging Initiative. 2016. High-order resting-state functional connectivity network for MCI classification. *Human Brain Mapping*, **37**(9): 3282–3296.

Chen Y, Yu J, Niu Y, Qin D, Liu H, Li G, Hu Y, Wang J, Lu Y, Kang Y, Jiang Y, Wu K, Li S, Wei J, He J, Wang J, Liu X, Luo Y, Si C, Bai R, Zhang K, Liu J, Huang S, Chen Z, Wang S, Chen X, Bao X, Zhang Q, Li F, Geng R, Liang A, Shen D, Jiang T, Hu X, Ma Y, Ji W, Sun YE. 2017. Modeling rett syndrome using TALEN-edited MECP2 mutant cynomolgus monkeys. *Cell*, **169**(5): 945–955, e910

Ferraro TN, Golden GT, Smith GG, DeMuth D, Buono RJ, Berrettini WH. 2002. Mouse strain variation in maximal electroshock seizure threshold. *Brain Research*, **936**(1–2): 82–86.

Ferraro TN, Golden GT, Snyder R, Laibinis M, Smith GG, Buono RJ, Berrettini WH. 1998. Genetic influences on electrical seizure threshold. *Brain Research*, **813**(1): 207–210.

Fischer W, Muller M. 1988. Pharmacological modulation of central monoaminergic systems and influence on the anticonvulsant effectiveness of standard antiepileptics in maximal electroshock seizure. *Biomedica Biochimica Acta*, **47** : 631–645.

Garant DS, Gale K. 1983. Lesions of substantia nigra protect against experimentally induced seizures. *Brain Research*, **273**(1): 156–161.

Gogtay N, Giedd JN, Lusk L, Hayashi KM, Greenstein D, Vaituzis AC, Nugent TF 3rd, Herman DH, Clasen LS, Toga AW, Rapoport JL, Thompson PM. 2004. Dynamic mapping of human cortical development during childhood through early adulthood. *Proceedings of the National Academy of Sciences of the United States of America*, **101**(21): 8174–8179.

Iadarola MJ, Gale K. 1982. Substantia nigra: site of anticonvulsant activity mediated by gamma-aminobutyric acid. *Science*, **218**(4578): 1237–1240.

Jinnai D, Mogami H, Mukawa J, Iwata Y, Kobayashi K. 1969. Effect of brain-stem lesions on metrazol-induced seizures in cats. *Electroencephalography and Clinical Neurophysiology*, **27**(4): 404–411.

Kamei C, Masuda Y, Oka M, Shimizu M. 1978. Effects of antiepileptics on both behavioral and electrographic seizure patterns induced by maximal electroshock in rats. *Epilepsia*, **19**(6): 625–636.

Keezer MR, Sisodiya SM, Sander JW. 2016. Comorbidities of epilepsy: current concepts and future perspectives. *The Lancet Neurology*, **15**(1): 106–115.

Knickmeyer RC, Gouttard S, Kang C, Evans D, Wilber K, Smith JK, Hamer RM, Lin W, Gerig G, Gilmore JH. 2008. A structural MRI study of human brain development from birth to 2 years. *The Journal of Neuroscience*, **28**(47): 12176–12182.

Kreindler A, Zuckermann E, Steriade M, Chimion D. 1958. Electro-clinical features of convulsions induced by stimulation of brain stem. *Journal of Neurophysiology*, **21**(5): 430–436.

Li G, Liu T, Ni D, Lin W, Gilmore JH, Shen D. 2015. Spatiotemporal patterns of cortical fiber density in developing infants, and their relationship with cortical thickness. *Human Brain Mapping*, **36**(12): 5183–5195.

Li G, Nie J, Wang L, Shi F, Lin W, Gilmore JH, Shen D. 2013. Mapping region-specific longitudinal cortical surface expansion from birth to 2 years of age. *Cerebral Cortex*, **23**(11): 2724–2733.

Li G, Wang L, Shi F, Lyall AE, Ahn M, Peng Z, Zhu H, Lin W, Gilmore JH, Shen D. 2016. Cortical thickness and surface area in neonates at high risk for schizophrenia. *Brain Structure and Function*, **221**(1): 447–461.

Löscher W. 2011. Critical review of current animal models of seizures and epilepsy used in the discovery and development of new antiepileptic drugs. *Seizure*, **20**(5): 359–368.

Loyens E, Vermoesen K, Schallier A, Michotte Y, Smolders I. 2012. Proconvulsive effects of oxytocin in the generalized pentylenetetrazol mouse model are mediated by vasopressin 1a receptors. *Brain Research*, **1436**(3): 43-50.

Miao MS. 1997. Experimental Animal and Animal Experimental Techniques. Beijing: China Press of Traditional Chinese Medicine.

Mirski MA, Ferrendelli JA. 1986. Selective metabolic activation of the mammillary bodies and their connections during ethosuximide-induced suppression of pentylenetetrazol seizures. *Epilepsia*, **27**(3): 194–203.

Murakami A, Ishikawa T, Takechi K, Ago J, Matsumoto N, Kamei C. 2007. Effects of certain antiepileptics on behavioral and electromyographic seizure patterns induced by maximal electroshock in mice. *Journal of Pharmacological Sciences*, **104**(1): 56–60.

Stiles J, Jernigan TL. 2010. The basics of brain development. *Neuropsychology Review*, **20**(4): 327–348.

Xu SY, BIan RL, Chen X. 2011. Pharmacological Experimental Methodology. Beijing: Military Science Publishing House.

A transgenic monkey model for the study of human brain evolution

Lei Shi[1,2], Bing Su[1,2,3,*]

[1] *State Key Laboratory of Genetic Resources and Evolution*, *Kunming Institute of Zoology*, *Chinese Academy of Sciences*, *Kunming Yunnan* 650223, *China*

[2] *Primate Research Center*, *Kunming Institute of Zoology*, *Chinese Academy of Sciences*, *Kunming Yunnan* 650223, *China*

[3] *Center for Excellence in Animal Evolution and Genetics*, *Chinese Academy of Sciences*, *Kunming Yunnan* 650223, *China*

Why humans have large brains with higher cognitive abilities is a question long asked by scientists. However, much remains unknown, especially the underlying genetic mechanisms. With the use of a transgenic monkey model, we showed that human-specific sequence changes of a key brain development gene (Primary microcephaly 1, *MCPH1*) could result in detectable molecular and cognitive changes resembling human neoteny, a notable characteristic developed during human evolution. This study was published in *National Science Review* (Shi et al., 2019).

Neoteny has been hypothesized to help explain why we differ from our close relatives, such as the chimpanzee (*Pan troglodytes*) (Liu et al., 2012). Also called juvenilization, neoteny is the delay in or slowing down of physiological development of a species (Skulachev et al., 2017). Neoteny in humans is the retention of juvenile features into adulthood and is exaggerated compared to that in non-human primates. The neotenous human brain provides an extended window for the plasticity of the neural network, and therefore a longer time for learning, which may be crucial for the formation of human cognition (Bufill et al., 2011).

In the past two decades, comparative genomic studies have identified many candidate genes that carry human-specific sequence changes potentially contributing to human brain evolution (Bustamante et al., 2005; Clark et al., 2003). However, functional dissection of these candidate genes, particularly the phenotypic consequences of human-specific mutations, is lacking. As a model organism, transgenic mice (*Mus musculus*) have been used in the study of human brain function; for example, the study of *Foxp2* that carries two human-specific amino acid changes (Enard et al., 2009). However, compared to the human brain, the mouse brain is dramatically different in size, structure, developmental pattern, and function, and therefore is not an ideal model to study human brain evolution. In contrast, the rhesus monkey (*Macaca mulatta*), an Old-World primate species widely used in biomedical research, is a better animal model due to its high sequence similarity with humans (>93% for protein coding genes) (Yan et al., 2011;

Zhang et al., 2014), yet relatively large phylogenetic distance (~25 million years of divergence from humans), which alleviates certain ethical concerns (Coors et al., 2010). These advantages have been demonstrated in the use of transgenic monkey models of human diseases (Chen et al., 2017; Liu et al., 2016; Luo et al., 2016; Qiu et al., 2019; Yang et al., 2008; Zhang et al., 2018).

MCPH1 is a key gene regulating brain development in humans, and its truncate mutations can cause primary microcephaly (Jackson et al., 2002). Similarly, *MCPH1* knockout in mice and monkeys can recapitulate the microcephaly phenotype (Gruber et al., 2011; Ke et al., 2016), highlighting its critical role in mammalian brain development. In previous research, we demonstrated accelerated protein sequence changes in *MCPH1* during primate evolution, especially in the lineage leading to the origin of our own species (Wang & Su, 2004). Furthermore, *in vitro* functional analysis showed that human-specific *MCPH1* changes resulted in functional divergence between human and non-human primates (Shi et al., 2013). Such lines of evidence raise the question as to what phenotypic changes would appear following the introduction of human *MCPH1* copies into the rhesus monkey genome.

Using lentivirus delivery, we successfully generated 11 transgenic monkeys carrying 2−9 copies of human *MCPH1*. Brain image analysis showed that the transgenic monkeys had similar brain volume and cortex thickness as the controls, but their relative brain volume and gray matter percentage were higher. Importantly, the transgenic monkeys exhibited delayed cortex gray matter development compared to the

controls. Furthermore, the transgenic monkeys had more immature and fewer mature neurons and glial cells than the controls, which, according to the transcriptome data, was likely caused by the suppression of many neuron maturation- and neuron differentiation-related genes. This observation was further illustrated by detailed analysis of developing brain laminas at the neurogenesis peak during fetal development.

Finally, to test whether the observed delay in brain development had any impact on behavior and cognition, we tested working memory in the transgenic monkeys using delayed matching-to-sample tasks. Notably, the transgenic monkeys exhibited better working memory and shorter reaction time than the controls, suggesting that neotenous brain development in the transgenic monkeys was beneficial for the formation of cognitive abilities, confirming the proposed evolutionary advantage of human neoteny. In our future work, we will: (1) examine the molecular pathway explaining how human *MCPH1* copies delay brain development and neural maturation, thus identifying more neoteny-related genes; and (2) apply more sophisticated tests to further understand how the neotenous brain affects cognitive formation in transgenic monkeys.

This study represents the first attempt to utilize a transgenic monkey model to study human brain evolution. It also provides the first molecular genetic evidence showing neotenous changes during brain development caused by human-specific mutations of a single gene. The results highlight the great potential of non-human primate models in studying human evolution and may pave the way for future studies to explore the genetic mechanisms of human-specific traits and elucidate the etiology of human brain disorders such as autism and Alzheimer's disease.

COMPETING INTERESTS

The authors declare that they have no competing interests.

AUTHORS' CONTRIBUTIONS

L.S. and B.S. wrote the manuscript. All authors read and approved the final version of the manuscript.

REFERENCES

Bufill E, Agustí J, Blesa R. 2011. Human neoteny revisited: The case of synaptic plasticity. *American Journal of Human Biology*, **23**(6): 729–739.

Bustamante CD, Fledel-Alon A, Williamson S, Nielsen R, Hubisz MT, Glanowski S, Tanenbaum DM, White TJ, Sninsky JJ, Hernandez RD, Civello D, Adams MD, Cargill M, Clark AG. 2005. Natural selection on protein-coding genes in the human genome. *Nature*, **437**(7062): 1153–1157.

Chen Y, Yu J, Niu Y, Qin D, Liu H, Li G, Hu Y, Wang J, Lu Y, Kang Y, Jiang Y, Wu K, Li S, Wei J, He J, Wang J, Liu X, Luo Y, Si C, Bai R, Zhang K, Liu J, Huang S, Chen Z, Wang S, Chen X, Bao X, Zhang Q, Li F, Geng R, Liang A, Shen D, Jiang T, Hu X, Ma Y, Ji W, Sun Y. E. 2017. Modeling rett syndrome using TALEN-Edited MECP2 mutant cynomolgus monkeys. *Cell*, **169**(5): 945–955.

Clark AG, Glanowski S, Nielsen R, Thomas PD, Kejariwal A, Todd MA, Tanenbaum DM, Civello D, Lu F, Murphy B, Ferriera S, Wang G, Zheng X, White TJ, Sninsky JJ, Adams MD, Cargill M. 2003. Inferring nonneutral evolution from human-chimp-mouse orthologous gene trios. *Science*, **302**(5652): 1960–1963.

Coors ME, Glover JJ, Juengst ET, Sikela JM. 2010. The ethics of using transgenic non-human primates to study what makes us human. *Nature Reviews Genetics*, **11**(9): 658–662.

Enard W, Gehre S, Hammerschmidt K, Hölter SM, Blass T, Somel M, Brückner MK, Schreiweis C, Winter C, Sohr R, Becker L, Wiebe V, Nickel B, Giger T, Müller U, Groszer M, Adler T, Aguilar A, Bolle I, Calzada-Wack J, Dalke C, Ehrhardt N, Favor J, Fuchs H, Gailus-Durner V, Hans W, Hölzlwimmer G, Javaheri A, Kalaydjiev S, Kallnik M, Kling E, Kunder S, Mossbrugger I, Naton B, Racz I, Rathkolb B, Rozman J, Schrewe A, Busch DH, Graw J, Ivandic B, Klingenspor M, Klopstock T, Ollert M, Quintanilla-Martinez L, Schulz H, Wolf E, Wurst W, Zimmer A, Fisher SE, Morgenstern R, Arendt T, de Angelis MH, Fischer J, Schwarz J, Pääbo S. 2009. A humanized version of Foxp2 affects cortico-basal ganglia circuits in mice. *Cell*, **137**(5): 961–971.

Gruber R, Zhou Z, Sukchev M, Joerss T, Frappart PO, Wang ZQ. 2011. MCPH1 regulates the neuroprogenitor division mode by coupling the centrosomal cycle with mitotic entry through the Chk1-Cdc25 pathway. *Nature Cell Biology*, **13**(11): 1325–1334.

Jackson AP, Eastwood H, Bell SM, Adu J, Toomes C, Carr IM, Roberts E, Hampshire DJ, Crow YJ, Mighell AJ, Karbani G, Jafri H, Rashid Y, Mueller RF, Markham AF, Woods CG. 2002. Identification of microcephalin, a protein implicated in determining the size of the human brain. *American Journal of Human Genetics*, **71**(1): 136–142.

Ke Q, Li W, Lai X, Chen H, Huang L, Kang Z, Li K, Ren J, Lin X, Zheng H, Huang W, Ma Y, Xu D, Chen Z, Song X, Lin X, Zhuang M, Wang T, Zhuang F, Xi J, Mao FF, Xia H, Lahn BT, Zhou Q, Yang S, Xiang AP. 2016. TALEN-based generation of a cynomolgus monkey disease model for human microcephaly. *Cell Research*, **26**(9): 1048–1061.

Liu X, Somel M, Tang L, Yan Z, Jiang X, Guo S, Yuan Y, He L, Oleksiak A, Zhang Y, Li N, Hu Y, Chen W, Qiu Z, Paabo S, Khaitovich P. 2012. Extension of cortical synaptic development distinguishes humans from chimpanzees and macaques. *Genome Research*, **22**(4): 611–622.

Liu Z, Li X, Zhang JT, Cai YJ, Cheng TJ, Cheng C, Wang Y, Zhang CC, Nie YH, Chen ZF, Bian WJ, Zhang L, Xiao J, Lu B, Zhang YF, Zhang XD, Sang X, Wu JJ, Xu X, Xiong ZQ, Zhang F, Yu X, Gong N, Zhou WH, Sun Q, Qiu Z. 2016. Autism-like behaviours and germline transmission in transgenic monkeys overexpressing MeCP2. *Nature*, **530**(7588): 98–102.

Luo X, Li M, Su B. 2016. Application of the genome editing tool CRISPR/Cas9 in non-human primates. *Zoological Research*, **37**(4): 214–219.

Qiu P, Jiang J, Liu Z, Cai Y, Huang T, Wang Y, Liu Q, Nie Y, Liu F, Cheng J, Li Q, Tang YC, Poo MM, Sun Q, Chang HC. 2019. BMAL1 knockout macaque monkeys display reduced sleep and psychiatric disorders. *National Science Review*, **6**(1): 87–100.

Shi L, Li M, Lin Q, Qi X, Su B. 2013. Functional divergence of the brain-size regulating gene MCPH1 during primate evolution and the origin of humans. *BMC Biology*, **11**: 62.

Shi L, Luo X, Jiang J, Chen Y, Liu C, Hu T, Li M, Lin Q, Li Y, Huang J, Wang H, Niu Y, Shi Y, Styner M, Wang J, Lu Y, Sun X, Yu H, Ji W, Su B. 2019. Transgenic rhesus monkeys carrying the human MCPH1 gene copies show

human-like neoteny of brain development. *National Science Review*, doi: 10.1093/nsr/nwz043.

Skulachev VP, Holtze S, Vyssokikh MY, Bakeeva LE, Skulachev MV, Markov AV, Hildebrandt TB, Sadovnichii VA. 2017. Neoteny, prolongation of youth: from naked mole rats to "naked apes" (humans). *Physiological Reviews*, **97**(2):699–720.

Wang YQ, Su B. 2004. Molecular evolution of microcephalin, a gene determining human brain size. *Human Molecular Genetics*, **13**(11): 1131–1137.

Yan G, Zhang G, Fang X, Zhang Y, Li C, Ling F, Cooper DN, Li Q, Li Y, van Gool AJ, Du H, Chen J, Chen R, Zhang P, Huang Z, Thompson JR, Meng Y, Bai Y, Wang J, Zhuo M, Wang T, Huang Y, Wei L, Li J, Wang Z, Hu H, Yang P, Le L, Stenson PD, Li B, Liu X, Ball EV, An N, Huang Q, Zhang Y, Fan W, Zhang X, Li Y, Wang W, Katze MG, Su B, Nielsen R, Yang H, Wang J, Wang X, Wang J. 2011. Genome sequencing and comparison of two nonhuman primate animal models, the cynomolgus and Chinese rhesus macaques. *Nature Biotechnology*, **29**(11): 1019–1023.

Yang SH, Cheng PH, Banta H, Piotrowska-Nitsche K, Yang JJ, Cheng EC, Snyder B, Larkin K, Liu J, Orkin J, Fang ZH, Smith Y, Bachevalier J, Zola SM, Li SH, Li XJ, Chan AWS. 2008. Towards a transgenic model of Huntington's disease in a non-human primate. *Nature*, **453**(7197): 921–924.

Zhang W, Wan H, Feng G, Qu J, Wang J, Jing Y, Ren R, Liu Z, Zhang L, Chen Z, Wang S, Zhao Y, Wang Z, Yuan Y, Zhou Q, Li W, Liu GH, Hu B. 2018. SIRT6 deficiency results in developmental retardation in cynomolgus monkeys. *Nature*, **560**(7720): 661–665.

Zhang XL, Pang W, Hu XT, Li JL, Yao YG, Zheng YT. 2014. Experimental primates and non-human primate (NHP) models of human diseases in China: current status and progress. *Zoological Research*, **35**(6): 447–464.